

VON KARMAN INSTITUTE

FOR FLUID DYNAMICS

Lecture Series 1995-03

INDUSTRIAL COMPUTATIONAL FLUID DYNAMICS

DTIC USERS ONLY

April 3 - 7, 1995

Volume 2

19971010 022



RHODE SAINT GENESE BELGIUM

DTIC QUALITY INSPECTED 3

ISSN0377-8312

von Karman Institute for Fluid Dynamics
Chaussée de Waterloo, 72
B - 1640 Rhode Saint Genèse - Belgium

Lecture Series 1995-03

INDUSTRIAL COMPUTATIONAL FLUID DYNAMICS

April 3 - 7, 1995

Lecture Series Directors : J-M. Buchlin & Ph. Planquart

DTIC QUALITY INSPECTED 3

D/1995/0238/430

VKI LS 1995-03

©1995 by the von Karman Institute

*The contents of this book are the property of the von Karman Institute for Fluid Dynamics.
No part of this book may be reproduced or distributed in any form of by any means, or stored in a
database or retrieval system, without the prior written permission of the von Karman Institute.*

TABLE OF CONTENTS

VOLUME 1:

Foreword

HIRSCH, C. - *Vrije Universiteit Brussel, Belgium*

State of the art of computational fluid dynamics in industry

VANDROMME, D. - *INSA de Rouen, France*

Overview of turbulence models for CFD in industry

BIDOT, T. & CHARGY, D. - *SIMULOG, France*; POT, G. - *EDF/DER, France*

CFD applications in the automotive industry using the N3S code

FONTAINE, J.R. - *INRS, France*

CFD applications in ventilation

VOLUME 2:

WILD, P.N. & BOYSAN, H.F. - *Fluent Europe, UK*

Modelling mass transfer, chemical reactions and combustion

SPALDING, B. - *CHAM, UK*

- Modelling conductive, convective and radiative heat transfer
- Numerical simulation of heat transfer using PHOENICS

DILBER, I. - *FDI, USA*

- Modelling multiple phase flow and phase change
- Applications of multiple phase modeling using FIDAP

CROCHET, M.J. - *POLYFLOW S.A., Belgium*

Numerical simulation in non-Newtonian fluid mechanics

SUBBIAH, S. - *Fluent Inc., USA*

- Modelling of flows with unknown free surfaces
- Numerical simulation of coating flows using NEKTON

VERGISON, E. - *SOLVAY S.A., Belgium*

Dispersion of pollutants

von Karman Institute for Fluid Dynamics

Lecture Series 1995-03

INDUSTRIAL COMPUTATIONAL FLUID DYNAMICS

April 3 - 7, 1995

MODELLING MASS TRANSFER, CHEMICAL REACTIONS AND COMBUSTION

P.N. Wild & H.F. Boysan

Fluent Europe, UK

Course Content

- 1 Introduction.
 - 1.1 An overview of combustion phenomena.
 - 1.2 Classification of combustion problems.
- 2 Modelling the combustion reactions.
 - 2.1 Chemical kinetics
 - 2.2 Global kinetics
 - 2.3 Modelling combustion reactions in turbulent flow
- 3 Modelling variable density reacting flow.
- 4 Additional sub models.
 - 4.1 Radiative heat transfer
 - 4.2 Second phase models
- 5 Predicting NO_x emissions.
- 6 Conclusion.

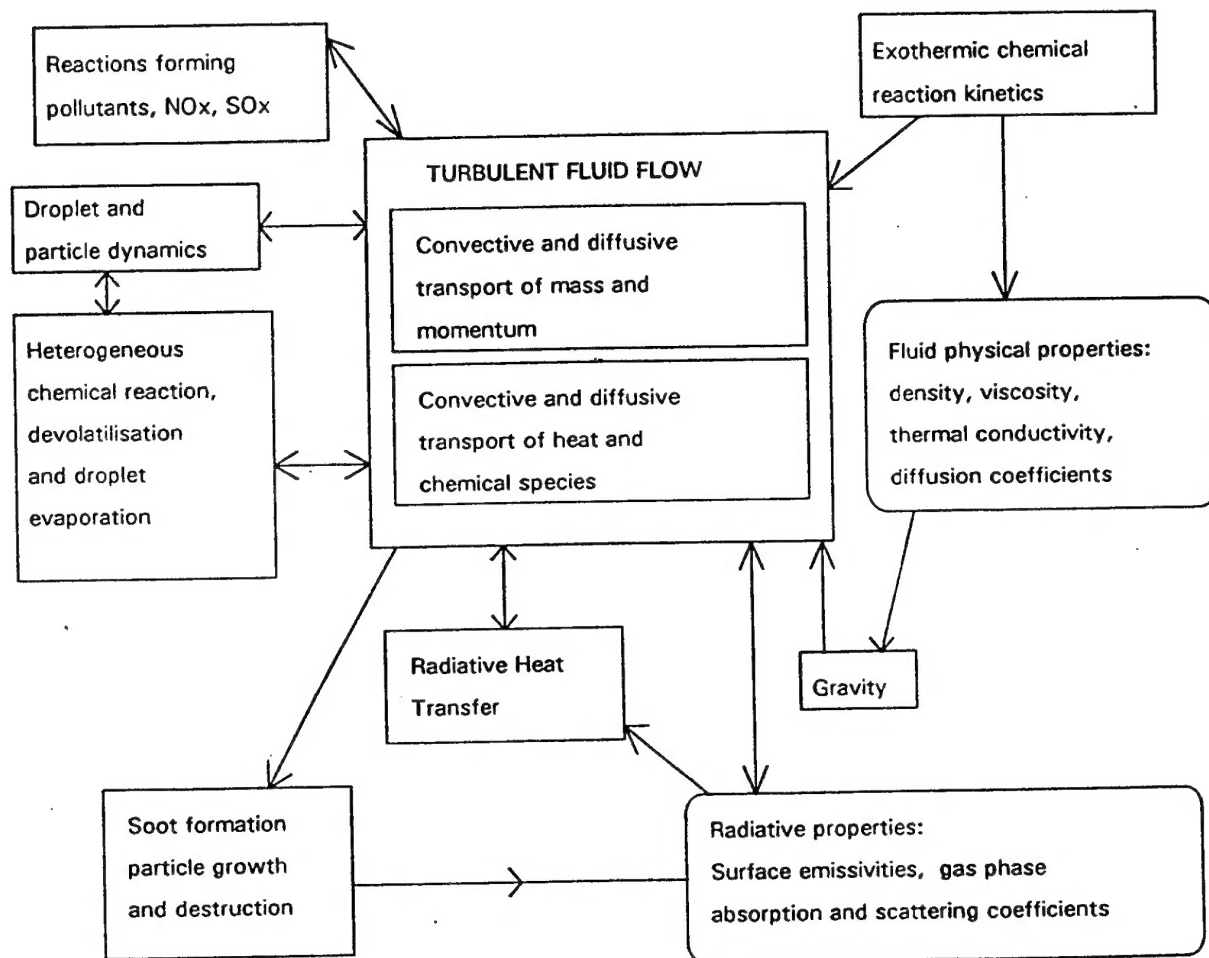
1 Introduction

1.1 An overview of combustion phenomena

- Question 1** What are the chemical and physical phenomena occurring in combustion systems?
- Question 2** How do these phenomena interact with each other?
- Question 3** For a given application, which of the above are most important and how can they be represented in a numerical model?

Processes Occurring in Turbulent Combustion and Their Interaction

Answer 1, 2



Answer 3

Dependent on the type of application.

Different boundary conditions will lead to different combustion regimes for which different model approximations may be appropriate.

Dependent on the level of information required from the model.

For example, if the code is not required to predict wall temperatures, or is not required to predict NO_x emissions, a simpler modelling strategy might be employed.

1.2 Classification of combustion problems.

Interaction of combustion chemistry and turbulence.

The Damköhler number.

The Damköhler number is a ratio of characteristic flow time to chemical reaction time:

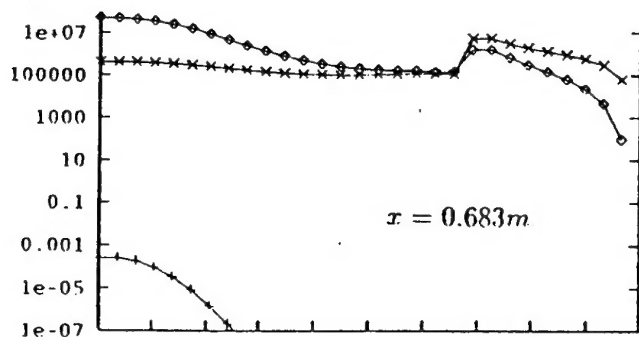
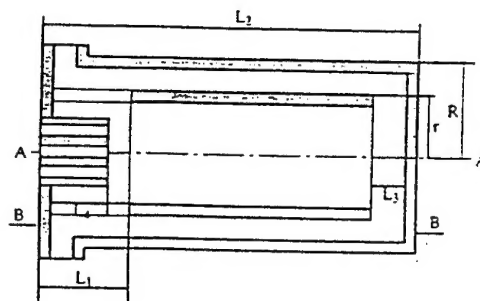
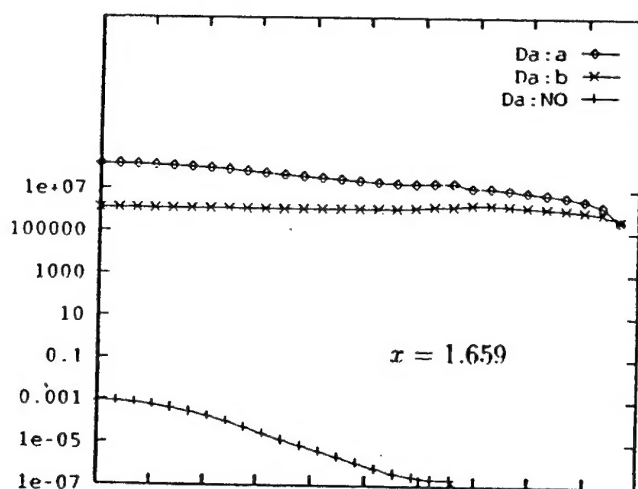
$$Da = \frac{\tau_F}{\tau_r} = \frac{\ell}{u' \tau_r}$$

where ℓ and u' are turbulent length and velocity scales respectively.

Using the k, ϵ turbulence model and an Arrhenius kinetic rate expression we may write:

$$D = \frac{k}{\epsilon} \left(AT^n e^{-\frac{T_a}{T}} \right)$$

Values of D for an industrial propane burner. Taken from computations by Bai, X. S. and Fuchs, L.¹



¹Bai, X. S., and Fuchs, L, Improved Efficiency of Combustion in Furnaces with Flow Redistribution, Royal Institute, Stockholm.

Low Damköhler number flames:

$$Da \ll 1$$

Chemical reactions are orders of magnitude slower than turbulent mixing rates and the influence of turbulence on reaction can be neglected.

High Damköhler number flames:

$$Da \gg 1$$

Finite rate chemistry can be neglected as turbulent mixing controls combustion.

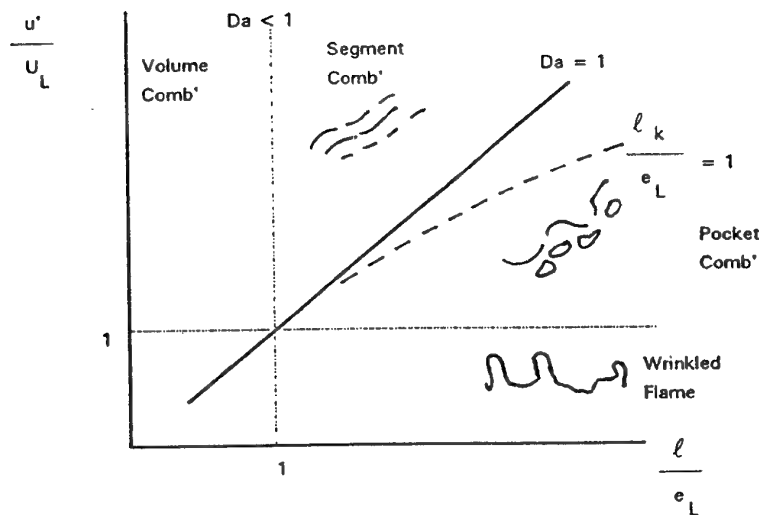
Intermediate Damköhler number:

Both turbulent mixing and finite rate chemistry must be considered.

An important classification for flames is into the categories of Diffusion and Premixed.

For premixed flames there is a laminar flame speed U_L which defines a scale of thickness, e_L .

$$Da = \left(\frac{\ell}{u'} \right) / \left(\frac{e_L}{U_L} \right) = \left(\frac{\ell}{e_L} \right) \left(\frac{U_L}{u'} \right)$$



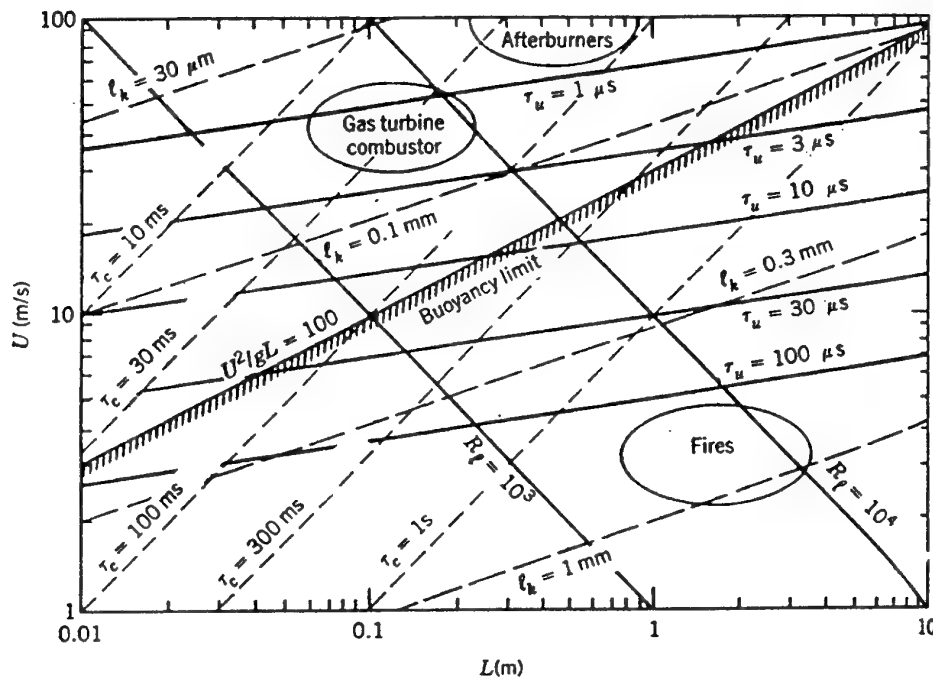
Types of turbulent premixed flame

taken from Borghi, H., and Pourbaix, E²

²Borghi, H., and Pourbaix, E., On the Coupling of Complex Chemistry with a turbulent Combustion Model, PCH, 1981.

Characteristic Scales, Buoyancy and Froude Number.

For combustion chambers of characteristic size L and mean velocity U a dimensional graph can be constructed.

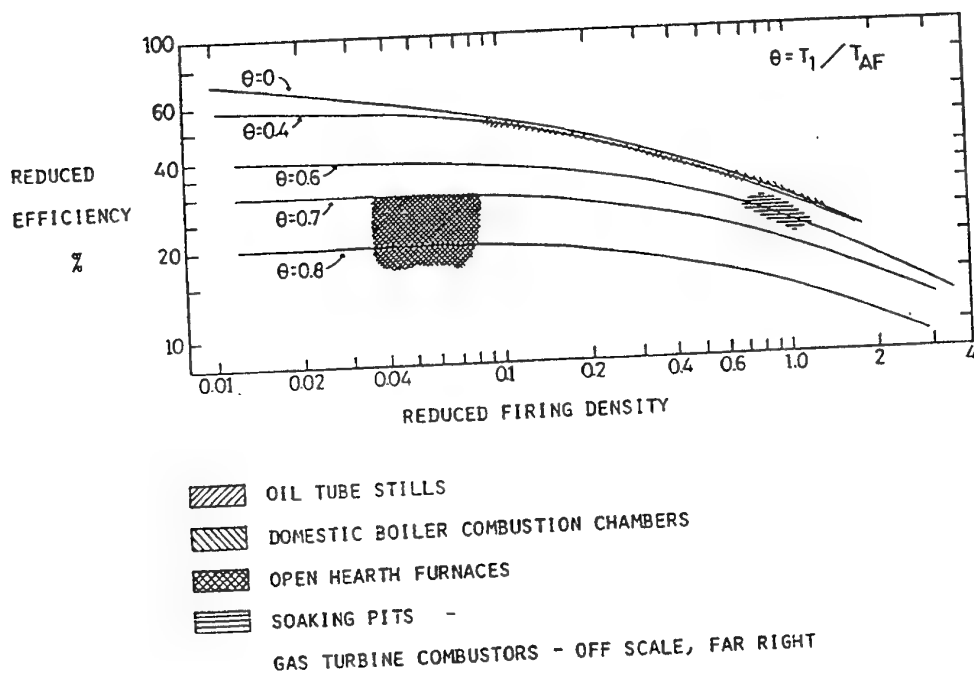


Parameters for combustion with air at atmospheric pressure.

$$\text{Froude number: } Fr = \frac{U^2}{gL}$$

g = acceleration due to gravity.

Classification of Radiative Heat Transfer



Hottel's diagram for Radiative Heat Transfer in furnaces and combustors.

Different practical applications are seen to occupy different regions on the graph.

Hottel's model is based on a well stirred reactor with speckled walls and grey gas.

Reduced Efficiency =

$$\mu_R = \left[\frac{q}{H_{in}} \right] \left[\frac{T_{AF} - T_o}{T_{AF}} \right]$$

Reduced Firing Density =

$$D_R = \frac{H_{in}}{\sigma A_T T_{AF}^3 (T_{AF} - T_o)} \left[\frac{1}{\epsilon_G} + \frac{1}{C\epsilon_1} - 1 \right]$$

A_T	= the chamber surface area
C	= the fraction of surface acting as heat sink
H_{in}	= the enthalpy of entering streams
T_{AF}	= the adiabatic flame temperature
T_o	= the base temperature
T_1	= temperature of sink surface
q	= heat flux to sink
ϵ_G and ϵ_1	= the emissivities of gas and surface respectively

The proportion of energy transferred to the walls by radiation may be negligible in the gas turbine combustor while it is the dominant heat transfer mechanism in industrial furnaces.

2 Modelling the combustion reactions

2.1 Chemical kinetics

A detailed description of methane combustion chemistry typically contains 20 to 100 individual reactions and their associated rate coefficients.

	Reaction	B^b	α^b	$E^b (= RT_a)$
9.1	$O_2 + H \rightarrow OH + O$	2.00×10^{14}	0.00	70.30
9.1 ^b	$OH + O \rightarrow O_2 + H$	1.40×10^{13}	0.00	3.20
9.2	$O + H_2 \rightarrow H + OH$	1.50×10^7	2.00	31.60
9.2 ^b	$H + OH \rightarrow O + H_2$	6.73×10^6	2.00	22.35
9.3	$OH + H_2 \rightarrow H + H_2O$	1.00×10^8	1.60	13.80
9.3 ^b	$H + H_2O \rightarrow OH + H_2$	4.62×10^8	1.60	77.50
9.4	$OH + OH \rightarrow H_2O + O$	1.50×10^9	1.14	0.42
9.4 ^b	$H_2O + O \rightarrow OH + OH$	1.49×10^{10}	1.14	71.14
9.5 ^c	$H + O_2 + M \rightarrow OH_2 + M$	2.30×10^{18}	-0.80	0.00
9.6	$HO_2 + H \rightarrow OH + OH$	1.50×10^{14}	0.00	4.20
9.7	$HO_2 + H \rightarrow H_2 + O_2$	2.50×10^{13}	0.00	2.90
9.8	$HO_2 + H \rightarrow H_2O + O$	3.00×10^{13}	0.00	7.20
9.9	$HO_2 + OH \rightarrow H_2O + O_2$	6.00×10^{13}	0.00	0.00
9.10	$CO + OH \rightarrow CO_2 + H$	4.40×10^6	1.50	-3.10
9.10 ^b	$CO_2 + H \rightarrow CO + OH$	4.96×10^8	1.50	89.71
9.11	$CH_4 + H \rightarrow H_2 + CH_3$	2.20×10^4	3.00	36.60
9.11 ^b	$H_2 + CH_3 \rightarrow CH_4 + H$	8.83×10^2	3.00	33.53
9.12	$CH_4 + OH \rightarrow H_2O + CH_3$	1.60×10^6	2.10	10.30
9.13	$CH_3 + O \rightarrow CH_2O + H$	7.00×10^{13}	0.00	0.00
9.14	$CH_3 + OH \rightarrow CH_2O + H + H$	9.00×10^{14}	0.00	64.80
9.15	$CH_3 + OH \rightarrow CH_2O + H_2$	8.00×10^{12}	0.00	0.00
9.16 ^d	$CH_3 + H \rightarrow CH_4$	6.00×10^{16}	-1.00	0.00
9.17	$CH_2O + H \rightarrow CHO + H_2$	2.50×10^{13}	0.00	16.70
9.18	$CH_2O + OH \rightarrow CHO + H_2O$	3.00×10^{13}	0.00	5.00
9.19	$CHO + H \rightarrow CO + H_2$	2.00×10^{14}	0.00	0.00
9.20	$CHO + OH \rightarrow CO + H_2O$	1.00×10^{14}	0.00	0.00
9.21	$CHO + O_2 \rightarrow CO + HO_2$	3.00×10^{12}	0.00	0.00
9.22 ^c	$CHO + M \rightarrow CO + H + M$	7.10×10^{14}	0.00	70.30
9.23	$CH_3 + H \rightarrow CH_2 + H_2$	1.80×10^{14}	0.00	63.00
9.24	$CH_2 + O_2 \rightarrow CO_2 + H + H$	6.50×10^{12}	0.00	6.30
9.25	$CH_2 + O_2 \rightarrow CO + OH + H$	6.50×10^{12}	0.00	6.30
9.26	$CH_2 + H \rightarrow CH + H_2$	4.00×10^{13}	0.00	0.00
9.26 ^b	$CH + H_2 \rightarrow CH_2 + H$	2.79×10^{13}	0.00	12.61
9.27	$CH + O_2 \rightarrow CHO + O$	3.00×10^{13}	0.00	0.00
9.28	$CH_3 + OH \rightarrow CH_2 + H_2O$	1.50×10^{13}	0.00	20.93
9.29	$CH_2 + OH \rightarrow CH_2O + H$	2.50×10^{13}	0.00	0.00
9.30	$CH_2 + OH \rightarrow CH + H_2O$	4.50×10^{13}	0.00	12.56
9.31	$CH + OH \rightarrow CHO + H$	3.00×10^{13}	0.00	0.00

Mechanism for methane oxidation (Peters, N., and Williams, F. A., Combustion and Flame, Vol 65, 1987). (Units cm mol K kJ)

$$k = BT^\alpha \exp(-E/RT)$$

Detailed mechanisms have only been derived for a relatively small number of simple hydrocarbons.

Even when available the application of such mechanisms in CFD presents many problems:

1. Large computer storage and CPU requirements.
2. Difficulty in solving coupled non-linear rate terms with differing time scales.
3. Difficulty in coupling to other parts of the CFD model, in particular in dealing with the interaction of turbulence and chemistry.

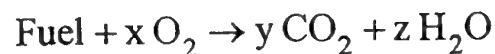
2.2 Global kinetics

Simpler descriptions of chemistry are available based on empirically derived global mechanisms.

The detailed mechanism is replaced by a small number of steps which describe the course of reaction by means of the major reactants and products.

Example:

Single step irreversible reaction:



$$\frac{d[\text{Fuel}]}{dt} = A \exp\left(\frac{-E_a}{RT}\right) [\text{Fuel}]^a [\text{O}_2]^b$$

Rate parameters in the Arrhenius expression are selected to give agreement with experimental results in laminar flames or with computations performed using detailed kinetic models.

(Care must be taken to ensure that the model is applied under conditions for which is valid.)

Data is available for a range of hydrocarbon fuels.

Fuel	A	E_a	a	b
CH ₄	1.3×10^8	48.4	-0.3	1.3
CH ₄	8.3×10^5	30.0	-0.3	1.3
C ₂ H ₆	1.1×10^{12}	30.0	0.1	1.65
C ₃ H ₈	8.6×10^{11}	30.0	0.1	1.65
C ₄ H ₁₀	7.4×10^{11}	30.0	0.15	1.6
C ₅ H ₁₂	6.4×10^{11}	30.0	0.25	1.5
C ₆ H ₁₄	5.7×10^{11}	30.0	0.25	1.5
C ₇ H ₁₆	5.1×10^{11}	30.0	0.25	1.5
C ₈ H ₁₈	4.6×10^{11}	30.0	0.25	1.5
C ₈ H ₁₈	7.2×10^{12}	40.0	0.25	1.5
C ₉ H ₂₀	4.2×10^{11}	30.0	0.25	1.5
C ₁₀ H ₂₂	3.8×10^{11}	30.0	0.25	1.5
CH ₃ OH	3.2×10^{12}	30.0	0.25	1.5
C ₂ H ₅ OH	1.5×10^{12}	30.0	0.15	1.6
C ₆ H ₆	2.0×10^{11}	30.0	-0.1	1.85
C ₇ H ₈	1.6×10^{11}	30.0	-0.1	1.85

Single step rate parameters due to Westbrook and Dryer³
(units cm, sec, kcal, K).

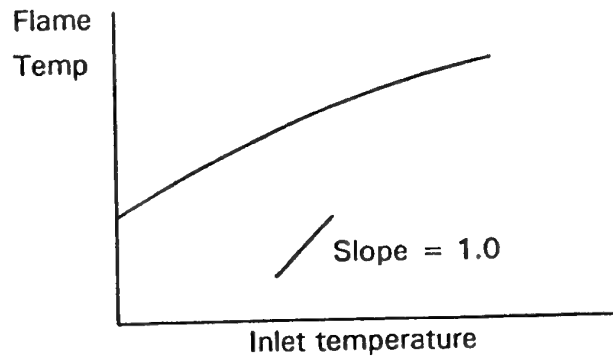
Constants are selected to correctly predict flammability limits and laminar flame speed over a range of equivalence ratios and pressures.

Single step mechanisms over predict adiabatic flame temperature.

The problem worsens with increasing equivalence ratio.
Incomplete conversion to CO₂ and H₂O is responsible.

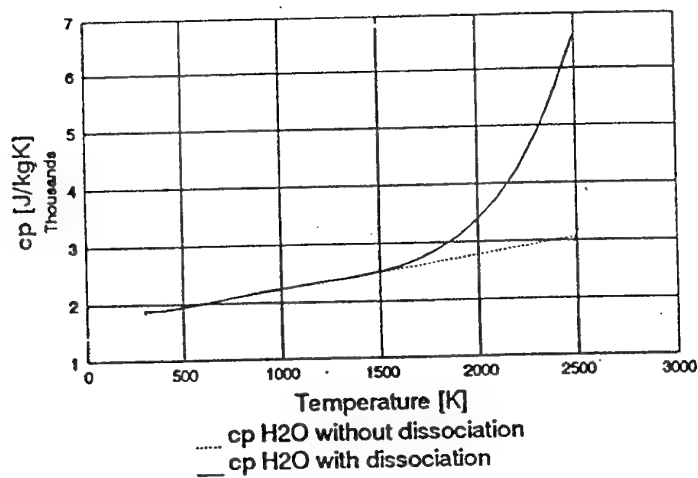
³Westbrook, C. K., and Dryer, F. L., Simplified Reaction Mechanisms for Oxidation of Hydrocarbon Fuels in Flames, Comb Sci Tech, Vol 27, 1981.

At temperatures over 2000 K significant amounts of dissociation products exist.

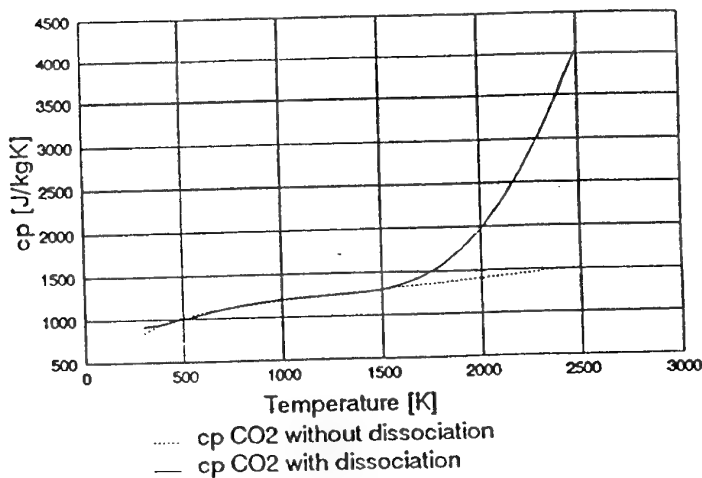


Effect of inlet temperature on flame temperature
(stoichiometric fuel air mixture at atmospheric pressure).

Water



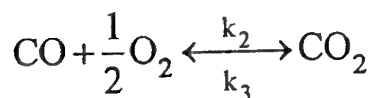
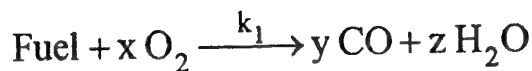
Carbondioxide



Effect of dissociation
on water and CO₂
specific heats

(equilibrium calculations)

Improvements can be made by introducing 2 or more reaction steps³



$$k_1 = A[\text{Fuel}]^a [\text{O}_2]^b \exp\left(\frac{-E_a}{RT}\right)$$

$$k_2 = 10^{14.6} \exp\left(\frac{-40000}{RT}\right) [\text{CO}] [\text{H}_2\text{O}]^{0.5} [\text{O}_2]^{0.25}$$

$$k_3 = 5 \times 10^8 \exp\left(\frac{-40000}{RT}\right) [\text{CO}_2]$$

Fuel	A	E _a	a	b
CH ₄	2.8 × 10 ⁹	48.4	-0.3	1.3
CH ₄	1.5 × 10 ⁷	30.0	-0.3	1.3
C ₂ H ₆	1.3 × 10 ¹²	30.0	0.1	1.65
C ₃ H ₈	1.0 × 10 ¹²	30.0	0.1	1.65
C ₄ H ₁₀	8.8 × 10 ¹¹	30.0	0.15	1.6
C ₅ H ₁₂	7.8 × 10 ¹¹	30.0	0.25	1.5
C ₆ H ₁₄	7.0 × 10 ¹¹	30.0	0.25	1.5
C ₇ H ₁₆	6.3 × 10 ¹¹	30.0	0.25	1.5
C ₈ H ₁₈	5.7 × 10 ¹¹	30.0	0.25	1.5
C ₈ H ₁₈	9.6 × 10 ¹²	40.0	0.25	1.5
C ₉ H ₂₀	5.2 × 10 ¹¹	30.0	0.25	1.5
C ₁₀ H ₂₂	4.7 × 10 ¹¹	30.0	0.25	1.5
CH ₃ OH	3.7 × 10 ¹²	30.0	0.25	1.5
C ₂ H ₅ OH	1.8 × 10 ¹²	30.0	0.15	1.6
C ₆ H ₆	2.4 × 10 ¹¹	30.0	-0.1	1.85
C ₇ H ₈	1.9 × 10 ¹¹	30.0	-0.1	1.85

Reaction rate parameters for the 2 step combustion mechanism³.

For fuel rich cases further reaction steps are sometimes included to account for the presence of hydrogen in the combustion products.

2.3 Modelling combustion reactions in a turbulent flow

In turbulent flows we solve time average (or density weighted time average) transport equations. These require time average reaction source terms.

The basic problem:

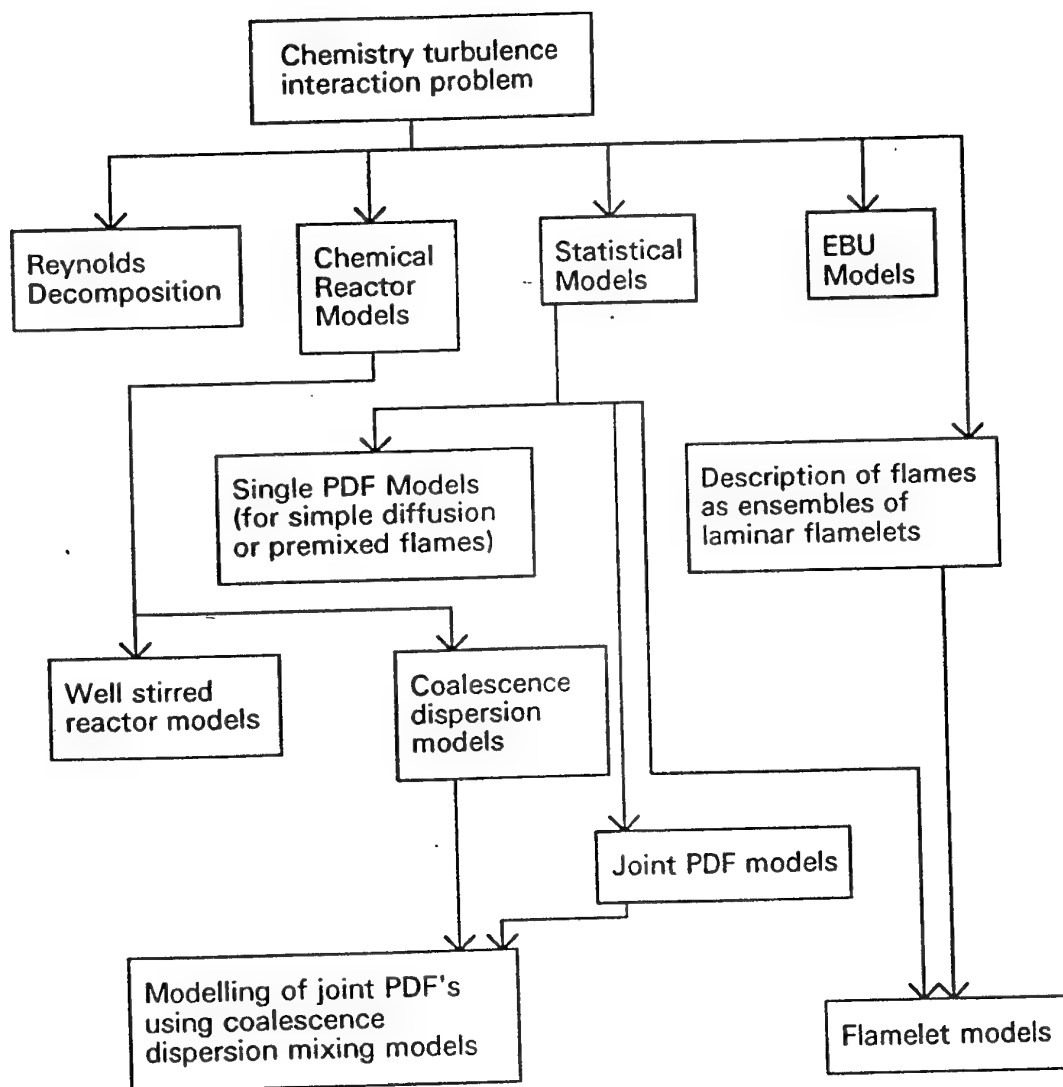
$$W = AT^\beta \prod_{j \text{ reactants}} [C_j]^{v_j} \exp(-E/RT)$$

$$\overline{W} \neq A\overline{T}^\beta \prod_{j \text{ reactants}} [\overline{C_j}]^{v_j} \exp(-E/R\overline{T})$$

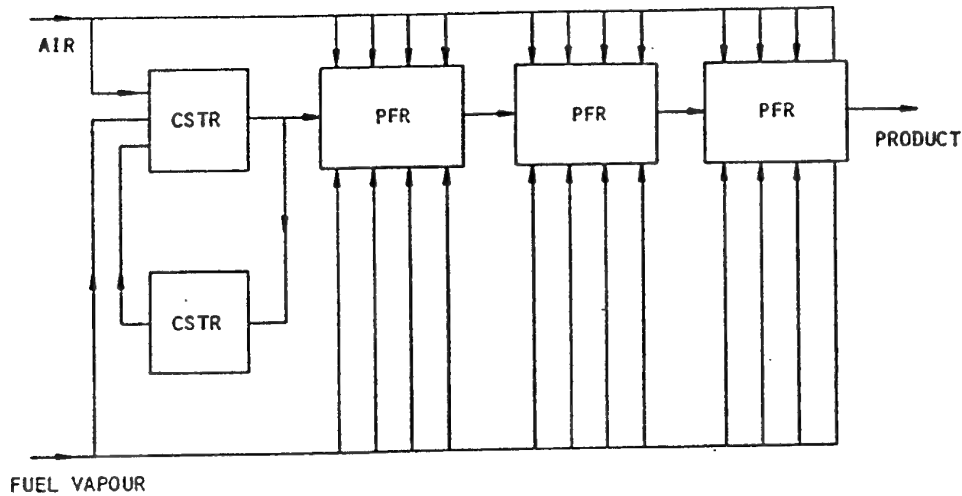
Possible solutions:

1. Chemical reactor models
2. Reynolds decomposition
3. EBU Models
4. Statistical descriptions
5. Turbulent flame speed in premixed systems

Summary of modelling approaches for the source terms due to chemical reaction



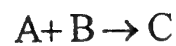
Chemical Reactor Models



Chemical Reactor Network
Representing a Gas Turbine Combustor

Reynolds Decomposition

For the reaction:



$$W = k\rho^2 m_A m_B$$

Decomposition:

$$m_A = \overline{m_A} + m'_A$$

$$m_B = \overline{m_B} + m'_B$$

For constant temperature and density:

$$\overline{W} = k\rho^2 \overline{m_A} \overline{m_B} \left(1 + \frac{\overline{m'_A m'_B}}{\overline{m_A} \overline{m_B}} \right)$$

Eddy dissipation or Eddy break up models.

FLUENT's formulation

This is a very flexible formulation allowing any number of reactions with kinetic or mixing control.

N transport equations for species mass conservation:

$$\frac{\partial}{\partial t}(\rho X_i) + \frac{\partial}{\partial x_i}(\rho U_i X_i) = \frac{\partial}{\partial x_i} J_i + R_i + S_i$$

A single energy conservation equation for multi component systems.

$$\frac{\partial}{\partial t}(\rho h) + \frac{\partial}{\partial x_i}(\rho u_i h) = \frac{\partial}{\partial x_i} \left(k \frac{\partial T}{\partial x_i} \right) - \frac{\partial}{\partial x_i} \sum_j h_j J_{ij} + S_h$$

The equation of state:

$$\rho = \frac{P}{RT \sum_i \frac{X_i}{M_i}}$$

Reaction rate model:

$$R_i = \sum_k R_{ik}$$

Where any of the following can be rate limiting:

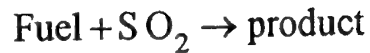
$$\text{I. } R_{ik} = v'_{ik} M_i T^{\beta_k} A_k \prod_{j \text{ reactants}} [C_j]^{v_{jk}} \exp(-E_k / RT)$$

$$\text{II. } R_{ik} = v'_{ik} M_i A_k \rho \frac{\varepsilon}{k} \frac{X_j}{v'_{jk} M_j} \quad \text{where } X_j \text{ are the reactants in reaction } k$$

$$\text{III. } R_{ik} = v'_{ik} M_i A_k \rho \frac{\varepsilon}{k} \sum_j \frac{X_j}{v'_{jk} M_j}$$

where X_j are the products of reaction k and Σ represents summation for all products in reaction k .

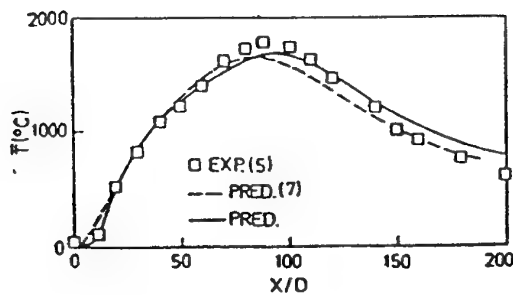
By appropriate selection of the rate constants the model of Magnussen and Hjertager⁴ for diffusion and premixed flames can be constructed:



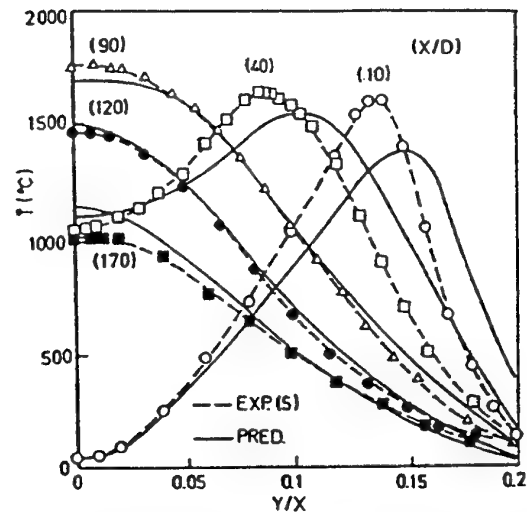
$$R = \left\| 4\rho \frac{\varepsilon}{k} X_{\text{fuel}}, 4\rho \frac{\varepsilon}{k} \frac{X_{\text{O}_2}}{S}, 2\rho \frac{\varepsilon}{k} \frac{X_{\text{product}}}{1+S} \right\|$$

(S is a mass stoichiometric constant.)

Magnussen's predictions for a gas diffusion flame.



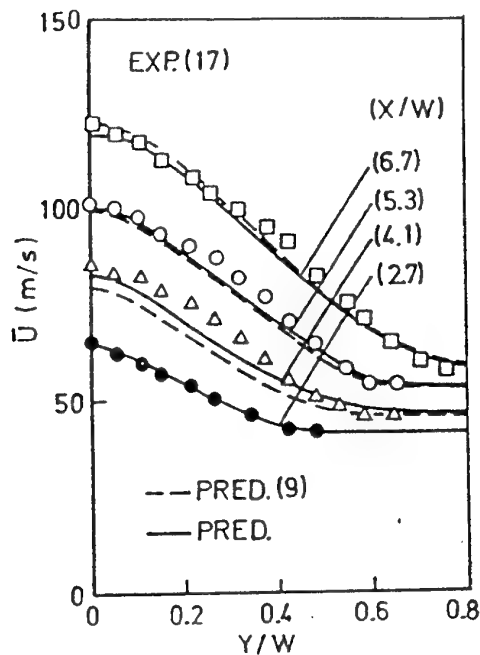
Experimental mean temperature on the axis of the city gas diffusion flame (Re 24000) compared with predictions



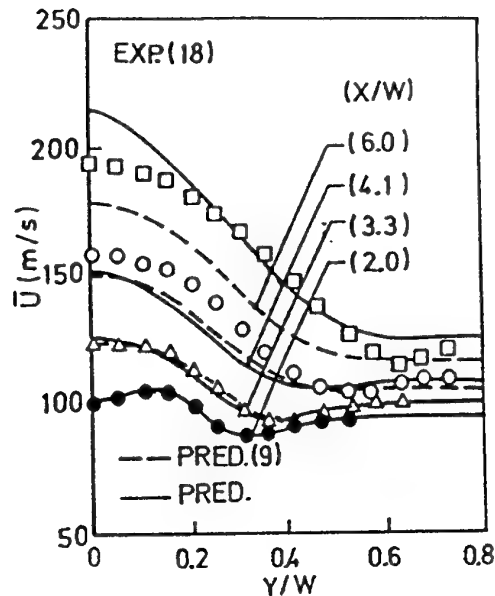
Experimental and predicted local mean temperatures of a city gas diffusion flame (Re 24000).

⁴Magnussen, B. F., and Hjertager, B. H., On Mathematical Modelling of Turbulent Combustion, 15th symposium on combustion.

Magnussen's predictions for a premixed propane wake flame⁴.



Mean axial velocity
(Inlet velocity 31 m/s)



Mean axial velocity
(Inlet velocity 76 m/s)

Advantages of the Magnussen formulation:

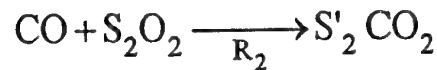
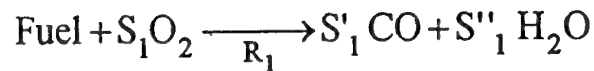
- Not computationally demanding
- Can be applied to premixed, diffusion and partially premixed flames
- Has been used widely

Disadvantages:

- Applies only for high Damköhler number flames. When chemical kinetics and mixing are simultaneously important the model is unreliable.
- Phenomena which depend on detailed chemical kinetics, such as stability can not be predicted.
- Intermediate species and dissociation can not be predicted. Flame temperatures are over predicted.
- There is uncertainty regarding the values of the Magnussen constants.

Extension to multiple step reaction.

The following can be constructed for diffusion flames.



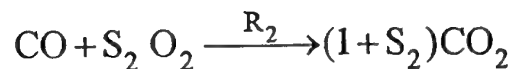
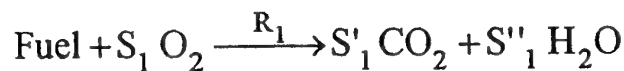
$$R_1 = \left\| R_{1k}, 4\rho \frac{\varepsilon}{k} X_{\text{fuel}}, 4\rho \frac{\varepsilon}{k} \frac{X_{\text{O}_2}}{S_1} \right\|$$

$$R_2 = \left\| R_{2k}, 4\rho \frac{\varepsilon}{k} X_{\text{CO}}, 4\rho \frac{\varepsilon}{k} \frac{X_{\text{O}_2}}{S_2} \right\|$$

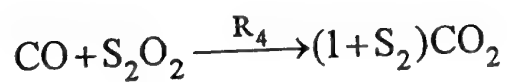
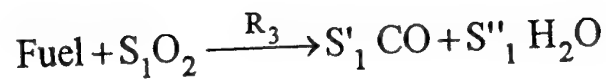
There exists little theoretical basis for this model.

A more rigorous two step eddy dissipation model is being developed by the IFRF (such a model is easily implemented into FLUENT via user subroutines).

Oxygen rich condition $\lambda \geq 1$. (Dissipation of fuel and CO eddies control rates R_1 and R_2 respectively.)



Fuel rich condition $\lambda < 1$ (Dissipation of oxygen containing eddies control rates R_3 and R_4).



Where R_1, R_2, R_3, R_4 , are obtained using the eddy dissipation concept.

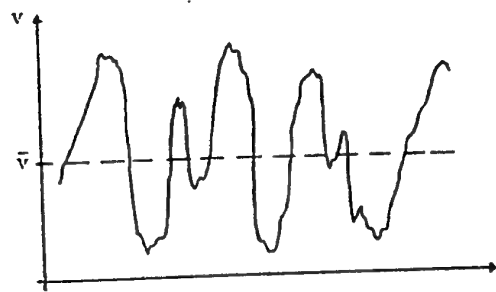
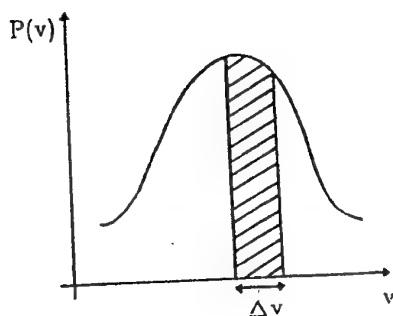
The model applies in the fast chemistry limit for diffusion flames, where improved flame temperature predictions have been obtained.

Statistical Treatments

Concept of the PDF (Probability Density Function)

The PDF $P(V)$ is defined: $P(V)\Delta V = \frac{\lim_{t \rightarrow \infty} 1}{t} \Sigma \Delta t$

So that $P(V) \Delta V$ is the fraction of time that the variable V lies in the range V to $V + \Delta V$



It follows that:

$$\int_{-\infty}^{\infty} P(V) dV = 1$$

$\int_{-\infty}^a P(V) dV$ = the fraction of time that the random variable takes on a value less than a .

If $W = f(V)$,

then a property of the PDF is that:

$$\bar{W} = \int_{-\infty}^{\infty} W(V) P(V) dV$$

Statistical Treatments for Diffusion Flame Modelling

The Conserved Scalar Approach

- Well established
- Computationally efficient
- Allows intermediate species formation and dissociation effects to be predicted with little additional computer effort
- Allows true mean densities to be used in the flow field calculation

BASIS: Under certain simplifying assumptions the instantaneous thermochemical state is a function of a single conserved scalar quantity known as the mixture fraction f

$$f = \frac{Z_k - Z_{ko}}{Z_{kF} - Z_{ko}}$$

REQUIREMENTS ARE:

- Diffusion type flame with discrete fuel and oxidiser inlets
- Negligible heat loss to surroundings
- Negligible radiative transfer
- Unity Lewis number

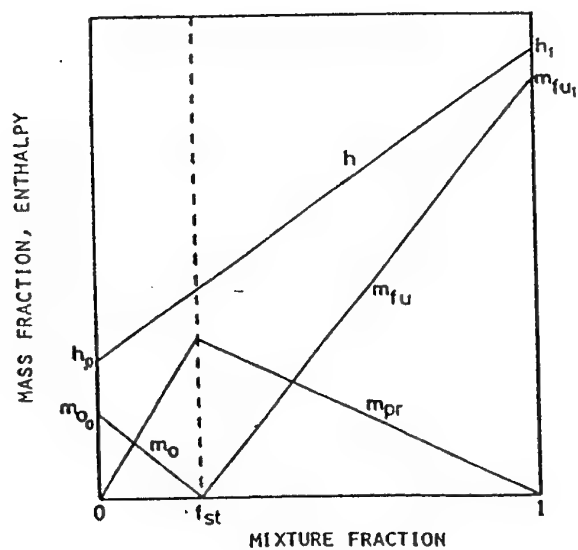
If

$$\phi_i = \phi_i(f)$$

$$\bar{\phi}_i = \int_0^1 P(f) \phi_i(f) df$$

Determination of $\phi_i(f)$

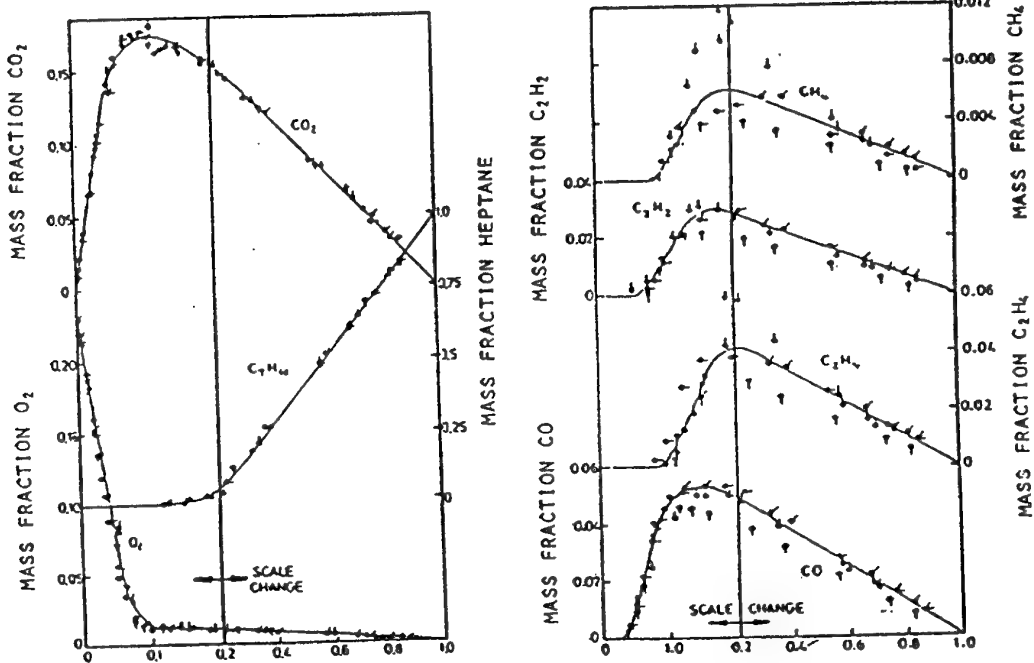
- 1) Assuming Fast Irreversible Reaction
(the Flame Sheet Description)



2) The Flamelet Description

Assumes that reaction zones within a turbulent flame possess a laminar structure.

Experimental data or laminar flame models then provide the conserved scalar relationship.



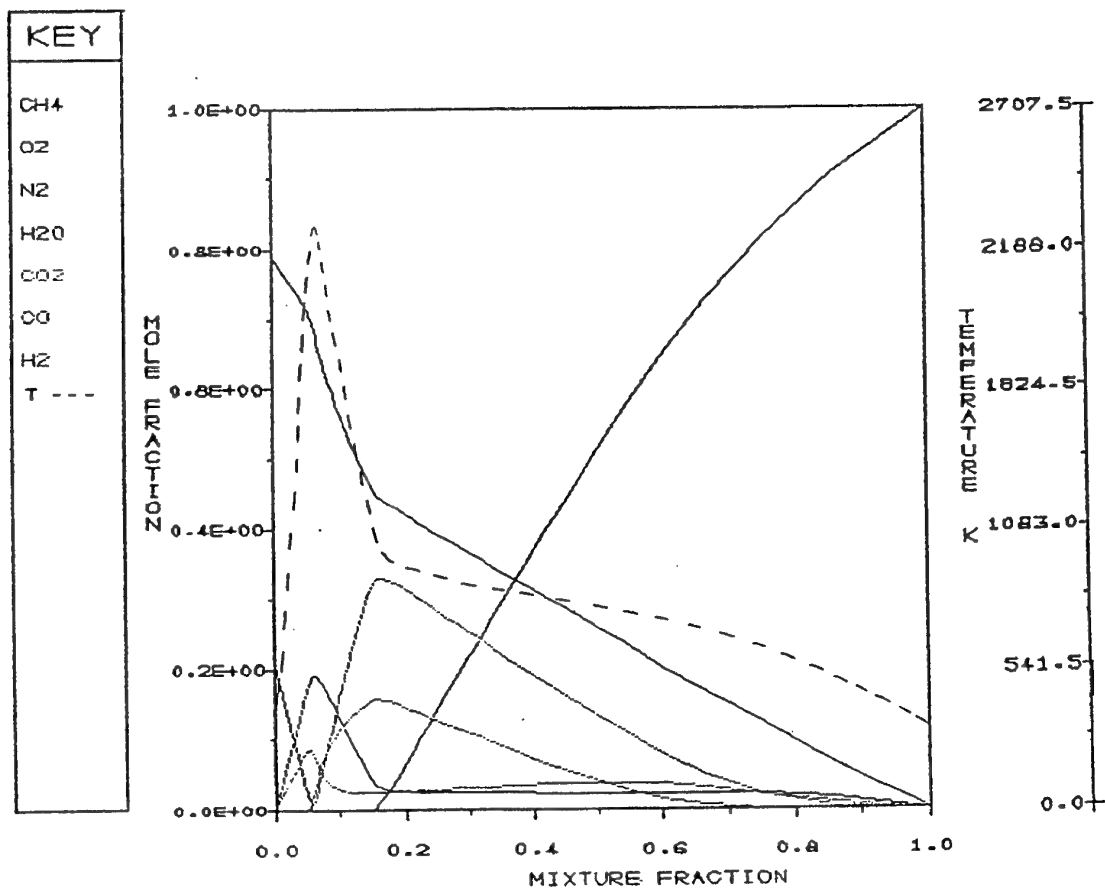
Composition correlation for heptane diffusion flame
(Ticks on Data Points indicate position of radial traverse around cylinder)

3) The Equilibrium Description

The chemistry is assumed rapid enough for equilibrium always to be attained.

An equilibrium calculation can be performed to provide the conserved scalar relationships.

An algorithm using minimization of Gibbs free energy can be employed for the above.

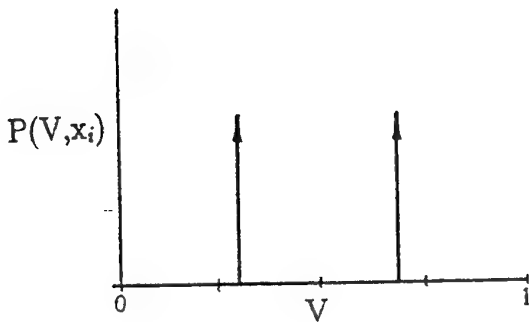


Equilibrium relationship for a methane air flame.

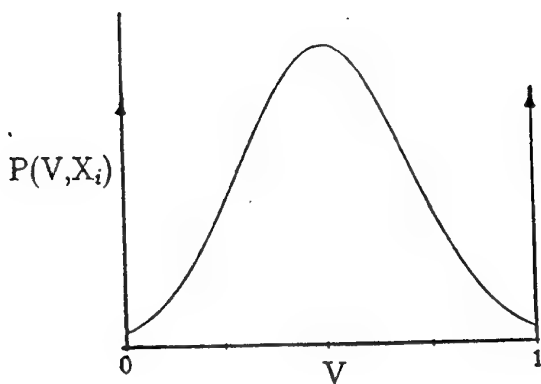
Determination of $P(f)$

Prescription of the PDF

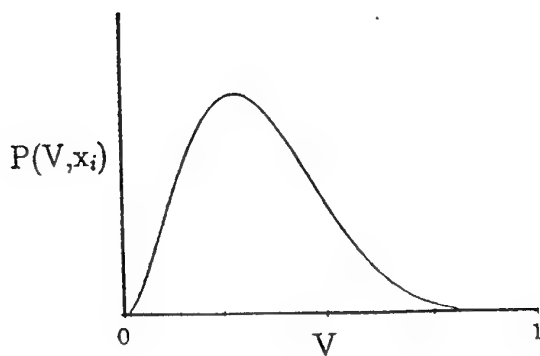
A two parameter PDF is usually employed. The function is then fully defined by the mean and variance of the fluctuating quantity.



(A) Double Delta Probability Density Function



(B) Clipped Gaussian Probability Density Function



(C) β Probability Density Function

Determination of $P(f)$

A beta or double delta function can be employed if \bar{f} and $\overline{f^2}$ are known

Two Transport equations are solved.

The equation for conservation of mixture fraction.

$$\frac{\partial}{\partial x_i}(\rho u_i \bar{f}) = \frac{\partial}{\partial x_i} \left(\frac{\mu_t}{\sigma_t} \frac{\partial \bar{f}}{\partial x_i} \right)$$

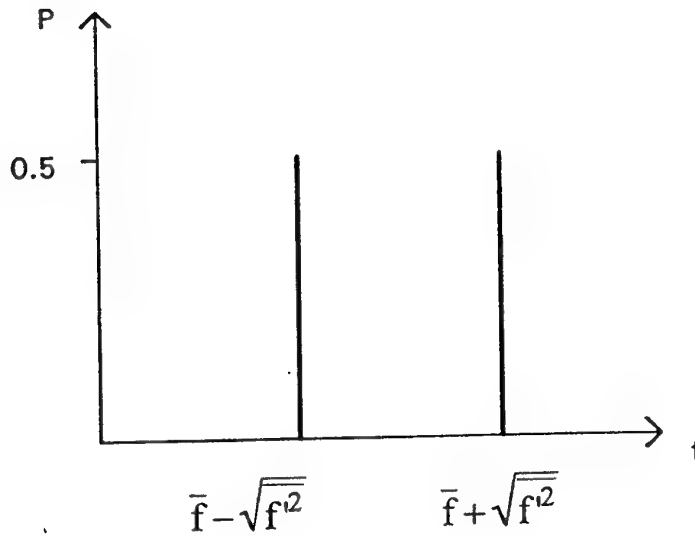
The conservation equation for mixture fraction variance.

$$\frac{\partial}{\partial x_i}(\rho u_i \overline{f^2}) = \frac{\partial}{\partial x_i} \left(\frac{\mu_t}{\sigma_t} \frac{\partial \overline{f^2}}{\partial x_i} \right) + \frac{2\mu_t}{\sigma_t} \left(\frac{\partial \bar{f}}{\partial x_i} \right)^2 - C_d \rho \frac{\varepsilon}{\kappa} \overline{f^2}$$

The double delta function is given by:-

$$P(f) = 0.5 \quad @ \quad f = \bar{f} - \sqrt{\bar{f}^2}$$

$$P(f) = 0.5 \quad @ \quad f = \bar{f} + \sqrt{\bar{f}^2}$$



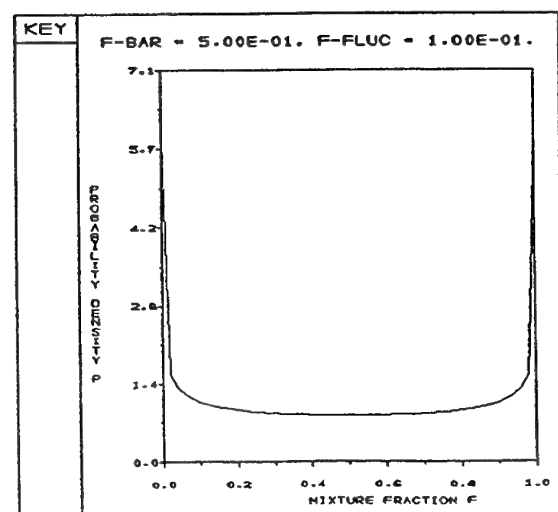
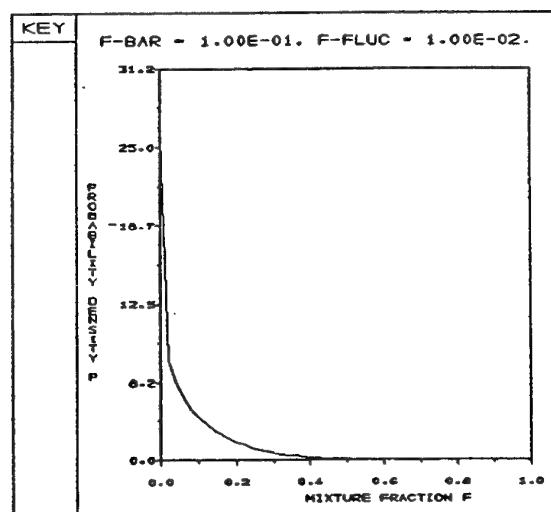
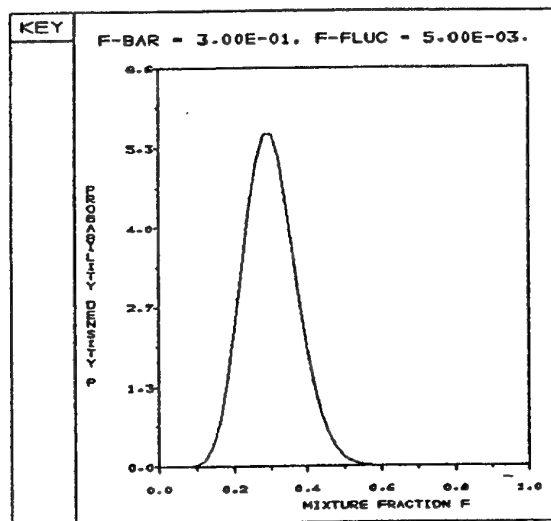
The beta function is more computationally expensive but is thought to better represent experimentally observed PDF shapes.

$$P(f) = \frac{f^{\alpha-1}(1-f)^{\beta-1}}{\int f^{\alpha-1}(1-f)^{\beta-1} df}$$

$$\alpha = f(\bar{f}(1-\bar{f})/\bar{f}^2 - 1)$$

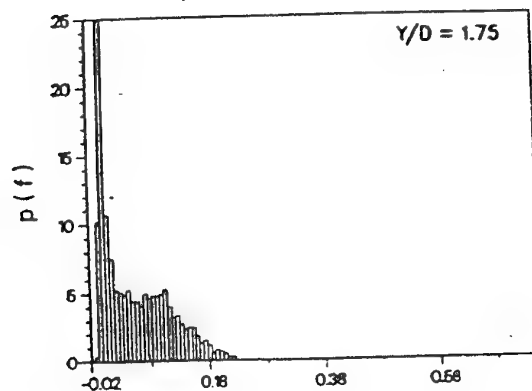
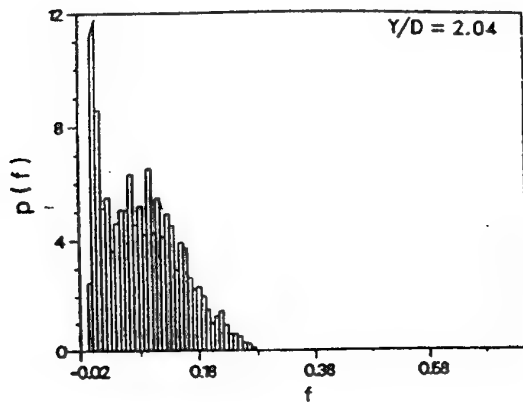
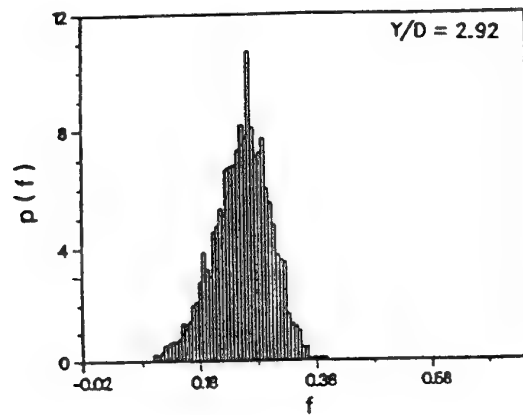
$$\beta = (1-\bar{f}) \left(\frac{\bar{f}(1-\bar{f})}{\bar{f}^2} - 1 \right)$$

PDF shapes for various values of mean and variance.



Experimentally measured Probability density functions of mixture fraction. Non-reacting propane jet mixing with a co-flowing air stream⁵

(Jet velocity = 53 m/s Co flow velocity = 9.2 m/s $x/D = 30$)



⁵ Schefer, R. W., and Dibble, R. W., AIAA J. 23, 1985.

Extending the model for non-adiabatic conditions.

- Under these conditions $\bar{\phi}_i$ is no longer a function only of f but depends also on enthalpy.
- A so called joint PDF can be employed to describe the simultaneous fluctuations of two or more variables.

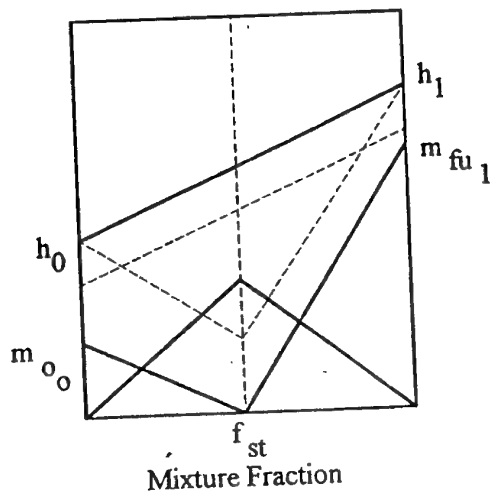
$$P = P(v_1, v_2)$$

then if $w = w(v_1, v_2)$

$$\bar{w} = \iint P(v_1, v_2) w(v_1, v_2) dv_1 dv_2$$

- Prescription of a 2 parameter PDF is no longer possible and the solution of joint PDF transport equations is not practical for engineering problems
- The solution normally adopted is to modify $h = h(f)$ in a prescribed manner

The relationship $\bar{\phi}_i = \bar{\phi}_i(f)$ is then retained, for any given mean enthalpy

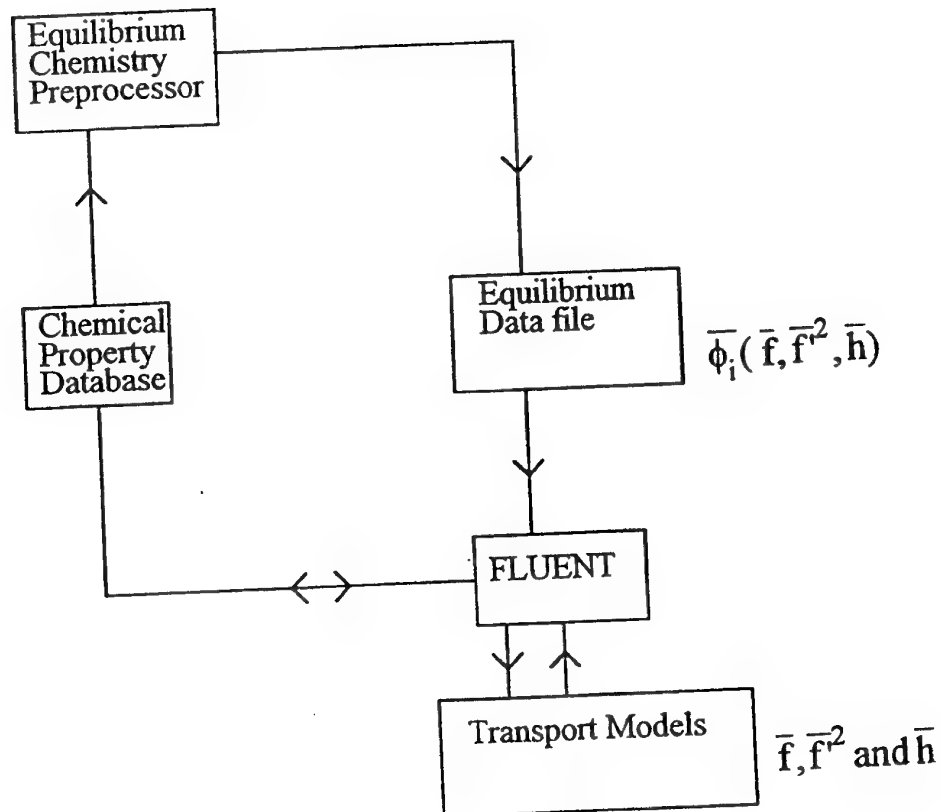


Modification of $h = h(f)$ for
non-adiabatic flames
(Fast irreversible reaction)

Diffusion Flame Model Program Structure FLUENT V4.3

Available user options

- adiabatic / non-adiabatic flames
- fast irreversible chemistry / equilibrium chemistry / user input flamelet relationships (adiabatic case only)
- double delta PDF / β function PDF



Statistical Treatments for Premixed Flame Modelling

A similar concept can be employed for the premixed problem.

Rather than f , a reaction progress variable C is defined.

$$\begin{array}{ll} C = 0 & \text{Unburnt mixture} \\ C = 1 & \text{Fully reacted mixture} \end{array}$$

If all rate determining variables are a function of the progress variable C :

$$W = W(C)$$

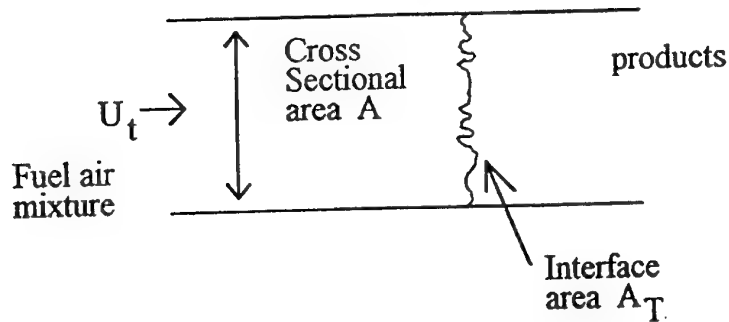
Determining a 2 parameter PDF $P(C, x_i)$

$$\overline{W}(x_i) = \int_0^1 W(C) P(C, x_i) dC$$

We may use a "look up" table of the function:

$$\overline{W}(x_i) = f(\overline{C}(x_i), \overline{C^2}(x_i))$$

The concept of Turbulent Flame Speed for modelling premixed flames



When combustion takes place in the wrinkled laminar flame regime

$$U_T = \frac{A_T}{A} U_L$$

where U_T = the turbulent flame speed

The flame can be modelled by solving the equation

$$\frac{\partial G}{\partial t} + \mathbf{u} \cdot \nabla G = -U_T |\nabla G|$$

where G is a scalar which tracks the front ($G=1$ at flame front)

A number of turbulent flame speed formula are available which describe the increase in area due to wrinkling

$$\frac{U_T}{U_L} = \exp\left(\frac{u'}{U_T}\right)^2 \quad \text{Yakhot's expression derived from RG theory}$$

⁶ Yakhot, V., Combustion Science and Technology, 1988.

3 Modelling Variable Density Reacting Flow

In combustion density fluctuations are not insignificant.

density, weighting, rather than Reynolds decomposition and averaging, is frequently employed

$$u_i = \bar{u}_i + u_i' \quad (3.1) \quad \bar{u}_i' = 0 \quad (3.2)$$

$$u_i = \bar{u}_i + u_i'' \quad (3.3) \quad \bar{u}_i'' \neq 0 \quad (3.4)$$

where $\bar{\sim}$ denotes a density weighted average defined by

$$\bar{\rho u}_i = \frac{1}{\Delta t} \int_t^{t+\Delta t} \rho u_i dt \quad (3.5)$$

Substitution of (3.3) into the conservation equations and time averaging results in the equations for density weighted quantities

For example the continuity equation $\frac{\partial}{\partial x_i} (\bar{\rho u}_i) = 0$

since $\overline{\rho u_i''} = 0$, density fluctuations are eliminated.

Employing the equations derived by Reynolds decomposition and neglecting all density fluctuations implicitly results in the calculation of density weighted quantities.

When PDF methods are employed it is possible to inter-convert between weighted and unweighted values.

$$\phi = \phi(f)$$

$$\tilde{\phi} = \int_0^1 \phi(f) \tilde{P}(f) df$$

$$\bar{\phi} = \bar{\rho}^{-1} \int_0^1 \frac{\phi(f)}{\rho(f)} \tilde{P}(f) df$$

$\bar{\rho}$ can be accurately calculated if $\rho = \rho(f)$

$$\bar{\rho} = \left[\int_0^1 \frac{\tilde{P}(f)}{\rho(f)} df \right]^{-1}$$

Close to density weighted quantities are measured by diagnostic methods such as isokinetic gas sampling and suction pyrometry.

The averaged quantity measured by LDA depends on the system employed and the experimental conditions.

4 Additional Sub Models

4.1 Radiative Heat Transfer

Two approaches are practical

- 1) differential models such as those derived using the P1 approximation
- 2) ray tracing methods such as the discrete transfer model

Differential Models

- Differential models are computationally efficient
- Perform well in optically dense media where the average distance travelled by photons before absorption or scattering is small
- Are suitable for many combustion problems where heat transfer from flame to walls predominates.

$$\frac{1}{3a} \nabla \cdot \frac{1}{a+s} \nabla \theta_R^4 - \theta_R^4 + T^4 = 0$$

where $\theta_R^4 = \frac{I}{4\sigma}$ and I is a composite radiative flux

a = absorption coefficient s = scattering coefficient

Discrete Transfer Models

- Are computationally more demanding
- Are more accurate, especially for clear gases and where wall to wall radiation is important in complex geometries
- Accuracy can be increased by increasing the number of rays traced

4.2 Second Phase Models

- Heat transfer to inert particles

$$m_p C_p \frac{dT_p}{dt} = hSA(T_\infty - T_p) + Q_{\text{rad}}$$

$$Nu = \frac{hD}{K_\infty} = 2.0 + 0.6 Re^{1/2} Pr^{1/3}$$

- Evaporation of droplets Mass transfer control

$$N_i = k_c (C_{is} - C_{i\infty})$$

$$Nu = \frac{k_c D}{D_{im}} = 2.0 + 0.6 Re^{1/2} Sc^{1/3}$$

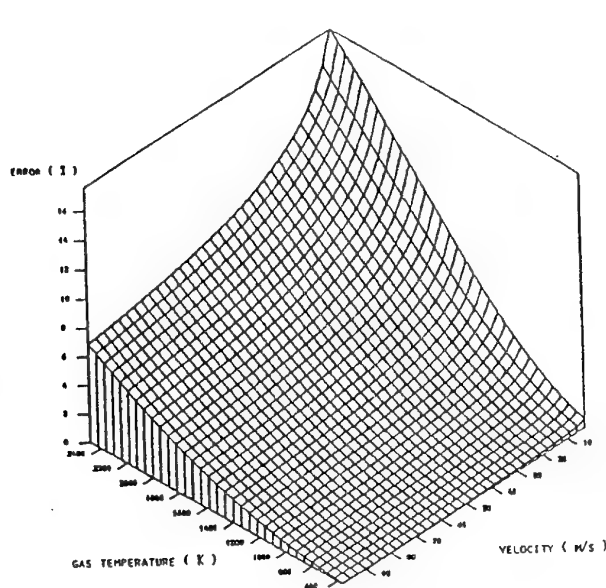
- Droplet boiling (evaporation at high temperature) Heat transfer control

$$\dot{m} = 2\pi D \left(\frac{k}{C_p} \right)_\infty \ln(1 + B_T)$$

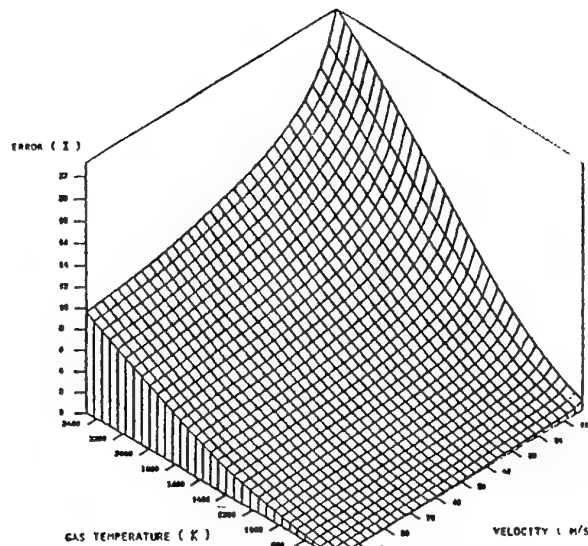
$$B_T = \frac{C_{pg}(T_\infty - T_b)}{L} f(Re, Pr)$$

- Devolatilisation
- Char Combustion

Radiative heat transfer to particles and drops

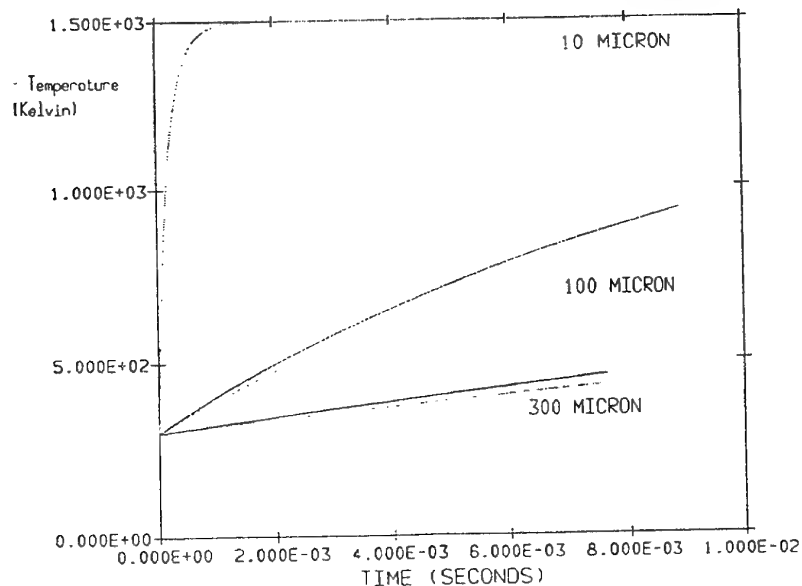


300 μm particle



700 μm particle

Error associated with neglecting radiative heat transfer for large particles.
Steady state solution. (Hot transparent gas, cold walls $\epsilon_p = 0.2$)



The effect of radiative heat transfer on heating rate for various particle sizes. (Transparent gas at 1500 K, walls at 1500 K, $\epsilon_p = 0.8$)

Subroutine USRLW7 allows a particle temperature history to be defined.

$$\frac{mC_p T_p}{dT} = hA_p (T_g - T_p) + A_p Q_k$$

$$h = \frac{2\lambda}{D_p}$$

$$Q_k = \varepsilon_p \sigma (T_w^4 - T_p^4)$$

Using the differential model for radiation

$$\frac{1}{3} \nabla \frac{1}{a_{\Sigma}} \nabla \theta_R^4 - a(\theta_R^4 - T^4) + \varepsilon_p A_p (T_p^4 - \theta_R^4) = 0$$

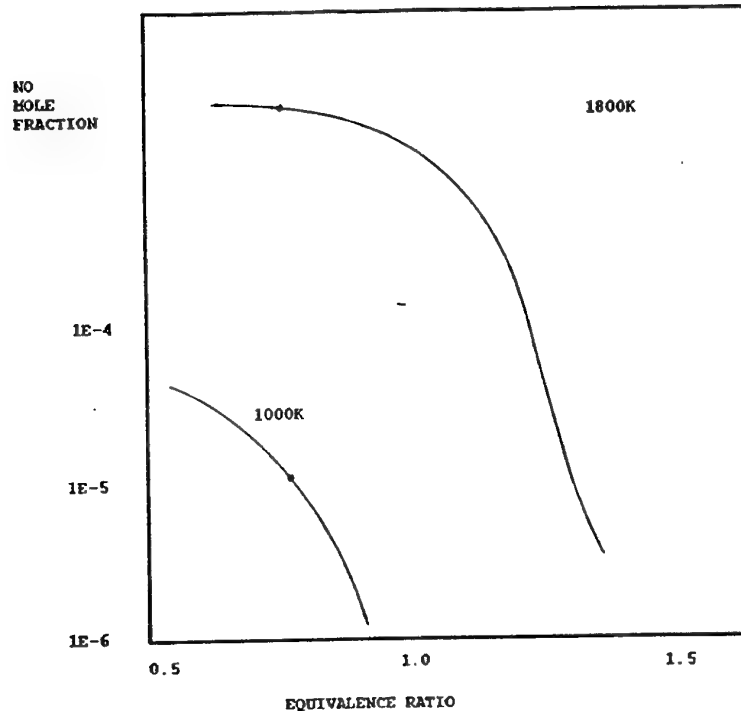
$$a_{\Sigma} = a + A_p \varepsilon_p$$

$$\frac{dm C_p T}{dt} = h A_p (T_g - T_p) + \epsilon_p A_p \sigma (\theta_R^4 - T_p^4)$$

5 Predicting NO_x Emissions

5.1 Introduction

- NO formation is of primary concern

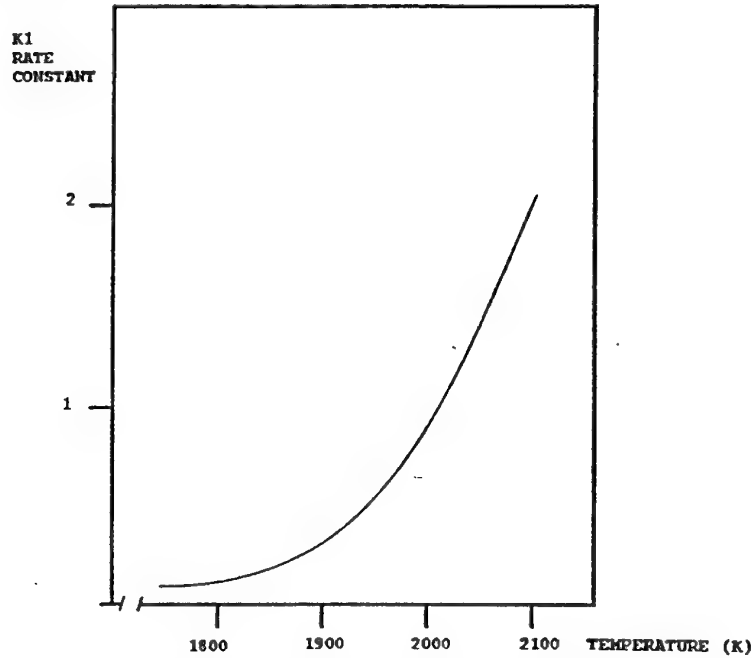


CH₄/Air 1 Atmosphere

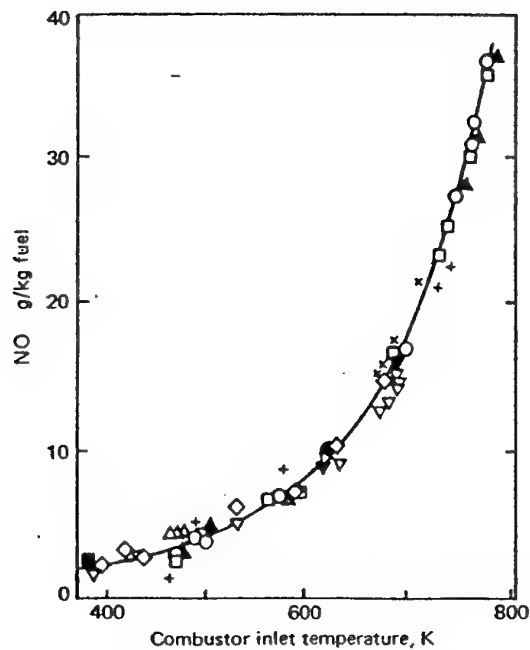
- Chemical kinetics are of key importance in predicting NO emissions
- In "clean" fuel combustion the thermal NO_x mechanism usually dominates. Prompt NO_x formation is of less significance
- As fuel Nitrogen content increases the fuel NO_x mechanisms become important

<u>Fuel</u>	<u>Nitrogen wt %</u>
Light distillates	0-0.4
Residual fuel oil	0.3-2.0
Bituminous coal	1.0-2.0

- Accurate flame temperature predictions are of importance for determining NO formation rates.



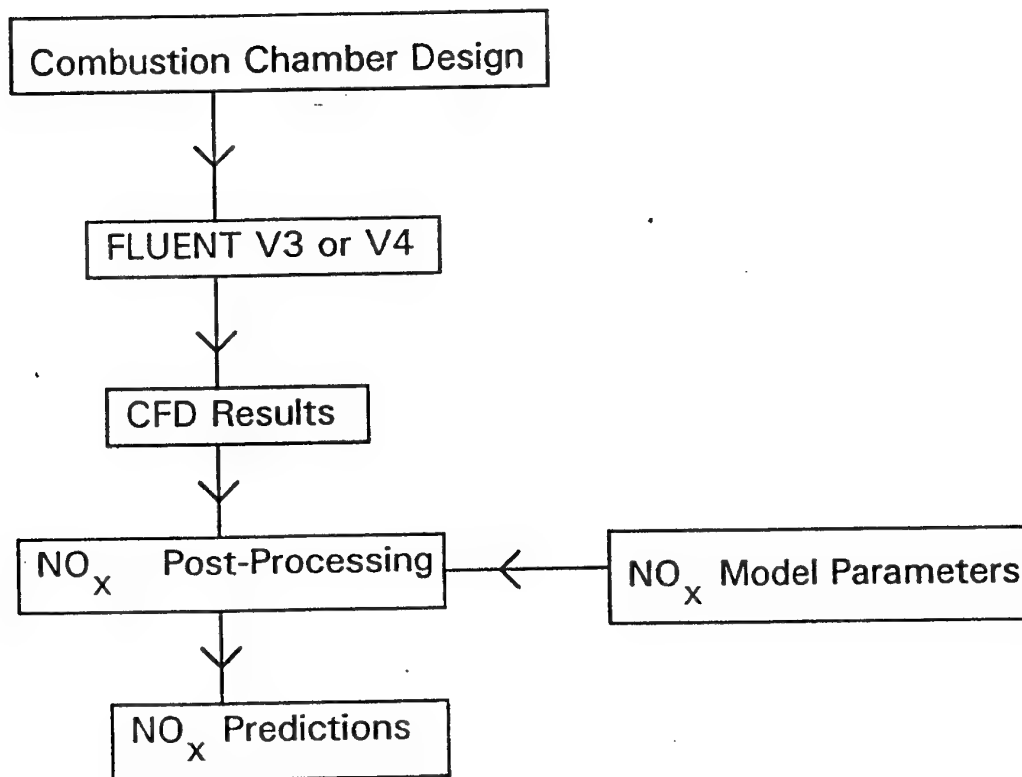
Rate Constant Versus Temperature for the Rate Controlling Thermal NO



Gas Turbine NO_x Emissions as a Function of Combustor Inlet Temperature

5.2 The Post Processing Concept

- NO_x reactions involve little heat release
- NO_x concentrations are low
- NO_x reactions have little influence on the main combustion or fluid dynamic processes



OBJECTIVE

- Solve the main combustion reactions and fluid dynamics as accurately as possible
- Solve a scalar transport equation for NO concentration:

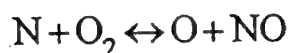
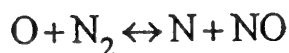
$$\frac{\partial X_{\text{NO}}}{\partial t} + \frac{\partial}{\partial x_i} (\rho u_i X_{\text{NO}}) = \frac{\partial}{\partial x_i} \left(\Gamma \frac{\partial X_{\text{NO}}}{\partial x_i} \right) + S_{\text{NO}}$$

REQUIREMENTS

- Good CFD and combustion modelling
- Solver for the NO transport equation
- Means to compute S_{NO} based on a knowledge of NO_x chemistry

5.3 Thermal NO_x

Formation determined by a set of highly temperature dependent chemical reactions known as the extended Zeldovich mechanism



A third reaction has been shown to contribute, particularly at near stoichiometric and in excess fuel mixtures



The rate constants for these reactions have been the subject of much study. The values recommended by Hanson and Salimian⁷ are given here:

$$K_1 = 1.8 \times 10^8 \exp\left(\frac{-38370}{T}\right) \text{m}^3 \text{mol}^{-1} \text{s}^{-1}$$

$$K_{-1} = 3.8 \times 10^7 \exp\left(\frac{-425}{T}\right) \text{m}^3 \text{mol}^{-1} \text{s}^{-1}$$

$$K_2 = 1.8 \times 10^4 T \exp\left(\frac{-4680}{T}\right) \text{m}^3 \text{mol}^{-1} \text{s}^{-1}$$

$$K_{-2} = 3.8 \times 10^3 T \exp\left(\frac{-20820}{T}\right) \text{m}^3 \text{mol}^{-1} \text{s}^{-1}$$

⁷ Hanson, R. K., and Salimian, S., Survey of rate constants in H/N/O system, Combustion Chemistry, 1984.

$$K_3 = 7.1 \times 10^7 \exp\left(\frac{-450}{T}\right) \text{m}^3 \text{mol}^{-1} \text{s}^{-1}$$

$$K_{-3} = 1.7 \times 10^8 \exp\left(\frac{-24560}{T}\right) \text{m}^3 \text{mol}^{-1} \text{s}^{-1}$$

Where K_1 , K_2 , and K_3 are the rate constants for the forward reactions.
 K_{-1} , K_{-2} and K_{-3} are the corresponding reverse rates.

The net rate of formation of NO is given by:

$$\begin{aligned} \frac{d[\text{NO}]}{dt} = & K_1[\text{O}][\text{N}_2] + K_2[\text{N}][\text{O}_2] + K_3[\text{N}][\text{OH}] - K_{-1}[\text{NO}][\text{N}] \\ & - K_{-2}[\text{NO}][\text{O}] - K_{-3}[\text{NO}][\text{H}] \end{aligned}$$

The formation rate is significant at high temperatures ($T > 1800 \text{ K}$) as large energy is required to break the N_2 triple bond $\left(\frac{E_1}{R} = 38370 \text{ K}\right)$.

Under the quasi steady assumption for nitrogen atoms:

$$\frac{d[\text{NO}]}{dt} = \frac{K_2[\text{O}_2] + K_3[\text{OH}]}{1 + K_{-1}[\text{NO}]}$$

$$\left(2K_1[\text{N}_2][\text{O}] - \frac{2K_{-1}K_{-2}[\text{NO}]^2[\text{O}]}{K_2[\text{O}_2] + K_3[\text{OH}]} - \frac{2K_{-1}K_{-3}[\text{NO}]^2[\text{H}]}{K_2[\text{O}_2] + K_3[\text{OH}]} \right) (\text{mol} / \text{m}^3 \text{s})$$

We can conclude:

1. High temperature \Rightarrow large thermal NO_x production
2. High O atom concentration \Rightarrow large thermal NO_x production
3. Thermal NO_x formation is independent of fuel type
4. To determine NO formation rate O and OH concentrations must be obtained.

We may predict the rate of NO_x formation by either:

1. Coupling the equations with a detailed hydrocarbon combustion mechanism,
- or
2. Using an assumption of equilibrium or partial equilibrium to obtain [O] concentration and assuming that for combustion of lean fuel air mixtures:

$$K_2[\text{O}_2]_{\text{eq}} \gg k_3[\text{OH}]_{\text{eq}}$$

Hence:

$$\frac{d[\text{NO}]}{dt} = \frac{2[\text{O}](K_1 K_2 [\text{O}_2][\text{N}_2] - K_{-1} K_{-2} [\text{NO}]^2)}{K_2 [\text{O}_2] + K_{-1} [\text{NO}]}$$

$$[\text{O}] = K_p [\text{O}_2]^{1/2}$$

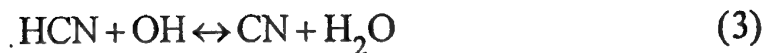
5.4 Prompt NO_x

A second NO_x formation mechanism was identified by Fenimore⁸ and is termed "prompt NO_x" formation.

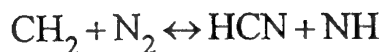
Prompt NO_x is significant:

1. where temperatures are low
- 2 where residence times are short
- 3 in the more recently designed "low NO_x" burners

The route for prompt NO_x formation:



Other reactions via CH, CH₂, C, C₂H:



⁸ Fenimore, C. P., 13th Symposium (International) on Combustion, p373, 1971.

We can conclude:

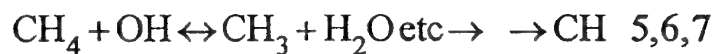
1. Prompt NO formation increases with increasing concentration of hydrocarbon radicals
2. Prompt NO formation is dependent on hydrocarbon radical concentration and not parent fuel type
3. Prompt NO formation increases with equivalence ratio provided O_2 is present for the oxidation step

It is thought that the CH reaction dominates NO formation and that it is the rate controlling step.

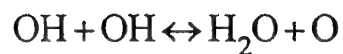
$$\frac{d[NO]}{dt} = K_1[CH][N_2]$$

Example of use for CH_4 combustion:

CH formation step



partial equilibrium assumption:



$$\frac{d[NO]}{dt} = k_1 k_5 k_6 k_7 K_e [H_2O]^{-1.5} [N_2] [CH_4]$$

Practical Limitations:

1. The radical reactions are not well defined for many fuels
2. Uncertainty exists over the rate constant for reaction 1

Solution:

Recourse is made to empirically derived global expressions as proposed by De Soete⁹

For example:

$$\frac{d[\text{NO}]}{dt} = K[\text{O}_2]^a[\text{N}_2][\text{FUEL}] \exp\left(\frac{-E_a}{RT}\right)$$

K, E_a and a are determined from experimental study.

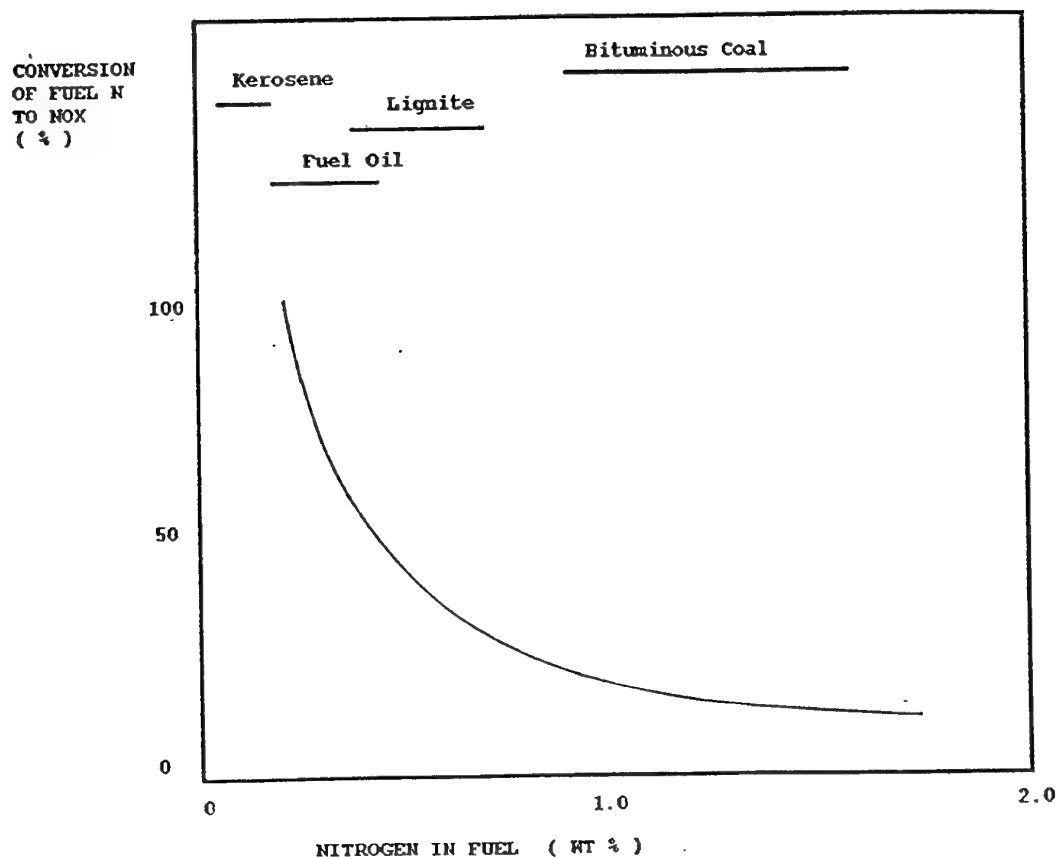
⁹ De Soete, G. G., 15th Symposium (International) on Combustion, p 103, 1975.

5.5 Fuel NO_x

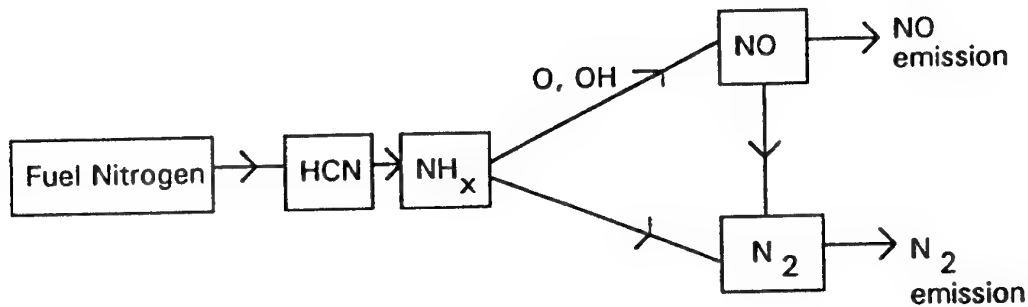
Formed by oxidation of fuel bound nitrogen.

- A major source of NO_x emissions in fossil fuel combustion
- NO_x formation is little influenced by the type of nitrogen containing compound (amines, pyridine, etc)
- Strongly depends on the local combustion environment (temperature and stoichiometry)
- Dependent on the fuel nitrogen concentration present in the reactants.

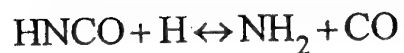
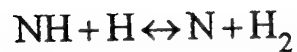
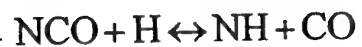
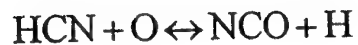
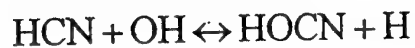
The fractional conversion of fuel nitrogen to NO is seen to decrease with increasing fuel nitrogen content.



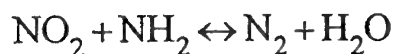
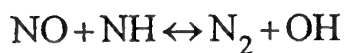
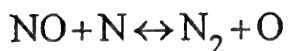
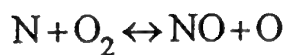
Chemical Mechanism:



- Fuel bound nitrogen containing compounds are released into the gas phase when fuel drops or particles are heated
- Thermal decomposition results in HCN formation (and some NH₃ formation)
- Reaction with OH initiates NO formation:



- NH_x so formed can be converted to NO or N_2



Complications:

- The kinetics of HCN formation are not well known.
- Under fuel lean conditions it is thought that O atoms may react directly with HCN to form NO
- Under very fuel rich conditions, hydrocarbon free radicals may react to remove NO. Carbon particles present in the fuel rich flame may also have this effect.

Solution:

Empirical rate expressions can be employed:

$$\frac{d[N_F]}{dt} = -R_{\text{oxi}} - R_{\text{Red}}$$

$$\frac{d[NO]}{dt} = R_{\text{oxi}} - R_{\text{Red}}$$

$$R_{\text{oxi}} = K_A [N_F] [O_2]^a \exp\left(\frac{-E_A}{RT}\right)$$

$$R_{\text{Red}} = K_B [N_F] [NO] \exp\left(\frac{-E_B}{RT}\right)$$

A global expression for fuel NO formation:

$$\frac{d[NO]_F}{dt} = \left(\frac{R_{\text{oxi}} - R_{\text{Red}}}{R_{\text{oxi}} + R_{\text{Red}}} \right) \frac{d[F]}{dt} X_{\text{NO}} \frac{M_{\text{NO}}}{M_N}$$

where X_{NO} = mass fraction of nitrogen in fuel

5.6 Modelling NO_x Chemistry Turbulence Interaction

To obtain time averaged NO production rates in a turbulent flow a statistical treatment is employed.

If $W = f(V)$

Then a property of the PDF $P(V)$ is that:

$$\overline{W} = \int_{-\infty}^{\infty} W(V)P(V)dV$$

If $W = f(V_1, V_2, \dots)$

a joint PDF can be employed $P(V_1, V_2, \dots)$

$$\overline{W} = \int W(V_1, V_2, \dots)P(V_1, V_2, \dots)dV_1dV_2, \dots$$

If W_{NO} is the rate of NO formation and is a function of the variables V_1 and V_2 .

Then:

$$\overline{W}_{NO} = \iint W_{NO}(V_1, V_2)P(V_1, V_2)dV_1dV_2$$

$$P(V_1, V_2) = P_1(V_1)P_2(V_2)$$

A two parameter PDF can be fully defined with knowledge of the mean and variance of the fluctuating quantity.

The β probability density function is described

$$P(V) = \frac{V^{\alpha-1}(1-V)^{\beta-1}}{\int V^{\alpha-1}(1-V)^{\beta-1} dV}$$

Where

$$\alpha = \bar{V}(\bar{V}(1-\bar{V})/\bar{V}^2 - 1)$$

$$\beta = (1-\bar{V})\left(\frac{\bar{V}(1-\bar{V})}{\bar{V}^2} - 1\right)$$

\bar{V} = the mean value of V

\bar{V}^2 = the variance of V

\bar{V} is known

\bar{V}^2 can be obtained from an additional modelled transport equation or an algebraic expression

$$\bar{V}^2 = \frac{\mu_t}{\rho} \frac{k}{\varepsilon} C \left(\left(\frac{\partial \bar{V}}{\partial x} \right)^2 + \left(\frac{\partial \bar{V}}{\partial y} \right)^2 + \left(\frac{\partial \bar{V}}{\partial z} \right)^2 \right)$$

6 Conclusion

- No general model exists which is suitable for all combustion applications
- Limitations exist in the models for turbulence and for turbulence chemistry interaction
- Useful engineering predictions can be obtained provided an appropriate model is used under conditions where it is valid
- Pollutants such as NO_x can be computed by decoupling from the main combustion calculation. Useful predictions can be obtained but the chemistry of NO_x formation is still an active area of research

von Karman Institute for Fluid Dynamics

Lecture Series 1995-03

INDUSTRIAL COMPUTATIONAL FLUID DYNAMICS

April 3 - 7, 1995

MODELLING CONDUCTIVE, CONVECTIVE AND RADIATIVE HEAT TRANSFER
NUMERICAL SIMULATION OF HEAT TRANSFER USING PHOENICS

B. Spalding
CHAM, UK

VKI Lecture Series on

INDUSTRIAL COMPUTATIONAL FLUID DYNAMICS

April 3-7 1995

Lectures by Professor Brian Spalding

on

LE3-1 Modelling conductive, convective & radiative Heat Transfer.

LE3-2 Numerical simulation of heat transfer using PHOENICS.

The first lecture sets out general ideas, describing the main components of computer modelling of heat transfer, and indicating some difficulties and their partial solution.

The second lecture consists primarily of a set of how-to-do-it demonstrations, with the aid of PHOENICS and a personal computer.

"Shareware" versions of PHOENICS will be provided to any participants who wish to make copies on their own 3 $\frac{1}{2}$ inch diskettes. Alternatively, they can be ordered from CHAM:

Address: Bakery House, 40 High Street, Wimbledon Village,
London SW19 5AU, United Kingdom

Tel: 0181 947 7651

Fax: 0181 879 3497

E-Mail: PHOENICS@CHAM.DEMON.CO.UK

Modelling heat transfer, 1	1 ---- 46	Modelling convective, conductive and radiative heat transfer by Brian Spalding (CHAM Ltd)
<p>Contents of the lecture:</p> <ul style="list-style-type: none"> * The nature of modelling * The components of modelling <ol style="list-style-type: none"> 1. Engineering formulae 2. Differential equations 3. Models of complex physical processes <ol style="list-style-type: none"> 3.1 Turbulence 3.2 Radiation 4. Numerical analysis 5. Computer software * Recent advances and developments <p>Note: Exemplifications are provided in a companion lecture</p>		

Modelling heat transfer, 1	2 ---- 46	Definitions of modelling: (a) mathematical (b) physical
<p>Modelling is the attempt to predict what will happen in not-yet-arisen circumstances, by either:</p> <ul style="list-style-type: none"> (a) solving mathematical equation systems which embody relevant scientific and empirical knowledge, or (b) conducting physical experiments on (usually) small-scale replicas of the apparatus or environment in question. <p>Both techniques have their own advantages and disadvantages.</p> <p>They are best used in concert, experiments on the physical model being used to test the validity of the mathematical one, which can then be used for speedy extrapolation.</p>		

Modelling heat transfer, 1	3 ---- 46	Mathematical modelling of conductive, convective and radiative heat transfer: the main components
<ol style="list-style-type: none"> 1. "Engineering formulae" ----- These embody the results of previously-conducted experiments or calculations in easily-usable form. When available and applicable, they often provide the quickest, cheapest and most reliable predictions. 2. Differential (or integro-differential) equations ----- These embody some aspects of scientific knowledge in a general and compact form. Sometimes (but rarely) they may be solved (ie caused to yield formulae amenable to manual evaluation) by analytical (ie not numerical) maths. 		

Modelling heat transfer, 1	4 ---- 46	Mathematical modelling of conductive, convective and radiative heat transfer: the main components; continued.
----------------------------------	-----------------	---

3. Models of complex physical processes

The word "model" is here used in a different sense, namely for a set of equations (differential or algebraic) which may approximately represent the important features of complex physical phenomena without attention to all their details.

The models relevant to heat transfer are those of:

- * turbulence, * radiation, * multi-phase flow,
 and * chemical reaction.

This lecture concerns only the first two.

Modelling heat transfer, 1	5 ---- 46	Mathematical modelling of conductive, convective and radiative heat transfer: the main components; continued
----------------------------------	-----------------	--

4. Numerical analysis

The differential equations can be solved by numerical methods which usually involve:-

- * discretization, ie confinement of attention to a finite number of locations in the space-time domain in question;
- * formulation of algebraic equations embodying as much as possible of the content of the differential equations;
- * solution of the resulting equations by iterative successive-adjustment procedures, conducted by means of a digital computer.

Modelling heat transfer, 1	6 ---- 46	Mathematical modelling of conductive, convective and radiative heat transfer: the main components; concluded
----------------------------------	-----------------	--

5. Computer software

Computer codes, often general-purpose ones with special-purpose adaptivity, are used to instruct the computer.

They usually comprise:-

- * a pre-processor for input of data on:
 - problem-defining geometry,
 - initial/boundary conditions,
 - numerical-solution-control data;
- * a main processor for solving the equations;
- * a post-processor for displaying and interpreting the simulated phenomena.

Modelling heat transfer, 1	7 ---- 46	The components in more detail 1. Engineering formulae Steady conduction
----------------------------------	-----------------	---

* "Shape-factor" formulae connect steady-state heat-flux QDOT, with conductivity K, temperature difference DT, and shape factor S, by $QDOT = K * DT * S$ where:

S = area / thickness for a plane wall
S = 2 * PI * length * ln(R2/R1) for concentric cylinders
S = 4 * PI * (1/R1 - 1/R2) for concentric spheres
S = 2 * PI * length /
 $cosh_minus_1((R2^{**2} + R1^{**2} - E^{**2})/(2 * R1 * R2))$
for eccentric cylinders
S = 4 * PI * R1 / (1 - 0.5*R1/H) for a sphere buried H deep

* These formula are copied from AF Mills, "Heat Transfer", published by Irwin, 1992, where more can be found.

Modelling heat transfer, 1	8 ---- 46	The components in more detail 1. Engineering formulae Transient (ie time-dependent) conduction)
----------------------------------	-----------------	---

* Engineering formulae for time-dependent conduction are more numerous and more complex, because there is one more dimension (viz time) and two more relevant properties (viz density and heat capacity).

An example is: $Q = DT * SQRT((K * CP * RHO)/(PI * TIME))$
where Q is the heat flux into a semi-infinite cold body of which the temperature is suddenly raised.

However, few transient-heat-conduction formulae are so brief; and they are restricted to:

- * a few simple geometries,
- * uniform material properties,
- * simple initial conditions (eg uniform temperature),
- * simple boundary conditions (eg uniform heat flux).

Modelling heat transfer, 1	9 ---- 46	The components in more detail 1. Engineering formulae Convective heat transfer and friction
----------------------------------	-----------------	---

* Formulae for forced and free convection at surfaces of simple geometry with simple boundary conditions are usually presented as relations between:

CF, the friction coefficient or CD the drag coefficient,
NU, the Nusselt Number or ST the Stanton Number,
and
RE, the Reynolds Number,
PR, the Prandtl Number, and (for free convection)
RA, the Rayleigh Number

They may be found in textbooks and handbooks; that by AF Mills (loc cit) provides formulae for 25 configurations.

However, to assemble formulae for all needs is impossible.

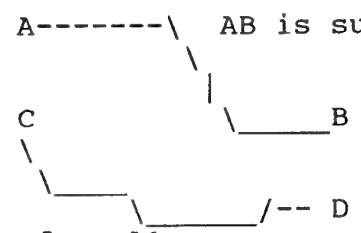
Modelling heat transfer, 1	10 ---- 46	The components in more detail 1. Engineering formulae Radiation from surface to surface
----------------------------------	------------------	---

* Formulae for the heat radiated by surface A1 across a wholly transparent space to surface A2 are usually expressed as:
 $Q_{DOT1} = \text{SIGMA} * T1^{**4} * \text{EMISSIVITY} * A1 * \text{VF12}$
where SIGMA is $5.6697\text{E-}8 \text{ W/m}^{**2} \text{ K}^{**4}$,
VF12 is the proportion of the radiation emitted by A1 which impinges on A2, and
EMISSIVITY is a fraction, less than unity, which depends on the material in question, its surface finish and on its temperature T1.

VF12, called either view factor or shape factor, depends on the shapes, sizes and relative locations of A1 and A2. If these are sufficiently simple, VF12 can be computed from a formula. Examples follow.

Modelling heat transfer, 1	11 ---- 46	The components in more detail 1. Engineering formulae Radiation between surfaces, continued
----------------------------------	------------------	---

For an inner concentric cylinder, $\text{VF12} = 1$
For an outer concentric cylinder, $\text{VF12} = A2 / A1$
For long parallel plates of width W and separation S, $\text{VF12} = \text{SQRT}(1 + (S/W)^{**2}) - (S/W)$
For long surfaces with parallel edges, A, B, C and D, Hottel's "string rule" is:

$$\text{VF12} = \frac{(AD + BC - AC - BD)}{LAB}$$

where AD, BC etc are the distances apart of the edges indicated, and LAB is the distance from A to B along surface A1.

Modelling heat transfer, 1	12 ---- 46	The components in more detail 1. Engineering formulae Radiation between surfaces, concluded
----------------------------------	------------------	---

Formulae for more complex three-dimensional shapes are either much more complex than the above (see AF Mills, loc cit) or non-existent.

When the intervening space itself absorbs part of the radiation directed through it, the only simple formula for VF12 is that for two surfaces of dimensions which are small in comparison with the intervening distance D12, and for a uniformly absorptive medium. It is:

$$\text{VF12} = \exp(-\text{ABSRPTVTY} * D12) * A2\text{projctd} / (\text{PI} * D12 * L12^{**2})$$

To take full account of practically-encountered geometries, materials and thermal conditions defeats formula makers.

Modelling heat transfer, 1	13 ---- 46	The components in more detail 1. Engineering formulae Concluding remarks
<p>* The engineering formulae have great practical value, because, even when their conditions of applicability are not wholly complied with (eg because of non-uniform heat-flux or temperature conditions, or of geometric complexity) they can often yield realistic order-of-magnitude answers to prediction questions.</p> <p>* However, when such answers are too imprecise, only computer-based mathematical modelling can suffice, as will be explained; for this can handle complex geometries, non-uniform properties and boundary conditions, and processes in which conduction, heat-transfer and radiation (AND two-phase and chemical-kinetic effects) all participate.</p>		

Modelling heat transfer, 1	14 ---- 46	The components in more detail 2. Differential equations The main conservation laws
<p>* The differential (and integro-differential) equations used in modelling heat transfer represent balances, over space-time domains of infinitesimal size, of the entities (whether of the total prevailing mixture or for distinct phases or substances within it):</p> <ul style="list-style-type: none"> - mass, expressed by way of density and concentration, - momentum, expressed by way of velocity, - energy, expressed by way of temperature or enthalpy. <p>* The equations balance the CHANGES WITH TIME, and the SOURCES AND SINKS, within the domain, against the INFLOWS AND OUTFLOWS across the surface of the domain.</p>		

Modelling heat transfer, 1	15 ---- 46	The components in more detail 2. Differential equations The main conservation laws, contd.
<p>* CHANGES WITH TIME are expressed as: $d(\text{property} * \text{entity value per unit mass} * \text{density}) / d(\text{time})$</p> <p>* SOURCES are expressed as: rate of creation of entity per unit volume and time</p> <p>* INFLOWS and OUTFLOWS per unit area are expressed as:</p> <ul style="list-style-type: none"> - CONVECTION fluxes, viz velocity * density * entity value per unit mass, and - DIFFUSION fluxes, often represented by (negative of) gradient of entity_per_unit_mass * exchange_coefficient <p>* Insofar as diffusion fluxes are ill-represented by the gradient formula, corrections are added to the sources.</p>		

Modelling heat transfer, 1	16 ---- 46	The components in more detail 2. Differential equations The main conservation laws, concluded
----------------------------------	------------------	---

* The differential equations form a rather secure foundation for the mathematical modelling process. They express well-established laws of physics.

* Less certainty attaches to the AUXILIARY RELATIONS which are needed to complete them, namely:

- thermodynamic relations connecting density (say) with temperature, pressure and concentration;
- transport-property relations from which exchange coeffs. (viscosity, thermal conductivity and diffusivities) can be derived; and
- relations connecting the absorptivity and emissivity of materials with wave-length, temperature and concentration.

Modelling heat transfer, 1	17 ---- 46	The components in more detail 3. Models of complex physical processes Introduction
----------------------------------	------------------	--

* "Models" of complex physical phenomena, in the sense of panel 4 above, are the result of deliberate ignorance. They are answers to the question: "What can we ignore, yet still retain the essence?" There are no "right answers".

* Even well-established laws such as Newton's viscosity law, are "models", valid only in restricted circumstances. Thus viscosity ceases to be a useful model for shear stresses in gases when the distance between molecules ceases to be much smaller than the apparatus dimensions. The viscosity concept ignores the distance-between-molecules effect.

* The use of the viscosity concept for atmospheric-pressure flows entails little error; other models are more dubious.

Modelling heat transfer, 1	18 ---- 46	The components in more detail 3. Models of complex physical processes 3.1 Turbulence models; general
----------------------------------	------------------	--

* Turbulent fluctuations involve times which are too short, and distances which are too small, to be resolved by present-day computational techniques. Therefore the details are deliberately ignored, and attention is focussed on time-average quantities such as the energy of the fluctuating motions and the average length scale of the fluctuations.

* Most models derive from the ideas of Ludwig Prandtl, who saw turbulent fluids as being like gases: the energy of the turbulent fluctuations corresponded to the gas temperature; and the length scale to the average distance between molecules, ie the mean free path. By analogy with molecular theory:

"turbulent viscosity" = const * SQRT(energy) * length

Modelling heat transfer, 1	19 ---- 46	The components in more detail 3. Models of complex physical processes 3.1 Turbulence models; general (contd)
----------------------------------	------------------	--

* The differential equations for turbulent flows are thus often regarded as similar to those of laminar flows, with time-average velocities, energies and concentrations in the places of the instantaneous ones, and "turbulent viscosities" and other transport properties in the places of the true (ie laminar-flow) ones.

* The question then is: How can the "turbulent transport properties" be computed? And, if the answer is "from the energy and length scale", the next question is: "Then how are these to be computed?"

* The commonly-used turbulence models differ mainly in the ways in which these questions are answered.

Modelling heat transfer, 1	20 ---- 46	The components in more detail 3. Models of complex physical processes 3.1 Turbulence models; general (contd)
----------------------------------	------------------	--

* Prandtl proposed in 1925 that the length scale should be proportional to the distance across the mixing layer, and the energy to the square of (velocity gradient times length scale). This "mixing-length" theory remains one of the more reliable models; but one needs not-always-available data for the proportionality constants.

* In 1945, he made a different proposal for getting the energy of turbulence, namely from a differential equation of the same form as that used for thermal energy (see above); but the length was still prescribed in the same way as before.

* However, in 1942 Kolmogorov had already proposed a means of getting also the length-scale from a differential equation.

Modelling heat transfer, 1	21 ---- 46	The components in more detail 3. Models of complex physical processes 3.1 Turbulence models; general (contd)
----------------------------------	------------------	--

* Nowadays, most turbulence models are developments of the first "two-differential-equation" turbulence model, which in effect combined Prandtl's and Kolmogorov's ideas, albeit by re-discovery rather than development.

* The first re-discoveries took place in 1968, when Harlow and Nakayama invented the k-epsilon model, and Saffmann and Spalding (independently of each other) invented the k-W model.

epsilon = energy-dissipation rate = const*energy**1.5/length

W = (vorticity fluctuations)**2 = const*energy/length**2

Modelling heat transfer, 1	22 ---- 46	The components in more detail 3. Models of complex physical processes 3.1 Turbulence models; general (contd)
----------------------------------	------------------	--

* All the above authors, and their successors, have had to make guesses about the diffusional-transport mechanism and about the source and sink (ie negative source) terms. They have differed only in detail.

* The diffusional term is easiest: let the diffusivities of k , ϵ , W , etc equal a constant * turbulent viscosity.

* The source of energy is also easy, viz the turb. viscosity times the sum of appropriate velocity gradients. Then the sources of ϵ , W etc are taken as proportional to this.

* The sink terms are similarly treated. The big question is: What are the values of the proportionality constants?

Modelling heat transfer, 1	23 ---- 46	The components in more detail 3. Models of complex physical processes 3.1 Turbulence models; general (concluded)
----------------------------------	------------------	--

* Almost all authors propose constants which enable predictions based on the models to fit (selected) experimental data. No-one has ever succeeded in finding constants which will procure agreement with all data.

* Moreover, as even Harlow and Nakayama recognised, the "constants" are in fact dependent on (at least) Reynolds number; and the interaction of density fluctuations with body-force fields introduces new and important influences requiring further terms in the equations and further experimentally-derived constants to go with them.

* Some authors have sought to escape the difficulties by introducing more differential equations,

Modelling heat transfer, 1	24 ---- 46	The components in more detail 3. Models of complex physical processes 3.1 Turbulence models; advances.
----------------------------------	------------------	--

* A major motive for solving MORE differential equations is to be enabled to abandon the Prandtl-Kolmogorov turbulent-viscosity hypothesis, which is known not to fit all data, some of which imply that the viscosity must be negative!

* Two distinct directions have been taken, namely:

- (1) To invent and solve differential equations having the turbulent-stress components (ie the "Reynolds Stresses") as the solved-for variables.
- (2) To treat a turbulent fluid as a mixture of (at least) two distinct fluids, each having its own set of velocity components, temperatures, etc.

Modelling heat transfer, 1	25 ----- 46	The components in more detail 3. Models of complex physical processes 3.1 Turbulence models; advances (contd)
----------------------------------	-------------------	---

* While researchers have been proposing ever more complex models (which so far are notable more for their promise than their achievement), the application of turbulence modelling in practical circumstances has necessitated a return to models which employ FEWER differential equations.

* Many practical circumstances involve simultaneous convection in a fluid and conduction within numerous solids immersed within it. Because the spaces between the solids are small,
(1) the local Reynolds numbers are low, and
(2) the number of grid nodes is too small to allow accurate computation of turbulence energy generation.

* Two recent developments (Spalding, 1994) provide a solution.

Modelling heat transfer, 1	26 ----- 46	The components in more detail 3. Models of complex physical processes 3.1 Turbulence models; advances (contd)
----------------------------------	-------------------	---

* The first development is the so-called LVEL model, which postulates that the local effective (ie laminar + turbulent) viscosity depends only upon the local velocity, the distance from the nearest solid wall, the distance between the two nearest walls, and the local laminar viscosity.

* An analytical relationship exists between these quantities, derived from a formulation of the "universal law of the wall" (Spalding, 1961).

* The calculation of the said distances is effected by way of by the second development. This entails the once-for-all solution of an elliptic differential equation of Laplace type at the start of the calculation. This is easy.

Modelling heat transfer, 1	27 ----- 46	The components in more detail 3. Models of complex physical processes 3.1 Turbulence models; advances (conclud)
----------------------------------	-------------------	---

* The merits of the LVEL model are:

- it is inexpensive computationally;
- it can therefore be applied to practical problems, for example those arising in electronics cooling;
- it yields predictions which are in accordance with measurements when the nearby walls are wide and parallel;
- it yields results which are at least plausible in all other circumstances.

* On the other hand, it is new and therefore relatively little tested.

* Exemplifications of LVEL and other models will be provided in the companion lecture.

Modelling heat transfer, 1	28 ---- 46	The components in more detail 3. Models of complex physical processes 3.2 Radiation: general
----------------------------------	------------------	--

Models of radiation involve the deliberate ignoring of one or more of:-

- * Absorption and emission by the medium through which the radiation passes. This may be valid when the medium is room-temperature air or the distances between solid surfaces are small.
- * The possibility that very little of the radiation is absorbed or scattered as it passes through the medium. This may be valid when the medium is "murky", as in a coal-fired furnace. It is of course at the opposite extreme from the first presumption.

Modelling heat transfer, 1	29 ---- 46	The components in more detail 3. Models of complex physical processes 3.2 Radiation: general (continued)
----------------------------------	------------------	--

or the ignoring of:-

- * The dependences of the radiative properties of the materials on temperature and wave-length. This may be valid for some solids, but never for gases.
- * The fact that rays are transmitted at all angles, not just at right angles to surfaces at solids. This is valid only in rare circumstances.

Often the ignored factors are of practical significance; so simulations of heat-transfer processes which involve radiation are frequently of low accuracy.

Modelling heat transfer, 1	30 ---- 46	The components in more detail 3. Models of complex physical processes 3.2 Radiation: general (continued)
----------------------------------	------------------	--

The most accurate radiation calculations are made when the medium is very "murky" indeed; for then the "mean free path" of radiation is small compared with the size of the apparatus and the effect of radiation is akin to that of heat conduction.

The effective conductivity of such a mixture is equal to:

$$3 * \sigma * (\text{absolute temperature})^3 / (a + s)$$

where a and s are respectively the absorption and scattering coefficients.

This is added to the laminar and turbulent components.

Modelling heat transfer, 1	31 ---- 46	The components in more detail 3. Models of complex physical processes 3.2 Radiation: general (concluded)
----------------------------------	------------------	--

The conductivity approximation is congenial to those who are already simulating conduction and convection, because it fits into the already-existing calculation scheme, namely that for solving elliptic differential equations.

So valuable is this feature that several other models have been devised so as to have the same merit, if possible with less departure from realism.

However, no attempt of this kind can succeed fully, because the equations which describe radiation correctly are of INTEGRO-differential kind.

Radiation involves "action at a distance".

Modelling heat transfer, 1	32 ---- 46	The components in more detail 3. Models of complex physical processes 3.2 Radiation: particular models
----------------------------------	------------------	--

* The "six-flux" model used in some computer codes limits the angular distribution of radiation to 6 bundles of rays, positively and negatively directed in the three coordinate directions.

It involves the solution of three rather simple elliptic equations (unless distribution in wave-length space is to be considered also).

It is usable for both dense and transparent media, and is most accurate when the radiation flux approaches one-dimensionality.

The six-flux model originated in astrophysics, and is associated with the names of Shuster and Schwarzschild.

Modelling heat transfer, 1	33 ---- 46	The components in more detail 3. Models of complex physical processes 3.2 Radiation: particular models (contd)
----------------------------------	------------------	--

* A more elaborate method than the six-flux model is the "discrete-transfer" method of Lockwood and Shah (18th Combustion Symposium, 1980). This allows for radiation in a greater number of directions, and so is better able to account for geometrical complexity. The computational expense is proportionatly greater.

* A method which is simpler than either is that based upon the "Eddington spherical-harmonic approximation". This involves the solution of only one elliptic equation, and has been used with some success for coal-fired furnaces (Liu and Swithenbank, Eurotherm 17, 1990). It appears to be restricted to rather dense media; but it is more widely applicable than the conduction approximation.

Modelling heat transfer, 1	34 ---- 46	The components in more detail 3. Models of complex physical processes 3.2 Radiation: particular models (concl)
----------------------------------	------------------	--

* The "zone method" of Hottel and Sarofim (Radiative Transfer, McGraw Hill, 1967) is potentially the most accurate method; for it seeks to account for all directions of radiation, and for all absorptions, reflections and re-emissions. Moreover it can be fitted into the computational framework of a computer code for solving conduction and convection. It is however generally believed to be prohibitively costly to implement; and it is certainly little used.

* Another expensive method, which has however the merit of representing the physical processes rather faithfully, is the Monte Carlo method of Howell (Advances in Heat Transfer, Acad Press, 1968). As computers become more powerful, its expense may become less of a deterrent to use.

Modelling heat transfer, 1	35 ---- 46	The components in more detail 3. Models of complex physical processes 3.2 Radiation: a particular need
----------------------------------	------------------	--

Radiative heat transfer in congested spaces

* Just as the commonly-used turbulence models have proved unsuitable for electronics-cooling simulation, and for other problems in which many solids are distributed within the fluid, so is it also with radiation.

* On the one hand the calculation of all the view factors is a huge task, because account has to be taken of which surfaces are obscured from view by intervening objects.

* On the other hand, the medium is almost completely non-absorbing and non-scattering; so the conduction and Eddington approximations are invalid.

Modelling heat transfer, 1	36 ---- 46	The components in more detail 3. Models of complex physical processes 3.2 Radiation: a particular need (concl)
----------------------------------	------------------	--

A suggestion for development

* The radiant flux from a wide plate to another parallel to it increases with the temperature difference; so one can define an "effective conductivity for the empty space.

* However, the flux is independent of the distance apart; so the conductivity must depend upon (indeed be proportional to) that distance.

* The inter-wall distances can now be calculated from an elliptic equation, as explained in connexion with the LVEL model of turbulence. Could this not be used as the basis of a conduction model for empty spaces? Yes, it could.

Modelling heat transfer, 1	37 ---- 46	The components in more detail 4. Numerical analysis Overview
----------------------------------	------------------	--

The numerical-analysis component of heat-transfer modelling is a large subject which can not be thoroughly expounded here. Therefore only a few aspects will be highlighted and briefly discussed, namely:-

- * Grids and solution algorithms
- * The main difficulties
- * Some ways of diminishing them

Modelling heat transfer, 1	38 ---- 46	The components in more detail 4. Numerical analysis 4.1 Grids and solution algorithms
----------------------------------	------------------	---

- * Most methods for solving the differential equations of CFD involve "discretising" the space and time dimensions, so as to form a "grid", of which the nodes, surfaces and volumes define which elements of the space-time continuum will be selected for attention.
- * What happens between the selected nodes and surfaces is not ignored; but it is guessed as being deducible from what is computed for the considered elements by way of simple interpolation formulae.
- * Therefore human choice enters the simulation and influences (perhaps impairs) its results, rendering them at least somewhat uncertain.

Modelling heat transfer, 1	39 ---- 46	The components in more detail 4. Numerical analysis 4.1 Grids and algorithms (concluded)
----------------------------------	------------------	--

- * Once the grid and the interpolation formulae have been chosen, there are further parameters to introduce which, though they should not influence the final solution. will have an effect on how quickly (indeed even whether!) the results will be obtained.
- * So-called "relaxation factors" are of this kind. Correctly chosen, they bring speedy convergence of the iterative calculation procedure; wrongly chosen they may introduce numerical instability, causing the computer to "crash".
- * Further choices concern the type of linear-equation solver (Gauss-Seidel, Stone, conjugate-gradient, etc). Some are good for some problems, but bad for others.

Modelling heat transfer, 1	40 ---- 46	The components in more detail 4. Numerical analysis 4.2 The main difficulties
<p>* What difficulties faced by the mathematical modeller of heat transfer can be deduced from the last two panels. They arise from the lack of any clear and certain knowledge about:-</p> <ul style="list-style-type: none"> - how fine a grid is necessary for the desired accuracy; - which of the available interpolation schemes is most suitable; - what values should be used for the relaxation factors (which may, and probably should, be different for each dependent variable and should change as convergence is approached); - which equation solver should be chosen for which variable. 		

Modelling heat transfer, 1	41 ---- 46	The components in more detail 4. Numerical analysis 4.2 The main difficulties (concluded)
<p>* Aggravating these difficulties is the knowledge that every increase in grid size makes the computation take longer and cost more.</p> <p>* Moreover, too large an increase may entail the necessity of gaining access to a larger machine.</p> <p>* Finally, once the computation has been completed, how is one to know whether the grid was fine enough to give the required accuracy, without repeating it with a finer grid and then a still finer one?</p> <p>* All this is on top of the doubtfulness regarding the models of turbulence, radiation, etc.</p>		

Modelling heat transfer, 1	42 ---- 46	The components in more detail 4. Numerical analysis 4.3 Diminishing the difficulties
<p>* ACCURACY ASSESSMENT is achievable without repeating the whole calculation; for one can make a cell-by-cell check to answer the question: "If this cell were subdivided, by how much would its influence on its immediate neighbours change? This is not costly, and may suffice.</p> <p>* FINE-GRID-EMBEDDING allows one to put cells only where they are (believed to be) needed. This can be done with grids which are basically structured: a completely-unstructured grid, which brings its own problems (computational expense; MORE questions to answer!) is not needed.</p> <p>* ADAPTIVE GRID REFINEMENT (or coarsening) combines the above two features. It is what all are vendors are seeking.</p>		

Modelling heat transfer, 1	43 ---- 46	The components in more detail 4. Numerical analysis 4.3 Diminishing the difficulties (concl'd)
----------------------------------	------------------	--

* GRID-LESS Modelling is what is needed by the users. Even though a grid may still be used, the users should not need to see it unless they want to. The "Virtual-Reality" front end is a move towards it.

Of course, the less the user does himself, the greater the amount of expertise that must be built into the software.

* "IN-FLIGHT" ADJUSTMENT of relaxation factors can make their initial choice less important.

All the above features are in embryonic existence. They can only improve with time.

Modelling heat transfer, 1	44 ---- 46	The components in more detail 4. Computer software General remarks
----------------------------------	------------------	--

* Most practitioners of heat-transfer modelling are more interested in heat transfer than in computer programming; so they prefer to use commercial packages than create their own.

* However, some of them still need access to (parts of) the source code, in order to add modelling, property or output features of their own. Some commercial codes allow this.

* Such codes are now cheaper to acquire than formerly; and some are even available as "shareware", which means that they may be freely copied.

* However, learning to use them still takes time.

Modelling heat transfer, 1	45 ---- 46	The components in more detail 4. Computer software General remarks (concluded)
----------------------------------	------------------	--

* Although the ideal of creating "expert" software packages is inspiring current developments, it is not yet a reality. Until it is, users of all software packages need to look critically at the results which they produce.

* When these results prove to be at variance with reasonable expectations, it is not necessarily the package which is at fault. The user may have supplied it with inappropriate data; or the phenomenon being simulated may be one for which the built-in science is not yet adequate.

* Modelling heat transfer still requires thought and care. Those who proclaim that it is easy do a disservice to the heat-transfer community.

Modelling heat transfer, 1	46 ---- 46	Recent developments and current trends
<p>Some allusions to developments and trends have already been made; and more will be mentioned in the companion lecture. Therefore here only two such topics will be mentioned, viz:</p> <ol style="list-style-type: none"> 1. Parallel computing. Recent developments with distributed-memory machines of low cost make unprecedentedly large problems affordable. Users should prepare themselves mentally (and financially) 2. Fluid flow and solid stress in one software package. The necessity to use two different packages, one for fluid flow and the other stresses in the solids within them, may soon disappear. The technique exists already. 		

Modelling heat transfer, 2	1 ----- 6	Modelling heat transfer by means of the PHOENICS Computer Code by Brian Spalding (CHAM Ltd)
<p>Purpose of the lecture</p> <p>-----</p> <p>This lecture illustrates some of the facts and arguments mentioned in lecture 1, by way of excerpts form the PHOENICS On-Line Information System (POLIS) and of demonstrations of PHOENICS in action.</p> <p>The following panels list topics which will probably be discussed; but wishes expressed by the audience will be followed as far as possible.</p>		

Modelling heat transfer, 1	2 ----- 6	General topics
<ul style="list-style-type: none"> * The structure of PHOENICS, seen via the "Commander" * The Application Album * The Encyclopaedia * The Satellite Menu, the libraries and tutorials * The demonstrations 		

Modelling heat transfer, 1	3 ----- 6	Turbulence-model topics
<ul style="list-style-type: none"> * Low-Reynolds-Number models * The Two-Fluid model * The LVEL model 		

Modelling heat transfer, 1	4 ---- 6	Radiation topics
<ul style="list-style-type: none"> * The six-flux model * Surface-to-surface radiation * The radiosity model 		

Modelling heat transfer, 1	5 ---- 6	Numerical-analysis topics
<ul style="list-style-type: none"> * The CLDA formulation * Other low-dispersion models * Fine-grid embedding * Expert 		

Modelling heat transfer, 1	6 ---- 6	Other topics
<ul style="list-style-type: none"> * Stress analysis in solids * Virtual reality * Shareware 		

von Karman Institute for Fluid Dynamics

Lecture Series 1995-03

INDUSTRIAL COMPUTATIONAL FLUID DYNAMICS

April 3 - 7, 1995

MODELLING MULTIPLE PHASE FLOW AND PHASE CHANGE

I. Dilber
FDI, USA

Modelling Multiple Phase Flow and Phase Change

Ilhan Dilber

Fluid Dynamics International
Evanston, Illinois, 60201, USA

1. Two-Phase Flows: Theoretical Foundations

1.1 Definition Of A Two-Phase Flow

There exists a variety of multiphase phase flows depending on combinations of phases as well as on their flow structure. In the typical engineering context, a material exists in one of three phases: Solid, Liquid or Gas. Early attempts at classifying two-phase flows were developed by Zuber (1971), Ishii (1971) and Kocamustafaogullari (1971) among others. These authors defined three classes of multiphase flows based on the geometry of the interfaces, i.e. separated flows, mixed flows and dispersed flows. The class of separated flows is characterized by the existence of a single interface. This is generally the case for jet flows, film boiling, crystal growth, solidification of metals, or layer flows of different liquids, as in coating or coextrusion problems. At the other extreme, dispersed flows are characterized by a large number of interfaces. This often occurs in particulate, bubbly and droplet flows such as sprays, sedimentation or erosion problems. The change in interfacial structures occurs gradually, which leads to a third class of multiphase flows characterized by the existence of both separated and dispersed flows. This would be the case in most steam-water systems.

Following on from the above concepts, we define a multiphase flow as one in which one or many materials coexist in any combinations of the three possible states of matter described above. This view extends the definition of multiphase flows to one that characterizes a multiphase flow by the existence of one or several interfaces irrespective of the materials present in the flow. Thus, we can have the following combinations: Gas-Liquid, , Gas-Solid, Solid-Liquid as well as immiscible liquid mixtures. The latter is clearly not a two-phase flow in the traditional sense, however for all practical purposes it can be treated as a two-phase flow mixture. Given this, the term "two-phase flow" is generally understood to mean a flow in which two material phases are simultaneously present. In most applications the two phases are phases of different materials, for example, dust particles (solid phase) in air (gas phase).

1.2 Engineering Applications

The analysis of two-phase or multiple phase flow has been increasingly important in engineering systems for design, optimization, or safety concerns.

- | | |
|----------------------------|---|
| <i>Power:</i> | Condensers, engines, conventional and nuclear reactors, desuperheaters, erosion; |
| <i>Heat Transfer:</i> | Heat exchangers, dryers, refrigerators, electronic cooling systems; |
| <i>Environmental:</i> | Air conditioners, dust collectors, sewage treatment plants, clarifiers, pollutant separators; |
| <i>Geo-Meteorological:</i> | Sedimentation, rain drops, snow drifts; |

Biological: Blood flows, separation devices;
Chemical Processes: Dissolution processes, crystallization;
Food Processing: Aseptic heating, dissolution, spray drying

1.3 Characteristics Of Two-Phase Flows

The two-phase flow classification by flow structure has important ramifications with respect to the mathematical model used to describe the physics of multiphase flows. A large class of separated flows usually involves the existence of a single interface between phases. For instance, in crystal growth or solidification problems the two phases are clearly separated in space. For such problems a two-phase flow model is not required; a single-phase model with adequate representation of the interfacial conditions is sufficient.

In theory, it is possible to formulate a two-phase flow problem in terms of the local instantaneous variables. In a dispersed flow problem such a formulation would ultimately lead to a multi-boundary problem with the location of the interface being unknown due to the coupling of the fields and the boundary conditions. The mathematical difficulties encountered in obtaining a solution are prohibitively great and for many practical problems, they are beyond our present mathematical capabilities. These difficulties stem from the existence of the deformable moving interfaces with their motions being unknown and from the existence of fluctuations of variables due to turbulence and to the motions of the interfaces. The first effect causes complicated coupling between the field equations of each phase and the interfacial conditions, while the second effect introduces a statistical characteristic caused by the instability of the Navier-Stokes equations and the interfacial waves. However in most practical engineering problems the microscopic details are rarely needed, but rather macroscopic aspects of the flow are much more important. There are in the literature two distinct modeling approaches, commonly known as the Eulerian and Lagrangian methods.

1.4 Modeling Approaches

Eulerian Approach

One approach consists in using averaging procedures that effectively eliminates the unwanted fluctuations. Note however that the statistical properties of the fluctuations which influence the macroscopic process are retained. In the Eulerian method each of the phases is treated as a continuum. This implies that there is a set of continuum equations (Navier-Stokes, energy, etc.) for each phase at every point in the computational domain. These equations are averaged with respect to time, space or statistics. To account for the fact that two-phases may simultaneously exist at a given point, a function which identifies whether one of the phases or possibly the interface itself occupies the locus of the point is introduced. The average of the function -spatial or temporal- is commonly known as the void or time fraction. The transfer of information between phases is then accounted for through momentum, energy and mass transfer terms as well as a void or volume fraction.

The Eulerian approach is generally advantageous in cases where high particle concentrations occur and where high volume fractions of particulate matter becomes a dominating flow parameter. A complete description of this approach is found in Durst (1984).

In the Eulerian approach, the particle phase is considered a "pseudo-fluid" in combination with a real fluid or gas. The "multi-fluid" model is characterized by

- the co-existence of the particle and fluid carrier phase at each geometric location,
- a "smeared" velocity, temperature, volume fraction for each particle phase,
- each size grouping of particles can have a continuous velocity, temperature, and volume fraction distribution,
- each particle phase having its own turbulent fluctuation resulting in turbulent transport of mass, momentum, and energy,
- particle fluctuations are determined by convective diffusion, production, and interactions with gas phase turbulence,
- the inclusion of large slip and particle diffusion

Lagrangian Approach

In the second approach the "dispersed" phase is represented by discrete particles that are continually introduced at a given mass flow rate. These particles coexist with the "carrier" phase in the flow domain. The conservation equations for the carrier phase are described by the standard Eulerian equations for conservation of mass, momentum, and energy while the motion of the particles is described in a Lagrangian frame of reference. The information transfer between phases is accounted for by the momentum, energy, and mass gains or losses along particle trajectories. This methodology, referred to as the "Lagrangian" model will be described in the following sections. The Lagrangian method assumes that the particles are dilute. This assumption means that the motion of particles is controlled by local aerodynamic forces. In a dense particle flow, the particle motion is controlled by particle-particle collisions. In other words, in this approach, particles have enough time to respond to aerodynamic forces before colliding with another particle. This assumption implies that information between phases is not carried through pressure waves but instead, along particle trajectories. Note that this model, currently does not account for break-ups, or coalescence and assumes a steady state simulation. There are, on the other hand, some problems that respond better to one approach than the other.

Solution by the Eulerian approach implies an elliptic system of equations and a boundary value type of solution. The Lagrangian approach with the solution along particle trajectories is parabolic in nature. An advantage of the Lagrangian approach is illustrated in by the injection of particles from a vertical source as shown in Figure 1.1. By considering a small computational domain or volume, one can see the possibility of particles both flowing upwards and downwards. The particle velocity would not be unique in this cell and definable in a two-fluid model. On the other hand, this application would offer no problem to the Lagrangian approach.

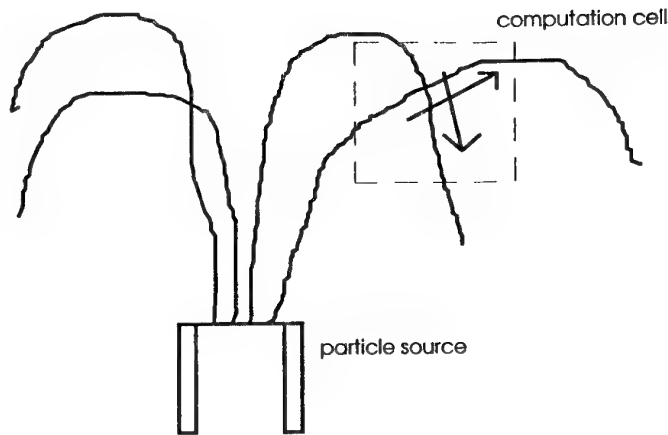


Figure 1.1 Particle Trajectories From A Vertical Source

The Lagrangian approach or "particle trajectory model" is characterized by

- the interaction through momentum, mass, and energy exchange between the continuum and dispersed phases,
- the capability of handling large slip and temperature variation between phases,
- the neglect of particle diffusion,
- the designation of particle groups by their size distribution.

It is interesting to note that the Lagrangian approach is fitted to the analysis of the dynamics of a single particle. The Lagrangian approach has proven to be particularly successful in simulating aerosols, atomizers, spray drying, spray combustion, pollutant dispersion, filtration, evaporation and condensation processes, and so forth. On the other hand the Eulerian approach is best suited to the analysis of the collective behavior of a cloud of particles. However, there is evidence in the literature, Durst (1984) that in the range of small void fractions, the "two-fluid" model and the "Lagrangian" model lead to similar predictions. Additional discussion on the Lagrangian approach is found in Crowe (1977, 1982).

1.5 Comparisons and Applicability

A brief summary and comparison of the Lagrangian (discrete) and Eulerian (continuous) approaches to modeling multi-phase flow is given in the following tables.

Table 1-1 Physical Characteristics of Modeling Approaches

Modeling Approach	Coordinates	Gas Phase Affected by Particles	Phase Slip	Particle Transport Properties
Continuum	Eulerian	considered	yes	diffusion
Discrete	Lagrangian	considered	yes	stochastic

Table 1-2 Applicability of Modeling Approaches

Model	Particle Number Density	$\frac{\tau'_p}{\tau_f}$	$\frac{\tau'_p}{\tau_{pp}}$
Continuum	no limit	small to moderate	no limit
Discrete	small or moderate	no limit	very small

The ratios present in the above table provide indications of the capability of the modeling approaches in certain flow situations. These "residence" times, briefly described here, will be discussed more fully later in the course. The fluid residence time is defined as the ratio of physical dimension of the flow field and the mean flow field velocity.

Flow time (residence time) $\Rightarrow \tau_f = L / U$

The particle relaxation time is thought of as the time that a particle can respond to changes in the surrounding flow field.

$$\text{Particle Relaxation Time} \Rightarrow \tau'_p = \tau_p \left(1 + \frac{\text{Re}_p^{2/3}}{6} \right) \quad (1.5.1)$$

$$\text{where } \tau_p = \frac{D_p^2 \rho_p}{18\mu}, \quad \text{Re}_p = \frac{|u - u_p| D_p}{\nu}$$

$$\text{Particle-particle Interaction time} \Rightarrow \tau_{pp} = (c\pi n_p r_p^2)^{-1} (u_p')^{-1}$$

where τ_p is based on Stokes Drag, and τ'_p accounts for non-Stokesian drag. From the above definitions, certain types of flow can be characterized. Strong slip flow (frozen or diffusion-frozen) is characterized with large ratios of the particle relaxation time to the flow time, $\frac{\tau'_p}{\tau_f} \gg 1$.

Flows characterized by small values of this ratio are usually defined as "small slip", equilibrium, or diffusion equilibrium flows. Flows with small values of the ratio of particle relaxation to particle-particle impacting times, $\frac{\tau'_p}{\tau_{pp}} \ll 1$, are usually classified as "dilute" suspension flows. "Dense"

suspension flows are classified with large values of this parameter.

1.6 Approximation Levels

Depending upon the characteristics of the problem under examination there are three levels at which a two-phase flow model can be applied. The following section outlines these three levels which, as will become apparent, increase in order of complexity.

Level One

Under certain conditions it may happen that the particles of the dispersed phase follow the paths of the particles of the carrier phase, have the same temperature and velocity as the carrier phase and do not gain or lose mass. In other words, the dispersed phase has no "life of its own". For this to be a reasonable approximation it is necessary that the dispersed phase be very dilute, that the densities of the two phases are not very different and possibly that some other restrictions hold as well. When all these requirements are met, we in fact no longer have a two-phase flow. For practical purposes we are essentially dealing with massless particles. This is clearly a trivial situation, which only formally belongs to the two-phase classification.

Level Two

At the next level of complexity the dispersed phase has "a life of its own," but the interaction between the two phases is strictly one-way. This means that while the dynamics of the carrier phase drives the motion of the dispersed phase, the presence of the dispersed phase has no effect on the dynamics of the carrier phase. To justify this model it is necessary that the dispersed phase should be dilute, that the particles of the dispersed phase be sufficiently small, and that the interfacial forces between the two phases be negligible.

Because of the one-way coupling in this model it is possible to solve problems in sequence; that is, first solve for the carrier phase then solve for the particulate phase. The equations of the carrier phase (which can also be regarded as the equations of the mixture) are the standard equations of fluid dynamics: momentum conservation, mass conservation, energy conservation, species transport, turbulent kinetic energy and turbulent dissipation. These are, of course, Eulerian equations, and once solved, give field variables such as velocity, pressure, temperature, etc., at every point in the computational domain.

For the next step, a Lagrangian approach is used to simulate the dispersed phase. The motion of an arbitrary particle of the particulate phase is followed by solving a Newtonian momentum balance equation for that particle: the mass-acceleration of the particle equals the net force on it. The forces acting on a particle of the dispersed phase certainly include the drag force exerted by the carrier phase (Stokes drag generalized for arbitrary Reynolds number). Other forces will be problem-specific, but may include gravitational, centrifugal or electrical forces.

The formulation allows a completely arbitrary force in the Lagrangian particle equation to be specified. It will also allow arbitrary settings of the initial position and velocity of the particle. At solid boundaries it will be possible to stipulate various conditions, including that the particle sticks or reflects back to the flow.

In a non-isothermal process there may be heat transfer between the dispersed phase and the particulate phase. An equation to account for this effect states that the rate of change of the particle's temperature is determined by the difference between the temperatures of the two phases, as well as the loss or gain of latent heat where appropriate. Other potential sources of temperature change are included through a user-definable heat-source function.

Similarly mass transfer between the phases, as occurs for example with evaporation, condensation, combustion, etc., is simulated by the inclusion of an equation for the rate of change of mass of a particle of the particulate phase. Mass transfer may be governed by a form of Fick's

law, relating the mass flux to the gradient of concentration between the dispersed phase and the carrier phase, or by a general rate equation. Other potential forms of mass transfer are included through a user-definable function.

It is interesting to note the limitations of this model, as implied by the preceding discussion. Since the carrier phase is assumed to be unaffected by what is happening in the dispersed phase, the amount of heat and mass gained or lost by the dispersed phase particles must be sufficiently small that the imbalance created by the model is not significant. If this criterion is violated the model fails, and it becomes necessary to choose the next level of complexity.

Level Three

A more general situation arises when there is non-negligible transfer of momentum, heat and mass between the phases, so that the interaction between them is a two-way coupling.

The solution procedure used in the Lagrangian two-phase flow model is an iterative one. First, a solution to the governing continuum equations for the carrier phase is obtained. Next the Lagrangian (ordinary differential) equations are solved, using the fields from the continuum solution, for a number of particles of different sizes and different starting locations.

To this point the method is the same as that used in the Level 2 model. It is recognized now, however, that the presence of the particulate phase affects the continuum phase by transfer of momentum, heat and mass from the former to the latter. This is quantified by means of the Particulate Source in Cell (PSIC) method: the computed trajectories, temperatures, and masses of the particles are combined into source terms for momentum, heat and mass, which are then inserted into the right-hand sides of the respective continuum equations. Specifically, the equations of motion for the particle trajectories provide the source term for the momentum equations, the heat transfer equations for the particles provide the source term for the continuum energy equation and the mass transfer equations for the particles provide the source terms for the continuity and species equations.

The continuum equations are next solved again, with these source terms in place. The output of this computation is then used to specify a new set of field quantities for the Lagrangian equations, which are then re-integrated. Modified source terms are calculated, substituted back into the continuum equations, and so on. The process of iteration is continued until an equilibrium has been attained between the solutions for the two phases.

In turbulent flow the effect of turbulent fluctuations on the motion of the particles will be taken into account by use of a stochastic model. Several references are provided which outline the theoretical basis of the Lagrangian approach to modeling two-phase flow. It is not unlikely that situations may exist where energy, momentum, or mass may be represented by a combination of a Level 2 and a Level 3 analysis.

2. Mathematical description (Lagrangian approach)

Modeling of multi-phase flows can be complicated by the fact that the flows can be laminar or turbulent. The particles can interchange momentum, energy, and mass with the surrounding fluid with two-way coupling. The Lagrangian approach, as presented in this course, assumes that the particles are dilute with no particle interaction.

One way to estimate the dilution of the particle field is to estimate the particle relaxation times for diffusion and particle-particle collisions. The particle time constant or relaxation time is an indication of how fast a particle responds to changes in the velocity of the surrounding carrier medium. Particles with small time constants (relaxation time) very quickly attain the velocity of the surrounding carrier medium. The relaxation time for particle-to-particle collision is a measure of the time, for a particle traveling at a given velocity, required between collisions. When the ratio of the particle time constant to the particle-particle collision time is very small, the particle suspension is considered dilute.

2.1 Conservation Of Particle Linear Momentum

The prediction of particle trajectories is determined by the Lagrangian formulation of particle motion. In its general form.

$$m \frac{d\mathbf{u}_p}{dt} = \mathbf{F}_{drag} + \mathbf{F}_{gravity} + \mathbf{F}_{coriolis} + \mathbf{F}_{centrifugal} + \mathbf{F}_{user} \quad (2.1.1)$$

A brief description of the forces follows

Drag Force

The drag force on a solid particle is a function of the relative velocity between the particle and the surrounding fluid, the fluid density, and the projected area of the particle. In general, the drag coefficient can be given in terms of the local particle Reynolds number. The Oseen force, which is a correction to the steady state drag, can be considered to be included into the general relationships for drag, some of which are provided later in this section.

$$\mathbf{F}_{drag} = \frac{3}{4} \frac{V_p}{D_p} \rho_f C_D (\mathbf{u}_f - \mathbf{u}_p) |\mathbf{u}_f - \mathbf{u}_p| \quad (2.1.2)$$

Gravity or Buoyancy Force:

$$\mathbf{F}_{gravity} = m \left(1 - \frac{\rho_f}{\rho_p} \right) \mathbf{g} \quad (2.1.3)$$

Centrifugal Force:

$$\mathbf{F}_{centrifugal} = -m\boldsymbol{\Omega} \times (\boldsymbol{\Omega} \times \mathbf{r}) \quad (2.1.4)$$

Coriolis Force:

$$\mathbf{F}_{\text{coriolis}} = -2m\boldsymbol{\Omega} \times \mathbf{u}_p \quad (2.1.5)$$

User supplied forces

$$\mathbf{F}_{\text{user}} = f(\text{geometry, field variables, } t) \quad (2.1.6)$$

The Lagrangian form of the particle equation with the drag and buoyancy forces included is

$$m \frac{d\mathbf{u}_p}{dt} = \text{Re}_p C_D \frac{\mu_f \pi D_p}{8} (\mathbf{u}_f - \mathbf{u}_p) + v(\rho_p - \rho_f) \mathbf{g} \quad (2.1.7)$$

Dividing through by the particle mass yields

$$\frac{d\mathbf{u}_p}{dt} = \frac{18\mu_f}{\rho_p D_p^2} \left(\frac{\text{Re}_p}{24} \right) C_D (\mathbf{u}_f - \mathbf{u}_p) + \left(1 - \frac{\rho_f}{\rho_p} \right) \mathbf{g} \quad (2.1.8)$$

The drag coefficient, C_D , can be given in terms of a polynomial expansion of the particle Reynolds number. If Stokes Drag applies ($C_D = 24/\text{Re}_p$) for the particles, the above equation reduces to

$$\frac{d\mathbf{u}_p}{dt} = \frac{(\mathbf{u}_f - \mathbf{u}_p)}{\tau_p} + \left(1 - \frac{\rho_f}{\rho_p} \right) \mathbf{g} \quad (2.1.9)$$

In general,

$$\tau_p = \frac{\rho_p D_p^2}{18\mu f} \quad \text{where} \quad f = \frac{C_D \text{Re}_p}{24} \quad (2.1.10)$$

The more commonly used models for the drag coefficient and alternatively for the parameter f are the polynomial models where

$$f = \frac{C_D \text{Re}_p}{24} = \left(a + b \text{Re}_p + c \text{Re}_p^2 + \frac{d}{\text{Re}_p} \right) \quad (2.1.11)$$

and power law models such as,

$$f = \frac{C_D \text{Re}_p}{24} = 1 + 0.15 \text{Re}_p^{0.687} \quad (2.1.12)$$

Additional relationships are available for non-Stokesian drag models, such as Eq. (1.5.1), or for instance, see Table 2-1 as given in White (1985).

Table 2-1 Drag vs Particle Reynolds Number

$f = \frac{C_D Re_p}{24}$	Re_p
1.0	$Re_p \leq 0.1$
$0.94708 + 0.15375 Re_p + \frac{0.00376}{Re_p}$	$0.1 < Re_p \leq 1.0$
$1.21527 + 0.05091 Re_p - \frac{0.16203}{Re_p}$	$1.0 < Re_p \leq 10.$
$1.9375 + 0.02569 Re_p - \frac{4.86250}{Re_p}$	$10. < Re_p \leq 100.$
$4.0970 + 0.01518 Re_p - \frac{115.750}{Re_p}$	$100. < Re_p \leq 1000.$
$6.19250 + 0.01487 Re_p - \frac{1979.16}{Re_p}$	$1000. < Re_p \leq 5000.$
$-20.4394 + 0.01916 Re_p + \frac{24,112}{Re_p}$	$5000. < Re_p \leq 10000.$
$-69.270 + 0.02163 Re_p + \frac{225,695}{Re_p}$	$10000. < Re_p \leq 50000.$
$0.0183 Re_p$	$Re_p > 50000.$

Example 1

Predict the terminal velocity of particles in a fluid having the following properties,

$$\mu_f = 2cp = .02 poise = .002 Pa - sec$$

$$\rho_p = 1100 kg / m^3$$

$$D_p = 75 \mu m$$

$$\rho_f = 1000 kg / m^3$$

The particle time constant, assuming Stokes flow, is given by Equation 2.1.10 with “f” =1.

$$\tau_p = \frac{\rho_p D_p^2}{18\mu_f} = 0.00017 sec$$

Substituting into Equation 2.1.9 with the condition on particle terminal velocity to be $\frac{d\mathbf{u}_p}{dt} = 0$, yields:

$$\bar{u}_{terminal} = \left(1 - \frac{\rho_f}{\rho_p}\right) \bar{g} \cdot \tau_p = 0.015 cm / sec = 0.15 mm / sec$$

Example 2

Determine the estimated relative velocity of air bubbles moving in a counter-flowing liquid stream having a downward velocity of $U = 0.1 \text{ m/sec}$. For the following conditions,

$$D_b = 0.001 \text{ m}$$

$$\mu_f = 1.2 \text{ E} - 03 \text{ Pa} - \text{sec}$$

$$\rho_f = 1000 \text{ kg} / \text{m}^3$$

$$\rho_p = 1.15 \text{ kg} / \text{m}^3$$

an estimate of the bubble upward terminal velocity, is calculated as

$$\vec{u}_{terminal} = \left(1 - \frac{\rho_f}{\rho_p} \right) \vec{g} \cdot \tau_p = 0.45 \text{ m} / \text{sec}$$

assuming a Stokes drag relationship yielding a particle time constant of $\tau_p = 5.3 \text{ E} - 05 \text{ sec}$. The resulting upward bubble velocity is 0.35 m/sec (as seen by a stationary observer).

The calculation of the particle Reynolds number yields a value of 900 which is definitely greater than that assumed for Stokes flow. Using Equations 2.1.10 for the drag coefficient, the relationship for bubble time constant becomes

$$\tau_p = \frac{4\rho_p D_p^2}{3C_D Re_p \mu_f}$$

Since the above equation is a function of Reynolds number and therefore, the relative velocity of the particle, an iterative procedure is employed. One first obtains the solution assuming Stokes flow and calculates the Reynolds number. With this as the first iteration, one estimates the value of the drag coefficient from Equation 2.1.12 for example. A new estimate of the particle terminal velocity is obtained from solving Equation 2.1.9. This process is repeated until the computed and estimated Reynolds number for the particle is identical to within a reasonable value. The final upward bubble velocity obtained is 0.112 m/sec which is significantly different than that assuming Stokes flow. Other drag coefficient versus Reynolds number relations are expected to yield similar results.

Particle Relaxation Time

The parameter, τ_p is a very important term. It is referred to as the particle relaxation time representing the time required by the particle to reduce or increase its velocity to e^{-1} th of its original value. It is a measure of the particle's responsiveness to changes in the surrounding flow field. The magnitude of the particle relaxation time, sometimes called the particle time constant, is important in understanding particle dynamics, as well as devising appropriate numerical strategies to predict trajectories. Discussions of the effect of the particle time constant on the numerical methods for calculating particle trajectories will be presented later.

The particle relaxation time is a time scale associated with contact forces and represents the time it takes for a particle to adjust to changes in the surrounding flow field and reach that state of equilibrium with the carrier phase. A small particle relaxation time (relative to the time scale of the fluid) means that the particle has a chance to reach a local equilibrium with the fluid before the fluid itself has a chance to change.

The *Stokes* number, $St^H = \frac{\tau_p}{\tau_f}$, is the ratio of the relaxation time of the particle to the fluid

residence time, $\tau_f = \frac{L}{u_f}$ within a given domain traveled by the particle. For very small *Stokes*

numbers, the particles can be considered to react instantaneously to the conditions of the surrounding flow field. As a result, the dynamics of the particle will be very similar to the dynamics of a massless particle and will follow the streamlines. Conversely, if the *Stokes* number for the particle is large, changes in the flow occur much faster than the particle can react. As a result, the dynamic behavior of the particle is governed by factors other than contact forces, and the particle trajectories are dissociated from the trajectory of a massless particle.

In a two-way (*Level 3*) coupling simulation, the particles of the dispersed phase are able to influence the dynamic characteristics of the carrier. This influence is made possible by an exchange of momentum between the phases due to contact forces. Momentum transferred from the particle to the carrier phase appears as a source term in the governing momentum equations for the carrier medium. Thus, in the absence of mass transfer:

$$\frac{\partial \rho u_i}{\partial x_i} = 0 \quad (2.1.13)$$

$$\frac{\partial}{\partial x_j}(\rho u_i u_j) = -\frac{\partial p}{\partial x_i} + \frac{\partial}{\partial x_j} \left[\mu \left(\frac{\partial u_i}{\partial x_j} + \frac{\partial u_j}{\partial x_i} \right) \right] + \Phi_i \quad (2.1.14)$$

where

$$\Phi_{ij} = \frac{\dot{\eta}_j}{V_e} \int \frac{m}{\tau} (u_i^f - u_i^p) dt \quad (2.1.15)$$

is the momentum transfer contribution of the j^{th} particle stream to the element source term. In the case where the particles are subject only to drag and gravity forces, and in the absence of mass transfer (the particle mass is not a function of time) the source term contribution with units of (Nt/m^3) is given by

$$\Phi_{ij} = \frac{\dot{m}_j}{V_e} \left[(u_{i_{out}}^p - u_{i_{in}}^p) - g_i \delta t_j \left(1 - \frac{\rho_f}{\rho_p} \right) \right] \quad (2.1.16)$$

2.2 Conservation Of Energy

Particles can exchange energy with the surrounding fluid medium. The standard energy equation satisfying the heat balance for a particle is given by

$$mc_p \frac{dT_p}{dt} = hA_p(T_f - T_p) + \Lambda \frac{dm}{dt} \quad (2.2.1)$$

This equation states that the total change of energy in the particle is due to the fluid/particle convection at the surface of the particle plus the energy created or destroyed by the mass transfer processes when they exist. The current model assumes that for phase change problems, the droplets are evaporating slowly, and for pure liquid droplets, the partial pressure at the surface of the each particle corresponds to saturation conditions at the droplet temperature. In other words, the liquid particles continuously evaporate, but their rate of evaporation varies with the temperature experienced by the droplets. This is not to be confused with a boiling problem, where the partial pressure is fixed, and therefore, the droplets evaporate at a constant temperature. It is assumed here that the temperature inside the particle is uniform and is accurately described by the temperature at the surface. The heat transfer coefficient, h , is generally calculated from empirical data. (2.2.1) is usually written in terms of the *Nusselt* number, Nu which is the ratio of the convection heat transfer at the surface of the particle to the heat transfer conducted through the fluid medium:

$$\frac{dT_p}{dt} = \frac{(T_f - T_p)}{\tau_T} + \frac{L}{mc_p} \frac{dm}{dt} \quad (2.2.2)$$

$$\tau_T = \frac{\rho_p c_p D_p}{6Nu k_f} \quad (2.2.3)$$

where density and specific heat are properties of the particle and conductivity is a fluid property. The *Nusselt* number is, in general, a function of the particle Reynolds number given in terms of the relative (slip) velocity between a particle and the surrounding fluid. An estimate of the particle *Nusselt* number, or *Sherwood* number in the case of mass transfer, for the limiting condition of a spherical particle in a stagnant gaseous medium (zero slip velocity) can be calculated from the equation for conduction from a sphere to a surrounding stagnant fluid layer

$$Q = \frac{2\pi\kappa\Delta T}{\left(\frac{1}{D_p} - \frac{1}{D_m}\right)} = \pi D_p^2 \cdot h_T \cdot \Delta T \quad (2.2.4)$$

where D_p and D_m are the diameters of the particle and medium surrounding the particle. In the limiting case when the diameter of the surrounding medium becomes infinite, the *Nusselt* number is determined by

$$Nu_{(\lim D_p \rightarrow \infty)} = \frac{h_T D_p}{k_f} = \frac{2 \cdot D_p}{D_p(1 - D_p / D_m)} = 2 \quad (2.2.5)$$

This limiting case is valid when the relative velocity between the fluid and particle is zero, i.e. the particle travels along the fluid streamline. This can also be the limiting condition when the particle momentum time constant is very small (Stokes flow - dilute system).

In the general case, there is a relative velocity between the particle and the surrounding fluid which results an increased particle heat transfer coefficient due to the relative convective effects of the surrounding fluid. This is represented by a functional relationship between the *Nusselt*, *Prandtl*, and *Reynolds* numbers.

$$\text{Nu} = \frac{hD_p}{k} = a + b\text{Re}_p^m \text{Pr}^n \quad (2.2.6)$$

where

$$\text{Re}_p = \frac{\rho_f D_p |\mathbf{u}_f - \mathbf{u}_p|}{\mu_f} \quad (2.2.7)$$

and

$$\text{Pr} = \frac{\mu_f c_p}{k_f} \quad (2.2.8)$$

While a set of coefficients for the *Nusselt* number relationship is available, such as

$$\text{Nu} = 2.0 + 0.6\text{Re}_p^{0.5} \text{Pr}^{0.33} \quad (2.2.9)$$

the user has the capability of supplying a *Nusselt* number of a general form such as

$$\text{Nu} = \frac{h_T \cdot d_e}{k} = 2 + 0.16\text{Re}_p^{0.667}; \quad \text{Re}_p < 150 \quad (2.2.10)$$

The *Nusselt* number given above is generally applied to heat transfer without evaporation or with low intensity evaporation. For high intensity evaporation or evaporation with combustion, the above relationship is modified to include

$$\text{Nu}_e = \text{Nu} \left(\frac{\ln(1+B)}{B} \right); \quad \text{where } B = \frac{c_p(T_f - T_w)}{\ell} \quad (2.2.11)$$

where c_p is the specific heat, ℓ is the latent heat of vapor. The ratio of $\ln(1+B)/B$ is smaller than unity which means that the total mass flux at the surface of the particle reduces the heat and mass transfer in evaporation. The total surface mass flux includes diffusive flux plus convective flux and is sometimes called the Stefan flux.

Particle Thermal Relaxation Time

The particle thermal relaxation time, τ_T , plays the same role as the particle relaxation time. In effect it measures the time required before the particle reaches a state of thermal equilibrium with the fluid. If the particle thermal relaxation time is large relative to the thermal time scale of the

fluid, the particle does not have time to adjust to the more rapidly changing energy levels in the fluid. If that is the case the particle temperature is determined essentially by its initial condition and factors other than the convective heat transfer between the two phases. Conversely, as the particle thermal relaxation time gets smaller, the particle temperature is able to adjust more quickly to changes in fluid temperature. We will see later that τ_T is an important parameter to consider in order to set an appropriate numerical procedure.

In a two-way (*Level 3*) coupling simulation, energy transferred to or from the particles to the fluid serves as a source or sink of energy with respect to the carrier phase.

$$\frac{\partial}{\partial x_j} \left(\rho c_{p_f} u_j T \right) = \frac{\partial}{\partial x_i} \left(k \frac{\partial T_f}{\partial x_i} \right) + \Psi \quad (2.2.12)$$

where

$$\Psi = \frac{\dot{\eta}_j}{V_e} \int \frac{c_p m}{\tau_T} (T_f - T_p) dt \quad (2.2.13)$$

is the energy per unit volume transferred from the particles to the carrier fluid. In the absence of mass transfer, (2.2.13) is integrated analytically and the source term becomes

$$\Psi = \frac{c_p \dot{m}}{V_e} (T_{p\ out} - T_{p\ in}) \quad (2.2.14)$$

where $T_{p\ out}$ and $T_{p\ in}$ are the particle temperatures at the entrance and at the exit of the element. In the case of phase change problems, better results were obtained by integrating (2.2.12) with a trapezoidal method despite the fact the accuracy of the integration is a function of the number of time steps a particular particle takes within the same element. An exception to this method is in effect when the mode of heat transfer is user defined. In that case the unpredictability of the heat transfer mode being specified by the user prohibits the use of the trapezoidal method. In that case the heat transfer between the phases is computed by

$$\Psi = \frac{\dot{\eta}}{V_e} \left[\left(mc_{p_p} T_p - m\Lambda \right)_{out} - \left(mc_{p_p} T_p - m\Lambda \right)_{in} \right] \quad (2.2.15)$$

2.3 Conservation Of Mass

Frequently, the standard conservation of mass for the particle is described by a form of Fick's law, relating the mass flux to the gradient of concentration between the dispersed phase and the carrier phase. Though one can use any other model, for the purpose of this course we will limit the discussion to the use of the Fick's law mode of mass transfer. The equation of conservation of momentum is given by:

$$\frac{dm}{dt} = Sh(\rho_f \alpha \pi D)(C_\infty - C_s) \quad (2.3.1)$$

where the *Sherwood* number, Sh , is the ratio of the mass transfer at the particle surface (or through a boundary layer) to the mass transfer rate in the bulk fluid due to diffusion. (2.3.1) is rewritten

$$\frac{dm}{dt} = \frac{m}{\tau_m} \quad (2.3.2)$$

where

$$\tau_m = \frac{\rho_p D^2}{6Sh(\rho_f \alpha)(C_\infty - C_s)} \quad (2.3.3)$$

This formulation isolates a time scale for the changes in particle mass. For many applications, the *Nusselt* number and *Sherwood* number have analogous forms and if knowledge of a relationship for the *Nusselt* number is available, it can be similarly applied as a *Sherwood* number with the correct interpretation. Generally

$$Sh = a + bRe_p^m Sc^n \quad (2.3.4)$$

As already noted above, in this model, the evaporation rate of the particle is dictated by the partial pressure at its surface.

$$C_s = \frac{pM_{wt}}{\rho_f RT} \quad (2.3.5)$$

An empirical equation to yield the vapor pressure can be derived by integrating the Clausius-Clapeyron's equation. The Clapeyron equation relates the saturation pressure, temperature, the change in enthalpy, and the change in specific volumes associated with both phases.

$$\left(\frac{dP}{dT} \right)_{sat} = \frac{\Lambda}{T v_{liquid-vapor}} \quad (2.3.6)$$

Using the assumption of an ideal gas, the above equation can be rewritten as

$$\int d \ln(P_{i,surf}) = \frac{\Lambda}{R_i} \int d \left(\frac{1}{T} \right) \quad (2.3.7)$$

Integrating between a reference point on the liquid-vapor interface yields

$$\ln(P_{i,surf}) = \ln(P_{ref}) - \frac{\Lambda}{R_i} \left(\frac{1}{T} - \frac{1}{T_{ref}} \right) \quad (2.3.8)$$

The coefficients depend upon the reference conditions (P_{ref}, T_{ref}) . This equation can be reformulated as

$$p = p_{ref} e^{-\frac{\Delta M_{wt}}{RT_{ref}} \left(\frac{T_{ref}}{T_p} - 1 \right)} \quad (2.3.9)$$

Since the thermodynamic diagrams representing the liquid-vapor interface are highly non-linear, care must be taken to "curve-fit" the above equations in the region of interest. Knowing the temperature of the particle, Equation (2.3.1) together with (2.3.5) and (2.3.9) can be solved at each iteration to determine the mass transfer due to evaporation.

Continuity

Note that in Equations (2.1.25), (2.1.26) and (2.2.5) it was assumed that the flow was incompressible and without mass transfer. As a result mass was conserved throughout the whole system and continuity still held. In this section as the particles increase or decrease in size, mass is transferred to the carrier phase. The effects are two-fold. On one hand, because mass is created or destroyed in the carrier phase, the continuity equation does not hold anymore, and is replaced by:

$$\frac{\partial \rho u_i}{\partial x_i} = \Gamma \quad (2.3.10)$$

with

$$\Gamma = \int_{\delta t} \frac{dm}{dt} dt = m_{out} - m_{in} \quad (2.3.11)$$

On the other hand, the mass created can be tracked throughout the domain with a species equation that reads

$$\frac{\partial}{\partial x_j} (\rho u_j c) = \frac{\partial}{\partial x_i} \left[\rho \alpha \frac{\partial c}{\partial x_i} \right] + \Gamma \quad (2.3.12)$$

If we assume that mass is not conserved, introducing (2.3.5) in (2.1.25), (2.2.5) and (2.3.7) yields

$$\rho u_j \frac{\partial u_i}{\partial x_j} + \Gamma u_i = -\frac{\partial p}{\partial x_i} + \frac{\partial}{\partial x_j} \left[\mu \left(\frac{\partial u_i}{\partial x_j} + \frac{\partial u_j}{\partial x_i} \right) \right] + \Phi_i \quad (2.3.13)$$

$$\rho c_{p_f} u_j \frac{\partial T}{\partial x_j} + \Gamma c_{p_f} T = \frac{\partial}{\partial x_i} \left(k \frac{\partial T_f}{\partial x_i} \right) + \Psi \quad (2.3.14)$$

$$\rho u_j \frac{\partial c}{\partial x_j} + \Gamma c = \frac{\partial}{\partial x_i} \left[\rho \alpha \frac{\partial c}{\partial x_i} \right] + \Gamma \quad (2.3.15)$$

Note that in the preceding equations we have assumed that particles of a given material evaporate to produce the vapor of that particular material. In that case we only need one specie equation.

It may happen however, that particles of different material are introduced. For instance we can consider a mixture of water and ethanol droplets flowing in air. If both materials are allowed to evaporate, we need two species equation to track the evolution of each particular vapor in the domain. Thus:

$$\rho u_j \frac{\partial c_1}{\partial x_j} + \Gamma c_1 = \frac{\partial}{\partial x_i} \left[-\rho \alpha_1 \frac{\partial c_1}{\partial x_i} \right] + \Theta_1 \quad (2.3.16)$$

$$\rho u_j \frac{\partial c_2}{\partial x_j} + \Gamma c_2 = \frac{\partial}{\partial x_i} \left[-\rho \alpha_2 \frac{\partial c_2}{\partial x_i} \right] + \Theta_2 \quad (2.3.17)$$

$$\frac{\partial \rho u_i}{\partial x_i} = \Gamma = \Theta_1 + \Theta_2 \quad (2.3.18)$$

2.4 Particles in Turbulent Flows

Turbulence in itself is a very complex phenomenon: in general it will not be possible for any computation to describe the details of the interactions between particles and turbulence and some kind of modeling is required. The model should describe the way particles behave in a turbulent flow and also the modification of the turbulent field due to the presence of particles. It is expected however, that, if the particle loading is sufficiently small, particles do not significantly affect the turbulent properties of the carrier phase. Regardless of particle loading, turbulence is the dominant mechanism by which momentum, heat and mass are transferred within the dispersed phase and between the dispersed phase and the carrier flow. In the absence of particle-particle interactions, it is the only mechanism which can lead to the spreading of particles.

In the Eulerian formulation the field variables are mean values obtained by time (or ensemble) averaging procedures complemented with closure models. The turbulence model for the particles, which are described via the Lagrangian approach, requires instead that some information be retrieved about the fluctuations of velocities, temperature and mass fraction of the species associated with the dispersed phase. Referring for the moment to isothermal flows, the heart of the model is the specification of the time history of the carrier fluid as experienced by the particles. This time history is the velocity to which the particles respond through the coupling terms in the equation of motion: the fluid velocity variations directly determine the extent of particle dispersion.

The typical approach for the approximation of the velocity experienced by the particle is a "random walk" model which assumes the carrier phase velocity be the sum of a local mean velocity and random fluctuations. The random fluctuation is selected from a Gaussian distribution with zero mean and a variance related to the turbulent velocity scale coming from the model used in the mean flow solution. A stochastic approach can be used in conjunction with the $k-\varepsilon$ model, which allows, under the assumption of isotropic turbulence, the evaluation of the velocity fluctuation from the kinetic energy obtained as field variable from the solution of the Eulerian problem.

$$u' = \lambda \left(\frac{2}{3} k \right)^{\frac{1}{2}} \quad (2.4.1)$$

where λ is the random generated number sampled from a normal distribution.

In addition to the velocity fluctuation, further information is required to model the particle-eddy interactions, that is the frequency of the fluctuation sampling. For the particle eddy interaction the "eddy lifetime" concept, initially developed by Gosman and Ioannides (1981) and successively modified by other authors, is used. An assumed eddy length is computed, based on the local kinetic energy and dissipation

$$L_e = C_\mu^{\frac{3}{4}} \frac{k^{\frac{3}{2}}}{\epsilon} \quad (2.4.2)$$

the eddy lifetime is estimated by

$$t_e = \frac{L_e}{\left(\frac{2}{3} k \right)^{\frac{1}{2}}} \quad (2.4.3)$$

In addition to the eddy lifetime, the time needed for the particle to cross the eddy of length L_e is computed. This takes into account the so called "crossing trajectories effect", that is the possibility that the particle can leave the eddy before the end of eddy lifetime. The transit time is found using the linearized equation of motion for a particle in a uniform flow

$$t_i = -2 \ln \left(1 - \frac{L_e}{\tau |\mathbf{u}_f - \mathbf{u}_p|} \right) \quad (2.4.4)$$

where $|\mathbf{u}_f - \mathbf{u}_p|$ is the relative velocity at the start of the interval and τ is the particle relaxation time. During the computation of the trajectories, whenever an interval of time equal to the minimum of (2.4.3) and (2.4.4) is elapsed, it is assumed that the interaction with a new eddy has begun and a new fluctuation is sampled.

In (2.4.4) if $L_e > \tau |\mathbf{u}_f - \mathbf{u}_p|$ no solution exists (the particle is captured within the eddy) and the interaction time is always taken to be t_e . The integration time step is also adjusted so that it can never be greater than the minimum of (2.4.3) and (2.4.4), in order to avoid loss of information about the particle-turbulence interactions.

Temperature and mass fraction associated with the particle also experience turbulent fluctuations: it is important, however, to point out that the velocity history has an indirect but very strong effect on the exchanges of heat and mass between the particles and the fluid since the state of the fluid surrounding the particle depends on where in the flow field the particles have been transported by mean and fluctuating fluid motions. In addition to this effect, local fluctuations of temperature and species composition are added to the mean (averaged solution), based on the temperature and species gradients.

$$T = \bar{T} + \lambda \theta' \quad (2.4.5)$$

where

$$\theta' = \sqrt{c_\mu \frac{k^3}{\epsilon^2 \sigma_t} \left(\frac{\partial \bar{T}}{\partial x_j} \frac{\partial \bar{T}}{\partial x_j} \right)} \quad (2.4.6)$$

$$c = \bar{c} + \lambda \varphi' \quad (2.4.7)$$

where

$$\varphi' = \sqrt{c_\mu \frac{k^3}{\epsilon^2 S_t} \left(\frac{\partial \bar{c}}{\partial x_j} \frac{\partial \bar{c}}{\partial x_j} \right)} \quad (2.4.8)$$

In the above formulas λ is the random generated number while σ_t and S_t are the turbulent *Prandtl* number and the turbulent *Schmidt* number. The eddy lifetime model is widely adopted in the computation of particles in turbulent flows. It has proven to give results in good agreement with experiments and with more sophisticated and expensive models for the point source dispersion. It has also successfully been used in spray computations and for particle laden swirling flows. Due to the assumption of isotropic turbulence in (2.4.1), it can be expected not to give accurate results if the particle dispersion is governed by the motion of strongly anisotropic eddies. Being a stochastic model, it requires a significant number of particles to be tracked before the statistical distribution can be reached. The number of paths depend on the level of accuracy required.

3. Numerical analysis

3.1 Non-dimensionalization

Non-dimensionalization of the governing equations is a powerful tool that increases our understanding of the physics at play as well as help us devise the most appropriate numerical technique. This is particularly true for dispersed two-phase flows. The table below summarizes some of the important non-dimensional parameters and variables relevant to two-phase flows. All the governing equations can be rewritten in non-dimensional forms with the use of these parameters.

Non-Dimensionalization of Flow Variables

$$\begin{aligned}
 x^* &= \frac{x}{L} & t^* &= \frac{tU}{L} & \rho_f^* &= \frac{\rho_f}{\rho_f} & \rho_p^* &= \frac{\rho_p}{\rho_f} \\
 u_f^* &= \frac{u_f}{U} & u_p^* &= \frac{u_p}{U} & T_f^* &= \frac{T_f}{\Delta T} & T_p^* &= \frac{T_p}{\Delta T} \\
 c_{p_f}^* &= \frac{c_{p_f}}{c_{p_f}} & c_{p_p}^* &= \frac{c_{p_p}}{c_{p_f}} & \alpha_f^* &= \frac{\alpha_{D_f}}{UL} = \frac{1}{Pe_c} & k_f^* &= \frac{\alpha_{T_f}}{UL} = \frac{1}{Pe_T} \\
 \mu^* &= \frac{\mu}{\rho_f UL} & \Lambda^* &= \frac{\Lambda}{c_{p_f} \Delta T} & p^* &= \frac{p}{\rho_f U^2} & R^* &= \frac{R \Delta T}{U^2} \\
 \Phi_M^* &= \frac{\Phi_M}{\rho_f U^2 L} & \Phi_T^* &= \frac{\Phi_T}{\left(\frac{k_f \Delta T}{L^2} \right) Pe_T}
 \end{aligned}$$

Fluid Time Constants

$$\begin{aligned}
 \tau_f &= \frac{L}{U_f} & \tau_T &= \frac{\rho_p D_p^2}{6Nu k_f} \\
 \tau_p &= \frac{\rho_p D_p^2}{18\mu_f} & \tau_m &= \frac{\rho_p D_p^2}{6Sh \rho_f \alpha_m}
 \end{aligned}$$

Dimensionless Parameters

$$\begin{aligned}
 Fr &= \frac{U_f^2}{gL} & St^H &= \frac{\tau_p}{\tau_f} = \frac{\tau_p U_f}{L} & Pr &= \frac{\mu_f c_p^f}{k_f} \\
 Load &= \frac{\dot{m}_p}{\rho_f U_f L^2} & St^T &= \frac{\tau_T}{\tau_f} & Sc &= \frac{\mu_f}{\rho_f D_{f,1}} \\
 Eck &= \frac{c \Delta T}{U_f^2} & Ste &= \frac{c_p^f (T_f - T_p)}{\lambda_i} & Pe &= \frac{U_f L}{D_{f,1}} \\
 St^M &= \frac{\tau_m}{\tau_f}
 \end{aligned}$$

The dimensionless parameters defined above are: **Fr**, the *Froude* number, is a ratio of the inertial to the gravitational forces in the system; **Load**, the *Loading* number, is the ratio of the particle mass flow to the fluid mass flow; **Sh**, the *Sherwood* number, is the ratio between the mass transfer at the particle surface or through the boundary layer to the mass transfer in the bulk fluid because of the diffusion mechanism; **Sc**, the *Schmidt* number, is the ratio of the momentum diffusivity to the mass diffusivity in the fluid; **Ste**, the *Stefan* number, is the ratio of sensible heat to latent heat;

St^H , St^M , St^T , the hydrodynamic, inertial and thermal *Stokes* numbers, respectively, are the ratio of the respective time constants to the fluid (system) time constant; *Eck*, the *Eckert* number, is the ratio of the thermal capacity of the fluid to the fluid kinetic energy.

The particle relaxation numbers do not provide enough information in and of themselves. These time scales need to be measured against the fluid, and that number is what characterizes a particular aspect of the flow. Clearly, when any of those numbers become very small the system of ODEs that need to be solved becomes stiff, and the evaluation of the right hand side of these equations is likely to result in overshoots and undershoots.

The *Froude* number measures the relative importance of gravitational forces. This influence competes with the hydrodynamic *Stokes* number. The source terms in the carrier phase are treated explicitly, that is they appear on the right hand side of the governing equation. As a result when these source terms are significantly larger than other terms in the equations, the problem gets more difficult to converge and typically, higher levels of relaxation are required. This may arise if the *Froude* number becomes exceedingly small. In most cases the mass flow rate is small enough that the total contribution of gravity to the source term remains small.

The following table attempts to illustrate the relative contribution of momentum and gravity to a discrete phase in a moving carrier medium. The carrier is assumed to have a average velocity of $U = 1.0$ m/sec and a characteristic length of $L = 1$ m. The particle transport equation can be written as

$$\frac{d\mathbf{u}_p^*}{dt^*} + \frac{\mathbf{u}_p^*}{St^H} = \frac{\mathbf{u}_f^*}{St^H} + \frac{1}{Fr'} \quad (3.1.1)$$

where

$$Fr' = \frac{U^2}{gL \frac{(\rho_p - \rho_f)}{\rho_p}}$$

The magnitudes of the Stokes and Froude numbers are:

Case	Particle Size (m)	Particle Density Kg/m ³	Carrier Fluid Density Kg/m ³	Carrier Fluid Viscosity Pa-sec	Stokes Number	Froude Number
A	1.0E-03	1200	1.2	1.8E-05	3.7	0.102
B	1.0E-03	1200	1000	1.0E-03	0.08	0.612
C	5.0E-05	1200	1000	1.0E-03	0.0002	0.612
D	1.0E-03	1.2	1000	1.0E-03	0.00007	-1.2E-04
E	1.0E-05	1.2	2500	1	5.0E-12	-5.0E-05

Cases A, B, and C illustrate the particle time constants for a solid particle in air and water. Cases D and E illustrate the particle time constant for air particles in water and glycerin. One can see

from the above table the first and second terms can have differences of many orders of magnitude in the worst scenario. As will be seen in the next section, the method that one uses to time integrate the equations for determination of particle trajectory can be computationally intensive depending on the magnitude of the terms on the right hand side of the equation.

3.2 Particle Integrators

The following section describes three methods to solve the ODEs describing the particulate phase, namely the explicit, the implicit, and the semi-analytical methods. It also suggests ways to choose between solvers to bypass potential difficulties.

In order to evaluate the benefits of each solver let us consider the general form of an ODE:

$$\frac{dy}{dt} = F(y, t) \quad (3.2.1)$$

The explicit method consists of a standard second order Runge-Kutta approach, that is

$$y_{i+1} = y_i + dt F\left(y_{i+\frac{1}{2}}, t_{i+\frac{1}{2}}\right) \quad (3.2.2)$$

with

$$y_{i+\frac{1}{2}} = y_i + \frac{dt}{2} F(y_i, t_i) \quad (3.2.3)$$

Being explicit, the Runge-Kutta method begins to break down when the system of equations becomes stiff. In such cases an implicit method is more reliable.

The implicit method used is a fully implicit method known as Backward Euler. Even though this method is one order less accurate than the explicit solver, the stability qualities of this solver compensate for the accuracy level. Note also that when used in conjunction with a variable step control algorithm the accuracy is increased to order 2. The algorithm reads

$$y_{i+1}^{k+1} = y_i + dt F(y_{i+1}^k, t_{i+1}) \quad (3.2.5)$$

The Semi-analytic algorithm assumes that within a time step, all quantities are constant and therefore the solution can readily be obtained with a simple integration between the beginning and the end of the time step:

$$y_{i+1} = \int_{t_i}^{t_i+dt} F(y_i, \tau) d\tau \quad (3.2.6)$$

In order to evaluate the merits of each solver relative to each other let us start with the following equation

$$\frac{d\Phi}{dt} = \frac{\Phi_{\infty} - \Phi}{\tau} + g \quad (3.2.7)$$

All the governing equations for the particle equations can be put in that format. For the sake of simplicity we will also assume that the Background velocity field is constant and that we are dealing with a Stokes flow for which the particle relaxation time is constant. The following table describes the solution at each time step given by each solver:

$x=dt/\tau$	Explicit	Implicit	Semi-Analytic
Φ_{i+1}	$\Phi_i + (\Phi_\infty - \Phi_i + g\tau) \left(x - \frac{x^2}{2} \right)$	$\frac{\Phi_i + x(\Phi_\infty + g\tau)}{1 + x}$	$\Phi_\infty - (\Phi_\infty - \Phi_i)e^{-x} + g\tau(1 - e^{-x})$
$\lim_{x \rightarrow 0}$	Φ_i	Φ_i	Φ_i
$\lim_{x \rightarrow \infty}$	∞	$\Phi_\infty + g\tau$	$\Phi_\infty + g\tau$

Clearly x never goes to zero or infinity, however the point of this exercise is to show how each solver behaves as x becomes very large or very small. A situation for which x is small occurs when the particle relaxation time is large and we look for an accurate solution by using a small DT. All three solvers are expected to give us the same solution in the extreme case where x is significantly small. For values of x significantly large, the explicit solver can not be used due to instabilities. In all other cases, any of the solvers can be used, the accuracy of the solution depends on the characteristics of the solver. For instance the explicit solver would be the most desirable alternative in that area since it enjoys the highest order of accuracy $O(h^2)$ for fixed time step and $O(h^3)$ for variable time step. As the particle relaxation time decreases (x increases) there comes a point where the time step required to keep $x < 1$ becomes prohibitively small and the explicit solver simply becomes unusable.

Example: Air bubbles in Water

$$\begin{array}{ll} \rho_p = 1.2 \text{ Kg} \cdot \text{s}^{-1} & D = 10^{-6} \text{ m} \\ \mu_f = 10^{-3} \text{ Kg} \cdot \text{m}^{-1} \text{s}^{-1} & \tau = \frac{\rho_p D^2}{18\mu} = 7.10^{-10} \text{ s} \end{array}$$

In order to properly integrate this system we would need a time step two orders of magnitude smaller than the particle relaxation time for a total x value of about 0.01. In that case any of the solvers would be appropriate. Unfortunately a time step of the order of $10\text{E}-12$ is prohibitively expensive. We have to find a solver that gives reasonable results even with a time step much larger than the particle relaxation time. The next choice could be the implicit solver or the Semi-analytic solver. The trick here is to compare the time scale of the particle to the time scale of the carrier phase, in other words the value of the Stokes number. If the Stokes number is significantly smaller than one, then we know from the discussion in section 2 that the particles essentially behaves like fluid. In this case we can use the Semi-analytic solver with a large time step for an economic run with very limited loss of accuracy. Ideally one would always use a time step that is smaller than the minimum between the particle relaxation time and the time scale of the carrier. Unfortunately, this is not always possible. The following table describes some of the strategies that we have found to work in most cases. It should be stressed that this is not a panacea, rather,

it is expected that the user will develop his/her own feel of the various trade-offs involved when switching from one solver to another. The first line represents actual Stokes numbers relevant to the problem, and the first column provides a range of time steps that a user may or may not be able to afford on his/her system.

	$St \ll 1$	$St \approx 1$	$St \gg 1$
$dt/\tau \ll 1$	Exp*/Imp/Semi	Exp*/Imp/Semi	Exp*/Imp
$dt/\tau \approx 1$	Imp*/Exp/Semi	Imp*/Exp/Semi	Imp*/Exp/
$dt/\tau \gg 1$	Semi*/Imp	Imp/Semi	Imp

REFERENCES

- Burmeister, L.C., Convective Heat Transfer, John Wiley & Sons, 1983, Chapter 2,
- Crowe, C. T., Sharma, M.P., and Stock, D.E., "Particle-Source-In Cell (PSI-Cell) Model for Gas-Droplet Flows, *Journal of Fluids Engineering*, June 1977, pp325-331.
- Crowe, C.T., "Review-Numerical Models for Dilute Gas-Particle Flows", *Journal of Fluids Engineering*, September, 1982, V104, pp287-302.
- Durst, F., Milojevic, D., and Schonung, B., "Eulerian and Lagrangian Predictions of Particulate Two-Phase Flows: A Numerical Study", *Appl. Math. Modeling*, 1984, V8, pp101-115.
- Hetsroni, G., Handbook of Multi-Phase Systems, Mc Graw Hill, 1982.
- Lixing, Z., *Theory and Numerical Modeling of Turbulent Gas-Particle Flows and Combustion*, CRC Press, Chapter 6, 1993
- White, B. R., "Particle Dynamics in Two Phase Flows", Encyclopedia of Fluid Mechanics, Vol. 4 Solids and Gas Flows, Cheremisinoff, N.P., ed.

Nomenclature

c, C	Mass fraction
C_D	Drag coefficient
c_p	Specific heat
D	Particle diameter
F	Force
g	Gravity
k	Conductivity
ℓ	Latent heat
L	Length
M	Vapor molecular weight
n	Number density
R	Universal gas constant
T	Temperature
c_p	Specific Heat
f	$\frac{C_D Re}{24}$
k	Turbulent kinetic energy
m	Mass
p	Pressure
t	Time
U, u, v	Velocity

Dimensionless Numbers

Fr	Froude number
Nu	Nusselt number
Pe	Peclet number
Re	Reynolds number
Sc	Schmidt number
Sh	Sherwood number
St	Stokes number
Ste	Stefan number

Superscript

M	Momentum
T	Energy
m	Continuity (Mass)

Subscript

p	Particle
s	Surface
t	Turbulent

Greek

α	Specie's diffusivity
ϵ	Turbulent dissipation rate
Λ	Length
λ	Random number
η	Number density, number of particles
μ	Viscosity
ν	Kinematic viscosity
ρ	Density
ϕ	Volume fraction
Φ	Source Term
ψ	Energy
τ	Relaxation time

von Karman Institute for Fluid Dynamics

Lecture Series 1995-03

INDUSTRIAL COMPUTATIONAL FLUID DYNAMICS

April 3 - 7, 1995

APPLICATIONS OF MULTIPLE PHASE MODELING USING FIDAP

I. Dilber
FDI, USA

Applications of Multiple Phase Modeling Using FIDAP

Ilhan Dilber
Fluid Dynamics International
Evanston, Illinois, 60201, USA

1. Particle Characteristics In Flow Fields

1.1 Basic Definitions

The volume or void fraction of the particulate phase is described by the density of the particulate in bulk form ("material" density or "bulk" density) and the density of the material as dispersed in the carrier medium ("apparent" density). The densities of the dispersed phase and the carrier medium are given by

$$\rho_p = \phi \bar{\rho}_p \quad (1.1.1)$$

Conversely, the apparent density of the carrier medium is given by

$$\rho_f = (1 - \phi) \bar{\rho}_f \quad (1.1.2)$$

The "*barred*" quantities are the "bulk" densities of the particulate and the carrier. The volume fraction, usually given as parts per million-*ppm*, is given as

$$\phi = \frac{\rho_p}{\bar{\rho}_p} \quad (1.1.3)$$

The volume fraction of the carrier fluid is defined as

$$\epsilon = 1 - \phi \quad (1.1.3a)$$

The mixture density and the mass ratio between the particle and fluid phases can now be written in terms of the mixture volume and bulk properties as

$$\rho_m = \rho_p + \rho_f = \phi \bar{\rho}_p + (1 - \phi) \bar{\rho}_f \quad (1.1.4a)$$

and

$$\frac{\rho_p}{\rho_f} = \frac{\phi}{1 - \phi} \frac{\bar{\rho}_p}{\bar{\rho}_f} \quad (1.1.4b)$$

In terms of a particle diameter, D_p , the mass of an individual particle can be given as

$$m_p = \frac{\pi}{6} D_p^3 \bar{\rho}_p \quad (1.1.5)$$

If the number of particles per unit volume, the particle density, is given by n_p , then the density of the dispersed particulate phase can also be written as

$$\rho_p = n_p m_p \quad (1.1.6)$$

An estimate of the particle spacing can be obtained by substitution of Equation 1.1.5 into 1.1.6 yielding

$$\phi = n_p \frac{\pi}{6} D_p^3 \quad (1.1.7)$$

where n_p is the particle number density. The ratio of the particle spacing to the particle diameter is equal to

$$\xi_p = \frac{\Gamma_p}{D_p} = \frac{n_p^{-1/3}}{D_p} = \left(\frac{\pi}{6\phi} \right)^{1/3} \quad (1.1.8)$$

For example, for a volume fraction of particles, $\phi = 0.01$ (10000 ppm), the particle spacing is approximately four (4) particle diameters. Estimates of the validity of the assumption of dilute particles neglecting multiple interactions between particles will be discussed in a later section.

In principle, the particle volume fraction can be calculated from the Lagrangian solutions of particle trajectories by summing up the volumetric contribution of all particles, of "i" different diameters, starting from "j" locations passing through a volume, V_e in a increment of time, δt .

$$\phi = \sum_i \sum_j \frac{\dot{m}_{i,j} \delta t}{\bar{\rho}_{p,i} V_e} \quad (1.1.9)$$

The residence time for the particle in the element of volume is δt . For a single particle diameter, the above equation can be written as

$$\phi = \frac{1}{V_e} \sum_j \frac{\eta_j m_p \delta t}{\bar{\rho}_p} = \frac{1}{V_e} \sum_j \frac{\eta_j V_p \delta t}{1} \quad (1.1.10)$$

where η_j is the particle frequency (number of particles per second), V_p and V_e are the particle and element volumes respectively.

1.2 Particle Dilution

For multi-phase flow analysis in FIDAP, a critical assumption is that the particle field is dilute and that no significant particle-particle interaction (collisions) takes place. It is important to obtain a prediction as to the validity of this assumption in order to obtain some confidence level that the analysis will capture the physics of the process correctly. This section presents the basic definitions of relevant parameters, and formulas to obtain an estimate of the valid particle loading range for a given problem.

The following table gives the definitions of some of the important parameters that are used for the derivation of the particle loading formulation:

Table 1.2.1 Parameter definitions relevant to particle dilution.

$\Gamma = \frac{1}{n^{1/3}} = \left(\frac{\pi}{6\phi} \right)^{1/3} D$	$\Lambda = \left(\sqrt{2} n \pi D^2 \right)^{-1}$	$\phi = \frac{\pi}{6} n D^3$
$\tau_{pp} = \frac{\Lambda}{\bar{u}_p}$	$\tau_{pf} = \frac{\Gamma}{\bar{u}} = \frac{D^2 \rho_p}{18 \nu \rho_f}$	$\alpha = \frac{\sqrt{\pi}}{2} \Lambda \bar{u}$

where Γ is the mean particle spacing (characteristic distance between particles); Λ is the mean free path (characteristic distance traveled by the particles); ϕ is the particle volume fraction; τ_{pp} is the characteristic particle-particle interaction time; τ_{pf} is the characteristic particle-fluid interaction time; n is the particle number density (number of particles/m³); \bar{u} is the characteristic fluid velocity (root-mean-square); \bar{u}_p is the characteristic particle velocity (root-mean-square); D is the particle diameter; ν is the kinematic viscosity; ρ is the density; α is the diffusivity.

For a system to be considered dilute, the ratio of particle-particle interaction time (τ_{pp}) to particle fluid interaction time (τ_{pf}) must be much greater than 1:

$$R^* = \frac{\tau_{pp}}{\tau_{pf}} = \frac{1}{\sqrt{2} n_p \pi D_p^2 \bar{u} \tau_{pf}} \gg 1 \quad (1.2.1)$$

This simply means that the time it takes a particle to collide with another is much greater than the time it takes for it to react to the flow. By using the definition of the particle volume fraction given in Table 1.2.1, the same ratio can be written in terms of ϕ :

$$R^* = \frac{D}{6\sqrt{2} \bar{u}_p \phi \tau_{pf}} \gg 1 \quad (1.2.2)$$

The particle fluid interaction parameter is defined as[†]

$$\kappa = 2\bar{u} \frac{\tau_{pf}}{\Lambda} \quad (1.2.3)$$

The ratio R^* can then be rewritten as

$$R^* = \frac{D/\Lambda}{3\sqrt{2}\phi\kappa} \frac{\bar{u}}{\bar{u}_p} \gg 1 \quad (1.2.4)$$

Rearranging Equation (1.2.4), and using the second definition of τ_{pf} and of α from Table 1.2.1, the following expression for ϕ is obtained:

[†] see Hetsroni, G., Handbook of Multi-Phase Systems, Mc Graw Hill, 1982.

$$\phi \ll \frac{3\sqrt{\pi} v \Lambda \rho_f \bar{u}}{2\sqrt{2} \alpha D \rho_p \bar{u}_p} \quad (1.2.5)$$

For small particles ($\kappa \ll 1$), the ratio $\bar{u}/\bar{u}_p \approx 1$, and for large particles ($\kappa \gg 1$), the ratio $\bar{u}/\bar{u}_p = (\kappa/\sqrt{\pi})^{1/2}$. This gives the following limiting expressions for the volume fraction:

$$\phi \ll \frac{3\sqrt{\pi} v \Lambda \rho_f}{2\sqrt{2} \alpha D \rho_p} \quad \text{for small particles} \quad (1.2.6)$$

$$\phi \ll \frac{1}{2} \left(\frac{v \rho_f}{\alpha \rho_p} \right)^{1/2} \quad \text{for large particles} \quad (1.2.7)$$

For example, for diffusivity of $2 \cdot 10^{-5} \text{ m}^2/\text{sec}$, and a fluid mean velocity of 2 m/sec , we have:

	for $\rho_p/\rho_f = 1000$	$\rho_p/\rho_f = 100$
small particle ($\sim 5 \mu\text{m}$)	$\phi < 0.5\%$	$\phi < 5\%$
large particle ($\sim 100 \mu\text{m}$)	$\phi < 0.5\%$	$\phi < 1.5\%$

As seen from this table, the volume fraction limit is independent of particle size for heavy particles. However, the limits are significantly different for lower density ratios.

An upper limit on ϕ can also be computed by requiring that the characteristic distance traveled by the particles (the mean free path) be greater than the distance between particles (particle spacing):

$$\Lambda > \Gamma \Rightarrow \phi < \left(\frac{1}{2} \right)^{3/4} \frac{1}{6\sqrt{\pi}} \quad \text{or} \quad \phi < 0.056 \quad (1.2.8)$$

A rough estimate of the validity of the model can be obtained as follows. The first check that can be performed is the evaluation of the mass loading number, defined as the ratio of the mass flow of the particles to the mass flow of the carrier phase. If the mass loading number is not much less than unity, the dispersed phase cannot be considered dilute.

The mass loading gives only a first approximation of the relative importance of the two phases in the flow, due to the large difference that can exist between the densities of the two phases. For this reason the volumetric loading, obtained dividing each of the mass flow rates by the respective densities, is a much better indicator of the relative importance of the dispersed phase.

A low value of the volumetric loading does not mean that the suspension is necessarily a dilute one. The reason for this is that the volumetric loading compares the volumetric flow of the particles to the whole flow rate of the carrier fluid, while the region where the

particles are injected could be only a limited part of the fluid domain. A more reliable information can be obtained computing the local volume fraction at the inlet section.

The computation of the volume fraction requires an estimate of a characteristic inflow velocity \bar{u}_p of the particles at the inlet section. The number of particles per unit time can be computed dividing the mass flow rate by the mass of the single particle.

$$\dot{n} = \frac{\dot{m}}{m} \quad (1.2.9)$$

For a given time interval δt , the number of particles entering the domain is

$$n_p = \dot{n} \delta t \quad (1.2.10)$$

and the distance traveled in that time is

$$L = \bar{u}_p \delta t \quad (1.2.11)$$

If A_i is the inlet area, the particles which have entered the domain in the interval δt will occupy a volume given by

$$V = A_i \bar{u}_p \delta t \quad (1.2.12)$$

The volume fraction of the dispersed phase can be computed dividing the total volume of the particles by the volume V

$$\phi = \frac{n_p \bar{u}_p}{V} \quad (1.2.13)$$

Substituting in (1.2.13) the expressions for n_p and V :

$$\phi = \frac{\dot{m}}{\rho_p A_i v_c} \quad (1.2.14)$$

If the particles are uniformly distributed in space, the volume fraction allows an estimate of the ratio of a typical particle-particle distance relative to the particle diameter

$$\frac{l}{d} = \left(\frac{\pi}{6\phi} \right)^{\frac{1}{3}} \quad (1.2.15)$$

The following table gives some characteristic values of the ratio l/d vs. the volume fraction. Values of ϕ around 0.01 are the upper limit for the dispersed phase solution to be considered dilute.

ϕ	l/d
10^{-4}	17
10^{-3}	8
10^{-2}	4
6.5×10^{-2}	2
10^{-1}	1.73
8×10^{-1}	1.

The volume fraction can reach values above the limits of applicability of the model if the mass flow is increased or if the inlet section is reduced. Note, however, that the volume fraction increases also if the particle inlet velocity is very low. This can be the case, for example, for very small bubbles rising in a quiescent fluid (the terminal velocity decreases with the square of the particle diameter) and imposes stringent limits to the mass flow rate that can be handled by the model.

1.3 Modeling Inlet Conditions

The above description of the volume fraction is based on particles in a three dimensional domain. Establishing flow boundary conditions for a 3D flow field analysis or a 2D approximation to a 3D field requires some interpretation. In a flowing system, the fluid and particle information must be supplied at the boundaries of the computational domain. The complete information on flow and particle fields must include fluid and particle mass flow rates, particle size, and material density, and frequency of particles flowing into the domain at all locations. This information at the boundary needs to be consistent with the volumetric descriptions of the particulate flow.

In general, flow fields with discrete particles are strictly three dimensional. Consider, for instance, a fluid/gas containing discrete particles flowing through a duct. Suppose the duct has a width, W , a height, H , and a length, L .

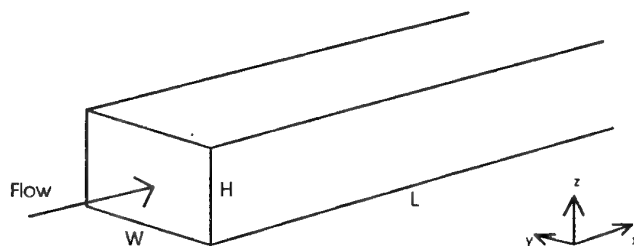


Figure 1.3.1 Geometry of Duct with a Multi-Phase Flow

Flow information is usually supplied by defining a particle loading, α , which is the ratio of the mass flow rate of particles to that of the carrier medium.

$$\alpha = \frac{\dot{m}_p}{\dot{m}_f} \quad (1.3.1)$$

The loading can also be given in terms of a) the particle and fluid velocities and the apparent densities or b) in terms of the particle and fluid velocities, the volume fraction of the particles, and the material densities.

$$\alpha = \left(1 - \frac{|\mathbf{u}_r|}{|\mathbf{u}_f|}\right) \frac{\rho_p}{\rho_f} = \left(1 - \frac{|\mathbf{u}_r|}{|\mathbf{u}_f|}\right) \left(\frac{\phi}{1-\phi}\right) \frac{\bar{\rho}_p}{\bar{\rho}_f} \quad (1.3.2)$$

where the "relative" velocity is defined as $|\mathbf{u}_r| = |\mathbf{u}_f - \mathbf{u}_p|$. In the case where the "relative" velocity is zero, the mass concentration and the loading are identical.

The total number of particles per unit time entering the domain, $\eta(\tau^{-1})$, or the particle frequency crossing the plane of the inlet can also be calculated knowing the material density and particle volume.

$$\eta' = \frac{\dot{m}_p}{\bar{\rho}_p V_p} \quad (1.3.3)$$

The total particle frequency, η' , is interpreted as the number of particles per unit time entering the domain. The particle frequency, η , at an individual location requires a knowledge of the total number of particles passing across the inlet plane. For a given particle volume fraction, ϕ , the particle spacing, $\xi_p = \frac{\Gamma_p}{D_p}$, can be determined from

Equation (1.1.8). As particles pass through the plane of the inlet, the projected area fraction of solid particles of diameter, D_p , can be given as the ratio of the projected particle area to the projected area of diameter Γ_p which characterizes as the spacing between particles.

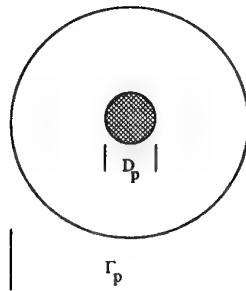


Figure 1.3.2 Area Fraction of Solid Material between Particles

$$\alpha_p = \frac{\frac{\pi}{4} D_p^2}{\frac{\pi}{4} \Gamma_p^2} = \frac{D_p^2}{\Gamma_p^2} = \frac{1}{\xi_p^2} = \left(\frac{6\phi}{\pi} \right)^{2/3} \quad (1.3.4)$$

The total number of particles per unit total area can be estimated by dividing Equation (1.3.4) by the projected area of a single particle yielding

$$\beta_p (\text{particles / total area}) = \frac{\alpha_p}{\frac{\pi}{4} D_p^2} = \frac{4}{\pi} \left(\frac{6\phi}{\pi} \right)^{2/3} \frac{1}{D_p^2} = \frac{1.96\phi^{2/3}}{D_p^2} \quad (1.3.5)$$

From Equation (1.3.5) and the total inlet area, the particle frequency at an individual location can be determined.

$$\eta = \frac{\eta'}{\beta_p A_{in}} \quad (1.3.6)$$

The total mass flow of particles across the inlet plane is the product of the particle frequency, particle material density, particle volume, particles per unit area, and total inlet cross sectional flow area

$$\dot{m}_p = \eta_p \bar{\rho}_p V_p \beta_p A_{inlet} \quad (1.3.7)$$

Substituting the above equation into Equation (1.3.5) yields an expression for the total inlet flow rate through a duct based upon a particle frequency at each location, the particle material density, a known particle diameter, D_p , a known particle volume fraction, ϕ , and the total inlet area.

$$\dot{m}_p = 1026 \eta_p \bar{\rho}_p D_p \phi^{2/3} A_{in} \quad (1.3.8)$$

The total number of particles crossing the inlet plane of a rectangular duct is

$$\tilde{n}_p = \beta_p W \cdot H = \left(\sqrt{\beta_p} W \right) \left(\sqrt{\beta_p} H \right) \quad (1.3.9)$$

For a circular duct of radius R , the expression becomes

$$\tilde{n}_p = \beta_p \pi R^2 = \pi \left(\sqrt{\beta_p} R \right) \left(\sqrt{\beta_p} R \right) \quad (1.3.10)$$

Example 1 : Determination of Particle Inlet Conditions in 3D

Consider a fluid flowing through a 5m by 5m duct as shown in Figure 1.3.1. The carrier fluid, material density of 1000 kg/m^3 , has a volumetric flow rate of 10 cubic meters per second. Particulate matter, $75\mu\text{m}$ in diameter with a material density of 1100 kg/m^3 has a

volume fraction given as 3500 ppm. Estimate the mass flow rate of particles, the particle frequency, and the number of particles in the inlet plane.

Material densities of the fluid and particles, particle diameter, inlet area and volume fraction for a duct flow with uniform particle distribution are

$$\bar{\rho}_p = 1100 \text{ kg} / \text{m}^3$$

$$\bar{\rho}_f = 1000 \text{ kg} / \text{m}^3$$

$$D_p = 75\text{E}-06 \text{ m}$$

$$A_{in} = H \cdot W = 5 \cdot 5 = 25\text{m}^2$$

$$|U|_{in} = 0.4\text{m} / \text{sec}$$

$$\phi = 3500 \text{ ppm} = 0.0035$$

Particles of this size fall in the range of coal dust, catalyst fines, and lint fibers.

Prior to any analysis being undertaken, the boundary conditions of the flow and particle fields at the inlet to the duct must be estimated. The particle spacing can be calculated from Equation (1.3.8)

$$\xi_p = \frac{\Gamma_p}{D_p} = \left(\frac{\pi}{6\phi} \right)^{\frac{1}{3}} = 5.3$$

$$\Gamma_p = \xi_p D_p = 5.3 \cdot 75\mu\text{m} = 0.0003975\text{m}$$

Assuming a uniform distribution of single sized particles, an estimate of the number of particles per unit area in the inlet plane can be given by

$$\beta_p = \frac{\alpha_p}{\frac{\pi}{4} D_p^2} = \frac{4}{\pi} \left(\frac{6\phi}{\pi} \right)^{2/3} \frac{1}{D_p^2} = \frac{1.96\phi^{2/3}}{D_p^2} = 8.035\text{E}+06 \text{ particles} / \text{m}^2$$

The total number of particles, \tilde{n}_p , passing through the plane of the inlet duct is therefore

$$\tilde{n}_p = \beta_p A_{in} = 2.01\text{E}+08 \text{ particles}$$

The particle loading, assuming equal particle and fluid velocities, is given by Equation (1.3.2)

$$\alpha = \left(\frac{\phi}{1-\phi} \right) \frac{\bar{\rho}_p}{\bar{\rho}_f} = 0.00386 \text{ kg}_p / \text{kg}_f$$

The particle flow rate is therefore

$$\dot{m}_p = \alpha(1-\phi)\dot{Q}\bar{\rho}_f = 38.47\text{kg}_p / \text{sec}$$

The frequency of particles (total number of particles per unit time) entering the duct at each of \tilde{n}_p locations is given by Equation (1.3.3)

$$\eta' = \frac{\dot{m}_p}{\bar{\rho}_p V_p \tilde{n}_p} = \frac{38.47}{1100 \cdot \pi \frac{D_p^3}{6} 2.01E+08} = 788 \text{ particles / sec / location}$$

For a correct interpretation of a uniformly distributed dispersed phase, a particle mass flow rate of 38.47 kg/sec results in approximately 788 particles per second being generated at each of 2.01E+08 particle locations in the inlet plane.

One can note that, if the inlet is discretized so as to provide one element (cell) for each particle, the mesh would be roughly 2.E+08 elements in the inlet. This is, of course, unrealistic from a computational viewpoint. What is usually done is to reduce the "resolution" of the mesh to something realistic numerically and decrease the total number of particle locations present in the inlet plane. If this is done, the particle frequency must increase to conserve the correct mass loading. The new particle frequency is the old particle frequency multiplied by the ratio of original number of particle locations to the new number of locations.

$$\eta' = \frac{\tilde{n}_p}{n'_p} \eta$$

Determination of Particle Inlet Conditions in 2D

One of the simplifying assumptions in CFD is to reduce a problem from a 3D to 2D. For a 2D analysis, several restrictive and physically unrealistic conditions must be applied. The first is that any variation of any variable in the "y" direction (Figure 1.3.1) must be negligible. This holds for the carrier medium and also for particulates. For instance, particle trajectories calculated in 2D must be identical along any plane in the "y" direction

The distribution of particles in the "y" direction must not vary in size or spacing. and the number frequency of particles at any location must remain constant. The inlet momentum of both particles and fluid must be identical along any plane normal to the "y" coordinate.

Referring to the previous example for all properties and conditions, the average flow rate of the fluid per unit depth is given by

$$U = \frac{\dot{Q}}{W} = \frac{10}{5} = 2.0 m^3 / \text{sec} - m$$

Dividing the particle mass flow rate by the material density and the depth dimension of the duct yields the average volume flow of particles per unit depth

$$\dot{m}'_p = \frac{\dot{m}_p}{\bar{\rho}_p W} = \frac{38.47}{1100 \cdot 5} = 6.998E-03 m^3 / m - \text{sec}$$

Based upon the given particle diameter of 75 microns, $V_p = 2.209E - 13 \text{ m}^3$, the number of particles per unit time per unit depth is

$$\eta' = \frac{\dot{m}_p}{V_p W \rho_p} = 3.164E + 10$$

In a two dimensional analysis, the concept of a unit depth implies lumping of all particles into a single particle located in the width direction per unit depth. In actuality this is the limiting case for the worst accuracy possible since all momentum is located at a single location. The highest accuracy would occur if the particle frequency in 2D would be equivalent to the particle frequency in a 3D solution. Since the volume concentration is known, the estimated particle spacing in the "y" direction can be used to distribute the particle momentum more evenly. Therefore, the number of particles per unit depth in the "y" coordinate becomes

$$\frac{\tilde{n}_p}{W} = \sqrt{\beta_p} = \sqrt{8.031E + 06} = 2.834E + 03 \text{ particles / unit depth}$$

The particle frequency per unit depth becomes

$$\eta'' = \frac{\eta'}{\sqrt{\beta_p}} = 1.1165E + 07$$

This still indicates that one particle location is present in the inlet of the 2D domain but $\frac{\tilde{n}_p}{W}$ are present in the depth direction. Obviously a better solution would be to distribute the particles to more locations along the inlet. Dividing the particle frequency per unit depth with the number of particles present across the height of the inlet, $(\sqrt{\beta_p} H)$, will yield a particle frequency identical to that in a 3D analysis:

$$\eta = \frac{1}{\sqrt{\beta_p} H} \eta'' = \frac{1}{1.417E + 04} \eta'' = 788 \text{ particles / sec}$$

To provide the correct mass flow of particles for a *Level 3* analysis, the number of particles in the inlet duct and the particle frequency required at the inlet for a consistent mass flow and momentum between 2D or 3D analyses is $\tilde{n}_p = 7.1E + 04 \text{ particles}$ and $\eta_p = 789 \text{ particles / sec}$. Again, it is obvious that discretizing the height of the inlet duct with approximately 70,000 elements would be unrealistic from a computational viewpoint. If the number of particle locations is reduced to 100 across the height of the duct, then the particle frequency would have to be increased to

$$\eta' = \frac{\tilde{n}_p}{100} \eta = 5.6E + 05 \text{ particles / sec/ location}$$

to provide the correct flow rate and particle momentum at the inlet.

IN SUMMARY, when undertaking a two dimensional analysis, care must be taken as to the interpretation of the third dimension. The mass flow rate obtained in the two dimensional analysis for a single phase flow is interpreted as flow per unit width of the channel. In a discrete phase analysis, the flow per unit width can be interpreted to range from a single particle to as much as the actual number of particles per unit width of duct.

Particle Size Distributions

At any point in the domain, particles can be introduced at a given mass flow rate. Given the number of particles and the mass flow rate, the number of particles per unit time, η , at each location is computed to be

$$\eta = \frac{\dot{m}_p}{\tilde{n}_p \bar{\rho}_p v_p}$$

Particles introduced at a point can be of a single size, or consist of a distribution of sizes. If injection is monodisperse, FIDAP, automatically calculates the particle frequency, η , if the mass flow rate/per location and size of particle are supplied. The mass flow rate per location in the last example is

$$\dot{m}_p'' = \frac{\dot{m}_p}{\tilde{n}} = 2.184E - 05 \text{ kg / sec / location}$$

The frequency of particles, calculated internally by FIDAP, is unavailable to the user but is calculated internally to be approximately 49 particles per second at each location. If injection is assumed monodisperse (same particle size) each command given to FIDAP for particle injection, assumes that the mass flow rate supplied is for "each" location specified by the user.

$$\dot{m}_p'' = \frac{\dot{m}_p}{\tilde{n}} = 2.184E - 05 \text{ kg / sec / location}$$

At each of the five (5) locations specified, FIDAP would utilize a particle frequency of

$$\eta' = \frac{\dot{m}_p / \tilde{n}_p}{\bar{\rho}_p V_p} = \frac{2.184E - 05}{850 \cdot \pi \frac{D_p^3}{6}} = 49.08 \text{ particles / sec}$$

Correct calculation of the particle frequency is important when a "two-way" coupling (Level 3 analysis) is undertaken.

Using a particle distribution at "each" location which is Gaussian, LogNormal or in the form of a histogram, the mass flow specified on the PARTICLE command in FIDAP is the total flow rate at an individual location. Based on the specified size distribution, FIDAP will calculate the particle frequencies for each size with the sum of the mass flows adding up to the total mass flow rate per location.

1.4 Two-Phase Capabilities in FIDAP

TWOPHASE COMMAND

The operations driven by the TWOPHASE command are independent of the various particles in the flow. The keywords in that command set general parameters ranging from integration parameters, to descriptions of forces applied to the particles.

SOURCE	SOLVER		ALGORITHM		INTEGRATION PARAMETERS	FORCES		HEAT TRANSFER MODE
FIPOST FISOLV	EXPLICIT SEMI-ANALYTIC		FIXED		DT TEND TSTART DTMAX DTMIN NSTEPS	DRAG		TMPUSER ISOTHERMAL TEMPERATURE
	IMPLICIT	TOLERANCE	VARIABLE	FRACTIONALERROR		BUOYANCY	GRAVITY THETA PHI	
				GLOBALERROR		CORIOLIS CENTRIFUGAL	OMEGA X Y Z	
				LOCALERROR WINDOW UCHAR VCHAR WCHAR SCHAR, SPEC=N			DRUSER	

MASS TRANSFER MODE	DRAG COEFFICIENT MODEL		NUSSELT NUMBER MODEL	SHERWOOD NUMBER MODEL	FLOW REGIME	SOURCE TERMS
PHUSER PHASECHANGE	MDNONEVAPORATE MDEVAPORATE MDUSER		MNNONEVAPORATE MNEVAPORATE MNUSER	MSHERWD MSUSER	LAMINAR TURBULENT	PUPDATE NOMASS NOMOMENTUM NOTEMPERATURE
PARTOLERANCE	POLYNOMIAL	ACOEf				
GASCONSTANT		BCOEf CCOEf Ecoef				

PARTICLE COMMAND

The role of the particle command is to provide a description of the particles that are to be introduced in the flow. These particle characteristics range from initial position, to chemical composition. Each particle command defines a set of particles that all have the same characteristics. The following tables summarize the keywords that may be used depending on the type of problem to be solved.

ISOTHERMAL PROBLEMS

PARTICLE ID	PARTICLE POSITION	INITIAL CONDITIONS	PARTICLE TYPE	PARTICLE SIZE	PROPERTIES
SET PARCEL MASSFLOW	COORDINATE ELEMENT NODES LOCAL X/ZC Y/RC Z	UX/UZC UY/URC UZ/UTHETA PSIZE	SOLID	GAUSSIAN LOGNORMAL HISTOGRAM MONO STANDARDDEV	DENSITY MSOLID

THERMAL PROBLEMS

PARTICLE ID	PARTICLE POSITION	PARTICLE VELOCITY	PARTICLE TYPE	PARTICLE SIZE	PROPERTIES
SET PARCEL MASSFLOW	COORDINATE ELEMENT NODES LOCAL X/ZC Y/RC Z	UX/UZC UY/URC UZ/UTHETA TEMPERATURE PSIZE	SOLID	GAUSSIAN LOGNORMAL HISTOGRAM MONO STANDARDDEV	DENSITY MSOLID MSSPHT

PHASE CHANGE PROBLEMS

PARTICLE ID	PARTICLE POSITION	INITIAL CONDITIONS	PARTICLE TYPE	PARTICLE SIZE	PROPERTIES	CHEMICAL COMPOSITION
SET PARCEL MASSFLOW	COORDINATE ELEMENT NODES LOCAL X/ZC Y/RC Z	UX/UZC UY/URC UZ/UTHETA TEMPERATURE PSIZE	MIXED EVAPORATING	GAUSSIAN LOGNORMAL HISTOGRAM MONO STANDARDDEV	MFLU MSOL MSPHT MSSPHT MVSPTH MLATENT MMVAPOR MCAP MVAPOR BOILING - VAPOR	SPECIES HUMIDITY CONTINUUM CONSTANT

PATH COMMAND

The path command is used purely for postprocessing purposes. This commands allows the user to display particle paths in variety of formats while providing plots for the analysis of a large number of fluid and particle variables.

PLOT TYPE	PATH TYPE	PARTICLE IDENTIFIER	DISPLAY TYPE	WINDOW	PRINTOUT	VARIABLES
CONTINUOUS DISCRETE CHAR	PARTICLE DYE MATERIAL PREVIOUS	ALL SET LIST ID	PLOT NOLOT LINEPLOT ARCLENGTH TIME	TSTART TEND DTPLOT DTMOV	PRINT FLPRINT NOPRINT FILE NOFILE	UPAR VPAR WPAR TPAR DIAM SPAR ALL FLOW VARIABLES

2. Level 1& 2 Examples

This section contains an assortment of one-way coupling problems designed to illustrate some of the concepts developed in the previous sections.

2.1 Flow Impingement On a Flat Plate

The analytical solution for the particle path in an inviscid flow near a stagnation point is presented. The inviscid flow near a 90 degree corner can be described by the complex potential

$$w(z) = U \left(z - \frac{z^2}{2} \right) \quad (2.1.1)$$

The analysis of inviscid flows through complex potential has shown that for such a complex potential

$$\frac{dw}{dz} = u - iv \quad (2.1.2)$$

In the case of a flow near a 90 degree corner, after the carrier velocities are given by

$$u_f = U \left(1 - \frac{x}{L} \right); \quad v_f = U \frac{y}{L} \quad (2.1.3)$$

Given the above carrier phase velocity field, and after non-dimensionalization, the particle trajectories are described by the following equations:

$$\begin{aligned} \frac{d^2x}{dz^2} + \frac{dx}{dz} + St_\tau x &= St_\tau \left(1 + \frac{\left(1 - \frac{1}{\rho_p} \right)}{Fr^2} \right) \text{ with } x(t=0) = 0 \text{ and } \frac{dx}{dt}(t=0) = U \\ \frac{d^2y}{dz^2} + \frac{dy}{dz} + St_\tau y &= 0 \text{ with } y(t=0) = 1 \text{ and } \frac{dy}{dt}(t=0) = 0 \end{aligned} \quad (2.1.4)$$

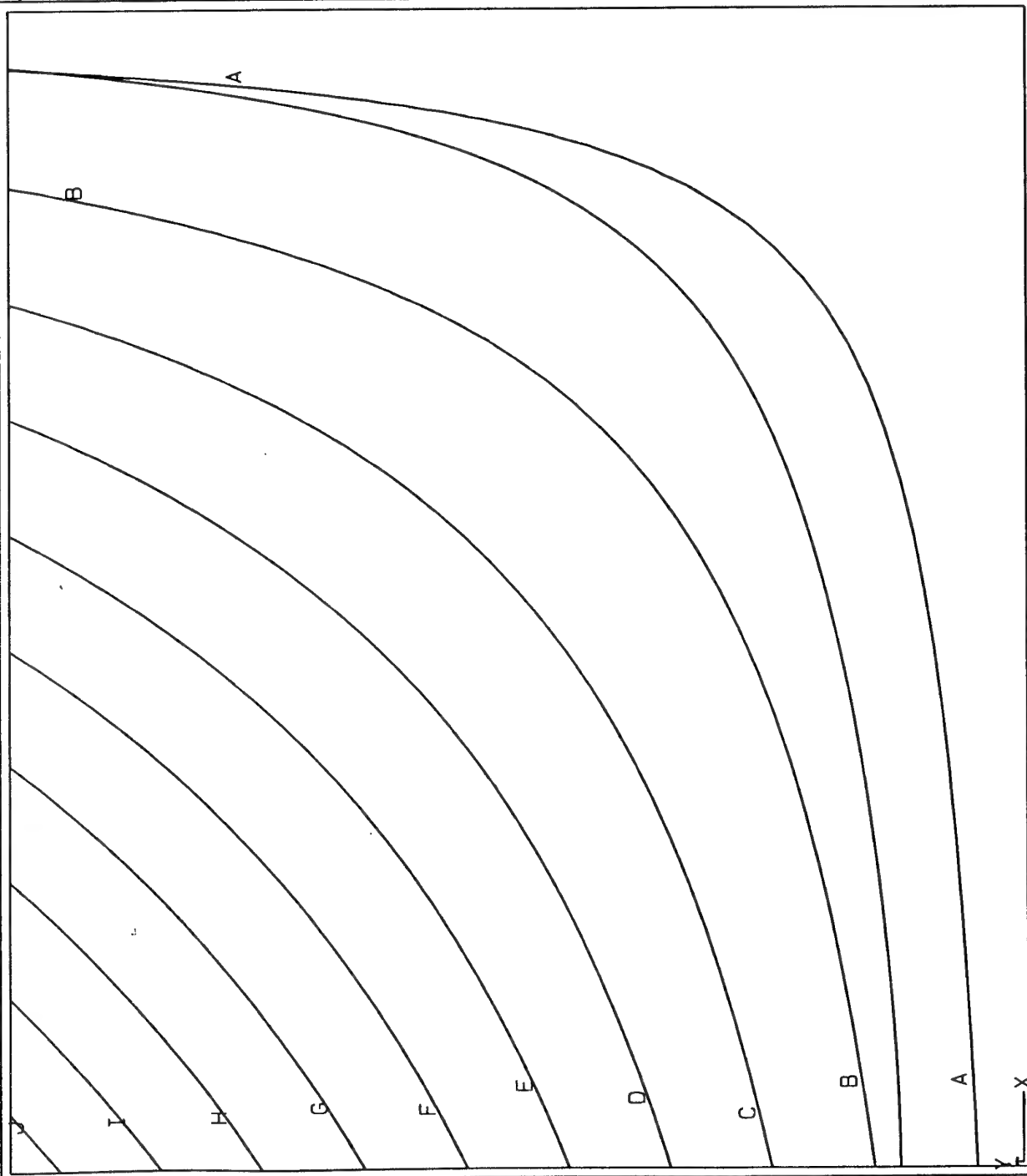
The analytical solution for this system reads:

$$\begin{aligned} x &= \frac{m_2 \left(1 + \left(1 - \frac{1}{\rho_p} \right) \frac{St}{Fr^2} \right) + St}{m_1 - m_2} e^{m_1 z} - \frac{m_1 \left(1 + \left(1 - \frac{1}{\rho_p} \right) \frac{St}{Fr^2} \right) + St}{m_1 - m_2} e^{m_2 z} + \left(1 + \left(1 - \frac{1}{\rho_p} \right) \frac{St}{Fr^2} \right) \\ y &= \frac{-m_2}{m_1 - m_2} e^{m_1 z} + \frac{m_1}{m_1 - m_2} e^{m_2 z} \end{aligned}$$

where

$$m = \frac{-1 \pm \sqrt{1 - 4St}}{2} \text{ and } z = \frac{t}{\tau} \text{ for } St < \frac{1}{4}$$

FLOW IMPINGEMENT ON A FLAT PLATE



PARTICLE
PATH PLOT

PARTICLE PATH

FROM TIME:
.0000E+00

TO TIME:
.2420E+01

SCREEN LIMITS

XMIN -.251E-02

XMAX .100E+01

YMIN -.201E-01

YMAX .802E+01

FIDAP 7.50

27 Jul 94

16:39:07

FLOW IMPINGEMENT ON A FLAT PLATE

PARTICLE
PATH PLOT

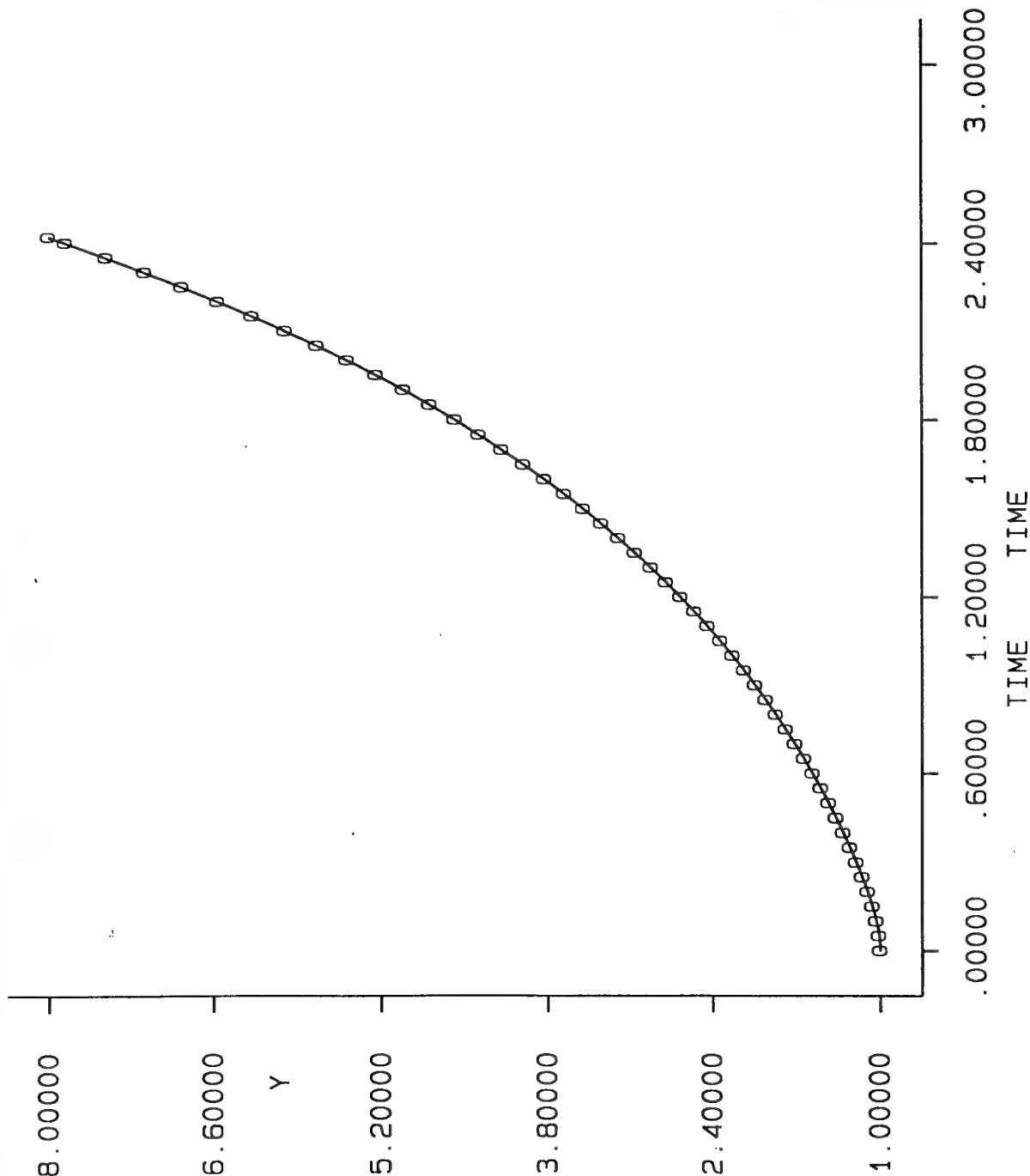
CARRIER PHASE
Y COORDINATE

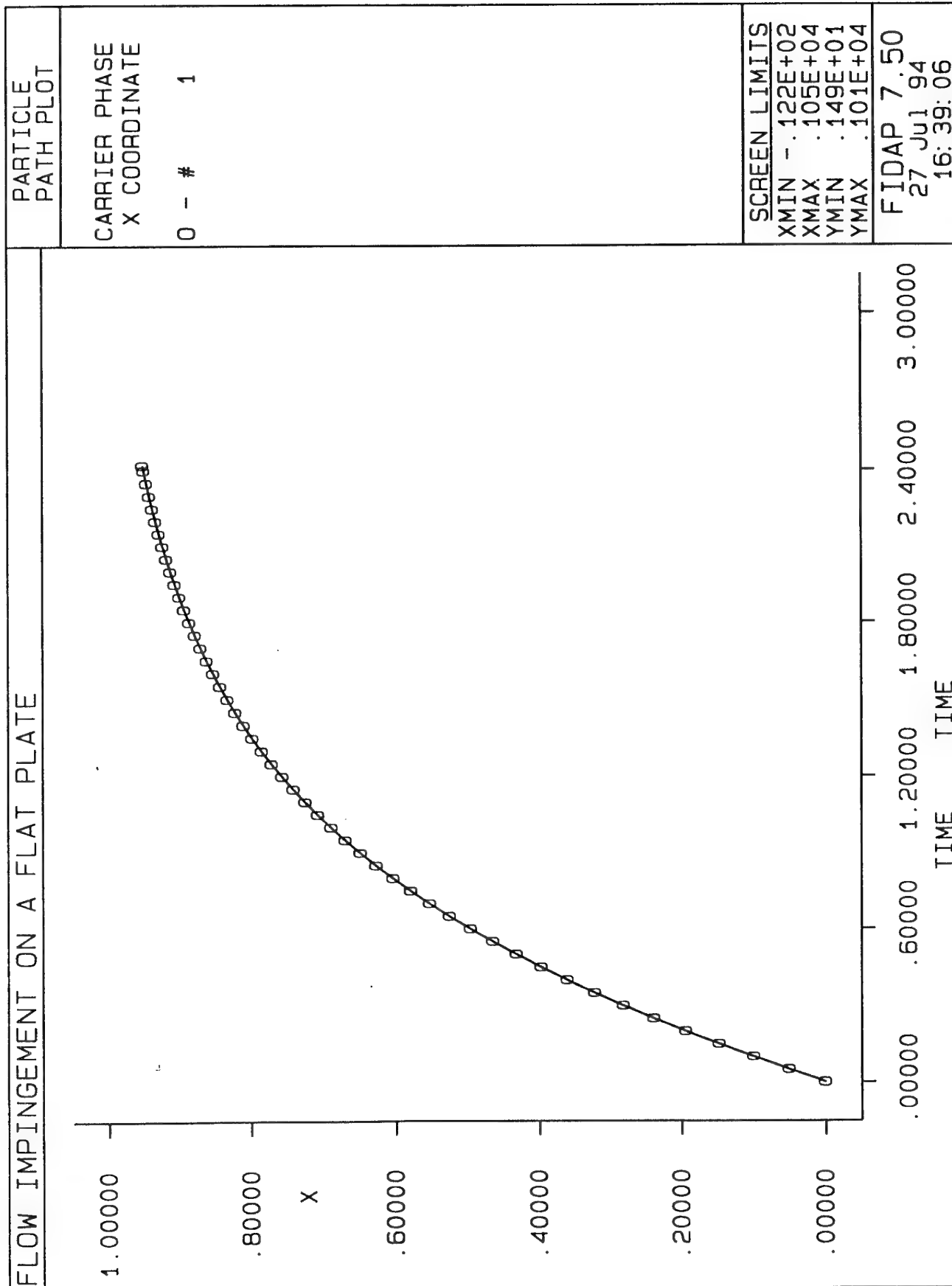
0 - # 1

SCREEN LIMITS

XMIN -.122E+02
XMAX .105E+04
YMIN .149E+01
YMAX .101E+04

FIDAP 7.50
27 Jul 94
16:39:06





2.2 Inviscid Flow Around a Cylinder

The analytical solution for the particle path in an inviscid flow around a cylinder is presented here. The objective of this example is to illustrate the use of user subroutines. The inviscid flow around a cylinder of radius a can be described by the complex potential

$$w(z) = U \left(z + \frac{a^2}{z} \right) \quad (2.2.1)$$

For this function, the corresponding velocities are:

$$u_f = U \left(1 + \frac{a^2(y^2 - x^2)}{(x^2 + y^2)^2} \right) \quad (2.2.2)$$

$$v_f = -\frac{2Ua^2xy}{(x^2 + y^2)^2}$$

we assume the Lagrangian model accurately describes the physics of the problem, and we assume the following drag model:

$$C_D = \frac{K_1}{\text{Re}_p} + \frac{K_2}{\text{Re}_p^2} + K_3 \quad (2.2.3)$$

The first approach to this problem is to use a user subroutine to define the drag coefficient. On the other hand, we may also choose to create a user defined force that applies to the particles. In this case, the momentum equation for the particle may be written:

$$\begin{aligned} \frac{du_{ip}}{dt} &= \phi_{i1} - \phi_{i2}u_{ip} + \phi_{i3}u_{ip}^2 \\ \phi_{i1} &= \frac{3\mu K_1 u_{if}}{4\rho_p D^2} + \frac{3\mu^2 K_2}{4\rho_p \rho_f D^3} + \frac{3K_3 \rho_f u_{if}^2}{4\rho_p D} \\ \phi_{i2} &= \frac{3\mu K_1}{4\rho_p D^2} + \frac{3K_3 \rho_f u_{if}}{2\rho_p D} \\ \phi_{i3} &= \frac{3K_3 \rho_f}{4\rho_p D} \end{aligned} \quad (2.2.4)$$

INVISCID FLOW AROUND A CYLINDER

PARTICLE
PATH PLOT

PARTICLE PATH

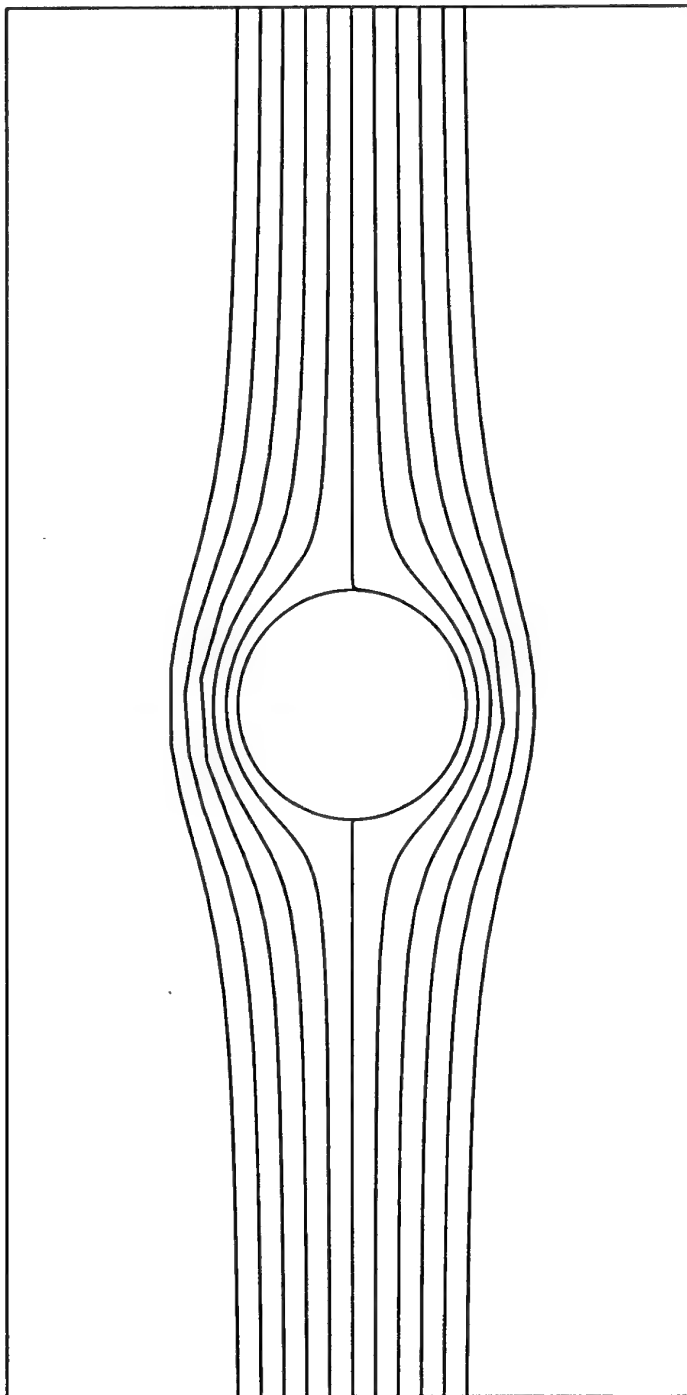
FROM TIME:
.0000E+00

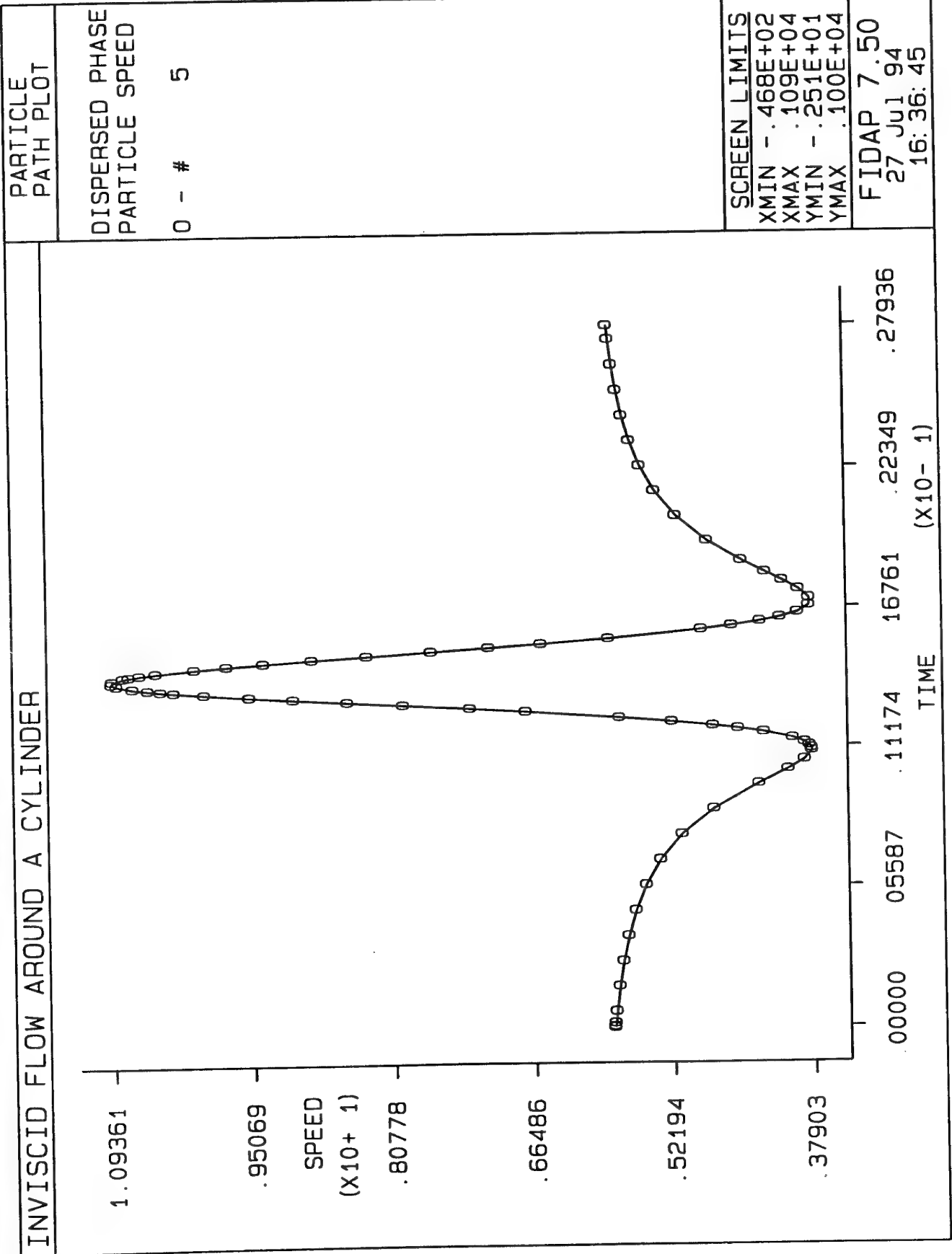
TO TIME:
.4140E-01

SCREEN LIMITS

XMIN -.754E-01
XMAX .754E-01
YMIN -.668E-01
YMAX .668E-01

FIDAP 7.50
27 Jul 94
16:36:45

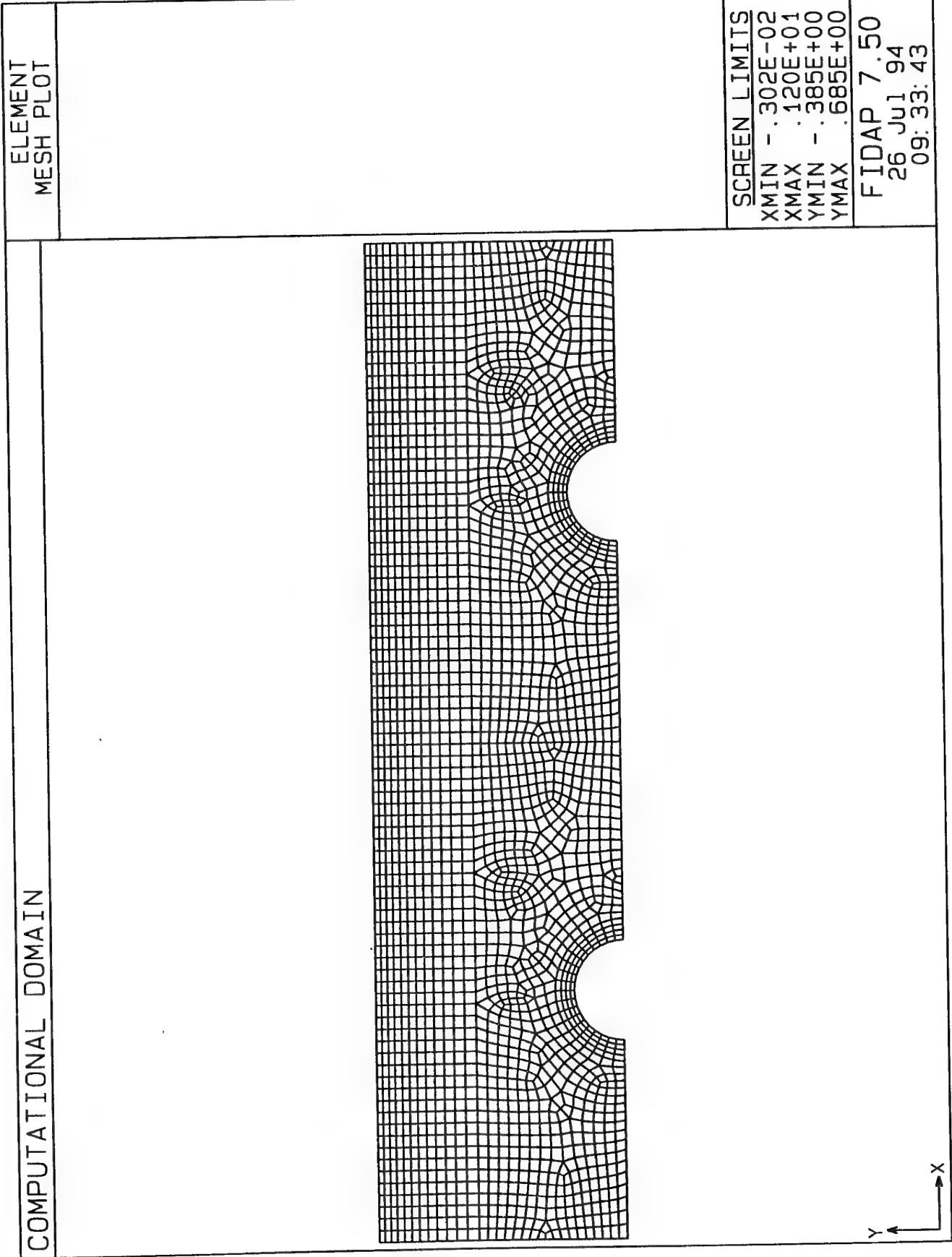




2.3 Turbulent Flow in a Bank of Tubes

This example illustrates the stochastic model for particle tracking available in FIDAP in conjunction with the $k - \epsilon$ closure for the Eulerian turbulent field. The geometry is shown in the following page and represents the flow past multiple tubes at a Reynolds number of 8000 with respect to the tube diameter (whose length is 12 cm.). For a given location, particles of different diameters are tracked using a Gaussian distribution.

The interaction between particle and turbulence is dictated by the particle relaxation time. For a particle density of 2000 kg/m^3 the larger particles (about 1mm.) experience a very small influence from the turbulent fluctuations due to their larger inertia. In other words, the eddy lifetime is too small compared to the particle relaxation time and the particles do not have time to respond to the velocity fluctuations caused by the eddy. The smaller particles have a lower relaxation time (note that the relaxation time changes with the square of the diameter) and their paths are substantially modified by the turbulent fluctuations, with particle paths reaching the zone in between the two cylinders. Note also that the velocity fluctuations can be responsible for multiple collisions between the particles and the tubes, especially if the restitution coefficient of the impact is close to unity.



VELOCITY VECTORS

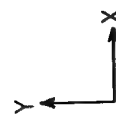
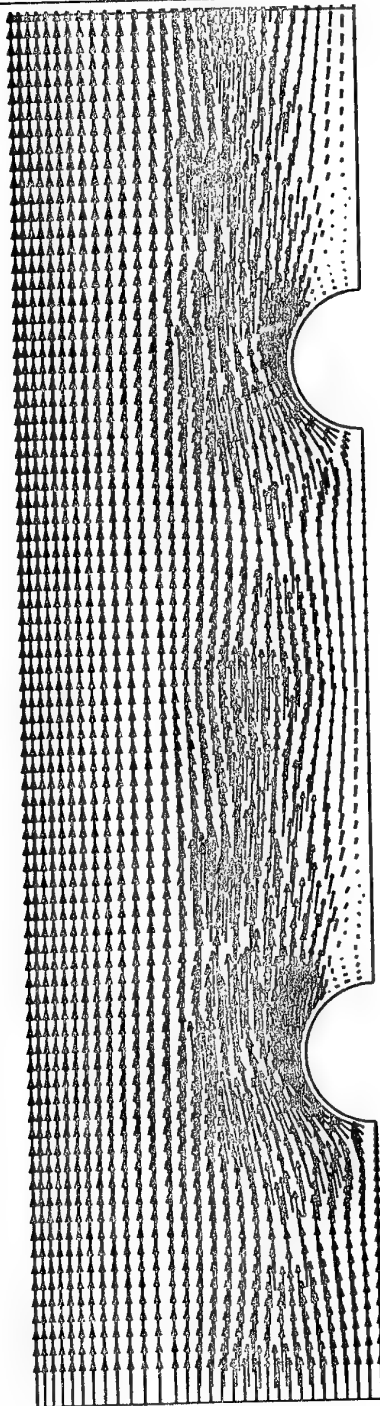
VELOCITY
VECTOR PLOT

SCALE FACTOR
.5000E+02

REFER. VECTOR
→ .1666E+01

MAX. VEC. PLOT'D
.1666E+01

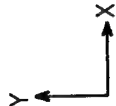
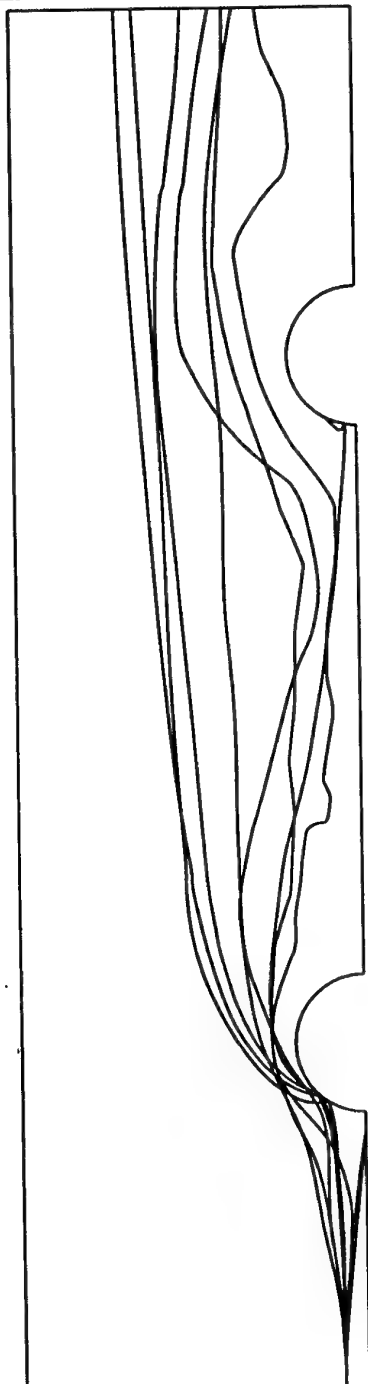
AT NODE 394



SCREEN LIMITS
XMIN - .302E-02
XMAX .120E+01
YMIN - .385E+00
YMAX .685E+00

FIDAP 7.50
25 Jul 94
16:56:18

PARTICLE PATHS IN TURBULENCE



PARTICLE
PATH PLOT

PARTICLE PATH

FROM TIME:
.0000E+00

TO TIME:
.1728E+01

SCREEN LIMITS

XMIN -- .302E-02
XMAX -- .120E+01
YMIN -- .385E+00
YMAX -- .685E+00

FIDAP 7.50

25 Jul 94

16: 55: 59

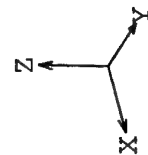
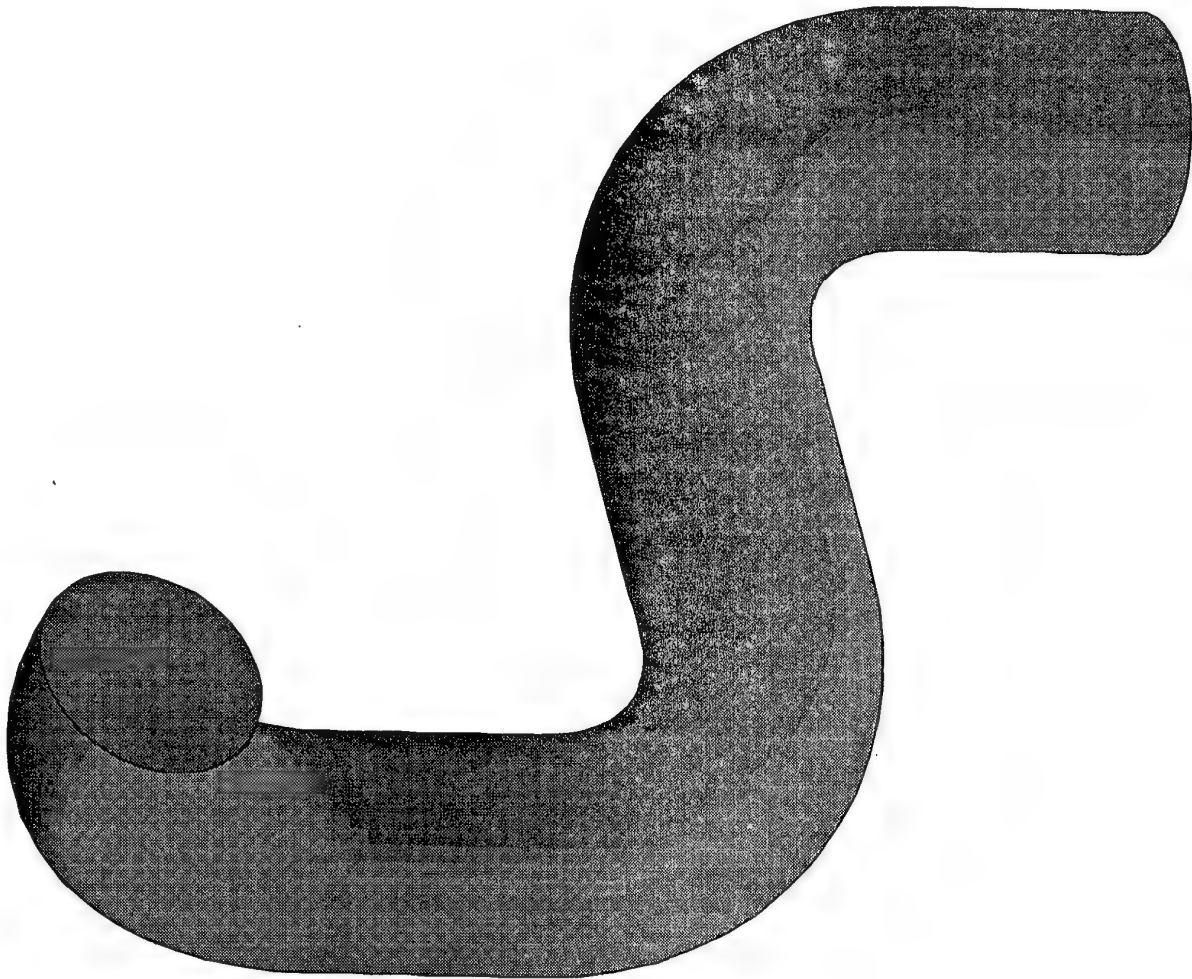
2.4 Erosion Estimation in Successive Elbows

In many industrial applications involving transport of abrasive granules, pipe erosion near elbows can create a significant problem. Certain combinations of elbows can increase the erosion significantly due to the cumulative effect of particle's inertia moving from one elbow to the next. This example attempts to demonstrate the effect of particle size in successive elbows. The fluid is air, and particles are sand particles. The Reynolds number of the flow is 45,000 and particles of 500 and 100 μm are tracked. As the trajectories reveal, larger particles can actually cause erosion on the back side of subsequent elbows. Furthermore, as the line plots of particle speed reveal, the large particles lose their momentum with every impact, whereas the small ones regain most of their momentum between impacts.

ELEMENT
EDGE PLOT

VIEW DIRECTION
VX 0.668E+00
VY 0.100E+01
VZ 0.585E+00
ANG -.128E+01

FIDAP 7.50
02/24/95
13:26:33



500 micron particles

PARTICLE
PATH PLOT

PARTICLE PATH

FROM TIME:
0.0000E+00

TO TIME:
0.6829E+02

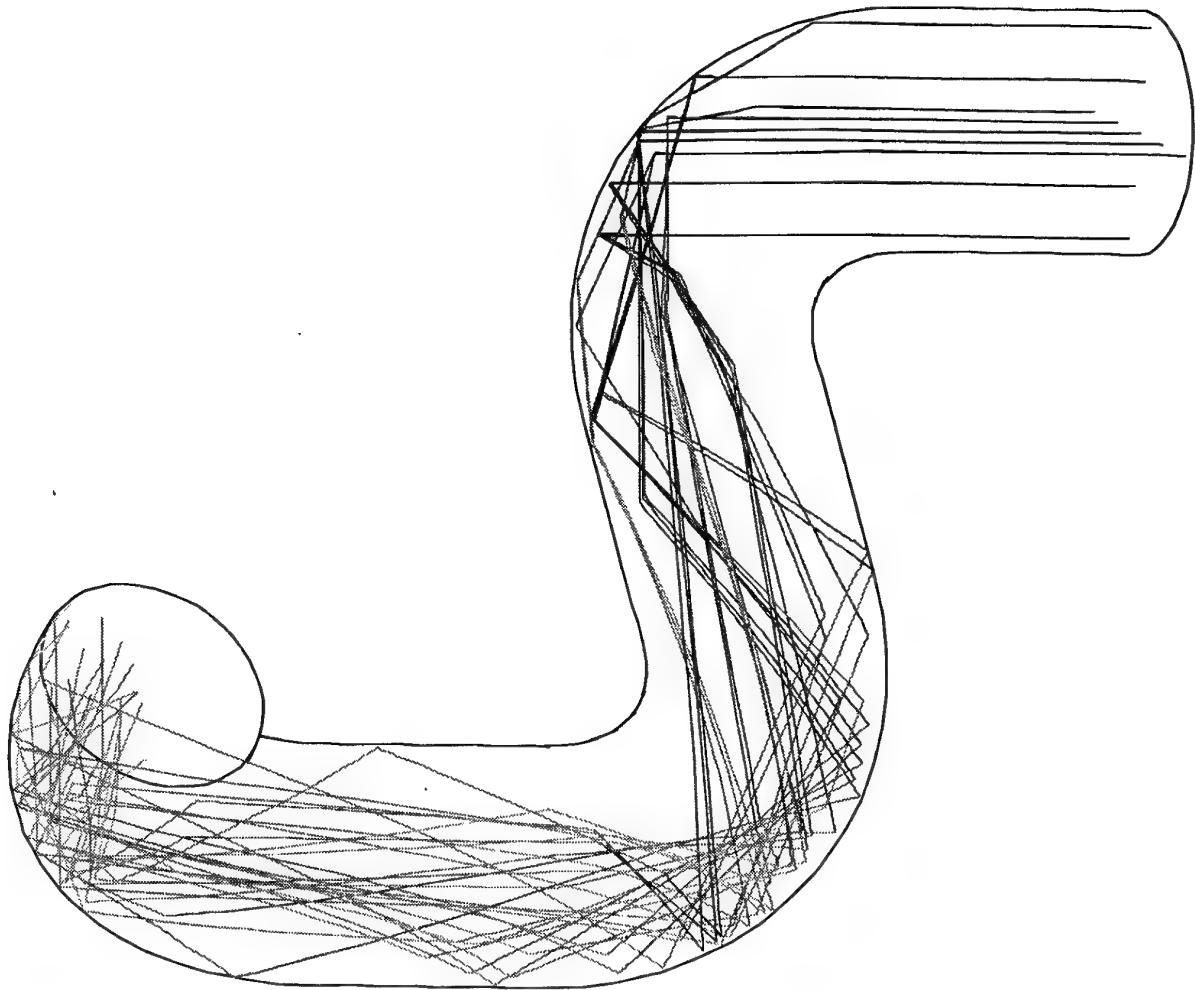
PARTICLE SPEED

0.902E+00
0.801E+00
0.700E+00
0.600E+00
0.499E+00
0.398E+00
0.298E+00
0.197E+00

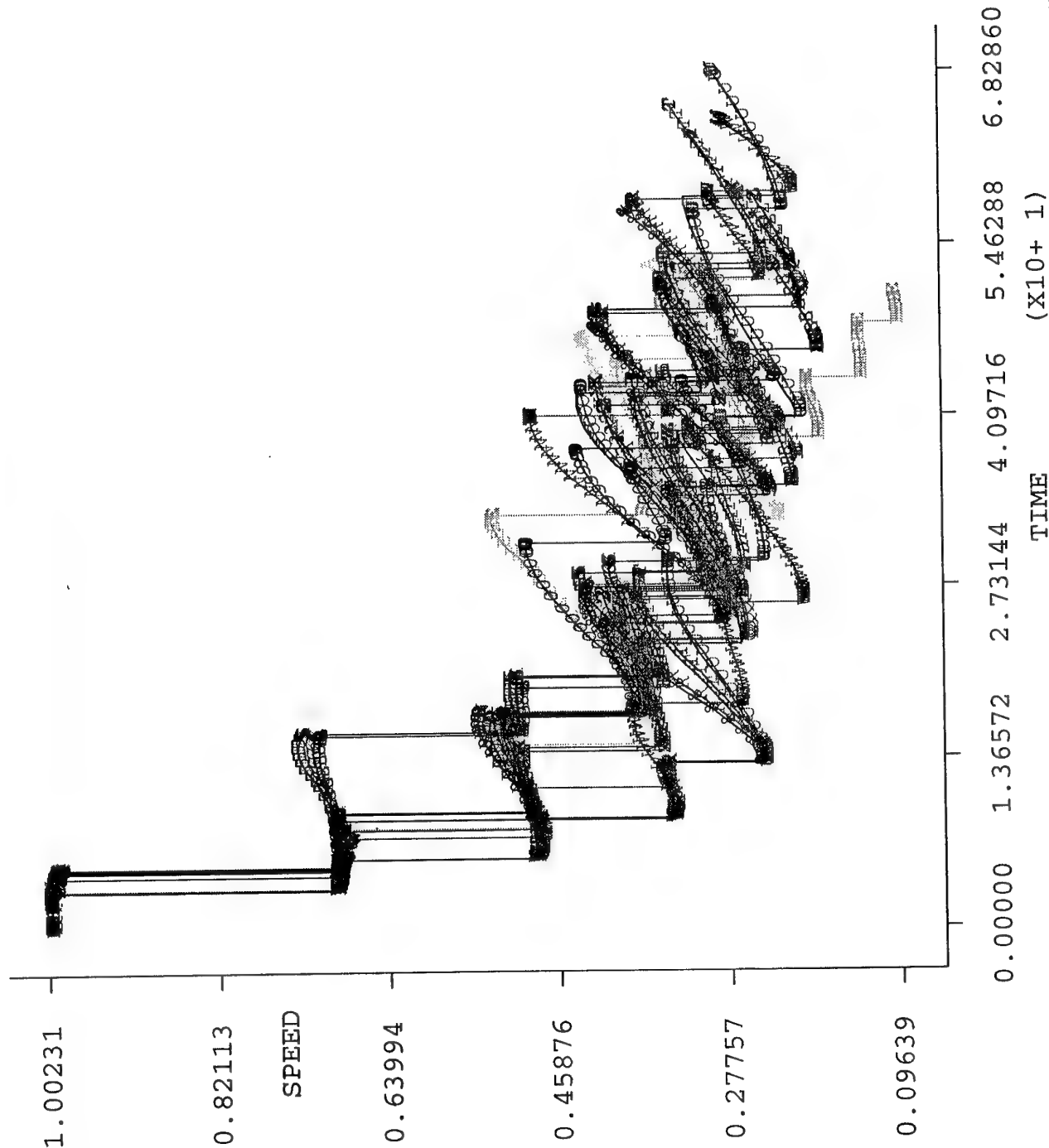
VIEW DIRECTION

VX 0.668E+00
VY 0.100E+01
VZ 0.585E+00
ANG -.128E+01

FIDAP 7.50
02/24/95
13:34:29



500 micron particles



PARTICLE PATH PLOT	
DISPERSED PHASE	PARTICLE SPEED
A	#
B	#
C	#
D	#
E	#
F	#
G	#
H	#
I	#
J	#
K	#
L	#
M	#
N	#
O	#
P	#
Q	#
R	#
S	#
T	#
	1
	2
	3
	5
	6
	8
	9
	11
	12
	14
	15
	17
	18
	20
	21
	23
	24
	26
	27
	29
VIEW DIRECTION	
VX	0.668E+00
VY	0.100E+01
VZ	0.585E+00
ANG	-.128E+01
FIDAP 7.50	
02/24/95	
13:34:42	

100 micron particles

PARTICLE
PATH PLOT

PARTICLE PATH

FROM TIME:
0.0000E+00

TO TIME:
0.5811E+02

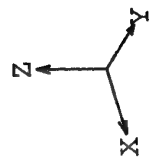
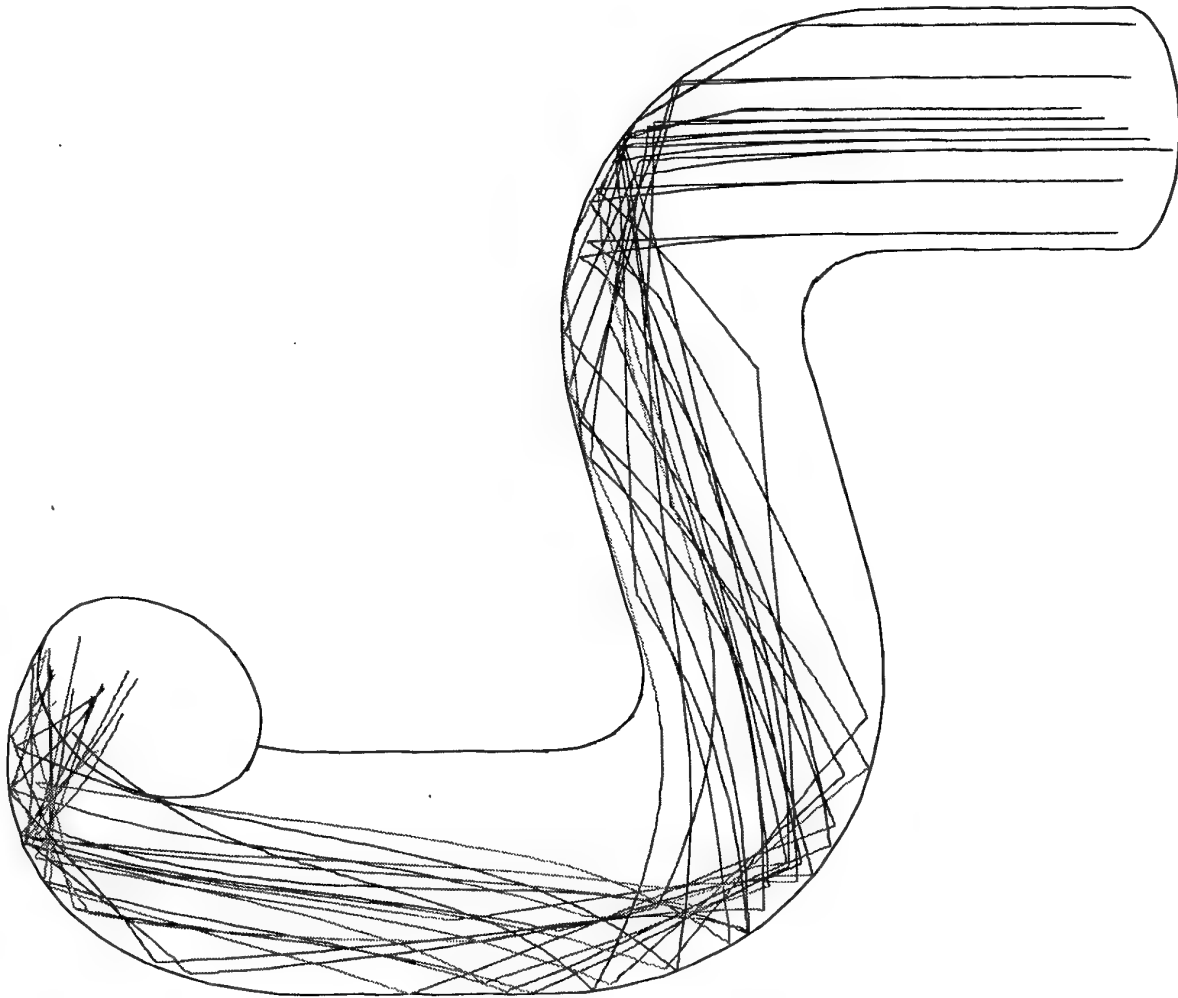
PARTICLE SPEED

-0.905E+00
-0.792E+00
-0.679E+00
-0.565E+00
-0.452E+00
-0.339E+00
-0.226E+00
-0.113E+00

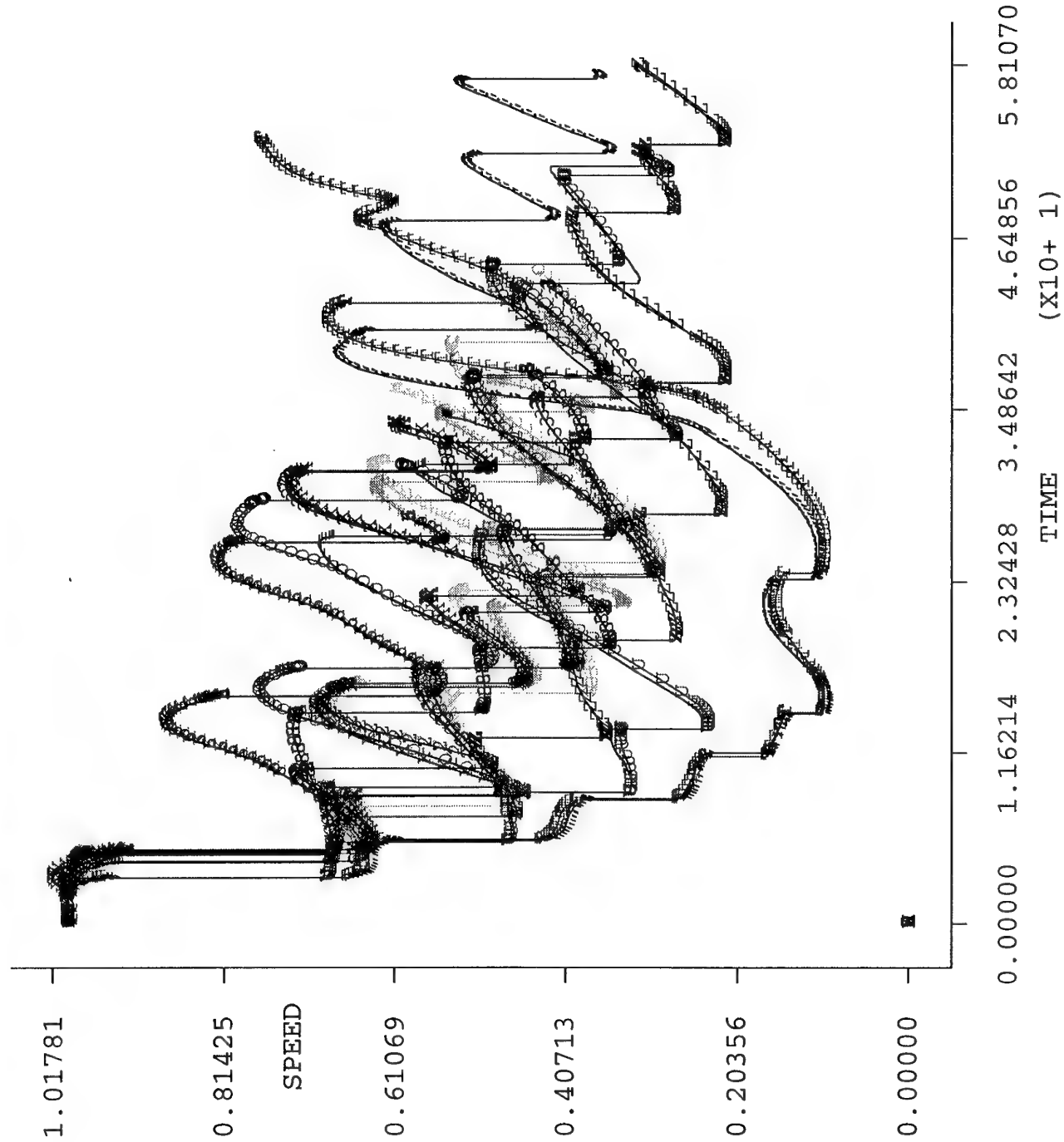
VIEW DIRECTION

VX 0.668E+00
VY 0.100E+01
VZ 0.585E+00
ANG -.128E+01

FIDAP 7.50
02/24/95
13:38:24



100 micron particles



PARTICLE PATH PLOT	
DISPERSED PHASE	PARTICLE SPEED
1	#
2	-
3	#
5	-
6	#
8	-
9	#
11	-
12	#
14	-
15	#
17	-
18	#
20	-
21	#
23	-
24	#
26	-
27	#
29	-
A	#
B	-
C	#
D	-
E	#
F	-
G	#
H	-
I	#
J	-
K	#
L	-
M	#
N	-
O	#
P	-
Q	#
R	-
S	#
T	-
VIEW DIRECTION	
VX	0.668E+00
VY	0.100E+01
VZ	0.585E+00
ANG	-.128E+01
FIDAP 7.50	
02/24/95	
13:38:35	

2.5 Virtual Impactor

This example illustrates a particle separation process using a virtual impactor device. The virtual impactor device is an inertial particle size separator. The incoming flow is assumed to contain 1 and 5 micron particles. Fresh air is introduced along the center line. The goal is to separate the two particle sizes such that the small ones go out from the outer ring (major flow), and the large ones from the center pipe (minor flow). The Reynolds number at the throat is 4000. Experiments indicate a 90% efficiency of the device. The trajectories of the two particle sizes predict the same efficiency.

LEGEND

-- -.352E+03
 -- -.3092E+03
 -- -.2918E+03
 -- -.2658E+03
 -- -.2484E+03
 -- -.2224E+03
 -- -.2050E+03
 -- -.1790E+03
 -- -.1616E+03
 -- -.1356E+03
 -- -.1182E+03
 -- -.9215E+02
 -- -.7479E+02
 -- -.4875E+02
 -- -.3139E+02
 -- -.5347E+01
 -- .1201E+02
 -- .3806E+02
 -- .5542E+02
 -- .8146E+02

**SEE PRINTOUT

MINIMUM

-.34823E+03

MAXIMUM

.85799E+02

SCREEN LIMITS

ZMIN -.460E+01

ZMAX .733E+01

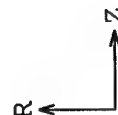
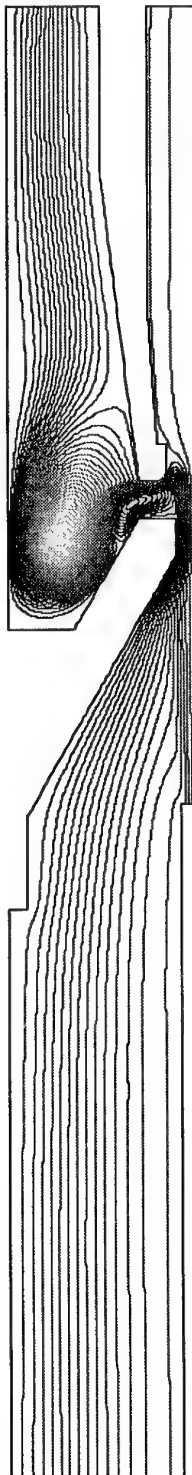
RMIN -.453E+01

RMAX .605E+01

FIDAP 7.50

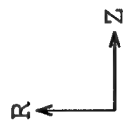
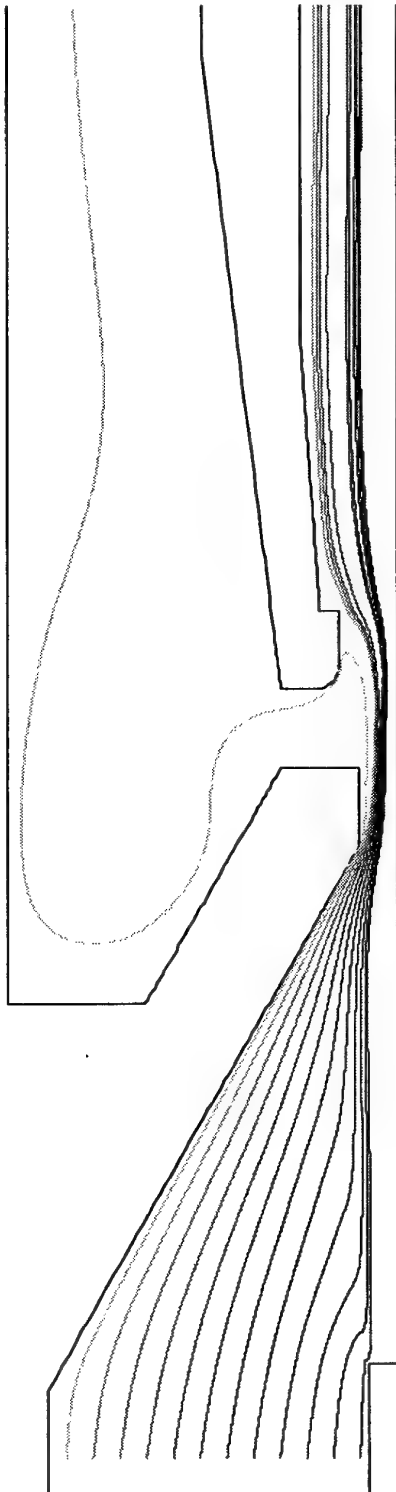
23 Feb 95

15:25:24

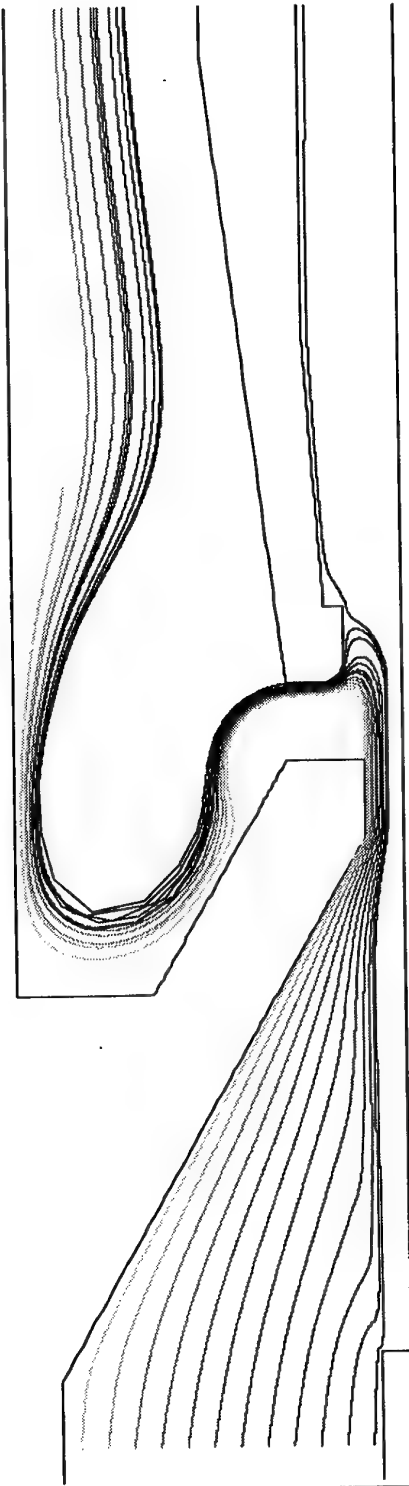


Virtual Impactor - 5 micron Particles

PARTICLE PATH PLOT
PARTICLE PATH FROM TIME: .0000E+00 TO TIME: .2992E+00
SCREEN LIMITS ZMIN .366E+00 ZMAX .613E+01 RMIN -.203E+01 RMAX .308E+01 FIDAP 7.50 23 Feb 95 14:53:39



Virtual Impactor - 1 micron Particles



R
Z

PARTICLE
PATH PLOT

PARTICLE PATH

FROM TIME:
.0000E+00

TO TIME:
.2394E+00

SCREEN LIMITS

ZMIN .366E+00
ZMAX .613E+01
RMIN -.203E+01
RMAX .308E+01

FIDAP 7.50
23 Feb 95
15:22:31

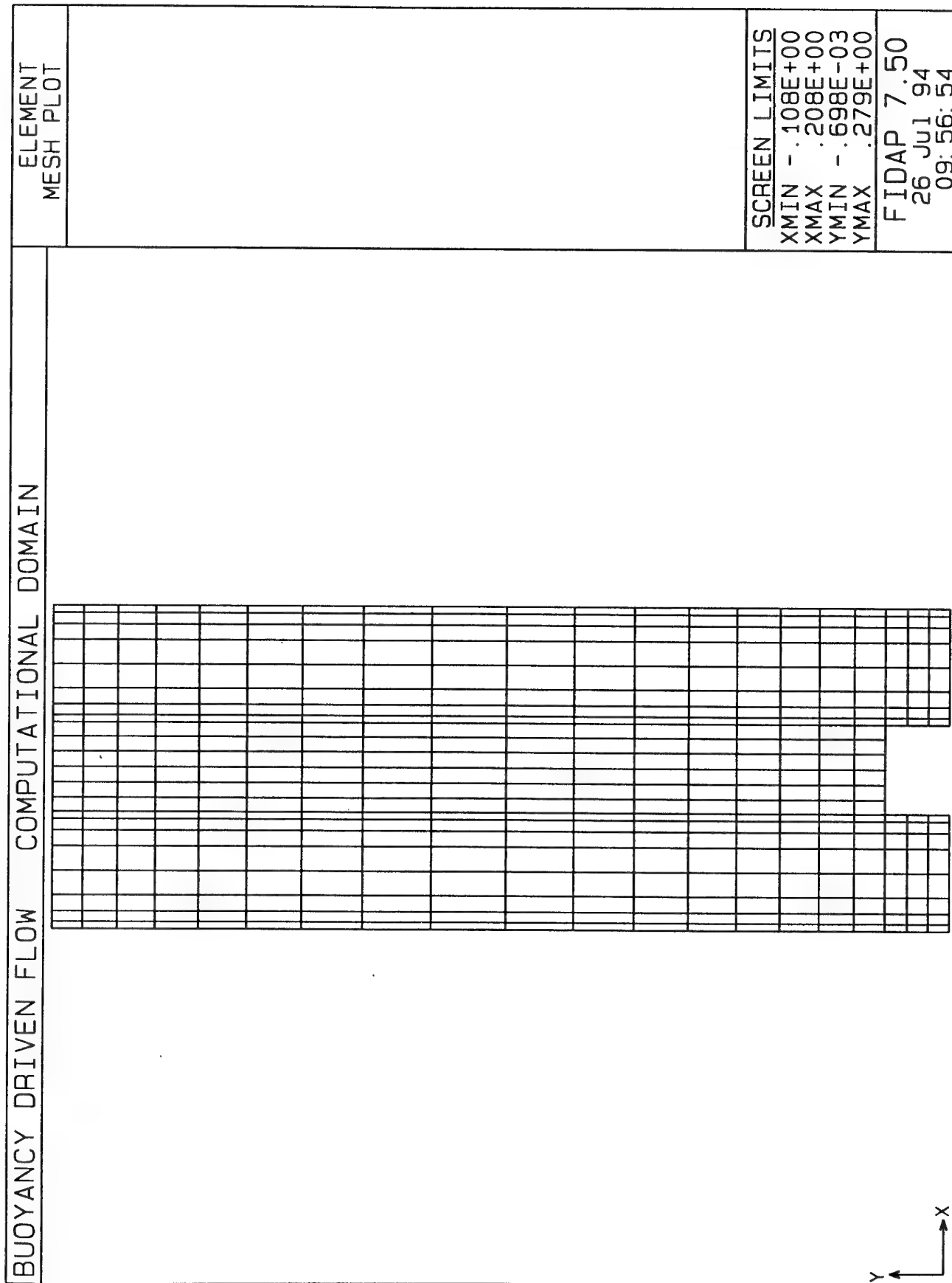
3. Level 3 Examples

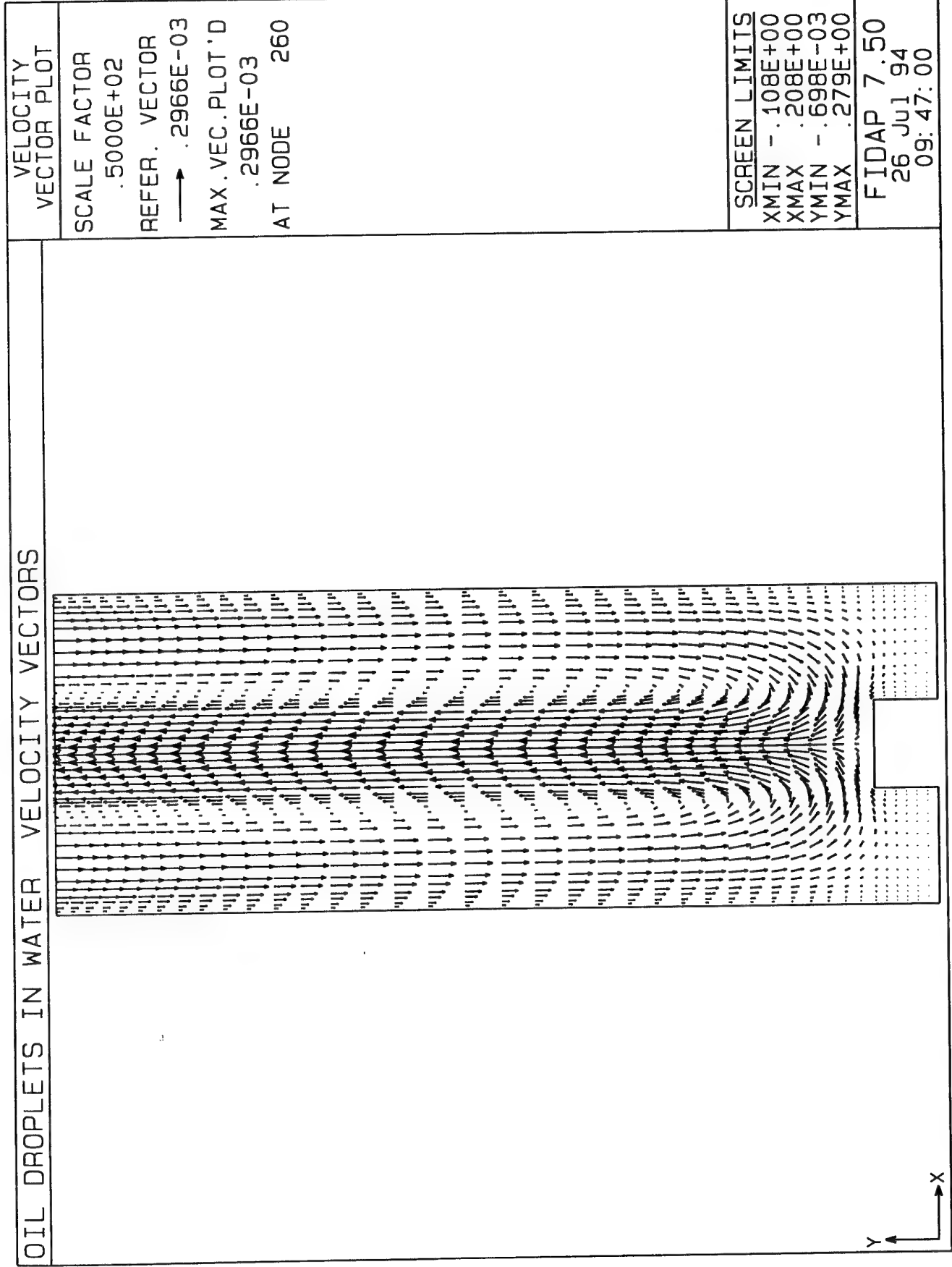
This section contains a few two-way coupling problems showing the full capabilities of multiple phase simulation in FIDAP.

3.1 Buoyancy Induced Flow in a Liquid Tank

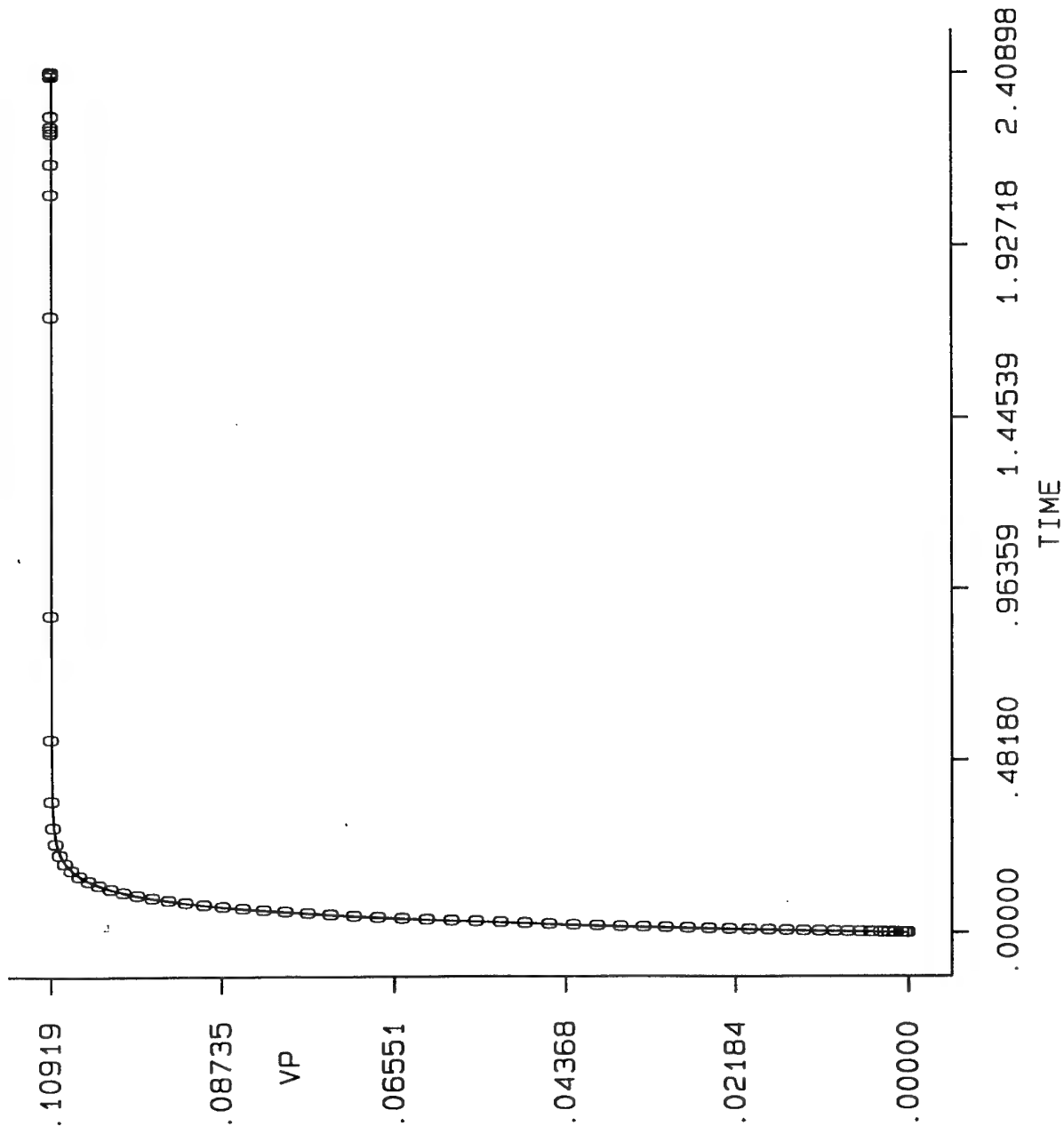
This example refers to the two-way coupling interaction between the fluid and the particles. A source term is included in the Navier-Stokes equation, accounting for the force exerted on the fluid that counterbalances the drag force on the particles. The force is expected to have some significant effect as a relative velocity between the two phases exists in a large region of the fluid domain. In this case the drift velocity is induced by the presence of lighter particles rising in the fluid. The computational domain and the input file are reported in the following pages.

The most significant parameters in this example are the density ratio between the two phases, the mass flow of the dispersed phase and the particle size. A large density between the two phases increases the buoyancy content of the particle and conversely the magnitude of the source term in the momentum equation. The induced fluid velocities are increased and the corresponding Reynolds number can reach values in the transition regime (9000 for air bubbles of 1mm. in water). Increasing the mass flow rate has the same effect as the density ratio in increasing the source term in the momentum equation. Also note that the same mass flow rate corresponds to very different volume loading and void fraction if the difference between the two phases is relevant. The particle size influences the terminal velocity: larger particles have a higher terminal velocity that can increase the magnitude of the source term. On the other hand, the smaller particles, being much slower, have a longer residence time in the element that translates in a larger volume fraction and by consequence a more considerable impact on the fluid flow. For this reason it is not to be expected that decreasing the particle size decreases the influence on the fluid flow if the mass flow rate is kept constant. Note also, that the smaller particles are more prone to respond to the instabilities that can occur in the convergence process and can therefore increase the effect of these instabilities.





OIL DROPLETS IN WATER PARTICLE VELOCITY



PARTICLE
PATH PLOT

DISPERSED PHASE
PARTICLE UY

0 - # 1

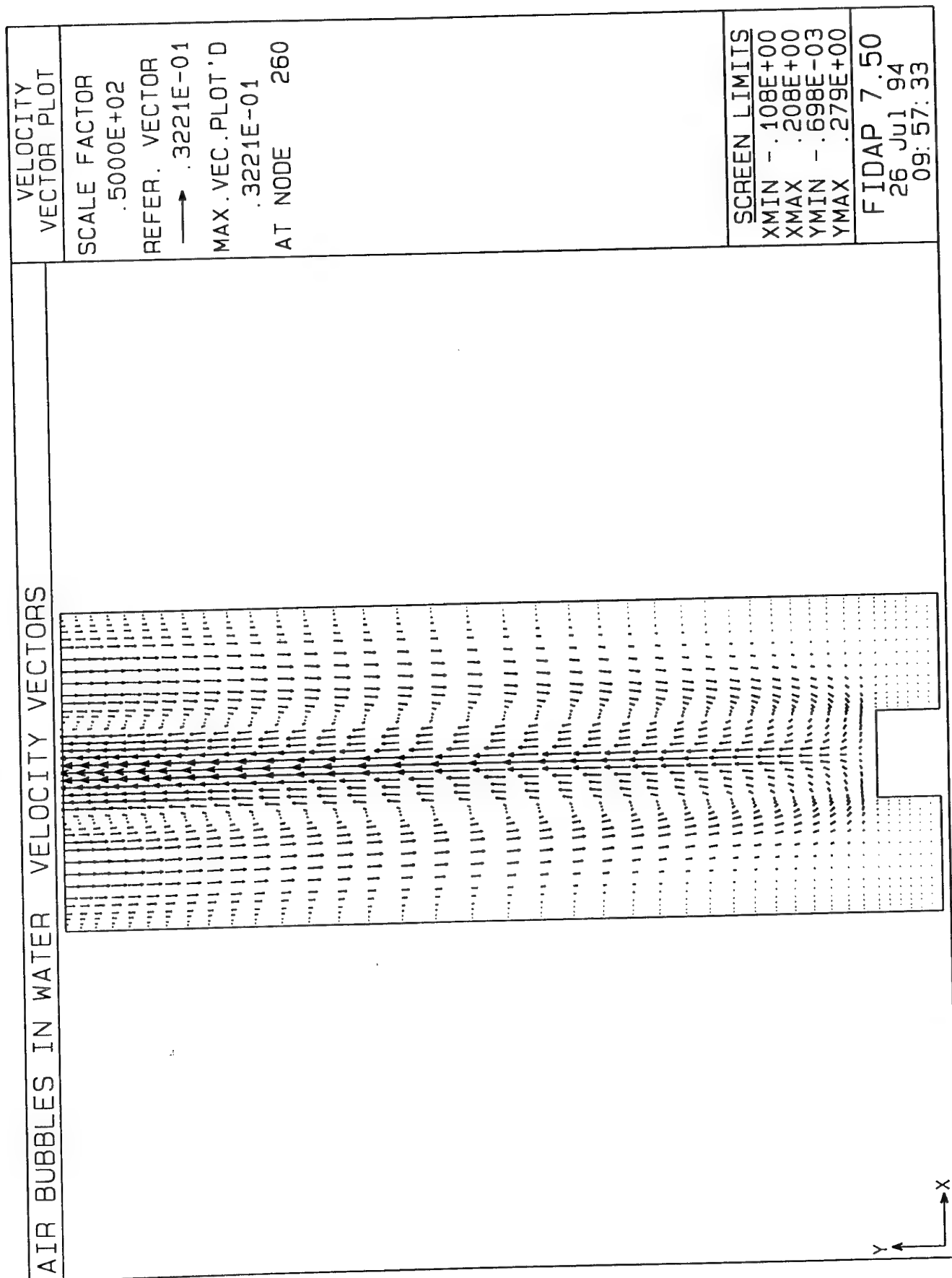
SCREEN LIMITS

XMIN - .467E+02
XMAX .109E+04
YMIN - .237E+01
YMAX .100E+04

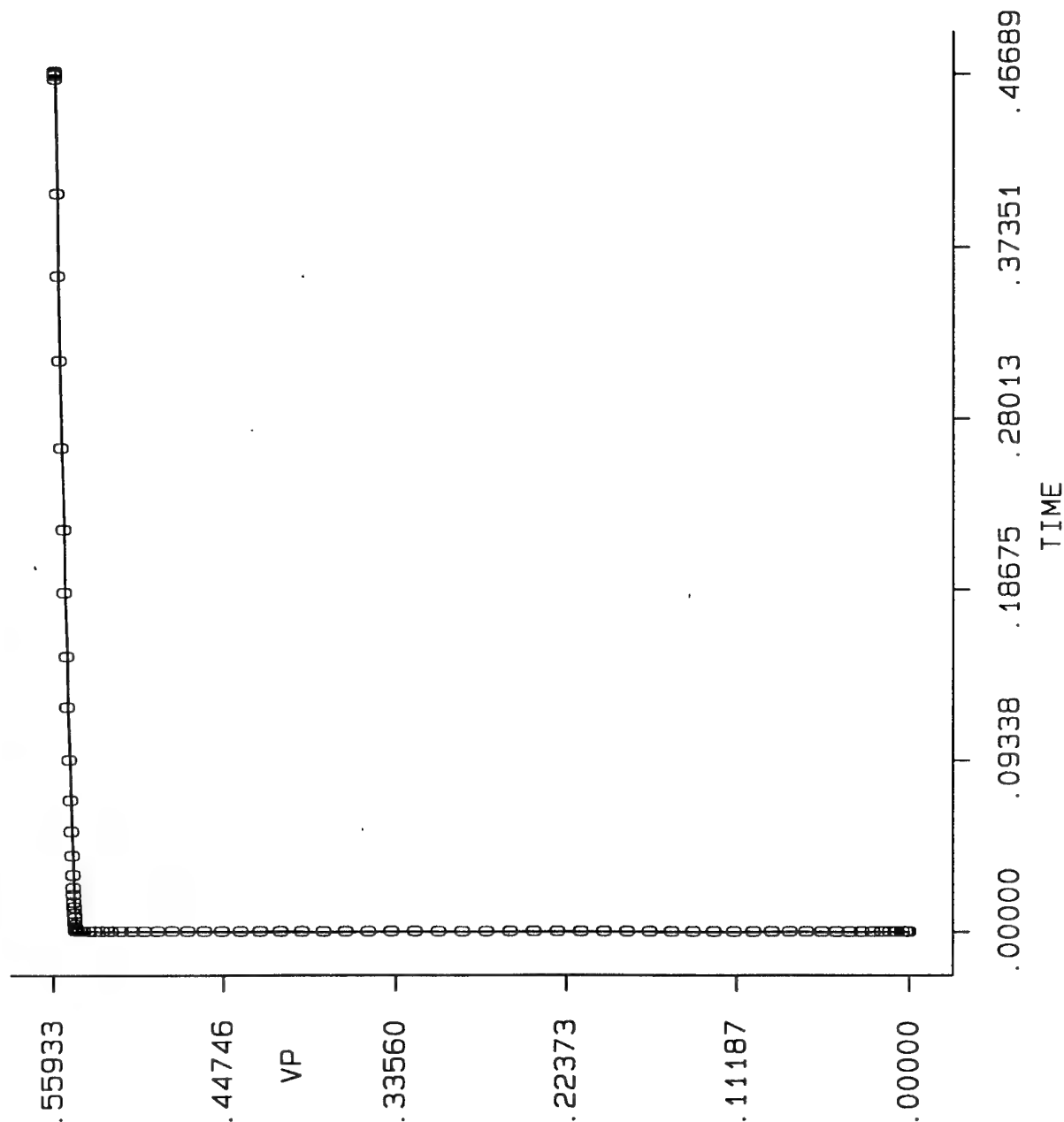
FIDAP 7.50

26 Jul 94

09: 45: 56



AIR BUBBLES IN WATER PARTICLE VELOCITY



PARTICLE
PATH PLOT

DISPERSED PHASE
PARTICLE UY

0 - # 1

SCREEN LIMITS

XMIN -.467E+02
XMAX .109E+04
YMIN -.237E+01
YMAX .100E+04

FIDAP 7.50

26 Jul 94

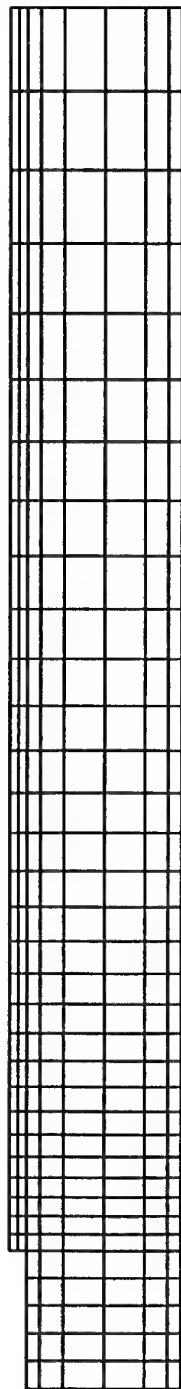
09: 58: 54

3.2 Spray Dryer

The fully coupled momentum, energy and mass transfer capabilities in FIDAP are presented in this example, which models the interaction between a flow of air and evaporating water droplets injected in the flow. The geometry and some of the results of the computation are shown in the following figures. The water droplets are injected on the top of the computational domain and have a lower temperature than the fluid, while the velocity is much higher. Droplets are also allowed to evaporate and the combined effect of evaporation and convective heat transfer determines the final temperature: the fluid temperature on its turn changes throughout the domain due to the source term in the energy equation. The mass lost by the droplets as result of the evaporation process is accounted for in the source term for a species equation. The vapor distribution is then computed as a transported variable. The problem is solved in a non-dimensional form.

COMPUTATIONAL DOMAIN

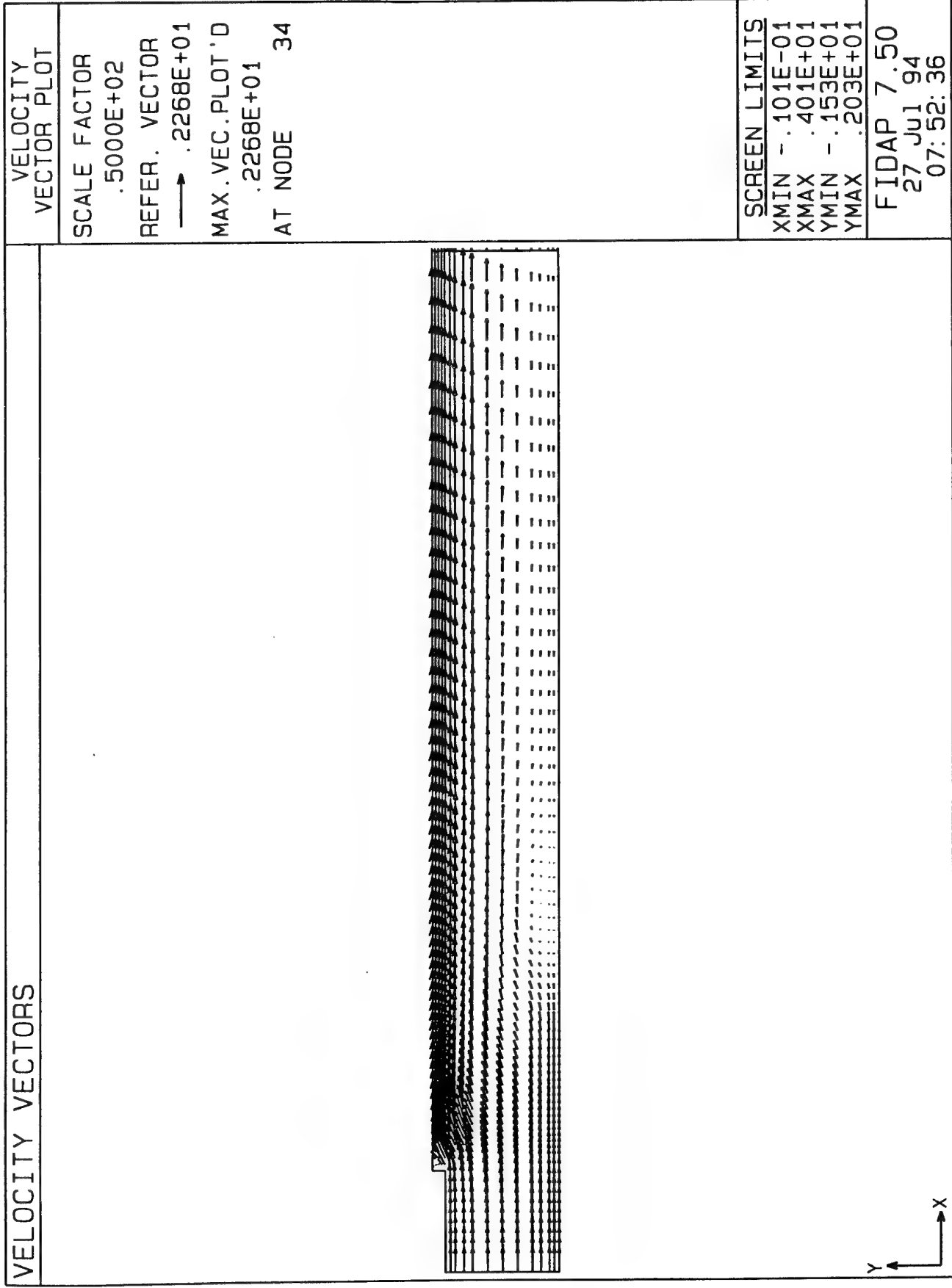
ELEMENT
MESH PLOT

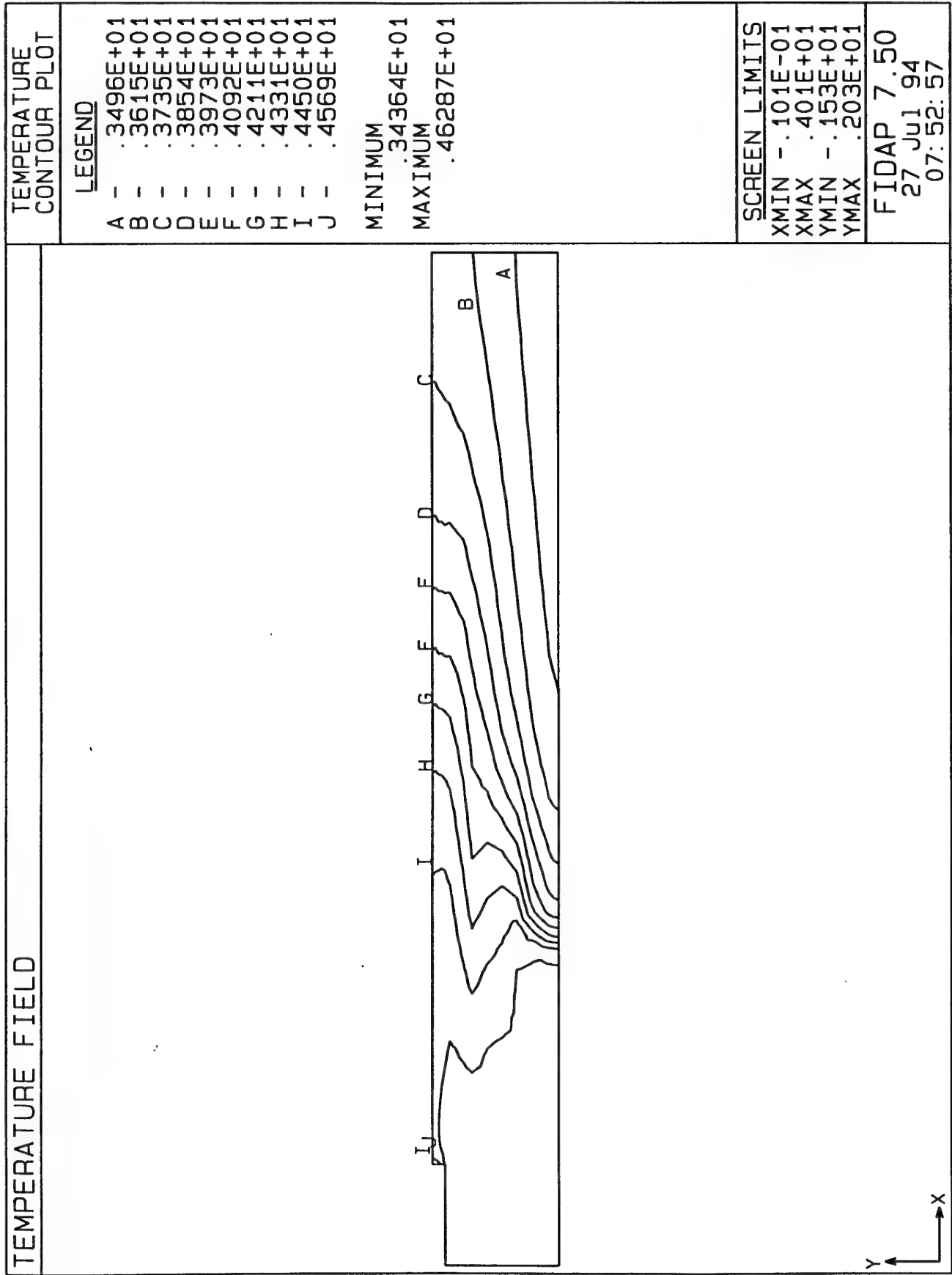


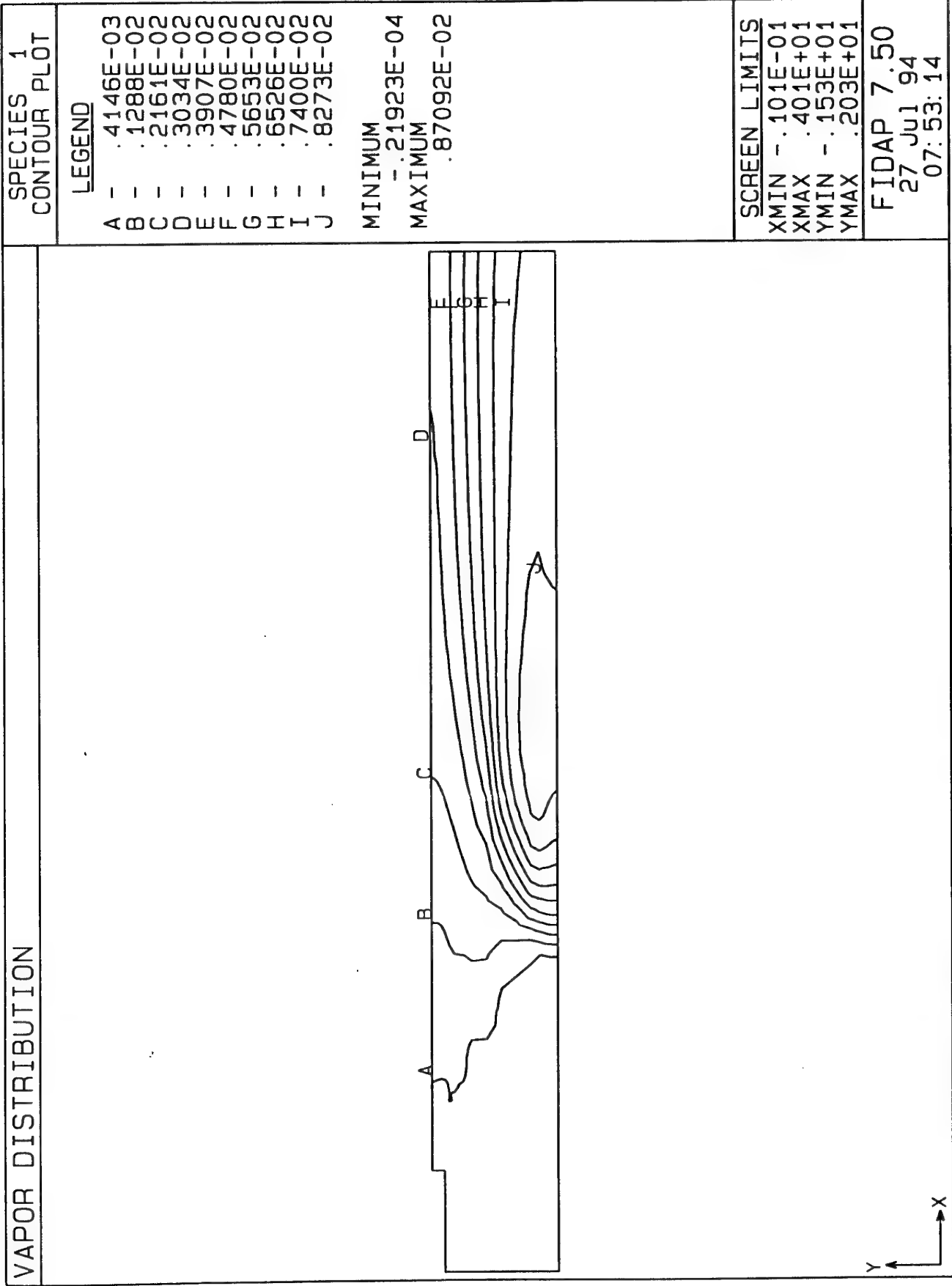
SCREEN LIMITS
 XMIN -.101E-01
 XMAX .401E+01
 YMIN -.153E+01
 YMAX .203E+01

FIDAP 7.50
 27 Jul 94
 07:51:48

VELOCITY VECTORS







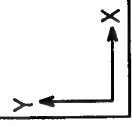
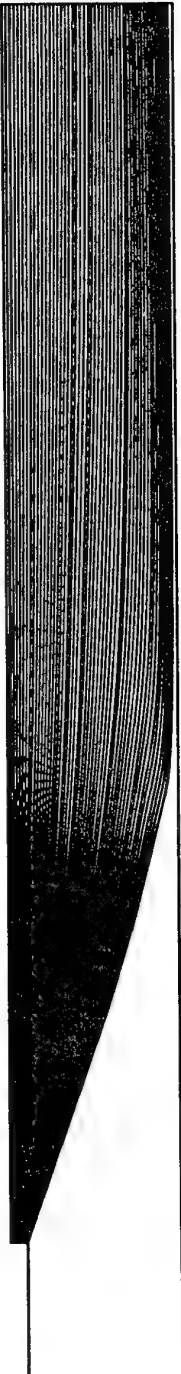
PARTICLE PATHS

PARTICLE
PATH PLOT

PARTICLE PATH

FROM TIME:
.0000E+00

TO TIME:
.1159E+01



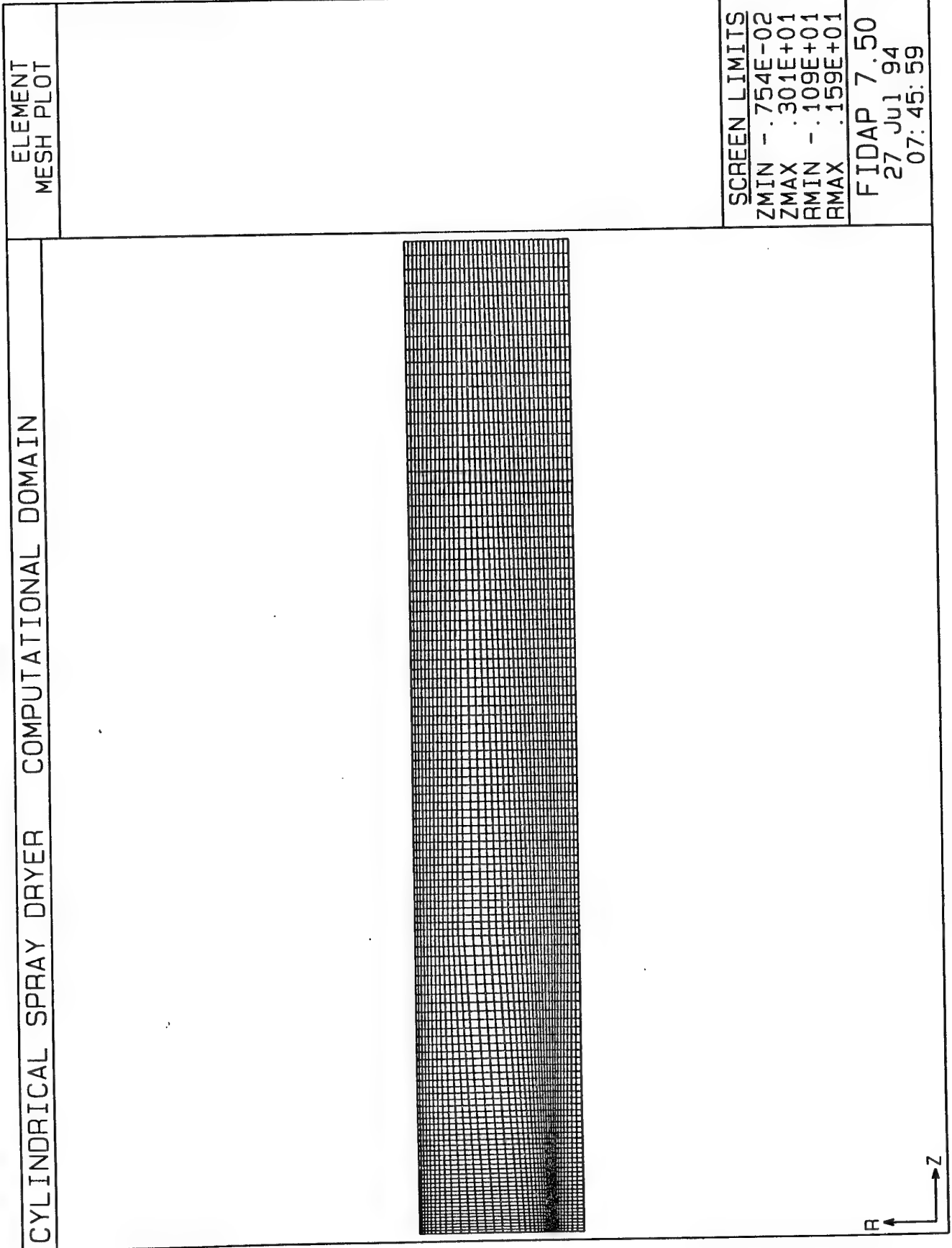
SCREEN LIMITS
XMIN -.101E-01
XMAX .401E+01
YMIN -.153E+01
YMAX .203E+01

FIDAP 7.50
27 Jul 94
07:53:35

3.3 Turbulent Cylindrical Spray Dryer

In the context of FIDAP simulations the term "cylindrical" refers to the kind of problems where three components of velocities are solved in a two-dimensional geometry (r - z). For the purpose of particle tracking the third component of velocity, which does not appear in the particle paths, is computed and used in the context of the two-way coupling capabilities. Furthermore the corrective terms for cylindrical geometries (centrifugal and Coriolis terms) are added in the momentum equations for the radial and axial direction.

In this example the particles (water droplets) are assumed to enter in the domain in a primary jet with higher velocities and lower temperature respect to the secondary air. The effect of turbulent fluctuations is to increase the spreading of the droplets. This spreading mechanism increases the thermal exchange due to the enhanced contact with the external (hotter) jet. No mass transfer model has been accounted for and the only term in the particle energy equation is the convective heat transfer due to the temperature difference between the two phases.



CYLINDRICAL SPRAY DRYER COMPUTATIONAL DOMAIN

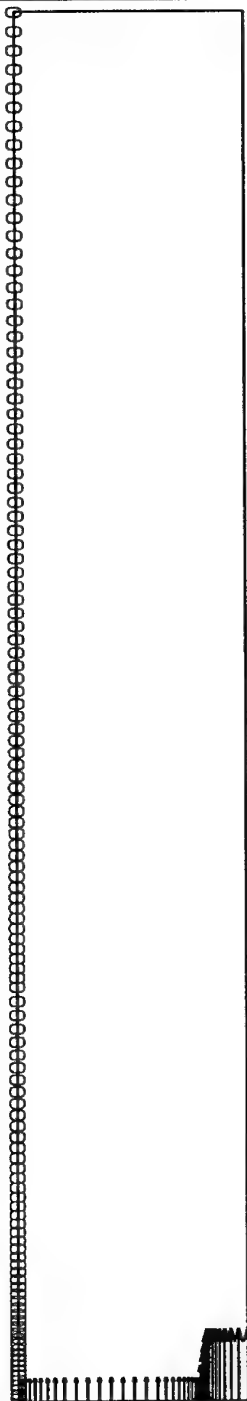
ELEMENT
EDGE PLOT

BCNODE - U

SCREEN LIMITS

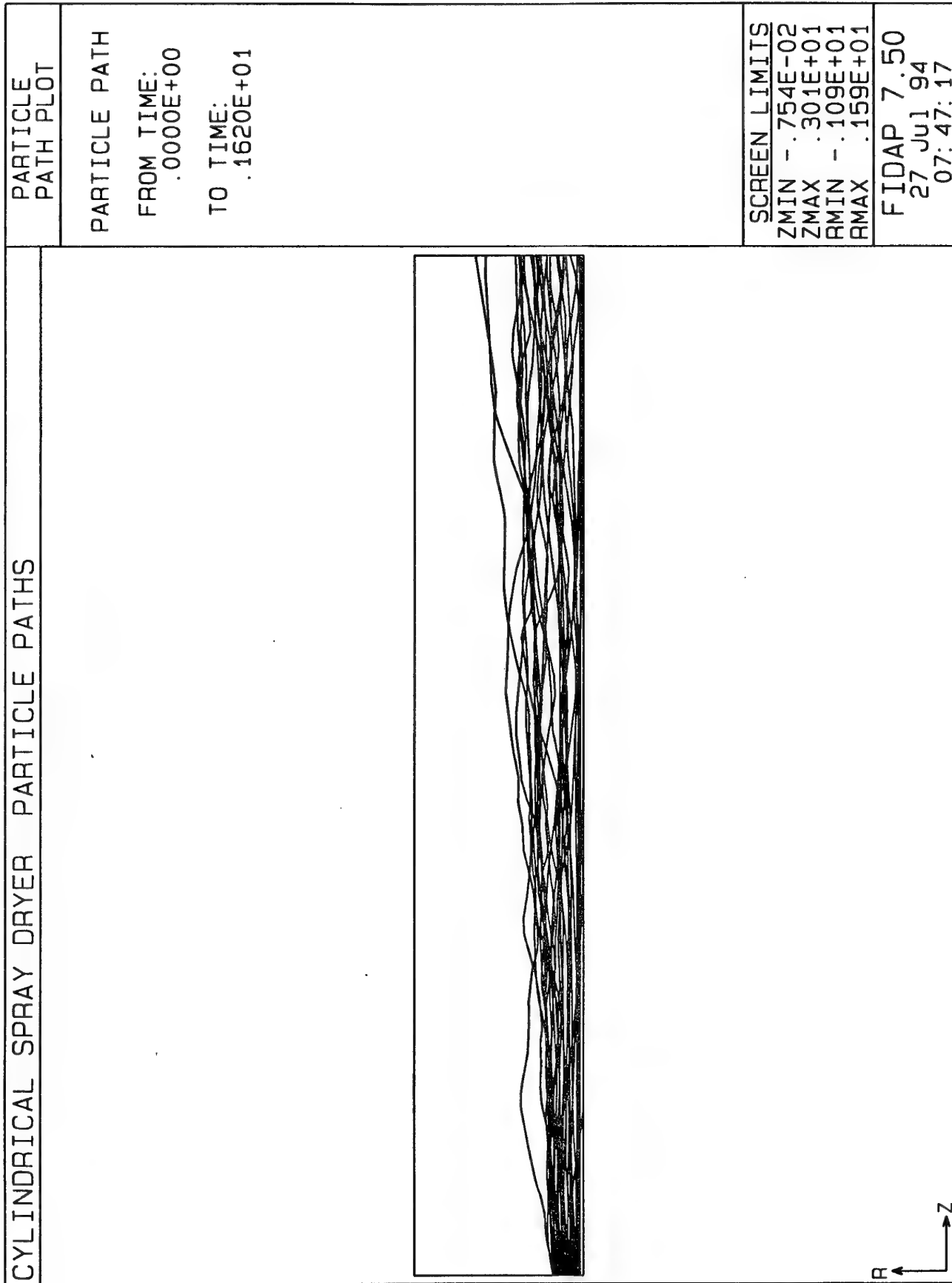
ZMIN - .754E-02
ZMAX .301E+01
RMIN - .109E+01
RMAX .159E+01

FIDAP 7.50
27 Jul 94
07: 45: 54

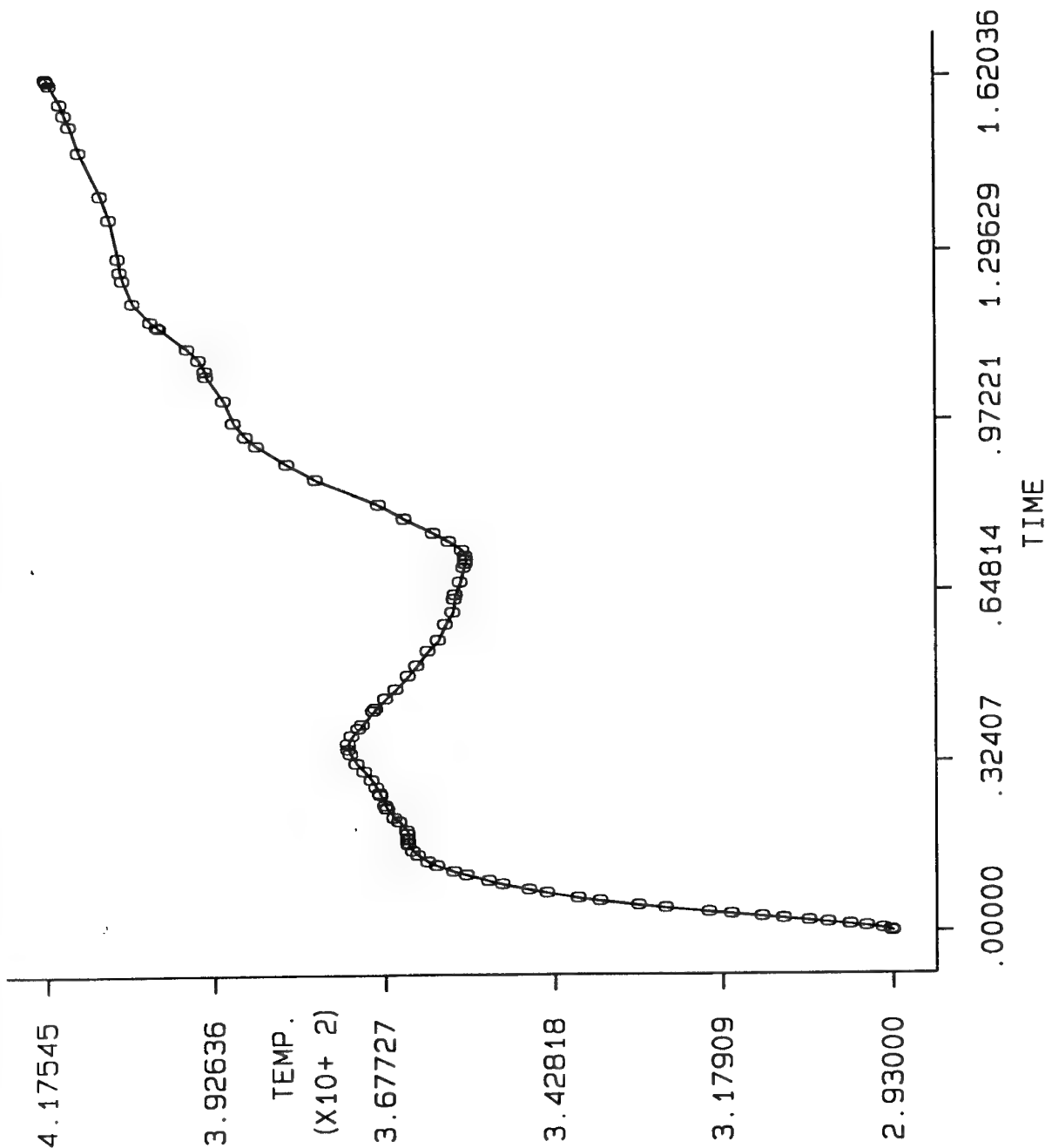


R
Z

CYLINDRICAL SPRAY DRYER PARTICLE PATHS



CYLINDRICAL SPRAY DRYER TEMPERATURE HISTORY



PARTICLE
PATH PLOT

DISPERSED PHASE
PARTICLE TEMP.

0 - # 30

SCREEN LIMITS

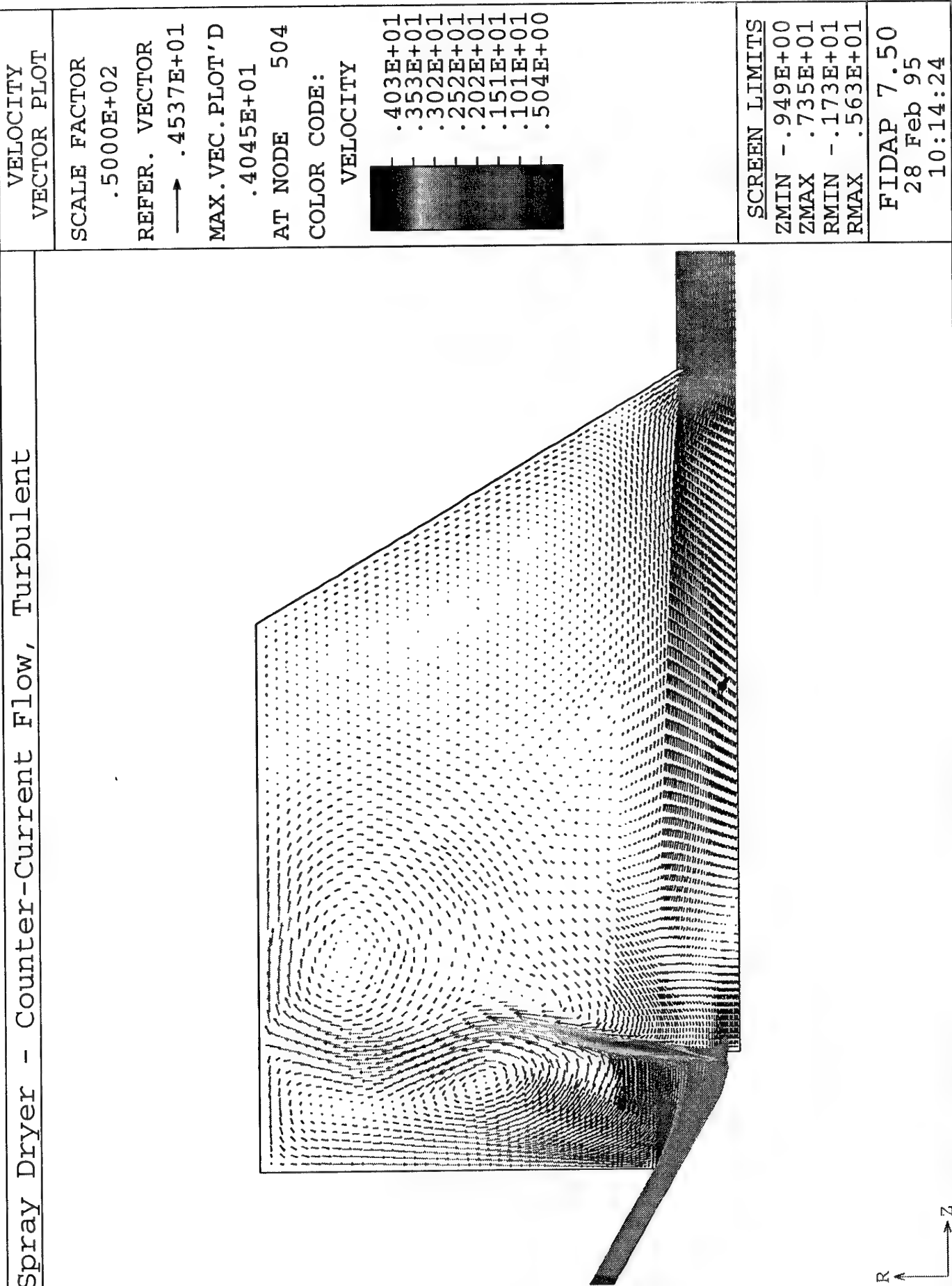
ZMIN -.453E+02
ZMAX .109E+04
RMIN -.226E+01
RMAX .100E+04

FIDAP 7.50
27 Jul 94
07:49:12

3.4 Fully Coupled Counter-Current Spray Dryer

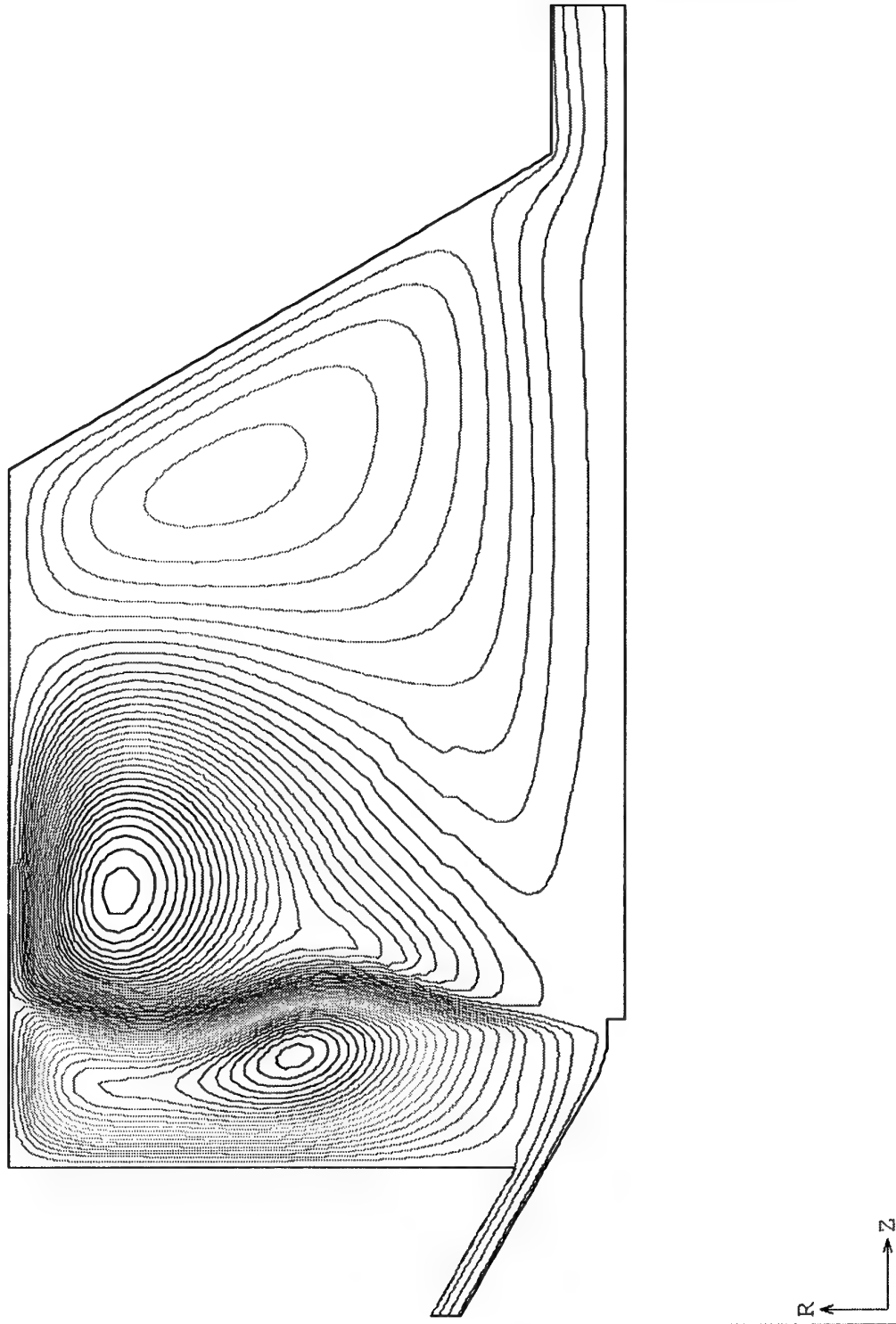
In this example, particles are injected from a spinning disk atomizer, sending them across the incoming air jet. Both the air flow and the particles have a tangential velocity component. The initial humidity factor of the particles is 80%. The air flow rate is about 36,000 kg/hr at 380°C, and the dry particle flow rate is about 1,500 kg/hr at 30°C. A gaussian distribution of particle diameter about 100 micron is used. Particle trajectories indicate that the large particles are caught in the recirculation near the top of the chamber and are likely to stick to the top before they have a chance to dry. Also, some smaller ones are caught in the lower recirculation region and trickle down the cone, and are likely to cause accumulation at the bottom part of the cone. The temperature and the humidity fraction (species contours) are also shown in the figures.

Spray Dryer - Counter-Current Flow, Turbulent



Spray Dryer - Counter-Current Flow, Turbulent

STREAMLINE CONTOUR PLOT	
LEGEND	
--	-.1038E+02
--	-.9236E+01
--	-.8473E+01
--	-.7329E+01
--	-.6567E+01
--	-.5423E+01
--	-.4660E+01
--	-.3516E+01
--	-.2754E+01
--	-.1610E+01
--	-.8470E+00
--	.2970E+00
--	.1060E+01
--	.2204E+01
--	.2966E+01
--	.4110E+01
--	.4873E+01
--	.6017E+01
--	.6779E+01
--	.7923E+01
**SEE PRINTOUT	
MINIMUM	-.10952E+02
MAXIMUM	.81140E+01
SCREEN LIMITS	
ZMIN	-.949E+00
ZMAX	.735E+01
RMIN	-.173E+01
RMAX	.563E+01
FIDAP 7.50	
28 Feb 95	
10:16:24	



Spray Dryer - Counter-Current Flow, Turbulent

PARTICLE
PATH PLOT

PARTICLE PATH

FROM TIME:
.0000E+00

TO TIME:
.4000E+02

SCREEN LIMITS

ZMIN -.949E+00

ZMAX .735E+01

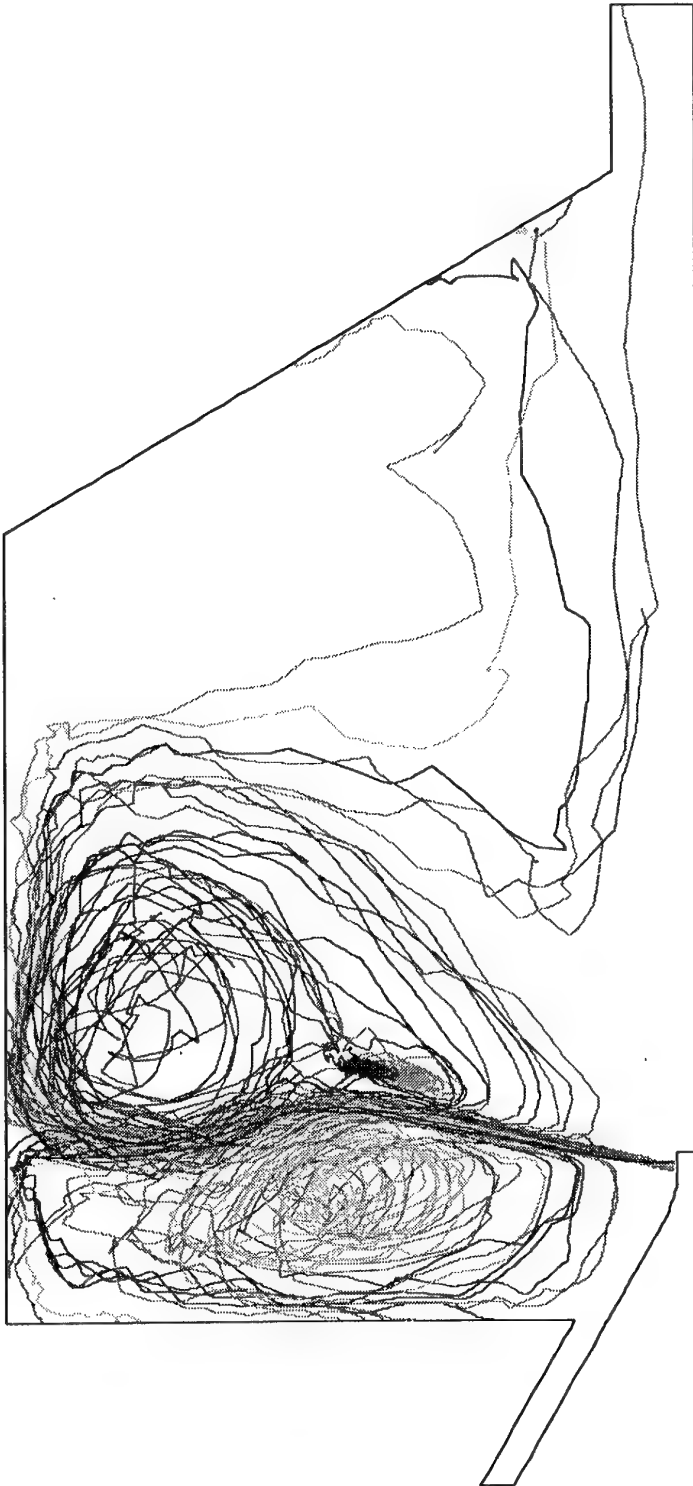
RMIN -.173E+01

RMAX .563E+01

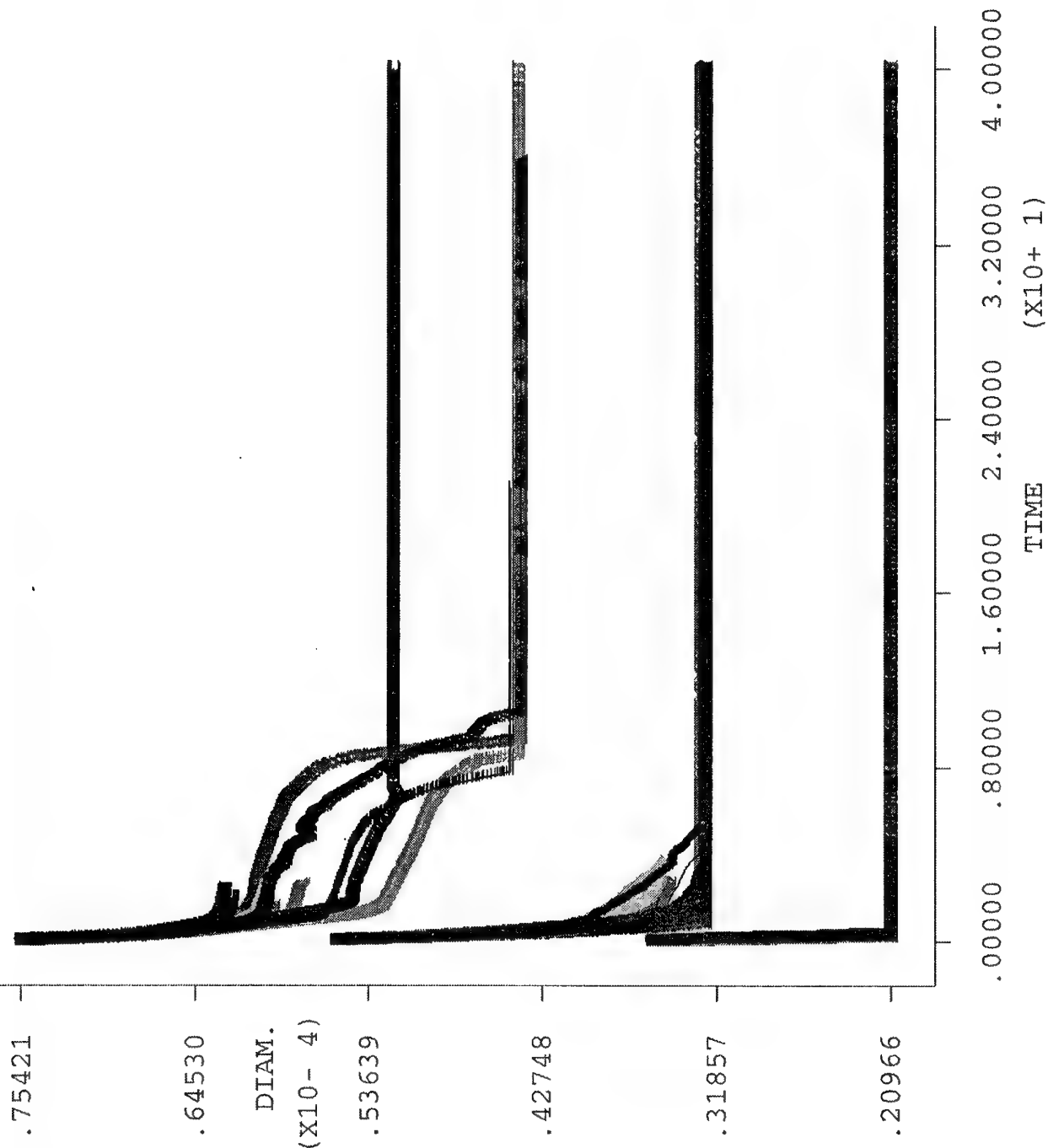
FIDAP 7.50

28 Feb 95

10:11:30

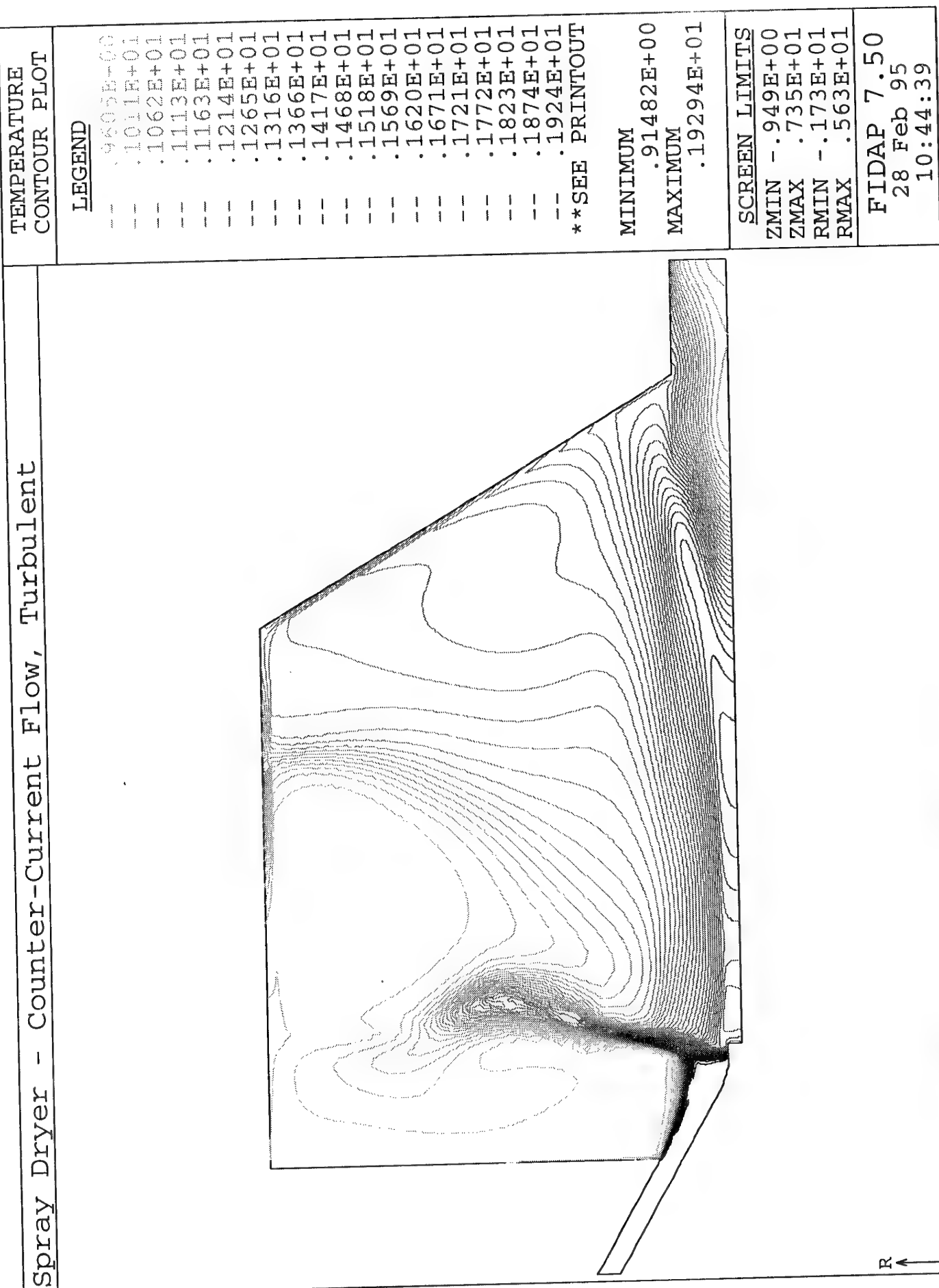


Spray Dryer - Counter-Current Flow, Turbulent



PARTICLE PATH PLOT	
DISPERSED PHASE	DIAMETER
A - #	1
B - #	2
C - #	4
D - #	6
E - #	8
F - #	10
G - #	11
H - #	13
I - #	15
J - #	17
K - #	19
L - #	20
M - #	22
N - #	24
O - #	26
P - #	28
Q - #	29
R - #	31
S - #	33
T - #	35
SCREEN LIMITS	
ZMIN	-.436E+02
ZMAX	.109E+04
RMIN	-.563E+00
RMAX	.100E+04
FIDAP 7.50	
28 Feb 95	
10:14:04	

Spray Dryer - Counter-Current Flow, Turbulent



TEMPERATURE
CONTOUR PLOT

LEGEND

- .9605E+00
- .1011E+01
- .1062E+01
- .1113E+01
- .1163E+01
- .1214E+01
- .1265E+01
- .1316E+01
- .1366E+01
- .1417E+01
- .1468E+01
- .1518E+01
- .1569E+01
- .1620E+01
- .1671E+01
- .1721E+01
- .1772E+01
- .1823E+01
- .1874E+01
- .1924E+01

**SEE PRINTOUT

MINIMUM

.91482E+00

MAXIMUM

.19294E+01

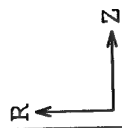
SCREEN LIMITS

- ZMIN -.949E+00
- ZMAX .735E+01
- RMIN -.173E+01
- RMAX .563E+01

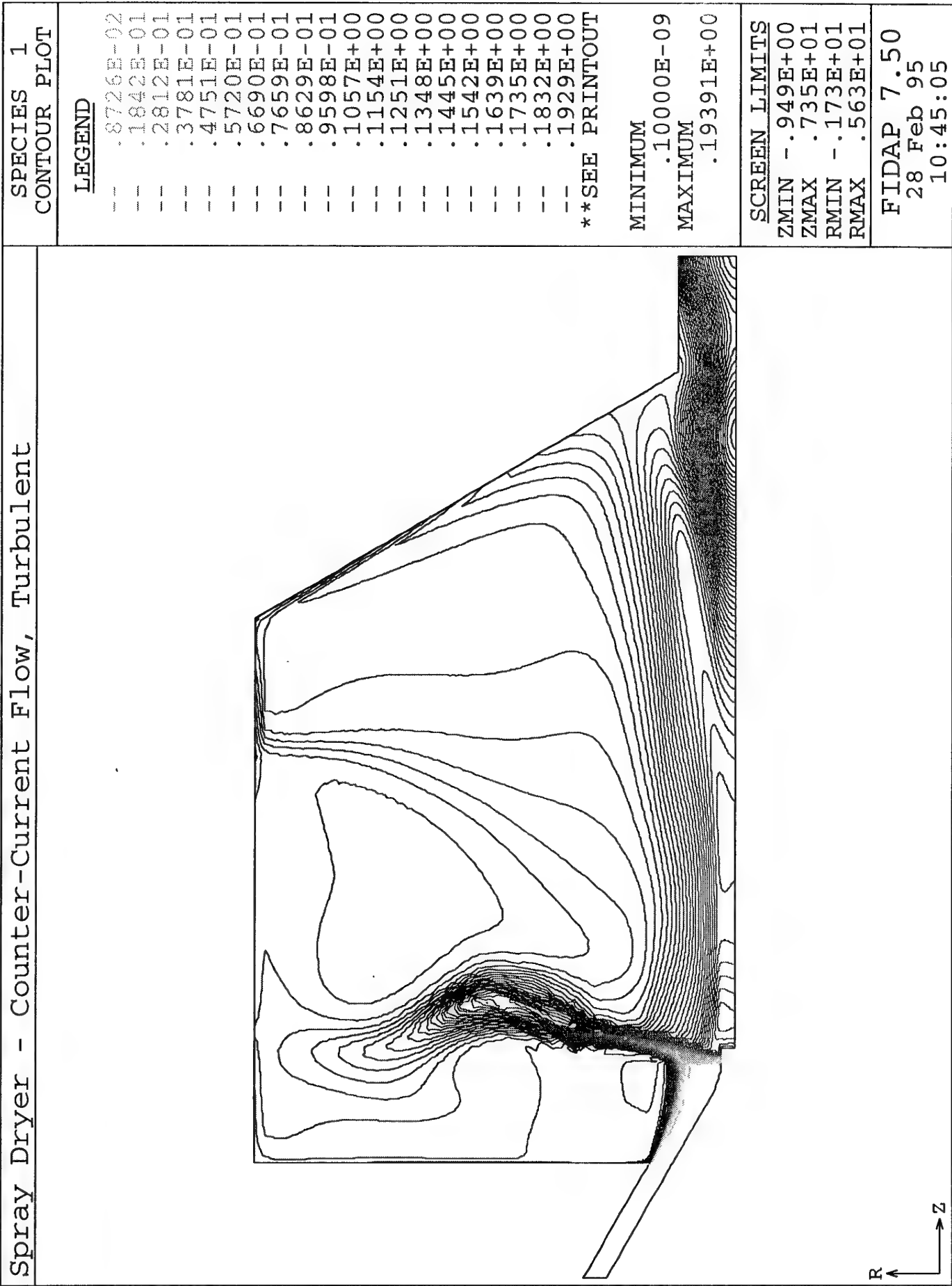
FIDAP 7.50

28 Feb 95

10:44:39



Spray Dryer - Counter-Current Flow, Turbulent



von Karman Institute for Fluid Dynamics

Lecture Series 1995-03

INDUSTRIAL COMPUTATIONAL FLUID DYNAMICS

April 3 - 7, 1995

NUMERICAL SIMULATION IN NON-NEWTONIAN FLUID MECHANICS

M.J. Crochet

POLYFLOW S.A., Belgium

1. Introduction

Rheology is defined as "the study of the deformation and flow of matter". This definition would allow a consideration of all materials, including the classic extremes of Newtonian fluids like water and elastic solids like rubber. However, these extremes are usually considered to be outside the scope of rheology and attention is restricted to materials that can be classified as "viscoelastic". If such materials are basically solid-like they are called "viscoelastic solids" and if they exhibit liquid-like behaviour they are now usually called "elastic liquids". An important class of industrial liquids are not strongly viscoelastic and yet possess features which cannot be associated with classical Newtonian behaviour. These so-called inelastic non-Newtonian liquids are certainly regarded as being within the scope of rheology and together with elastic liquids, form the basis for the important modern research field called non-Newtonian Fluid Mechanics. Most liquids of industrial interest are non-Newtonian. Multigrade oils, liquid detergents, paints, printing inks, contact adhesives and molten plastics are just some of the examples that come readily to mind, but the complete list would be endless.

It is useful at this stage to introduce the concept of Deborah number defined as

$$De = \lambda / T \quad (1)$$

where λ is a characteristic (relaxation) time of the material and T is a characteristic time of the flow process under consideration. λ would be zero for a Newtonian liquid and infinite for an elastic solid. For industrial materials λ might be expected to vary from 10^{-6} s for lubricating oils to seconds for many molten plastics. The concept of the Deborah number is useful since it highlights the fact that it is not only the material's relaxation time, λ , which determines material behaviour but also the time-scale of the deformation process. So, for example, a mobile liquid with a very modest relaxation time exposed to a very fast deformation process can lead to a high Deborah number, resulting in its behaviour appearing solid-like.

Computer-aided processing has made considerable advances over the last ten years. A better understanding of mathematical models for polymer behaviour has provided the necessary tools for progress in numerical analysis. Simultaneously, the fact that today's workstations calculate faster than super-computers of the early 80's has generated the possibility of solving problems of a size comparable to what is found in practical applications.

A number of polymer processes have already received attention with a view to specific improvements. In extrusion, for example, one may wish to calculate the flow between the rotating screw and the barrel in order to obtain better mixing or a more homogeneous temperature distribution. In extrusion too, die design is a central problem which can be formulated as follows : what should be the shape of the die in order to obtain an extrudate with a pre-assigned profile ? In blow moulding, a complete calculation should lead to a more homogeneous (or at least appropriate) thickness distribution in the final product. In spinning, numerical simulation allows us to calculate stresses in the jet, temperature distribution, free surface shapes. Similar questions are addressed in many other processes such as coextrusion, compression moulding, film casting, film blowing, etc.

In section 2, we examine some experimental observations which summarize typical non-Newtonian effects. In section 3, we briefly review the concepts of rheometry which allow us to characterize material properties. In section 4, we give a summary of mathematical models. Sections 5 and 6 are devoted to numerical methods, first for generalized Newtonian flow and next for viscoelastic applications, which are typical of polymer flow. We concentrate in particular on a number of industrial flows where numerical simulation is of considerable help for process improvement.

2. Experimental observations

In order to highlight the type and scale of the problems of current interest, it may be helpful to introduce a specific flow which has been taken as one of the benchmark problems by researchers in the field. Consider a 4:1 axisymmetric contraction in which a fluid is forced to flow from one capillary into another of smaller diameter through an abrupt contraction, the flow being generated by a pressure gradient. Of immediate concern are the general features of the flow in the case of rheologically complex fluids. Figure 1 shows a well-documented progression of the flow field as the pressure gradient is increased for one particular polymer solution [1]. The appearance of large vortices is a classic example of so-called vortex enhancement, which is directly attributable to viscoelasticity.

Another feature of interest relates to the extra pressure loss involved in forcing the elastic liquid through the contraction. This is studied through the so-called Couette correction, a typical schematic example of which is included in figure 2. The slight drop in the Couette correction at low values of De is difficult to measure experimentally, but numerical codes testify to its existence. The large increase in the Couette correction at high values of De is very easy to measure experimentally but provides significant challenges to numerical simulators as they attempt to model contraction flows for high elastic liquids.

Free-surface flow problems are also of interest in rheological computation. To illustrate one of the most popular flows we refer to so-called die swell, exhibited by an elastic liquid as it emerges from a capillary. It is well known that for a Newtonian liquid the diameter of the issuing liquid is either slightly greater than or slightly less than the diameter of the capillary, depending on the magnitude of the Reynolds number. For an elastic liquid, the ratio of the jet to capillary diameter can be significantly greater than unity and values as high as four have been observed. In some cases, "delayed die swell" can occur, as illustrated in figure 3. Only recently have numerical techniques been able to handle the "change of type" associated with the governing equations (see later).

Another well-known free-surface phenomenon in rheology is the so-called Weissenberg effect, which is demonstrated in figure 4. In the case of Newtonian liquids like water our expectation would be that the height of the free surface would increase with the radius in order to compensate for centrifugal forces, and this is indeed found to be the case. However, for elastic liquids, viscoelastic effects, manifested through so-called "normal-stress" effects result in a substantial rise in the free surface near the rotating rod. This "rod climbing" is called the Weissenberg effect.

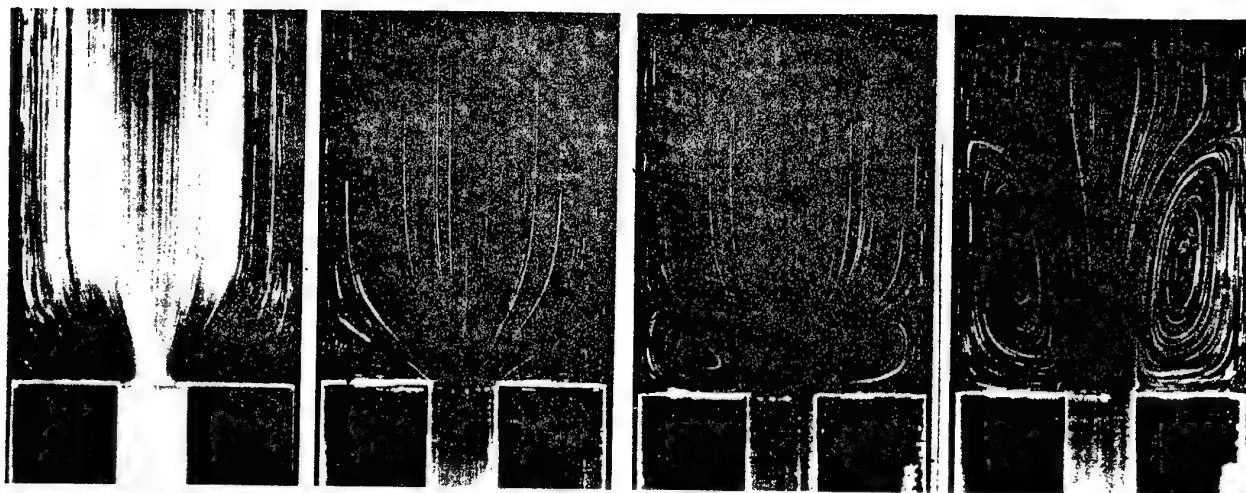


Figure 1. Vortex growth in a 4:1 axisymmetric contraction for 0.04 per cent polyacrylamide in corn syrup and water solution. The flow rate is progressively increased in moving through the sequence of photographs, the lowest flow rate being on the left [1].

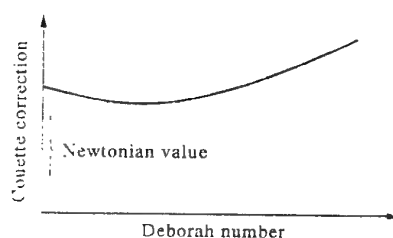


Figure 2. A schematic representation of the Couette correction as a function of the Deborah number for contraction flow.

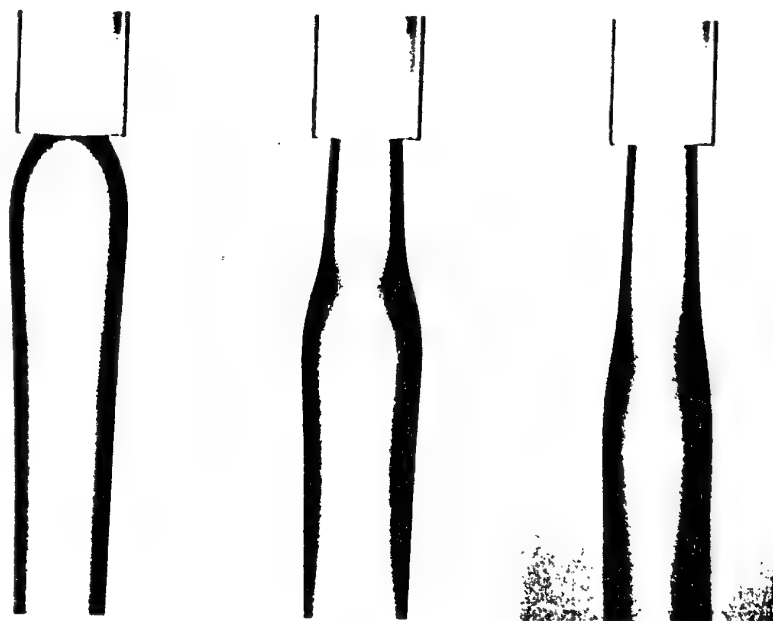


Figure 3. Delayed die swell for a 5 per cent aqueous solution of polyacrylamide. The flow rate is increased in moving through the sequence of photographs. As the flow rate increases, the conflict between fluid inertia and viscoelasticity is apparent and the swelling phenomenon is delayed [38], [43].

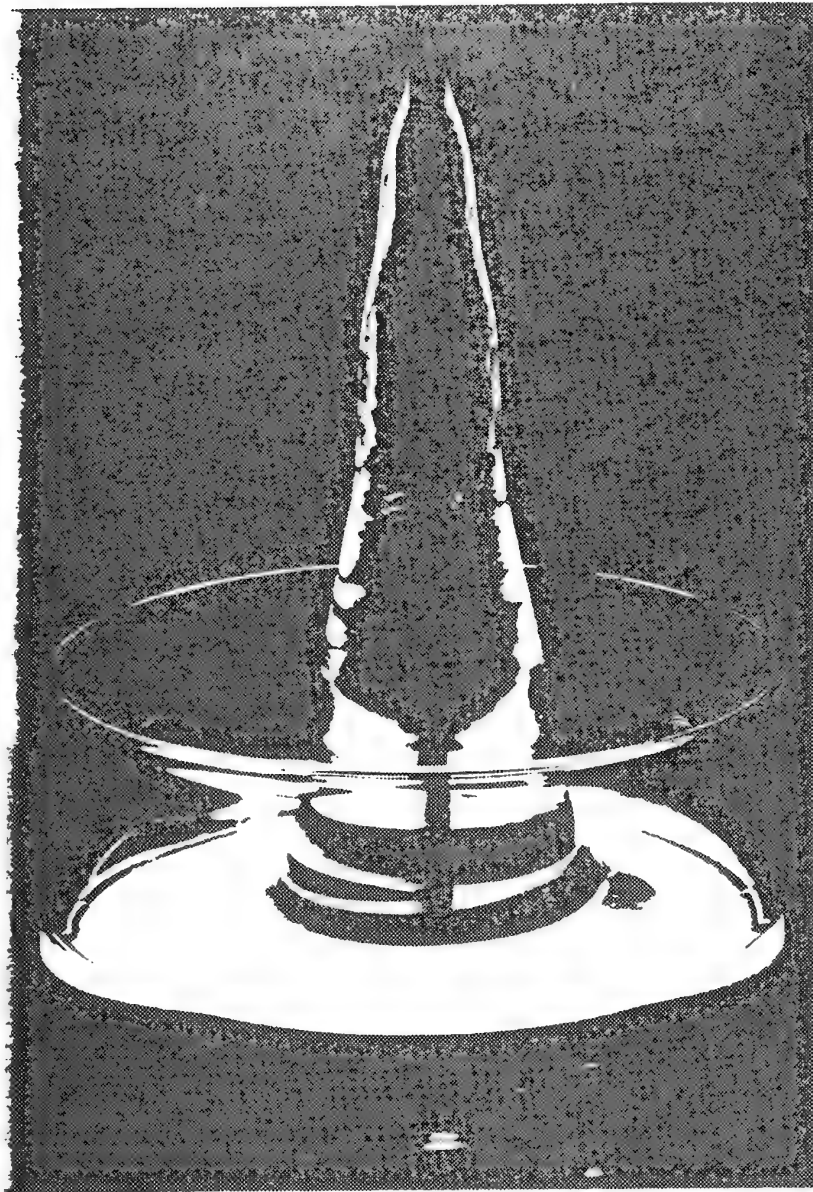


Figure 4. The Weissenberg effect shown for a solution of polyisobutylene (Oppanol B200) in polybutene [2].

3. Rheometry ¹

In Newtonian fluid mechanics, it is sufficient to know the value of the shear viscosity of the fluid under consideration as a function of temperature. Non-Newtonian fluids are much more complex. The selection of a mathematical model requires the identification of a number of material properties. As a good introduction to rheometry, the reader is referred to Barnes et al [2].

3.1. Shear flow

Viscoelastic fluids are endowed with a peculiar property called "normal stresses". Let us consider in figure 5 a simple shear flow : a viscoelastic fluid, say a polymer solution, is sheared between a fixed bottom plate and an upper one sliding at a constant velocity U . The shear rate is given by U/d , where d is the thickness of the fluid layer. Isaac Newton, writing in the *Principia* in 1687, pointed out that the fluid motion requires a tangential shearing force at the layer surface which is proportional to the shear rate $\dot{\gamma} = U/d$; such a "linear" behavior characterizes the Newtonian fluid.

The situation is much more complex in most real fluids. First, the shearing force is generally not proportional to the shear rate; most polymer fluids exhibit "shear-thinning", that is, the viscosity is a decreasing function of the shear rate. Secondly, most fluids exhibit what is commonly called "normal stress differences". In figure 5, we have indicated a set of orthogonal Cartesian axes. For a Newtonian fluid, the shearing motion requires only the application of an appropriate shear stress. For a viscoelastic fluid, the same flow requires normal stresses which differ in the x , y and z directions. More practically, a fluid layer of thickness d cannot be sheared unless it is acted upon by a normal force on its upper surface.

This flow can be conveniently expressed in terms of Cartesian coordinates in the following form :

$$v_x = \dot{\gamma} y, \quad v_y = v_z = 0 \quad (2)$$

where v_x , v_y and v_z are the velocity components and $\dot{\gamma}$ is a constant shear rate. For a non-Newtonian fluid, the corresponding stress distribution can be written in the form

¹ This section on rheometry is borrowed from "Rheometry: general concepts and measurement techniques", K. Walters, in Newtonian fluid mechanics, Lecture series 1994-03, von Karman Institute for Fluid Dynamics.

$$\sigma_{xy} = \sigma = \eta(\dot{\gamma}) \dot{\gamma}, \sigma_{xz} = \sigma_{yz} = 0, \quad (3)$$

$$\sigma_{xx} - \sigma_{yy} = N_1(\dot{\gamma}), \sigma_{yy} - \sigma_{zz} = N_2(\dot{\gamma}),$$

where σ is the shear stress, η the shear-dependent viscosity and N_1 and N_2 are the first and second normal stress differences, respectively. Rheometers can now be purchased to measure the viscosity $\eta(\dot{\gamma})$ over the complete range of interest, but at least three different instruments would be required for that purpose. For shear thinning materials, the general shape of the viscosity curve is shown in figure 6. The curves indicate that in the limit of very low shear rates (or stresses) the viscosity is constant, whilst in the limit of high shear rates the viscosity is again constant, but at a lower level. Equations that predict the shape of the general flow curve will be reviewed in the next section. Shear thickening is encountered in some non-Newtonian fluids. In almost all known cases of shear thickening, there is a region of shear thinning at low shear rates.

Viscosity can be measured using either rotational or capillary (or slit) viscometers. In rotational instruments, the geometry is usually either concentric cylinder, cone and plate or parallel plate.

So far as the normal-stress differences are concerned, typical behaviour for a polymer solution is provided in figure 7. The first normal stress difference can be much higher than the shear stress and can often be represented by a power-law equation (like the shear stress). The second normal stress difference is usually negative and much smaller than N_1 . As a rough guide, one can take $N_2 = -0.1N_1$. The Weissenberg effect and extrudate swell are the two most observable consequences of normal stress differences. Cone and plate flow (and to a lesser extent torsional flow) are the preferred flows for determining the normal stress differences.

3.2. Oscillatory shear

Small amplitude oscillatory shear flow is used to determine the functions relevant to linear viscoelasticity. Considering the system of figure 5, we apply an oscillatory shear rate of the form $\dot{\gamma}(t) = \dot{\gamma}^* \exp(i\omega t)$; the stress response is given by $\sigma(t) = \sigma^* \exp(i\omega t)$. We shall concentrate on the complex dynamic viscosity η^* , which is usually expressed in the form

$$\eta^* = \sigma^* / \dot{\gamma}^* = \eta' - \frac{iG'}{\omega} , \quad (4)$$

where η' is the dynamic viscosity and G' the dynamic rigidity.

Available controlled stress and controlled strain rate rheometers have been adapted to perform oscillatory shear experiments. In the controlled strain rate techniques, the sample is usually contained between a cone and plate or parallel plates. One member undergoes forced harmonic oscillations about its axis, while the other member is constrained by a torsion wire. The measured quantities are the amplitude ratio and phase lag between the motion of the two instrument members. These can be immediately converted into complex viscosity data provided non linear effects are not present and fluid inertia is not too strong. Typical dynamic data for a non-Newtonian liquid are given in figure 8.

3.3. *Extensional flow*

The subject of extensional flow received scant attention until the mid 1960's. Up to that time rheology was dominated by shear flows. In the last twenty years or so the situation has changed dramatically with the dual realization that extensional flow is of significant relevance in many practical situations and also that elastic liquids often exhibit dramatically different extensional flow characteristics from Newtonian liquids.

Various flows of relevance to polymer processing have strong extensional components. The turbulent drag phenomenon of drag reduction is also thought to be due to the extensional viscosity characteristics of the polymer solutions involved. These are just some examples of the importance of extensional flow within an industrial context. The subject is also important in that it provides a critical test of any proposed constitutive equation for rheologically complex fluids. To emphasise the second point made above it is only necessary to say that the extensional viscosity behavior is frequently qualitatively different from that of the shear viscosity. So, for example, highly elastic polymer solutions that possess a shear viscosity that decreases monotonically (showing shear-thinning) often exhibit an extensional viscosity that increases dramatically with strain rate (showing so-called tension-thickening).

For the velocity field

$$v_x = \dot{\epsilon}x , v_y = -\frac{\dot{\epsilon}}{2}y , v_z = -\frac{\dot{\epsilon}}{2}z \quad (5)$$

where $\dot{\epsilon}$ is a constant extensional strain rate. The corresponding stress distribution can be conveniently written in the form

$$\sigma_{xx} - \sigma_{yy} = \sigma_{xx} - \sigma_{zz} = \dot{\epsilon} \eta_E(\dot{\epsilon}) \quad (6)$$

where η_E is the (uniaxial) extensional viscosity. In general it is a function of the extensional strain rate $\dot{\epsilon}$. It can be shown that

$$\eta_E(\dot{\epsilon}) = 3\eta(\dot{\gamma}), \text{ for } \dot{\epsilon} \text{ and } \dot{\gamma} \Rightarrow 0. \quad (7)$$

The ratio between extensional and shear viscosity is called Trouton's ratio. Its value is 3 for Newtonian fluids but it can be much higher for polymeric liquids.

It is generally agreed that it is much more difficult to measure extensional viscosity than shear viscosity, this being especially so for mobile liquids. There is therefore a gulf between the strong desire to measure extensional viscosity and the likely expectation of its fulfilment. For stiff systems like polymer melts the basic problem is one of maintaining a uniaxial flow for a sufficient time for the stress (in a controlled strain-rate experiment, or the strain rate (in a controlled stress experiment) to reach a steady state, thus enabling the steady extensional viscosity η_E to be determined. Under these circumstances, it is convenient to define a transient extensional viscosity $\eta_E(\dot{\epsilon}, t)$ which is clearly a function of time as well as strain rate. The problems of determining the extensional viscosity of mobile liquids like dilute polymer solutions are even more acute, but they are of a different type from those experienced for stiff systems. With mobile liquids, severe difficulties arise in trying to achieve a continuous extensional flow field which approximates that given in (5). In general the most that one can hope for is to generate a flow which is dominated by extension and then to address the problem of how best to interpret the data in terms of material functions that are rheologically meaningful.

Amongst the many methods that are currently being employed are the following :

- I Homogeneous stretching method. This is only applicable to stiff systems.
- II. Spinning. The flow is clearly dominated by extension. The basic problem is not one of experimentation, but with data interpretation.
- III Open-syphon. Similar to II.
- IV Lubricated flows. Experimentation is extremely difficult

V. Contraction flows. Experimentation is relatively easy. Data interpretation is open to criticism.

VI Stagnation-point devices. These are applicable to all liquids and the flow contains a strong element of extension. Data interpretation is not beyond criticism.

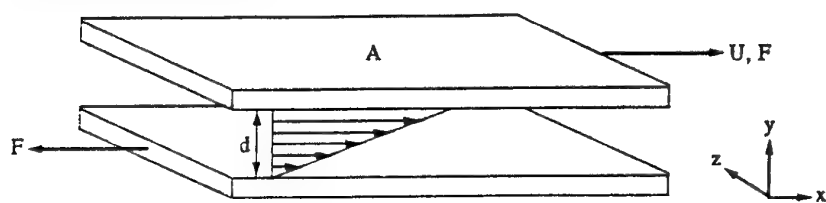


Figure 5. The geometry of a simple shear flow.

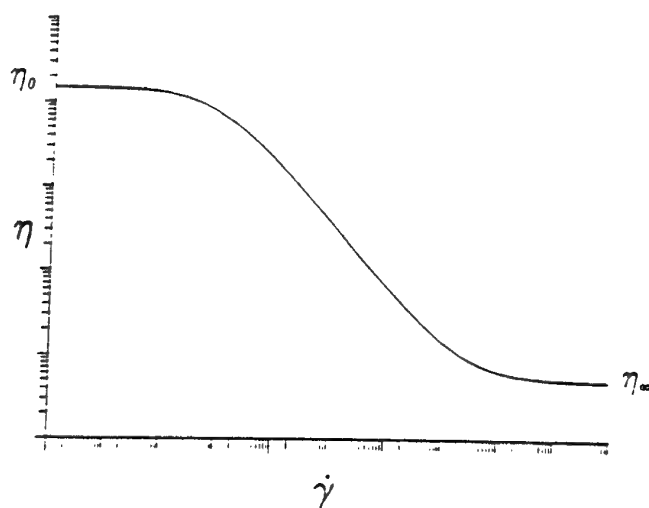


Figure 6. Schematic representation of the variation of viscosity with shear-rate for a shear-thinning fluid.

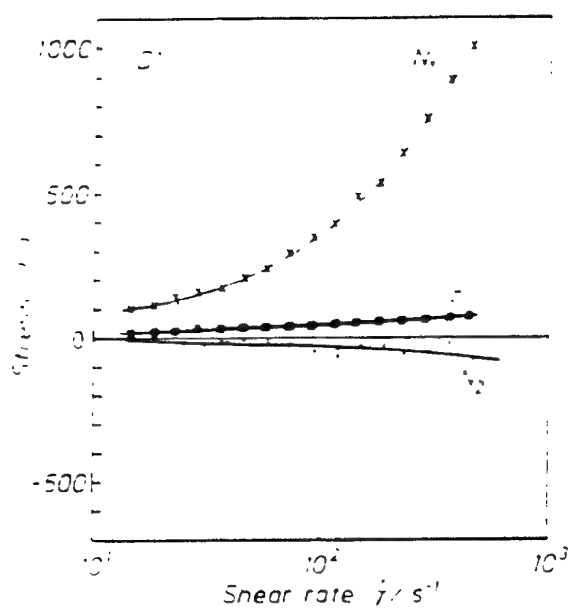


Figure 7. Typical viscometric data for a polymer solution.

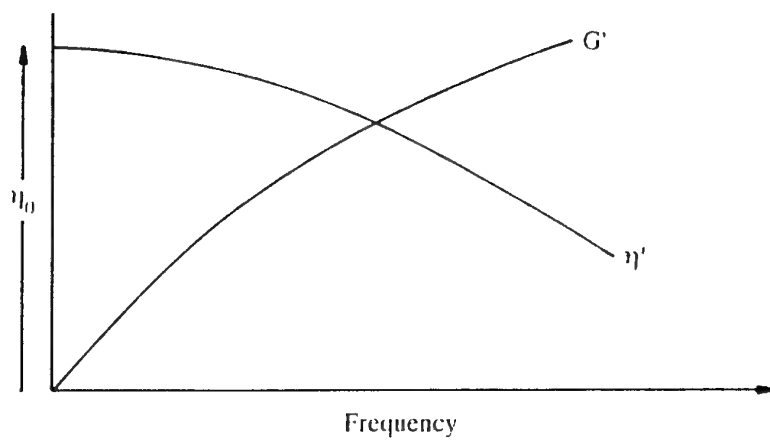


Figure 8. Typical dynamic data for an elastic liquid.

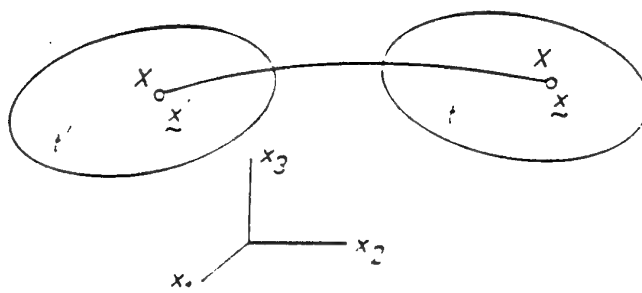


Figure 9. Motion of a continuum.

4. Mathematical model

The mathematical model consists of the field and constitutive equations together with appropriate boundary conditions. Let us limit ourselves in the present section to isothermal constitutive equations. Since we have assumed the fluid to be incompressible, the stress tensor σ is decomposed into an indeterminate pressure term $-p\mathbf{I}$ and the extra-stress tensor \mathbf{T} ,

$$\sigma = -p\mathbf{I} + \mathbf{T}. \quad (8)$$

The selection of an appropriate constitutive equation for \mathbf{T} is a central question in simulating the flow of complex fluids.

4.1. Generalized Newtonian flow

The simplest case is the Newtonian fluid for which

$$\mathbf{T} = 2\eta \mathbf{d}, \quad (9)$$

where \mathbf{d} is the rate of deformation tensor,

$$\mathbf{d} = [\nabla \mathbf{v} + \nabla \mathbf{v}^T]^{1/2}, \quad (10)$$

and η is the shear viscosity. The Newtonian model (9) is a low shear rate approximation of the dependence of the viscosity upon the rate of deformation tensor. With most fluids of practical importance in the study of flow processes, the viscosity depends upon the shear rate in a simple shear flow. Most commonly encountered is the shear-thinning behavior shown in figure 6. The viscosity is characterized by two Newtonian plateau zones for low and high shear rates; the corresponding viscosities may differ by several orders of magnitude. We write

$$\mathbf{T} = 2\eta(\dot{\gamma}) \mathbf{d} \quad (11)$$

where $\dot{\gamma}$ is the shear rate. For general flows, we must replace $\dot{\gamma}$ in (11) by an appropriate invariant of \mathbf{d} in (10) which reduces to $\dot{\gamma}$ in a simple shear flow. Satisfying such a condition is the expression

$$II_d = (2 \operatorname{tr} \mathbf{d}^2)^{1/2}. \quad (12)$$

The constitutive equation of the generalized Newtonian fluid is then given by

$$\mathbf{T} = 2\eta (\mathbf{II}_d) \mathbf{d} . \quad (13)$$

There exist several types of constitutive equations for characterizing generalized Newtonian fluids. Their name defines in fact the dependence of η upon $\dot{\gamma}$ at a fixed temperature. For the power-law fluid we have, at a reference temperature,

$$\eta = K \dot{\gamma}^{(n-1)} \quad (14)$$

where K is the consistency factor and n is the power-law index. The power law behavior correctly describes the linear part of the viscosity curve in figure 6. The Carreau model is given by

$$\eta - \eta_\infty = (\eta_0 - \eta_\infty) (1 + \lambda^2 \dot{\gamma}^2)^{-n/2} ; \quad (15)$$

it exhibits a zero shear rate viscosity η_0 , a viscosity η_∞ for large $\dot{\gamma}$ and a power law behavior at intermediate values. It is easily found that λ^{-1} is a characteristic shear-rate at which the material shifts from Newtonian to power-law behavior. For more details on various viscosity laws, the reader is referred to Bird et al [3].

4.2. Viscoelastic fluids of the differential type

We have seen in section 4.1 that, for generalized Newtonian fluids, the extra-stress tensor \mathbf{T} is given by an algebraic function of the local velocity gradient tensor which appears in the invariant \mathbf{II}_d in (12). For viscoelastic fluids, the tensor \mathbf{T} depends upon the strain history of the material particle. In figure 9, the stress \mathbf{T} at \mathbf{X} and time t depends upon the function $\mathbf{C}_t(\tau)$, where $\tau \leq t$ and \mathbf{C}_t is the relative right Cauchy-Green strain tensor. One may consider that, at time t , \mathbf{T} is the solution of a differential equation. The resulting constitutive equation is said to be of the "differential type". In section 4.3, we will consider an explicit dependence of \mathbf{T} at time t upon the relative strain history and thus define a viscoelastic fluid of the integral type.

Let us first consider the class of differential models for which \mathbf{T} is related to the velocity gradients by means of a differential equation. Let \mathbf{v} denote the velocity field and \mathbf{L} be its

gradient. The constitutive equation for the upper-convected Maxwell fluid (or Maxwell-B fluid) is given by

$$\mathbf{T} + \lambda \overset{\nabla}{\mathbf{T}} = 2\eta \mathbf{d} \quad , \quad (16)$$

where λ is a relaxation time, η a shear viscosity, while a triangle ∇ superscript denotes the upper-convected, or contravariant, derivative, i.e.

$$\overset{\nabla}{\mathbf{T}} = \dot{\mathbf{T}} - \mathbf{L}\mathbf{T} - \mathbf{T}\mathbf{L}^T \quad , \quad (17)$$

where a dot designates the material time derivative,

$$\dot{\mathbf{T}} = \frac{\partial \mathbf{T}}{\partial t} + \mathbf{v} \cdot \nabla \mathbf{T} \quad . \quad (18)$$

The Maxwell-B constitutive equation is not realistic for modeling polymer flow; in particular it is endowed with a constant shear viscosity and an infinite steady extensional viscosity at a finite value of the rate of elongation. The same is true for the often used Oldroyd-B fluid for which \mathbf{T} is given as follows,

$$\mathbf{T} = \mathbf{T}_1 + \mathbf{T}_2 \quad ,$$

$$\mathbf{T} + \lambda \overset{\nabla}{\mathbf{T}}_1 = 2\eta_1 \mathbf{d} \quad , \quad (19)$$

$$\mathbf{T}_2 = 2\eta_2 \mathbf{d} \quad ,$$

where one finds that \mathbf{T}_2 is a purely viscous part of the stress tensor. It is interesting to see the form of Equation (19) after elimination of \mathbf{T}_1 and \mathbf{T}_2 . One finds

$$\mathbf{T} + \lambda \overset{\nabla}{\mathbf{T}}_1 = 2(\eta_1 + \eta_2) (\mathbf{d} + \lambda' \overset{\nabla}{\mathbf{d}}) \quad , \quad (20)$$

where

$$\lambda' = \lambda \frac{\eta_2}{\eta_1 + \eta_2} \quad (21)$$

is called a retardation time. Equation (20) is a special case of the class of constitutive equations introduced by Oldroyd [4].

Despite their inability to quantitatively represent polymer behavior, Maxwell-B and Oldroyd-B fluids have frequently been used for developments in numerical simulation. With only two, or three, available material parameters, such models are easy to understand and, on a qualitative basis, they have been able to generate a number of macroscopic observations in polymer flow. Simultaneously, it has been found that the flow of such fluids is one of the most difficult to simulate among the set of available constitutive equations; in that sense, they have helped considerably in the development of numerical algorithms for modeling viscoelastic flow.

Several constitutive equations of the differential type with a more realistic behavior for modeling polymer flow have been used over the past few years in numerical simulation. With a single relaxation time, they may be written in the general form

$$Y(T) \dot{T} + \lambda \overset{\square}{T} = 2\eta \dot{d} \quad (22)$$

In this expression, a square superscript stands for a linear combination of the upper and lower convected derivatives

$$\overset{\square}{T} = (1 - \xi/2) \overset{\nabla}{T} + (\xi/2) \overset{\Delta}{T} \quad (23)$$

with

$$\overset{\Delta}{T} = \dot{T} + TL + L^T T \quad (24)$$

In Table I, we show the definition of $Y(T)$ and the value of ξ for some popular equations; ϵ and α are scalar parameters. As shown in Table I, the Leonov fluid appears as a special case of the Giesekus constitutive equation when the mobility parameter α equals 1/2, but this is only true in plane flow.

An accurate fit of experimental data will usually require the use of a spectrum of relaxation times; one writes

$$T = \sum T^{(i)}$$

(25)

$$Y(T^{(i)}) T^{(i)} + \lambda_i \dot{T} = 2\eta_i d \quad .$$

With most equations of Table I, it is also necessary to include in the $T^{(i)}$'s a purely viscous partial stress tensor without which the shear stress would go through a maximum at a finite value of the shear rate in simple shear flow.

Table 1. Nature of the function $Y(T)$ and of the ξ parameter for various models.

Type of fluid	ξ	$Y(T)$
Phan-Thien-Tanner [5]	$0 \leq \xi \leq 2$	$\exp(\epsilon \lambda / \eta \operatorname{tr} T) I$
Phan-Thien-Tanner [5]	$0 \leq \xi \leq 2$	$(1 + \epsilon \lambda / \eta \operatorname{tr} T) I$
Johnson-Segalman [6]	$0 \leq \xi \leq 2$	I
Leonov [7] (plane flow)	0	$I + 0.5 \lambda / \eta T$
Giesekus [8]	0	$I + \alpha \lambda / \eta T$
Upper-convected Maxwell	0	I

A discussion of the virtues and defects of these equations for modeling polymer flow lies beyond the scope of the present chapter; a detailed discussion and guidelines for practical applications may be found in Tanner 1985. Since numerical simulation is addressing flows in complex geometries, it is clear that the behavior of constitutive equations in extensional or time-dependent flows is of major importance. It is interesting at this stage to mention the FENE-P model based on kinetic theory; it will be used later in the analysis of some practical problems.

4.3. Viscoelastic fluids of the integral type

Differential models have generally been more popular than integral ones in numerical developments over the last ten years. Both types of models are representations of the simple fluid concept which defines the extra-stress tensor as a functional of the relative right Cauchy-Green tensor C ,

$$T = T[C(t'); -\infty < t' \leq t] \quad . \quad (26)$$

With integral models, the functional T is given as an integral relationship between $T(t)$ and $C(t')$. For Lodge's rubber-like liquid, the functional T takes the form

$$\mathbf{T} = \int_{-\infty}^t \mu(t-t') [\mathbf{C}^{-1}(t') - \mathbf{I}] dt' . \quad (27)$$

When the kernel function μ is expressed as a sum of exponentials, one recovers a summation such as Equation (25) where each partial stress is also satisfying the Maxwell-B constitutive Equation, with η_i and λ_i as material parameters. Of course Lodge's model, as compared to experimental behavior, has the same defects as the UCM fluid but, once more, its formal simplicity together with its complex behavior in numerical work has given it a special status in the development of algorithms for fluids of the integral type.

The other models of the integral type which have been used in the numerical literature belong to the KBKZ [10] family for which \mathbf{T} is given as follows,

$$\mathbf{T} = \int_{-\infty}^t \left[\frac{\partial U}{\partial I_{C-1}} \mathbf{C}^{-1}(t') + \frac{\partial U}{\partial I_C} \mathbf{C}(t') \right] dt' , \quad (28)$$

where U is a potential depending upon the trace I of \mathbf{C} and of its inverse.

Let us mention the idea of separability introduced by Wagner [11], which assumes that the integrand in Equation (28) may be written as the product of a factor depending solely upon the past time t' and another factor depending upon t' only through \mathbf{C} and its inverse. Assuming that the second term in the integrand on the right of Equation (28) may be neglected in front of the first, we may then write

$$\mathbf{T} = \int_{-\infty}^t m(t-t') H(I_{C-1}, I_C) \mathbf{C}^{-1}(t') dt' \quad (29)$$

A more empirical approach has been used by Papanastasiou, Scriven, and Macosko [12] for deriving a constitutive equation of the Wagner type with good response in shear and extension. The time function $m(s)$ is given by

$$m(s) = \sum_{k=1}^{\infty} \frac{a_k}{\lambda_k} \exp(-s/\lambda_k), \quad (30)$$

where a_k are elastic moduli corresponding to a spectrum of relaxation times λ_k , while the function H is given as

$$H = \alpha / [\alpha - 3 \beta I_{C-1} + (1 - \beta) I_C], \quad (31)$$

where α and β are constants which are selected for fitting experimental data.

For the Wagner [13] model, the damping function H is defined as follows

$$H = \exp [-n(\beta I_{C-1} + (1-\beta) I_C - 3)^{1/2}] \quad (32)$$

where n is a material parameter.

It is beyond the scope of this text to discuss the virtues and defects of these models and to compare them with differential models; the reader is referred to Tanner [9] and Larson [14] for a detailed analysis of the current state of the art in constitutive equations. It is important to note that, in numerical simulation, going from one model to another, as long as they belong to the same family (i.e., differential or integral) is not a major enterprise once an accurate algorithm has been developed for a particular constitutive equation. For differential models, the presence of the advective term $\mathbf{v} \cdot \nabla \mathbf{T}$ in Equation 18 presents a major challenge for the numerical integration while, for integral models, an accurate calculation of the strain history $\mathbf{C}^{-1}(t')$ is the most difficult part.

5. Numerical methods for generalized Newtonian flow

5.1. Numerical algorithms

Numerous techniques have been used to solve the equations governing the flow of rheologically complex fluids. Finite difference methods figured prominently in early developments, a major attraction being their relative ease of implementation. However, the finite element technique has dominated recent development and is the preferred one for most practitioners in the field. Indeed, all the examples we shall give in the next section were obtained using finite elements. Finite element codes may be relatively difficult to implement but there is no doubt that a code, once written, can be made very versatile. In recent years, finite-volume and boundary-integral techniques have also been used while spectral methods are also beginning to appear in the rheological literature.

There are many complex flows in industrial applications for which some of the major viscoelastic effects are unimportant. Such flows are typically dominated by shear viscosity; in that sense, they are non-Newtonian since the shear viscosity is highly shear-rate dependent, as we have seen in section 3.1. However, memory, extensional viscosity and normal stress difference may not dominate the flow. Under such circumstances, it is useless to make use of the arsenal of viscoelastic constitutive equations instead of concentrating on some simpler models which are able to generate very meaningful results. Flows in confined geometries are typical cases where the use of a generalized Newtonian fluid (possibly non-isothermal) is fully satisfactory. We show below several examples of such flows. Even in extrusion flows, the amount of shear thinning may be such that viscoelastic normal stress differences may not be necessary to generate useful results.

The basic algorithms to solve generalized Newtonian flow (GNF) are very similar to those used in Newtonian CFD and will not be detailed here. The velocity, pressure (and temperature) are the basic unknowns (see e.g. Crochet et al [15]). In many material processing problems, inertia effects are unimportant; however, non-linearities dominate through the viscosity laws and through geometrical complexity due to the presence of a priori unknown free surfaces, interfaces and contact areas. In POLYFLOW, we use fully implicit techniques which simultaneously solve the fluid motion and the geometrical problem. To solve the non-linear systems, we use Newton-Raphson's method together with automatic continuation techniques when the final result lies too far from the initial guess. It is then possible to select any material or geometrical parameter as the continuation variable. As a typical example, consider the case of non-isothermal polymer flow. Thermal conductivity is so low that it may be necessary to start the calculation with

a higher conductivity and to let the program progress step by step towards the desired material properties.

5.2. *Die design*

A typical application of the use of GNF is shown in figure 10, where one finds the geometry of a coat-hanger die. A polymer melt enters the die through the square cross section A and is distributed across the contour of the die through a peripheral channel. It is then flowing through a three-dimensional channel of low gap width towards the exit of the die. The objective of the calculation is to design the geometry of the channel in order to obtain a velocity distribution at the exit which is as uniform as possible.

An intrinsic difficulty here is that the first peripheral channel is essentially three-dimensional; further downstream, the gap width is so small that the flow should be considered as two-dimensional on a curved surface. The use of three-dimensional elements throughout the die would be very expensive and meaningless. In POLYFLOW, we have implemented an algorithm which allows us to link two-dimensional to three-dimensional flow domains while satisfying the necessary continuity requirements. In the two-dimensional flow domain, the non-uniform thickness of the gap is part of the data; we use the Hele-Shaw approximation to calculate the flow. Figure 11 shows the pressure distribution throughout the die. In figure 12, we show the uniformity (in %) of the velocity profile in the thin exit section corresponding to the design of figure 10. It is obvious that further iterations on the thickness distribution could lead to an even better velocity profile.

Another typical application of GNF in confined flow is shown in figure 13 where we find the geometry of the channel in a single screw extruder; a precise knowledge of material properties allows us to calculate the temperature and pressure distribution in the channel.

5.3. *Mixing*

The GNF model is useful in mixing problems. Let us examine the geometry of the Kenics mixer in figure 14. It is made of a cylindrical outer boundary containing a number of helical plates. The relative angular position of these plates is such that the fluid is sheared and periodically sliced; moreover, the angular rotation of the fluid changes sign when it moves from one plate to the next. Let us assume that, in the entry section, we introduce two fluids of similar viscosity but with different colors. After N plates, one expects the fluid to be made of 2^N layers of alternating color. Of course, one does not expect layers of uniform thickness; a typical distribution is shown in figure 15.

Flow analysis through CFD allows us to predict the final state of mixing and to calculate a number of interesting mixing parameters.

We have analyzed an experimental mixer through which two clays of different color were forced to flow (Avalosse [16]). A power-law fluid with a power index of 0.6 was used as the fluid model. In the present geometry, we can use spatial periodicity to calculate the flow. A geometrical element corresponding to one period is shown in figure 16; an additional torsion of the mesh is needed before the calculation. Figure 17 compares experimental and theoretical results. The shades correspond to clays of different color. The cross sections of figure 17 are obtained at 1/4, 2/4, 3/4 and 4/4 of the axial distance along the plates. The correspondance between theoretical and experimental results is remarkable. It is also worth noting that, experimentally, it is very difficult to distinguish between both fluids beyond the fourth plate. The same is true for numerical results in view of discretization errors.

5.4. *Blow molding*

Blow molding is a popular industrial process used to produce hollow bodies. Their shape can be very simple and axisymmetric (bottles for example), or may be complex and require a 3-D model. The quality and productivity requirements are severe, making the design of the process a challenging task. In particular, the thickness distribution of the blown product must be as uniform as possible.

Polyflow contains an efficient numerical tool for the simulation of the blow molding process, in 2-D as well as in 3-D cases. Typical outputs of the simulation are the final product thickness, the temperature profile during inflation (for non-isothermal simulations), and the total inflation time. Several models were already proposed for the simulation of blow molding [17]. Whilst most of those approaches are based on a (hyper)-elastic description of the material, we use the alternate description of the material as a fluid (viscoelastic or not). Indeed, polymers do not have a reference configuration at the process temperature.

The numerical technique is based on an implicit time-dependent simulation of a flow which involves internal and external free surfaces. Along the internal free surface, a normal force equal to the blowing pressure is applied. The model also incorporates contact detection between the fluid parison and the wall of the mold. The occurrence of the contact is unknown in time and space. Mechanical as well as thermal contacts are handled by means of penalty techniques. One of the obvious difficulties is that the flow involves large deformations and that a robust remeshing technique is required. For blow

molding, an elliptic remeshing algorithm based on a stationary form of a deformation energy guarantees the regularity of the mesh.

Our first example is two-dimensional, generalized Newtonian isothermal blow molding simulation. One wishes to make an axisymmetric product out of an extruded parison. The complete process has been simulated, including extrusion of the parison, closure of the mold and inflation of the parison. Once the material hits the wall, zero velocity boundary conditions apply, but the product thickness is still allowed to vary. Figure 18 shows the time evolution of the parison shape at various stages during the process. During the simulation, we track the position of material points and we locate their origin. This information is particularly useful to modify the initial parison shape (or its initial temperature) in order to control the product uniformity.

Our second example in blow molding is three-dimensional, generalized Newtonian and isothermal. An cylindrical parison is pinched in a three-dimensional mold and then inflated. Figure 19 shows the mold and the initial parison. In Figure 20, we present the shape of the final blown product. Based on our initial configuration, the thickness of the product is not very uniform so that the process conditions need to be optimized.

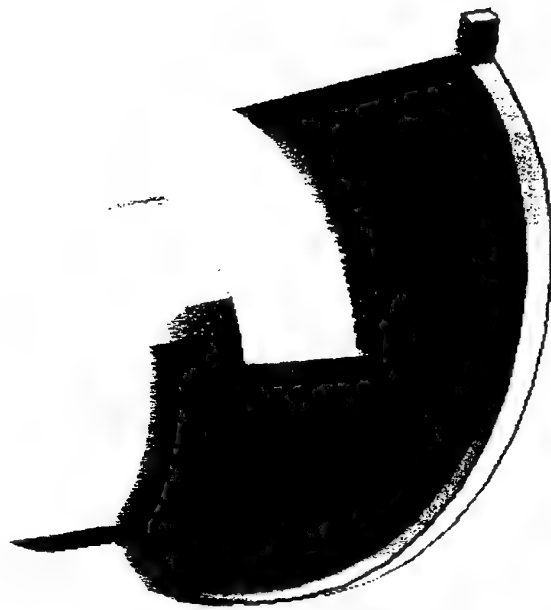


Figure 10. Geometrical configuration of a coat-hanger die.

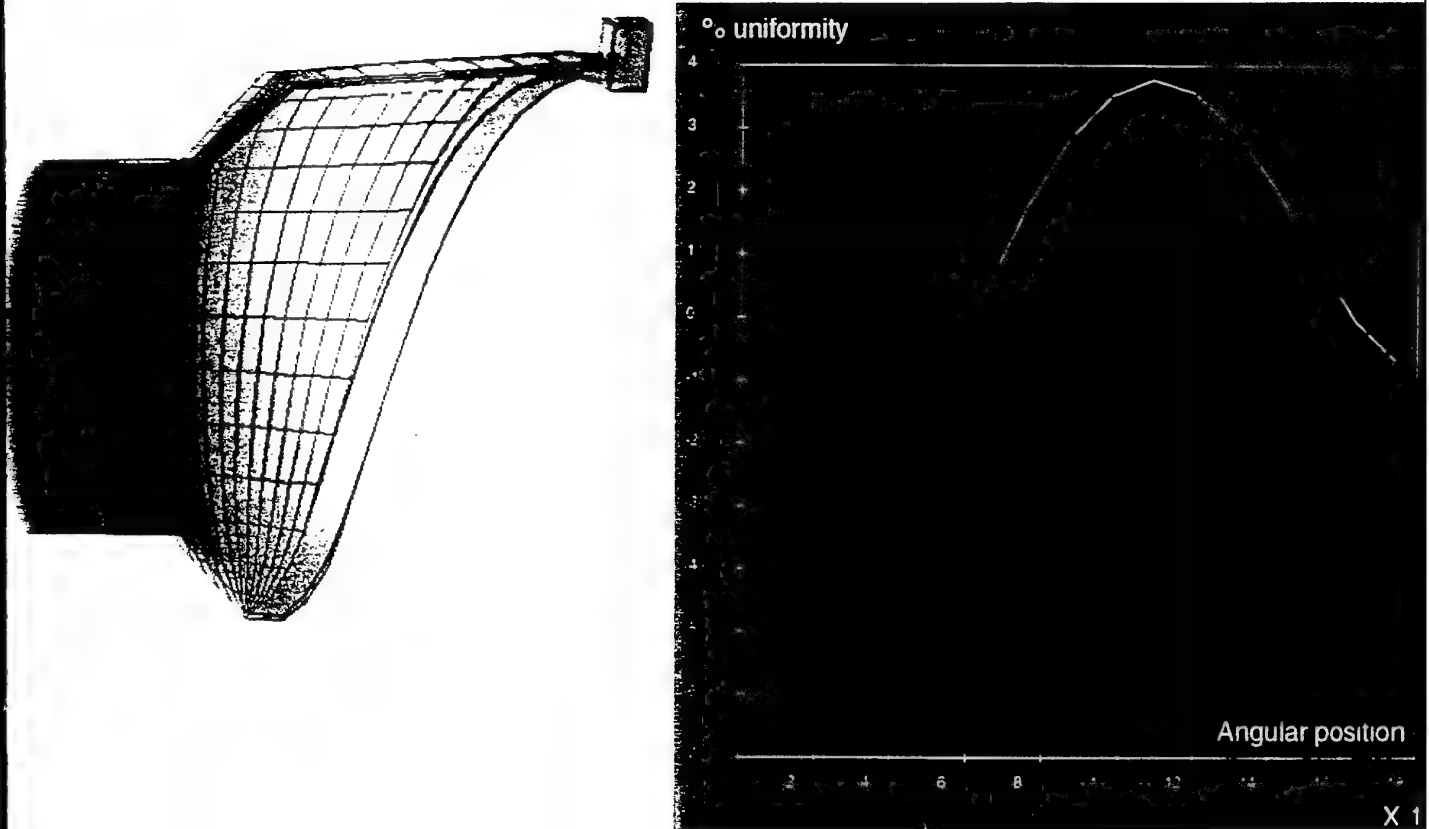


Figure 11. Pressure distribution through the coat-hanger die.

Figure 12. Uniformity of the velocity distribution as a function of the angular position in the coat-hanger die.

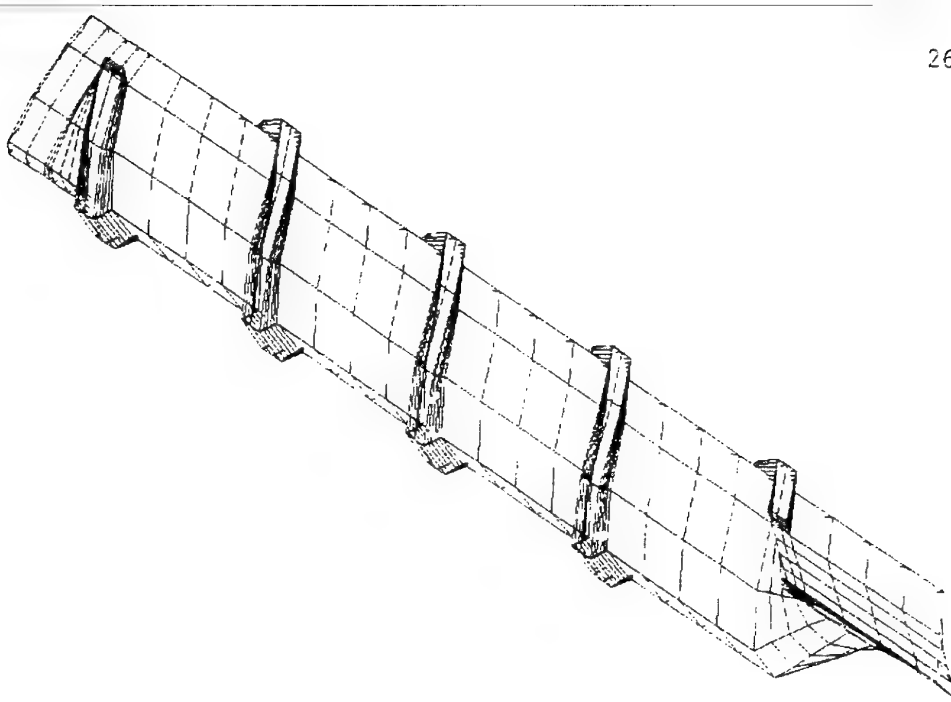


Figure 13. Finite element representation of the channel on a screw.

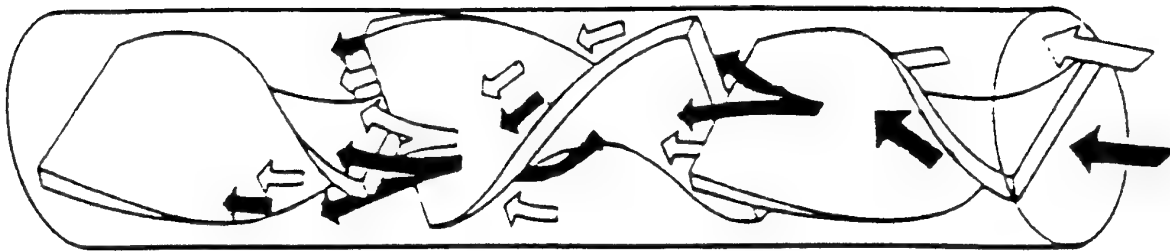


Figure 14. Geometry of the Kenics mixer.

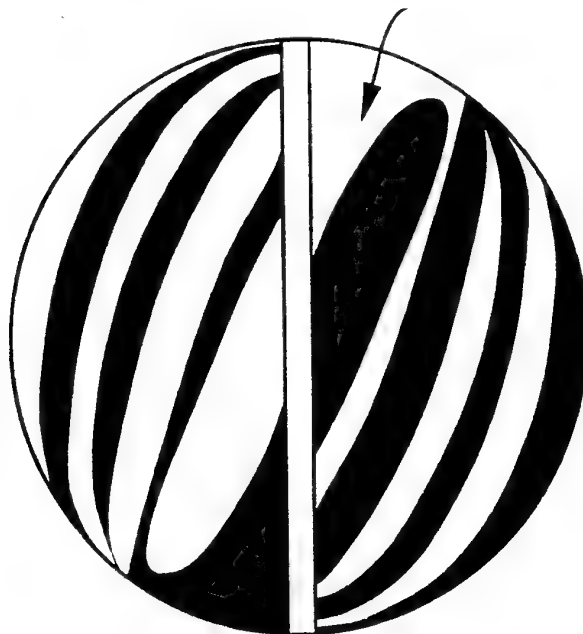


Figure 15. Typical cross-section showing the distribution of fluids mixed in a Kenics mixer.

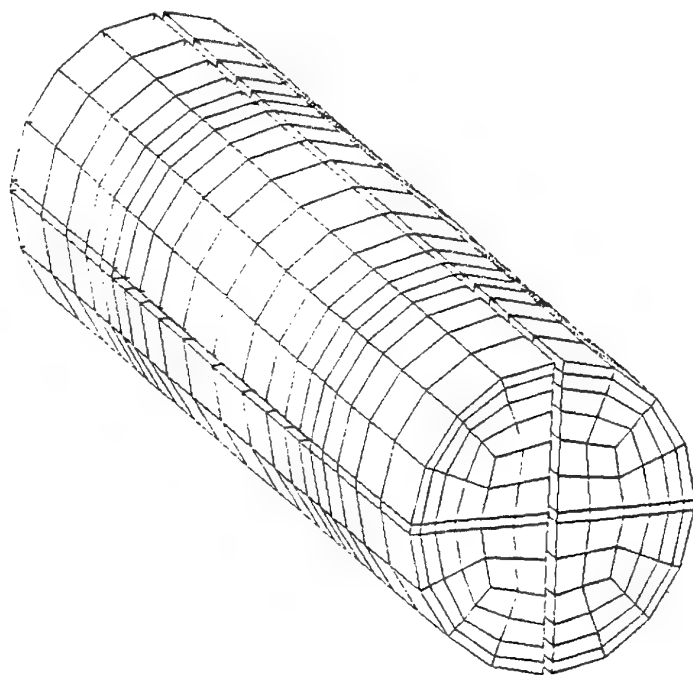
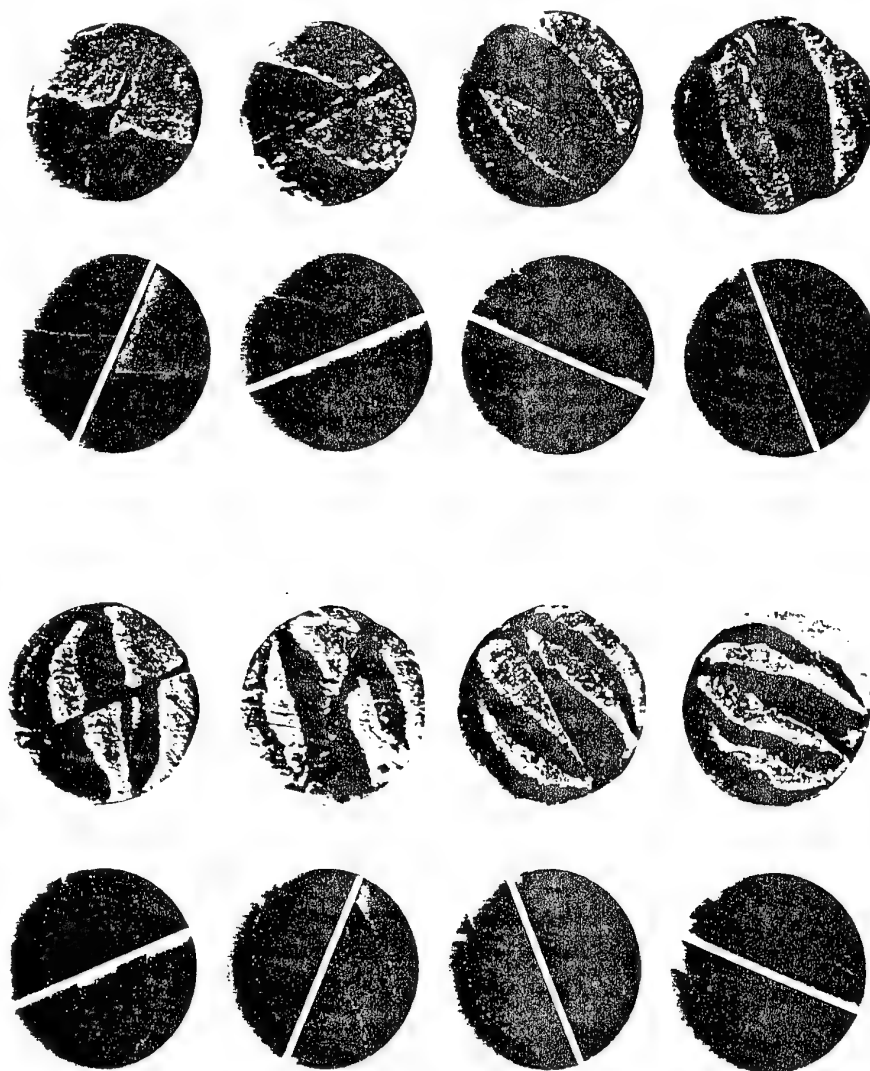


Figure 16. Finite element mesh for a spatial period of the Kenics mixer.



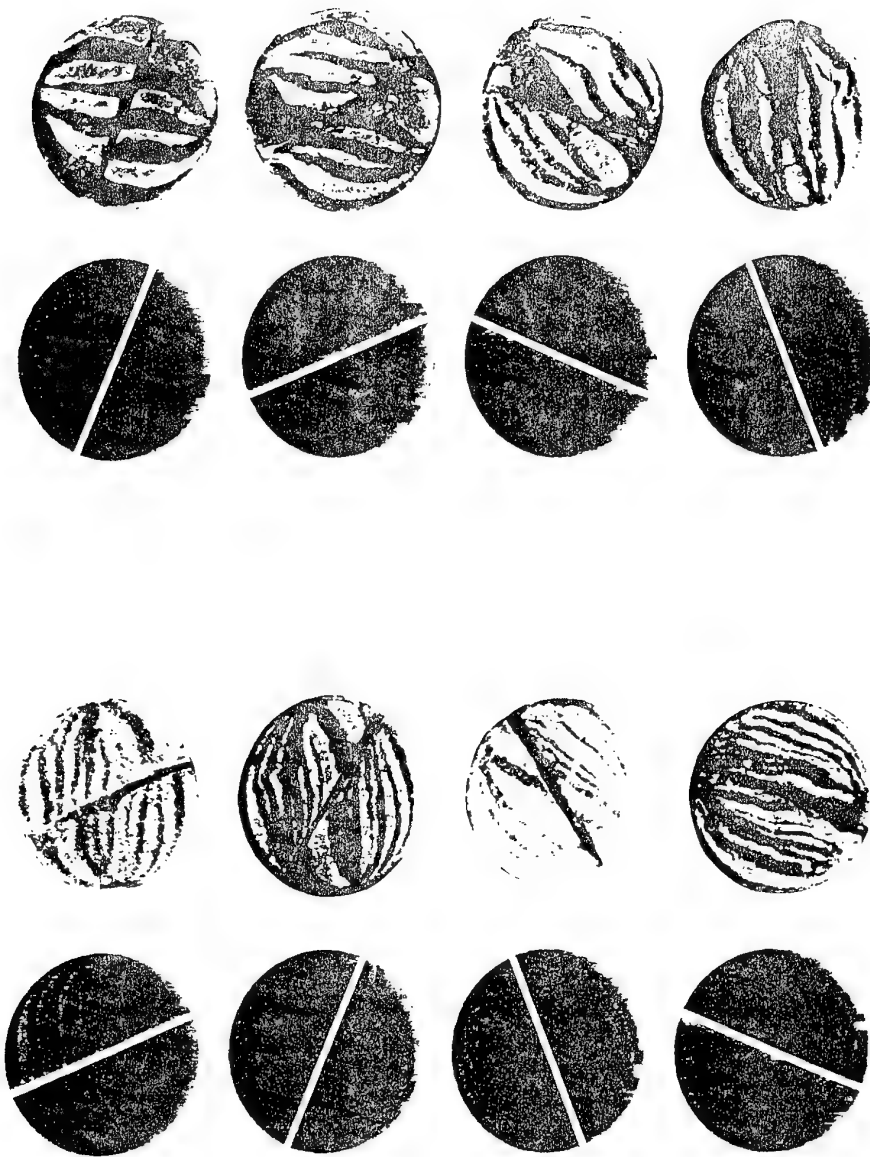


Figure 17. Comparison between experimental and calculated cross-sections showing the mixing of two colored fluids in a Kenics mixer.

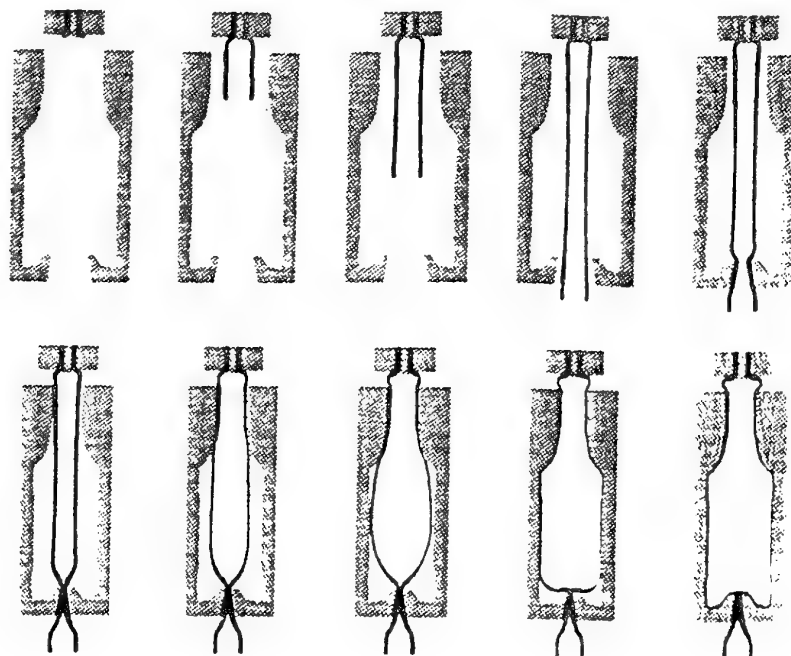


Figure 18. Axisymmetric blow-molding: time evolution of the parison.

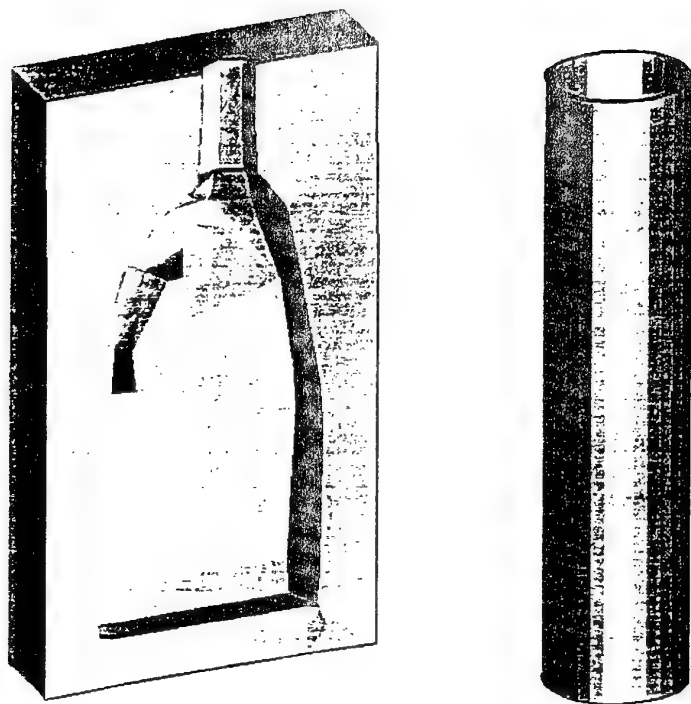


Figure 19. Shape of the mould and of the initial parison.

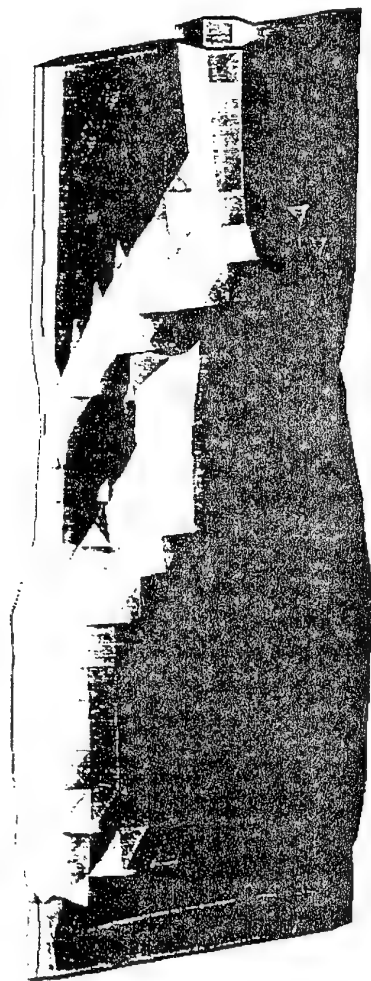


Figure 20. Thickness distribution in the final blown product.

5.5. Extrusion

Normal stresses can have a deep influence on fluid behaviour in free surface flows. Imagine that the shearing section of figure 5 is followed by a free flow where the fluid is not bounded by walls. It is then easy to understand the effect of the normal stresses we have described above : the unbounded fluid tends to swell in the absence of applied pressure on the free surface. This is called "die swell" or, more precisely, "extrudate swelling". The first picture in figure 3 shows a typical example of normal die swell. While it is known that at low Reynolds numbers Newtonian flow out of a capillary tube of circular cross-section generates a swelling of 13 per cent, polymer melts and polymer solutions produce jets with radii often more than three times as large as that of the capillary.

The effects that we have just described are important from two points of view. First, they are directly related to the physics of the fluid at hand; a good mathematical model must be able to generate such effects. At the same time, extrudate swelling has major consequences in the widely used extrusion process. The purpose of extrusion is to generate long cylindrical bodies with an assigned cross-section. Such cross-sections can have a very complicated shape. In extrusion, the molten polymer flows through a die which assigns the shape of the free surface. Because of normal stresses and other complications, the extrudate profile is never identical to the die profile. An accurate prediction of the final profile would be of considerable help in die design which would otherwise require a large number of costly iterations.

A peculiar difficulty of the simulation of extrusion is that the flow domain is a priori unknown; the shape of the free surface needs to be calculated together with the velocity, pressure, and possibly stress fields. Consider, for example, in figure 21a the cross-section of a straight capillary die which is followed, as an initial guess, by a jet of constant cross-section. The flow domain is covered by a mesh of initially rectangular elements associated with nodes at which one wishes to calculate velocity, pressure, and stresses in the case of viscoelastic fluids. Simultaneously, one wishes to calculate the location of the nodes of the free surface in order to satisfy free surface boundary conditions : fluid particles do not cross the free surface, while normal and tangential forces vanish there. Early calculations were made by Nickell et al [18] for generalized Newtonian flow based on a method of successive substitutions for predicting the final profile. However, a fully implicit technique introduced by L.E. Scriven and his collaborators [19] is now widely used for an accurate prediction of free surfaces. Figure 6b shows extrudate swelling of a Newtonian fluid; for a unit radius of the capillary, one

obtains a final radius of the jet equal to 1.13; figure 21b shows contourlines of the stream function within lines of uniform shading corresponding to the pathlines of fluid particles. It is interesting to note that even in the Newtonian case, the problem is nonlinear because of the kinematic condition defining the free surface shape.

We have already mentioned that an accurate numerical simulation would be most helpful in the design of complex shapes. In effect, this amounts to solving "an inverse problem": that is, for a given shape of the extrudate, what is the appropriate shape of the die? The problem is of course clearly three-dimensional. Early attempts made use of iterative techniques, the correct die shape being attained by means of successive corrections to the die.

However, the finite-element method provides the necessary tools for calculating once and for all the die profile once the shape at the end of jet is prescribed [20]. The problem is nonlinear in view of the free surface conditions and the rheology of the fluid, when this is non-Newtonian.

The discretization scheme is based on a Galerkin technique for the momentum, mass conservation and kinematic equations. For the velocity-pressure discretization, we use the mini-element developed by Fortin [21]. This element has proved to be stable for incompressible flows, whereas the number of variables is relatively low. Accuracy is surprisingly good when compared to more expensive stable elements such as the tri-quadratic velocity element. Extrusion flow problems involve the calculation of free surfaces, the position of which is governed by kinematic conditions. A variable h , called the geometrical degree of freedom is associated to that kinematic condition. Moving free surface nodes without updating internal nodes would lead to unacceptable element deformation. One needs to propagate the motion of the free surfaces into the interior domain according to a remeshing rule. In our calculations, we use either a Euclidean distance rule described in [22] or a new remeshing scheme called Optimesh based on energy considerations. The linearity of the rule allows us to derive a full Newton-Raphson scheme at a reasonable cost and to reach quadratic convergence.

Figure 22 shows an interesting example for the flow of a Newtonian fluid. The problem here is to define a cylindrical die profile for extruding a star-shaped jet; one finds that the die is characterized by sharp angles which are eroded during extrusion. One frequently observes that regions of low axial velocity in the die shrink in the free surface and that fine geometrical details of the die shape are erased during extrusion.

Figure 23 illustrates an Inverse Extrusion Problem involving internal and external free surfaces. The problem is to extrude a trilume silicon rubber tube used for medical applications. Many industrial profile extrusion processes operate at low speed, so that normal stress effects do not dominate with highly shear-thinning materials; one may then use a generalized Newtonian fluid model. Here, we use a power law described by equation (14) with a power index of 0.25. Figure 24 compares the prescribed extrudate shape and the calculated die lip section. The grey-scale represents the magnitude of the velocity vector, which is not uniform at the die exit while it is constant at the exit of the extrudate. The numerical simulation and the calculation of an improved die exit section has led to the production of tubes which correspond much more precisely to the required shape, and to maintain this shape when the extrusion velocity is increased [23].

Another interesting example is shown in figure 25. The dotted line shows the desired profile at the end of the jet. The plain line shows the required shape of the die which has been calculated with the inverse method of POLYFLOW. We also show in figure 25 the deformed finite element mesh in the exit section of the die.

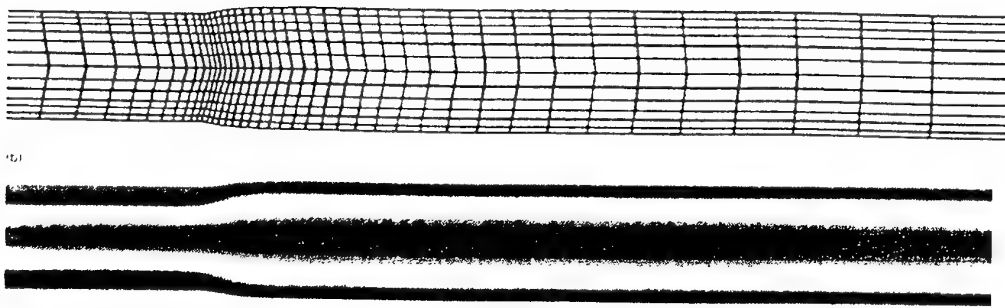


Figure 21. (a) Finite element mesh covering the central portion of the flow domain near the die lip; (b) circular extrudate swelling of a Newtonian fluid.

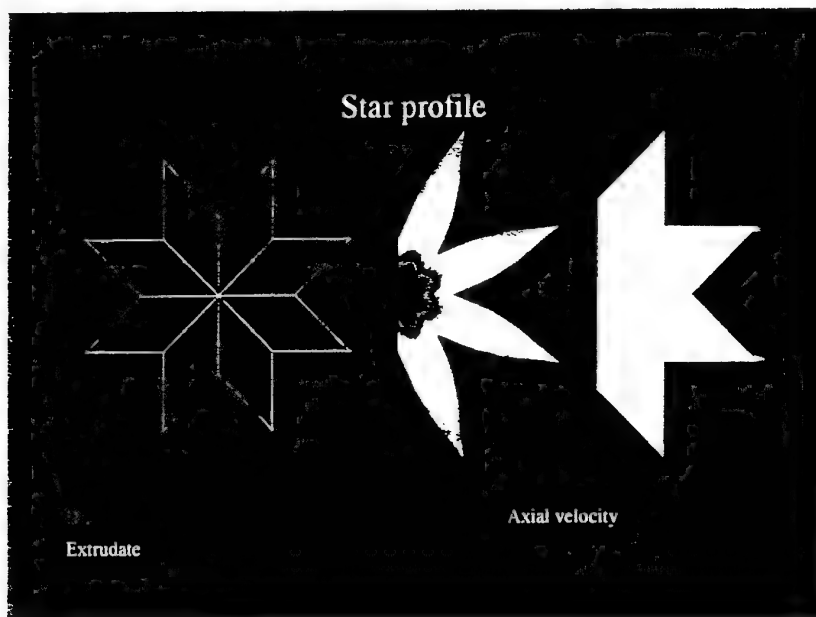


Figure 22. Shape of the die needed for extruding a Newtonian jet with a star cross-section. The angles in the die are much more acute than in the jet.

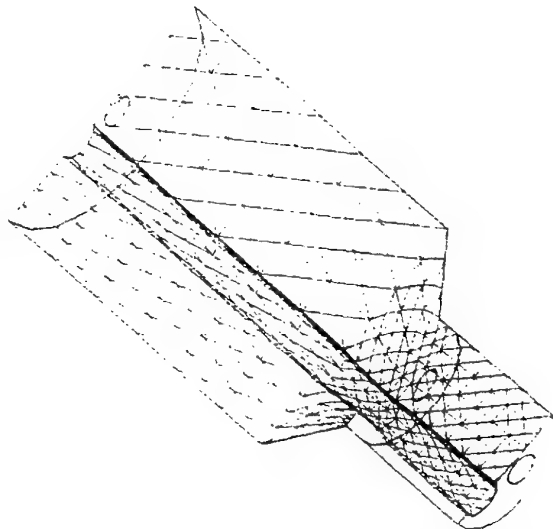


Figure 23. Finite element mesh for the numerical simulation of the processing of a trilume silicon rubber tube.

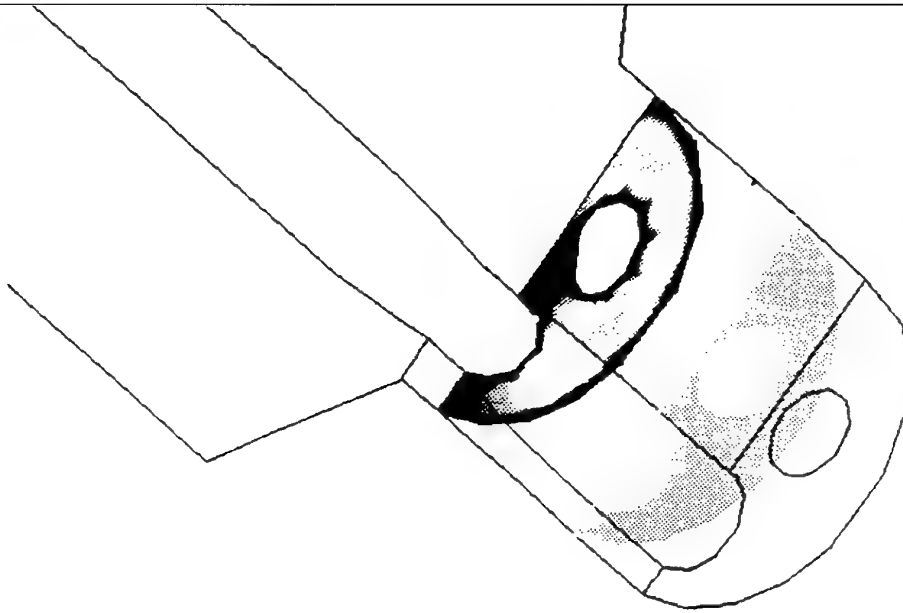


Figure 24. Comparison between the velocity profile in the die lip section and in the final extrudate section.

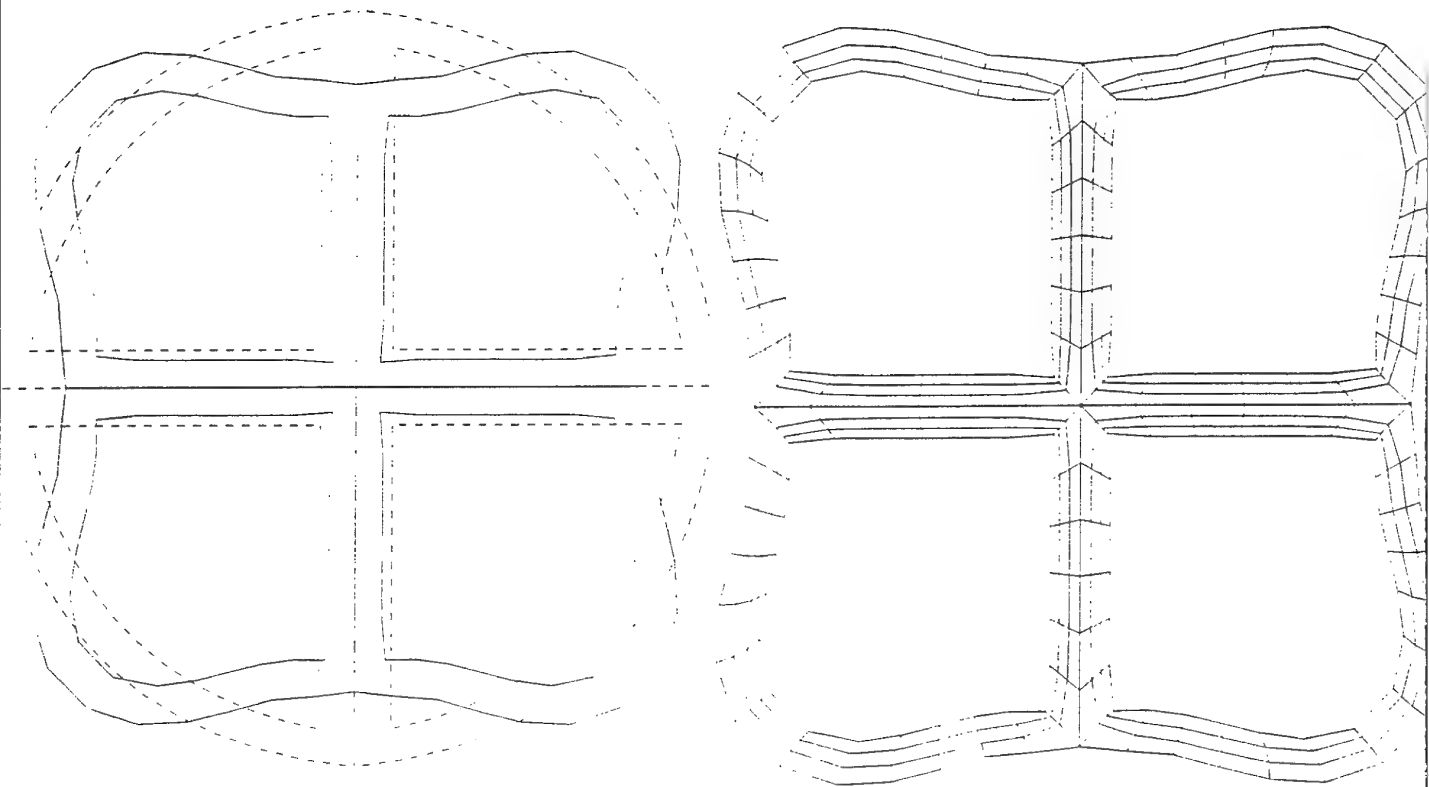


Figure 25. Comparison between the desired profile at the end of the jet (dotted) and the calculated shape of the die (plain); cross-section of the finite element mesh.

6. Numerical methods for viscoelastic flow

6.1 *Recent developments*

Early numerical work on the solution of viscoelastic flow only appeared in the mid-1970s, with the advent of powerful computers. The constitutive equations were now viewed as implicit equations for the stress components and the whole set of field and constitutive equations were solved with the stress components as variables in addition to the velocity components and the pressure involved in the solution of the corresponding Navier-Stokes equations. This fundamental development was therefore a major one, which introduced problems not hitherto encountered in Newtonian Fluid Mechanics. Developments up to the early 1980s are discussed in detail in [15] while more recent advances are covered by a review in [24].

Early developments were plagued by the so-called "high Weissenberg number problem"; numerical codes invariably broke down at relatively modest (and often frustratingly small) values of We [15]. Much research effort has been expended in tackling this important problem and there are strong indications that the basic difficulties are now resolved. Let us consider an example. One of the major interests in rheology is the calculation of non-Newtonian flow around obstacles, or the migration of solid bodies, and possibly bubbles, through a rheologically complex fluid. Settling in suspensions, fluidized beds, sperm navigation in biological fluids, are all examples of the practical relevance of the problems. Let us consider an apparently simple example but one which has recently served as a benchmark problem in computational rheology.

We consider the fall of a sphere along the axis of a vertical cylindrical tube, the radius of the cylinder being twice as large as that of the sphere. What we wish to predict here is fairly simple : considering a set of spheres, at what velocity do they fall? If the motion of the sphere starts from rest, is one able to predict the oscillatory motion which is sometimes observed when a sphere is dropped in a bath of real viscoelastic fluid? Once more, inertia effects are considered small as most experiments are performed in very viscous fluids. The Newtonian problem is simple; in fact, analytical solutions are available for evaluating the drag, including the effect of the cylindrical wall. In a viscoelastic fluid, the drag on the sphere for a given Weissenberg number is compared to the Newtonian drag in a medium of infinite dimensions, the ratio being called the "drag correction factor".

It turns out that the flow is extremely difficult to calculate. However, at least for low Weissenberg numbers and the case of an upper-convected Maxwell fluid, there is now

excellent agreement between various research groups [25-27] on the value of the drag correction factor up to a value of the Weissenberg number of 2. A plot of the drag correction factor is shown in figure 26.

The reasons for the difficulty appears in figure 27 where we show contour lines of the axial stress component in the flow domain near the sphere. It is found that normal stresses generate thin stress boundary layers near the wall of the sphere; a poor discretization is unable to resolve the boundary layer and leads to major discretization errors.

6.2. Algorithms for fluids of the differential type

Let us briefly review the algorithms for solving flows of the differential type; for the sake of simplicity, we examine the steady flow of a Maxwell fluid. We need to solve the following system of equations,

$$\mathbf{T} + \lambda \nabla \cdot \mathbf{T} = 2\eta \mathbf{d} \quad ,$$

$$-\nabla p + \nabla \cdot \mathbf{T} + \mathbf{f} = \rho \mathbf{a}, \quad (33)$$

$$\nabla \cdot \mathbf{v} = 0,$$

with appropriate boundary conditions on \mathbf{T} and \mathbf{v} . By comparison with Newtonian CFD, we realize immediately that the constitutive equations for \mathbf{T} are not explicit in the velocity field. It is thus not possible to obtain a system of p.d.e. in terms of \mathbf{v} and p . Mixed methods for viscoelastic flow use \mathbf{T} , \mathbf{v} and p as primitive variables. A central question is the selection of appropriate finite element representations for these variables. In early days (see Crochet et al [15]), a P2-C0 representation was used for \mathbf{T} and \mathbf{v} . It became clear however that such a selection could not satisfy the BBL condition of compatibility. In 1987, Marchal and Crochet [28] introduced the so-called 4x4 element: the velocity is represented by means of P2-C0 elements, but the stresses on a quadrilateral are discretized by means of 16 sub-elements on which one adopts a P1-C0 representation. Simultaneously, it was found that the hyperbolic character of the constitutive equations requires the use of upwinding techniques (SU or, better, SUPG). The 4x4 element has been widely used for numerous applications but its use is restricted to plane and axisymmetric problems in view of its high computational cost.

In 1990, Rajagopalan et al [29] introduced a new element called EVSS. Instead of \mathbf{T} , the method uses a new variable \mathbf{S} defined as follows,

$$\mathbf{T} = 2\eta\mathbf{d} + \mathbf{S}. \quad (34)$$

The advantage of the method is that it introduces a Newtonian-type term in the momentum equations and removes the above difficulty of compatibility between primitive variables. The method had been used earlier without success, because it was still expressed in terms of \mathbf{S} , \mathbf{v} and p . Rajagopalan et al [29] add the tensor \mathbf{d} as an additional variable and thus remove difficulties which had been encountered before. An advantage of the method is that it gives much freedom for the selection of polynomial representations and in that sense may be cheaper than the 4x4 element. A comparison between various types of interpolations has been recently given by Debae et al [30].

POLYFLOW makes use of the 4x4 element and of EVSS. The latter is especially useful for 3D extensions and for the use of constitutive equations with multiple relaxation times; under such circumstances, the use of 4x4 (or 4x4x4) would be prohibitive.

We wish to point out that, despite the fact that many problems are solved today up to appreciable (and practical) values of the Deborah number, viscoelastic flow is difficult. The continuation procedure implemented in POLYFLOW, using the relaxation time as an incremental variable, is unavoidable to reach significant values of the Deborah number.

6.3. *Algorithms for fluids of the integral type*

For fluids of the integral type, the constitutive equations have the general form (27). One realizes immediately that their form is entirely different from what one finds in Newtonian CFD. For steady-state flow, it is imperative to use an iterative method which may be briefly summarized as follows (the reader will find a detailed description in Goublomme et al [31]). The calculation starts from an initial guess, typically the solution of a GNF problem. For a given velocity field, it is then necessary to calculate the pathline of every quadrature point in the finite element mesh. Along these pathlines, on the basis of the velocity field, one then calculates the strain history. A numerical quadrature along the history leads to an evaluation of the stress tensor. The latter does not generally satisfy the momentum equations. A correction process on the velocity field, based on a perturbation of the constitutive equations, generates a new iteration. A difficulty with such a procedure is that it does not enjoy the convergence of Newton's method. Many iterations may be necessary to obtain converged results. However, integral models are

very useful for very accurate and realistic constitutive equations based on a spectrum of relaxation times, which are presently very costly for fluids of the differential type.

6.4. Extrusion.

Let us return to the axisymmetric problem considered in section 5.6 and examine the flow of an Oldroyd-B fluid through a capillary die. It is found that the amount of swelling increases considerably with the Weissenberg number. In figure 28, we show the jet configuration together with the streamlines for increasing Weissenberg numbers.

We conclude that, at least on a qualitative basis, viscoelastic constitutive equations, together with numerical simulation, are able to generate the extrudate swelling observed in polymer solutions and polymer melts. It is possible to simulate the intriguing phenomenon known as delayed die swell which was discussed earlier. It is clear from figure 3 that beyond a critical flow rate, one observes a change of curvature of the free surface up to the point where the swelling is truly delayed. An important observation made by D.D. Joseph et al [32] is that delayed die swell is a critical phenomenon : for a given fluid and a given capillary tube, it occurs only beyond a critical flow rate. Its explanation can be related to the well-known phenomenon of acoustic waves. Let us briefly consider the flow of a compressible fluid where the velocity of sound is denoted by c_p . As long as the velocity U of the fluid is lower than c_p , the pressure distribution is governed by an elliptic partial differential equation which changes type to a hyperbolic equation when U is larger than c_p . Hyperbolic equations produce characteristic features such as the generation of shock waves. Most viscoelastic fluids can be considered as incompressible and prevent the generation of acoustic waves. However, viscoelastic fluids are endowed with shear waves which travel at velocity c_p . In a Maxwell fluid, one can show that :

$$c_s = (\eta_0 / \lambda_1 \rho)^{1/2} \quad (34)$$

A critical state is reached in the viscoelastic flow as soon as the fluid velocity exceeds that of shear waves; Joseph et al [32] have shown that, under such circumstances, the vorticity equation becomes hyperbolic.

Delayed die swell is a critical phenomenon in the sense that it only occurs when the mean velocity in the capillary is higher than c_p . The occurrence of delayed die swell under increasing flow rate can be verified by numerical simulation. Figure 29 shows the configuration of streamlines for various values of the viscoelastic Mach number which is defined as follows :

$$M_v = v / c_s, \quad (35)$$

where v is the mean velocity of the fluid in the tube. When M_v is high enough, the central portion of the flow is not informed that the tube has ended; swelling is delayed and the curvature of the free surface is modified.

We have just considered some examples based on the use of a relatively simple Oldroyd-B fluid. We have found a correct qualitative behaviour, but the model is far too coarse to represent the behaviour of real polymer melts, if the associated numerical methods are to have an accurate predictive capability. Interestingly, a detailed analysis has recently been published by Goublomme et al [31] in order to predict the die swell results on high-density polyethylene published by Koopmans [33]. Koopmans used the experimental layout sketched in figure 30; the melt coming from the extruder flows through a capillary die preceded by a conical entry section with a 50° opening angle. The extrudate flows in an isothermal oil bath of equal density. The length of the capillary is 30mm, while its diameter is 2 mm. Special devices are used for monitoring the growth of the extrudate when it leaves the capillary tube. Constitutive models of the integral type are available for describing the behaviour of melts such as the high-density polyethylene under simple flow histories. The use of these models for simulating flows through complex geometries poses new challenges, and we wish to show some typical features. For a flow rate of $335 \text{ mm}^3\text{s}^{-1}$ through the capillary tube, Koopmans [33] obtained a swelling ratio of the order of 1.8 at a distance of 200mm from the die lip. In figure 31 we show how the upstream geometry of the die and the mathematical model can affect the final prediction. Figure 31a shows the streamlines and the shape of the free surface obtained with Wagner model [11] and the assumption that the die is a capillary tube of infinite length. The final swelling ratio is 1.44 as compared to 1.8 in the experiments. The low amount of swelling indicates the necessity of considering in the calculations a shorter capillary tube with a conical entry. The results, shown in figure 31b, come as a total surprise. One obtains a swelling ratio of the order of 8! In fact, we observe here the dominance of the elastic character of the fluid: the deformation of the fluid in the capillary occurs in such a short time that, according to the model used, the material behaves essentially like a piece of rubber which, squeezed through the capillary tube, would recover its shape at the other end. By adopting the "irreversible" version of the original Wagner model and by taking into account the second normal stress difference, Goublomme et al [31] were able to obtain the data shown in figure 31c. The theoretical swelling ratio of 1.86 is now very close to its experimental counterpart. The present example reveals that computational rheology can be used most effectively in

understanding the extrusion of complex fluids and eventually die design as we will now discuss within the context of three-dimensional problems.

The three-dimensional problem is much harder for the case of polymer melts endowed with a viscoelastic behaviour. The numerical method is more complex whilst the computation time is high. Moreover, normal stresses, and consequently swelling, increase with the flow rate. For the inverse problem, one thus expects a die shape which depends not only upon the required shape but also upon the assigned flow rate. The significant amount of swelling in viscoelastic flow results in a die profile which differs considerably from the jet profile. In figure 32 we show the cylindrical die shape required to obtain a cross-section of the jet with a viscoelastic fluid (more precisely a so-called Giesekus fluid) at an assigned flow-rate. One finds again that sharp angles in the die are necessary to produce the right angles in the extruded profile.

Our second example in 3-D extrusion is relative to an Inverse Problem for a differential viscoelastic fluid of the Giesekus type. The objective is to obtain an octagonal profile and the calculation provides the necessary die lip section required to achieve this goal. The problem was solved for various values of the relaxation time, ranging from 0 to 0.155 s. This last value is typical for highly elastic polymers. Figure 33 is a plot of the die lip shapes which have been calculated for various values of the relaxation time (the final shape of the extrudate is an octagon). The more elastic the fluid, the more the die lip shape deviates from the desired extrudate shape. For a viscoelastic fluid, there is a strong dependence of the die shape upon the extrusion speed.

6.5 Weissenberg effect.

We have already discussed in figure 4 the occurrence of the Weissenberg effect due to the presence of normal stresses in regions of high shear. The calculation of the free surface in such flows presents an additional difficulty as compared to the prediction of extrudate swelling. In the latter case, the velocity varies monotonically on the jet surface from the lip of the die to the outflow section of the jet; it is then possible to calculate the free surface by successive iterations between a trial velocity field and an estimated free surface. In figure 4 we are dealing with a "swirling flow": there are three velocity components depending upon two cylindrical polar coordinates r and z . The largest velocity component on the free surface occurs in the azimuthal direction; the radial and axial components are small and possibly nonmonotonic. It is then generally impossible to calculate the free surface iterations, and one needs an "implicit" method where the shape of the flow domain is calculated together with the pressure and the velocity and stress components. The problem has been recently solved by Debbaut and Hocq [34]

who found good agreement between their numerical simulations and some experimental data. Figure 34 shows the central part of the flow near the rod in a typical application, the bulge of the free surface being associated with a recirculating clockwise vortex; we also observe a partial view of the main counter-clockwise vortex.

Another interesting application is in the so-called "normal stress amplifier" shown in figure 35 [35]. Here, the viscoelastic fluid floats on a layer of water. The effect of the rotating rod is to provoke a small bulge on the upper free surface, together with a more pronounced bulge near the rod at the lower interface. One finds that the flow is characterized by a complex system of vortices of alternating directions.

The potential of such calculations is evident : numerical simulation allows a comparison between experimental data and theoretical results for a selection of constitutive equations and material parameters; complex free-surface flows of industrial importance are clearly within the orbit of available numerical techniques.

6.6. *Flow through contractions* .

We have observed in figure 1 the appearance of large vortices in the flow of a viscoelastic liquid through a 4:1 axisymmetric contraction. In that particular application, the liquid was a solution of polyacrylamide in glucose syrup and water called a "Boger fluid". Such fluids are highly viscoelastic and transparent at room temperature; they are used as substitutes for polymer melts in experimental investigations of non-Newtonian flow. A particular feature of these fluids is that, at low enough shear rates, their viscosity is constant, while the primary normal stress difference is a quadratic function of shear rate. For these reasons they are often assumed to behave as Oldroyd B fluids.

Remarkable photographs of vortex enhancement in Boger fluids were first published in the late 1970s [36]; they contributed to the excitement of computational rheologists who wanted to simulate such effects without realizing at the time that they were attempting to solve one of the most difficult problems in their field. Some real progress has been made, and a number of observed features are today very well understood.

A first encouragement came when numerical analysts discovered the existence of a slight Newtonian vortex which had not been observed before by experimentalists. A remarkable correspondence between calculated and observed streamlines is shown in figure 36. The fluid is Newtonian and the Reynolds number of the die flow is very low, so low in fact that inertia terms can be neglected in the momentum equations. Early attempts at flow calculation with the upper-convected Maxwell fluid met with failure. In

the 4:1 contraction flow, the relevant Weissenberg number is usually defined by the group $\lambda \dot{\gamma}_w$, where $\dot{\gamma}_w$ is the shear rate on the wall of the downstream tube. While experimentalists observed vortex enhancement at Weissenberg numbers of the order of 1, most numerical calculations failed to converge at about the same value and, when they did converge, they did not show any vortex enhancement! Such failure was a reflection of the "high Weissenberg number problem" discussed earlier.

Many possible causes of the problem have been put forward, but it has taken several years to understand that the true origin of the problem is related to numerical errors. A limited number of numerical methods have recently become available for solving flows at high Weissenberg numbers within the context of abrupt contractions and we show in figure 37 typical results showing vortex enhancement in the 4:1 contraction flow; in these figures, it is found that the vortex grows from the salient corner towards the axis of symmetry. Early calculations of such vortices [28] showed a correct qualitative behaviour, but the Weissenberg numbers at which they occurred differed by one order of magnitude from the observations. It took another five years for Boger et al [37] to realize that numericists and experimentalists were using different measures for the Weissenberg number, arising from the fact that the Oldroyd B model does not represent the properties of Boger liquids over a wide enough range of shear rates.

In passing, we remark that good semi-quantitative correspondence between calculated and observed vortices has also been found for the flow of low-density polyethylene through an abrupt contraction with the help of models of the integral type and several relaxation times.

While figure 37 shows that viscoelasticity does indeed generate recirculation regions, many outstanding problems remain to be solved. There is much experimental evidence that observed vortices are generated from the lip of the abrupt contraction and not by enhancement of the Newtonian corner vortex [38]. It is also true that the maximum size of vortices calculated at the present time is much smaller than that of the observations; the calculations seem to show saturation of the vortex size which is not observed experimentally. In fact, some experiments [39] reveal an apparent bifurcation from steady-state flow to a time-dependent rotating flow beyond some value of the Deborah number. Despite recent efforts in this direction bifurcations have not been detected in numerical simulations. The difficulty in simulating these complex patterns is presently attributable to at least three possible causes : a misunderstanding of the behaviour of the fluid near the re-entrant corner; the inability of the constitutive equations to capture the

behaviour of real fluids in complex flows; and the possible inadequacies of the numerical codes.

Quite recently, Purnode and Crochet [40] have reexamined the flow of Boger fluids and of polyacrylamide-in-water solutions through abrupt contractions of various ratio with the use of the FENE-P constitutive equation [41]. They have found a truly remarkable agreement between experimental observations and numerical results. In particular, they have obtained the appearance of "lip vortices" as shown in figure 38. Quite clearly, the constitutive equations are more problematic today than the numerical methods which have progressed considerably over the last ten years.

6.8 *Film casting.*

As a final example of viscoelastic effects, we wish to briefly describe briefly the film casting process where viscoelasticity plays a major role [42]. Film casting (also called film stretching) is a process commonly used to produce plastic films. The polymer exits a coat-hanger die, forms a free surface and is stretched by a take-up roll. During stretching the thickness is reduced by a factor 30..100, leading to a final thicknesses of the order of a small fraction of a millimeter. Typically, the width of the die is of the order of 1m and the distance between the die exit and the take-up roll is of the order of 0.5...1m. Although the 3-D free surface model described in section 2 could in principle be used, the thickness of the film is so small that the aspect ratio of the volume elements would be extremely large. This is the reason why we have developed a 2-D plane stress model where the thickness is being handled as a separate variable. However the model can be applied for differential viscoelastic fluids as well as for generalized Newtonian fluids. The model predicts the film thickness at every location on the film, as well as the position of side free surfaces which are updated according to a kinematic condition. Outputs of the model are the thickness distribution (for example on the take-up roll) and the absolute value of the 'necking' (width reduction as compared to the initial coat-hanger die width).

Let us first solve the problem for a generalized Newtonian fluid. We have considered the film stretching problem described in figure 39. The film thickness as well as the average velocity are imposed along the coat-hanger die exit (which is the entry section of our simulation domain). The position of the side free surfaces is a priori unknown : dynamic and kinematic conditions are imposed to locate those lines. In the exit section, we prescribe a fluid velocity equal to the linear speed of the roll. Figure 40 shows the film geometry for various values of the power law index n , for a draw ratio equal to 30.

Note the generalized Newtonian model predicts that the higher the draw ratio, the larger the necking will be.

In film stretching, fluid memory plays however a significant role because of the strong elongational character of the flow. It is found that viscoelastic results significantly differ from their Generalized Newtonian counterpart. Using a Giesekus model, we have solved the problem for the same value of the relaxation time for increasing values of the draw ratio D . Film geometry is shown in figure 41. As we would expect in view of the high extensional viscosity, the film necking is now much lower than for the generalized Newtonian case. One also observes an improved film thickness uniformity on the take-up roll. This prediction has been experimentally confirmed for some LDPE films.

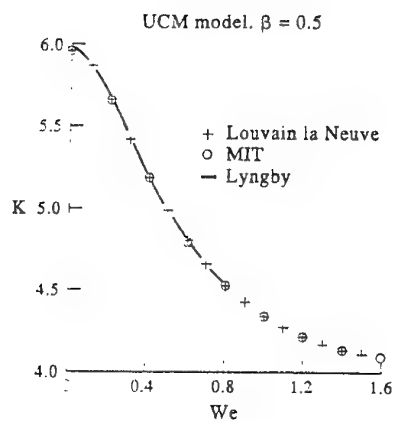


Figure 26. A plot of the drag correction factor as a function of Weissenberg number for an upper-convected Maxwell model. The radius of the cylinder is twice that of the sphere [25-27].

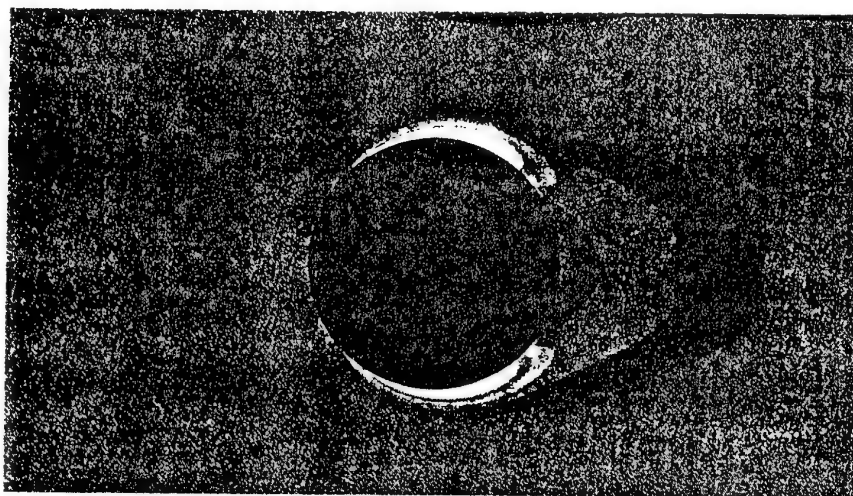


Figure 27. Contour lines of the axial stress components showing the intensity of the stress in boundary layers and in the wake of the sphere.

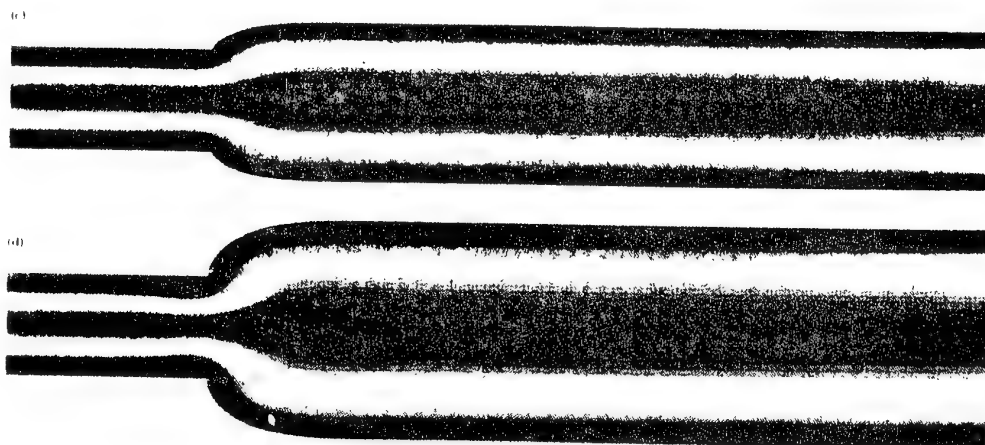


Figure 28. Circular extrudate swelling for an Oldroyd-B fluid at $De = 2$ and $De = 5$.

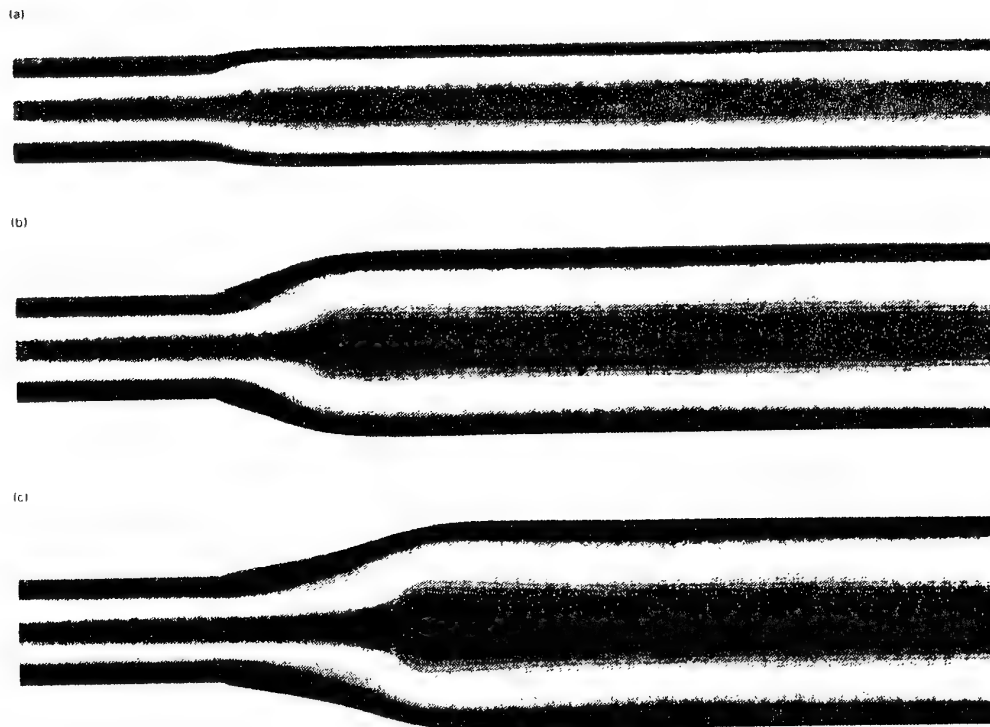


Figure 29. Shape of the jet in the case of delayed die swell; one observes the change of curvature of the free surface when M increases from 0.3 to 2.4 and eventually to 4.3.

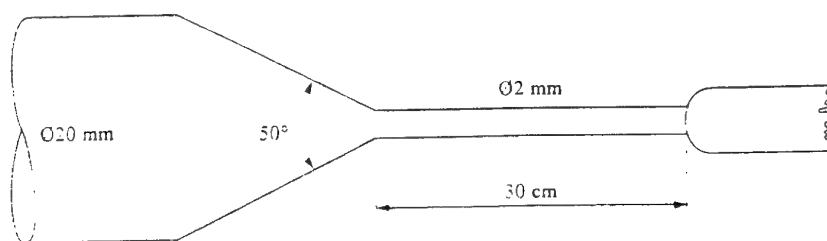


Figure 30. The capillary die is preceded by a conical entry section with an opening angle of 50° [33].

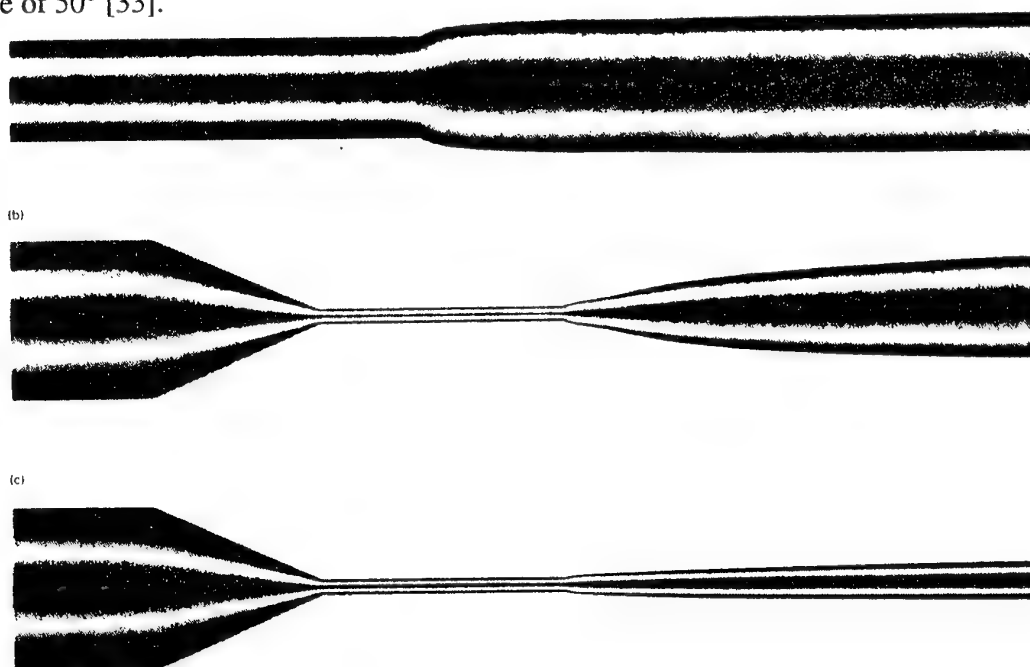


Figure 31. Simulation of the swelling of a high density polyethylene with a Wagner model (a) out of a long capillary tube and (b) out of a die with a conical entry section. The results are very similar to experimental data when one uses a modified rheological model (c).

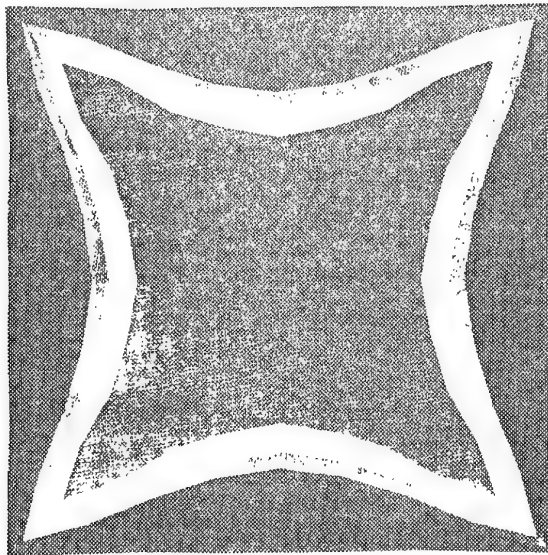


Figure 32. Die shape required for extruding a viscoelastic jet of square cross-section. The outer square represents the cross-section of the jet. The inner curves represent the shape of the die at various values of the flow rate.

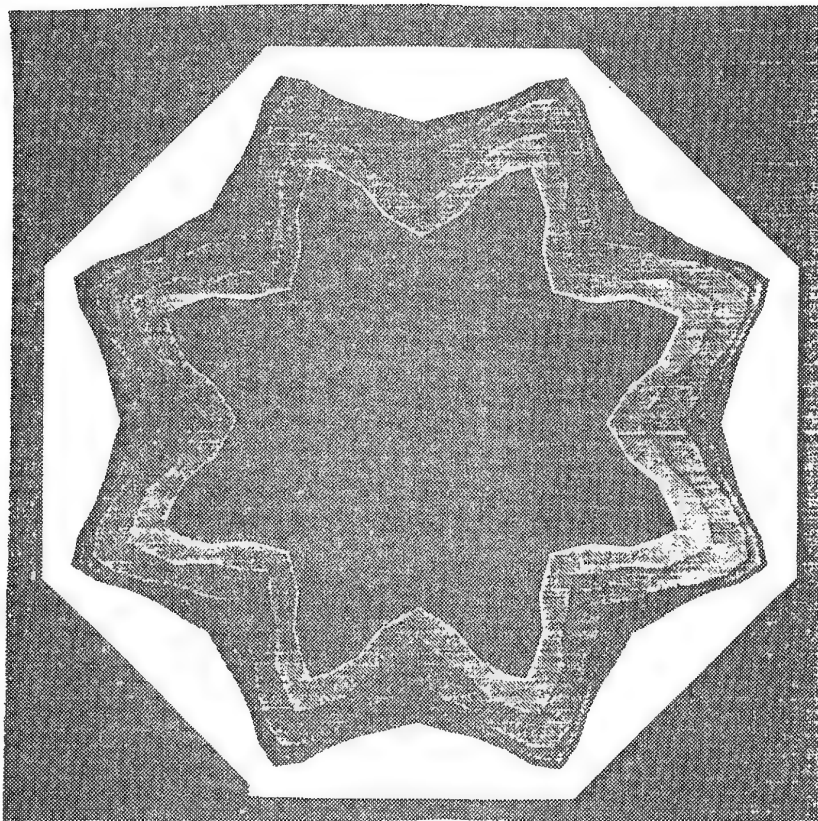


Figure 33. Die shape required for extruding a viscoelastic jet of octagonal cross-section. The outer curve represents the cross-section of the jet. The inner curves represent the shape of the die at various values of the flow rate.

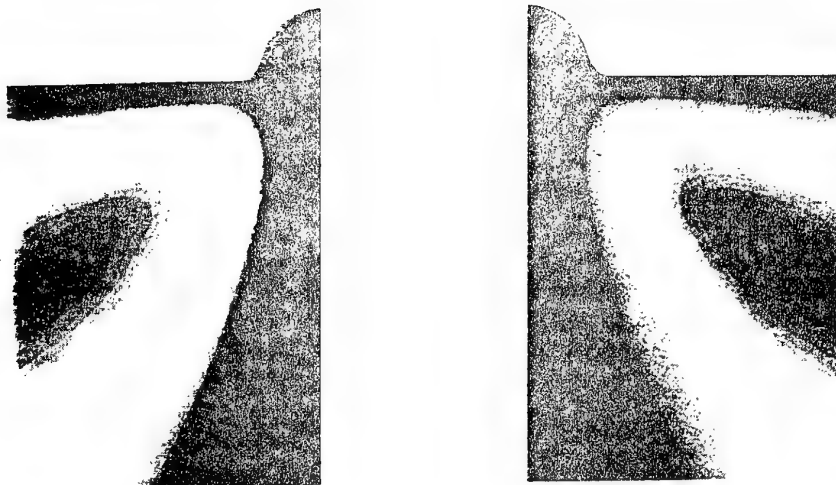


Figure 34. Central portions of the free surface for the flow of an Oldroyd-B fluid caused by a rotating rod, showing the Weissenberg effect.

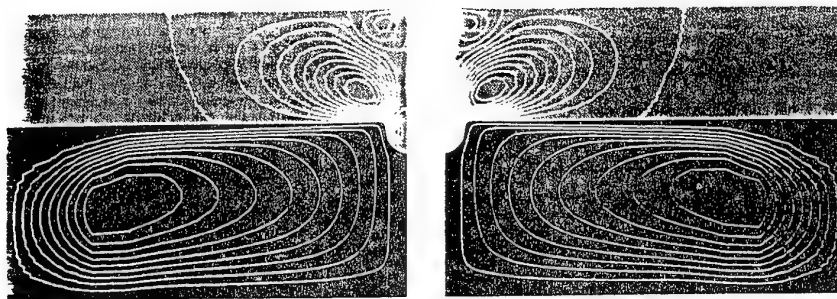


Figure 35. As for figure 34, except that the polymer fluid floats on water and creates a second lower bulge at the interface.

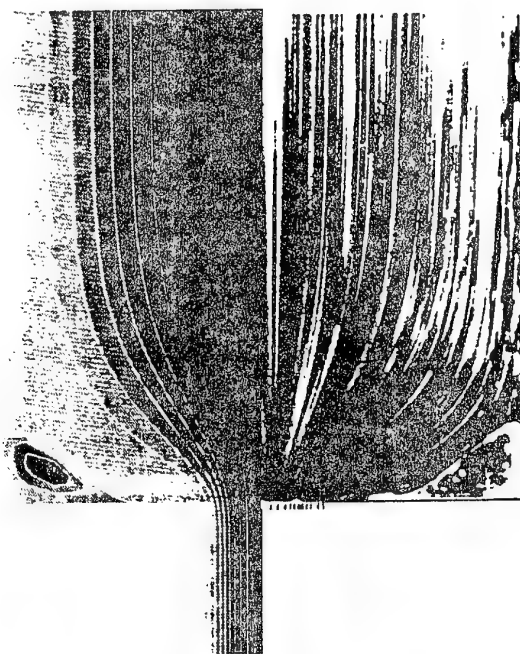


Figure 36. Comparison between experimental and calculated streamlines for the flow of a Newtonian fluid through a 4:1 contraction.

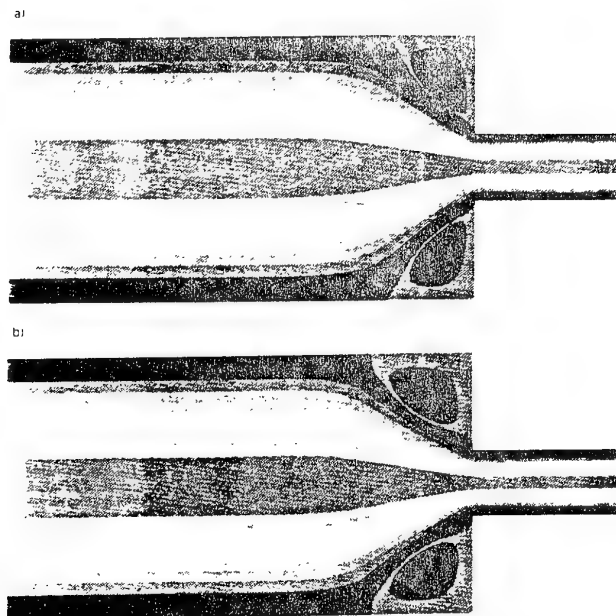


Figure 37. Vortex enhancement due to viscoelasticity in the 4:1 contraction problem (a) at $De = 15$ and (b) $De = 35$.

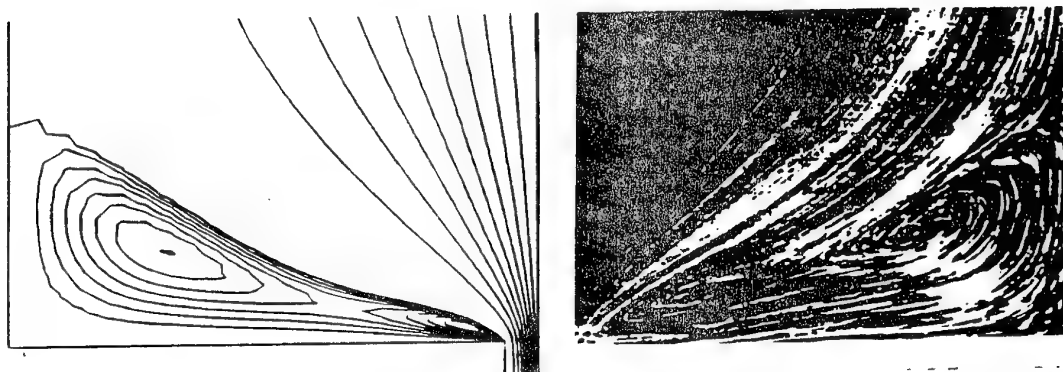


Figure 38. Comparison between experimental and numerical results showing the appearance of lip vortices in the flow of polyacrylamide-in-water solution through an abrupt contraction [40].

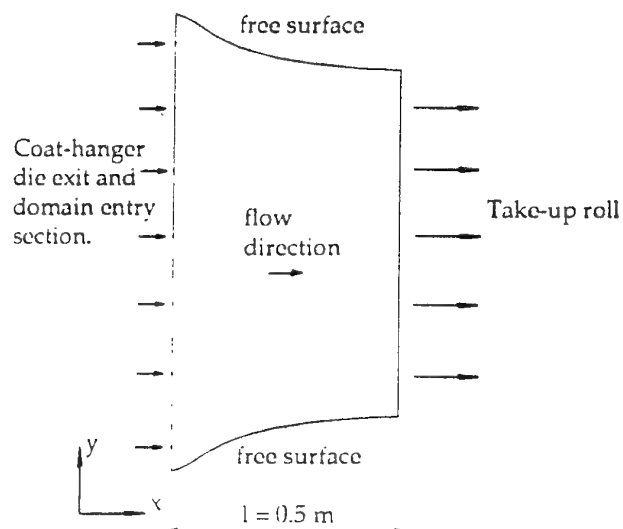


Figure 39. The film stretching process: geometry and boundary conditions.

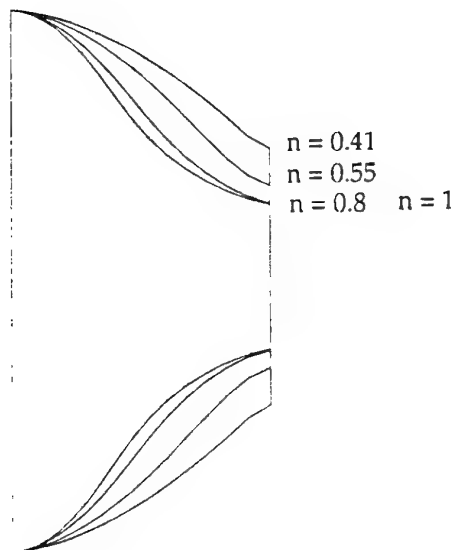


Figure 40. Necking for different values of the power-law index; the draw ratio is equal to 30.

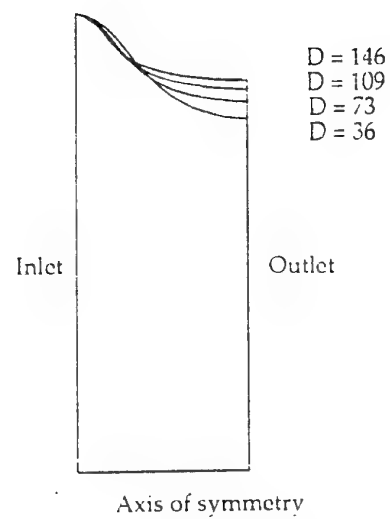


Figure 41. Numerical simulation of film stretching of a viscoelastic fluid with increasing values of the draw ratio.

References

- [1] D.V. Boger, D.U. Hur, R.J. Binnington, J. Non-Newtonian Fluid Mech., 20, 31 (1986)
- [2] H.A. Barnes, J.F. Hutton, K. Walters, An Introduction to Rheology, Elsevier (1989)
- [3] R.B. Bird, R.C. Armstrong, O. Hassager, Dynamics of Polymeric Liquids, Vol. 1: Fluid Mechanics, 2nd edition, Wiley, New-York (1987)
- [4] J.G. Oldroyd, Proc. Royal Soc., A200, 523 (1950)
- [5] N. Phan-Thien, R.I. Tanner, J. Non-Newtonian Fluid Mech., 2, 353 (1977)
- [6] M.W. Johnson, D. Segalman, J. Non-Newtonian Fluid Mech., 2, 255 (1977)
- [7] A.I. Leonov, Rheol. Acta 15, 85 (1976)
- [8] H. Giesekus, J. Non-Newtonian Fluid Mech., 11, 69 (1982)
- [9] R.I. Tanner, Engineering Rheology, Clarendon Press, Oxford (1985)
- [10] B. Bernstein, E.A. Kearsley, L.J. Zapas, Trans. Soc. Rheol., 7, 391 (1963)
- [11] M.H. Wagner, Rheol. Acta 16, 43 (1977)
- [12] A.C. Papanastasiou, L.E. Scriven, C.W. Macosko, J. Rheol., 27, 387 (1983)
- [13] M.H. Wagner, Rheol. Acta 15, 136 (1976)
- [14] R.G. Larson, Constitutive Equations for Polymer Melts and Solutions, Butterworths, Boston (1988)
- [15] M.J. Crochet, A.R. Davies, K. Walters, Numerical Simulation of Non-Newtonian Flow, Elsevier, Amsterdam (1984)
- [16] Th. Avalosse, Ph.D. Thesis, Louvain-la-Neuve, Belgium
- [17] K. Kouba, J. Vlachopoulos, Theoretical and Applied Rheology, vol 1., Elsevier 374 (1992)
- [18] R.E. Nickell, R.I. Tanner, B. Caswell, J. Fluid Mech. 65, 189 (1974)
- [19] S.F. Kistler, L.E. Scriven, Computational analysis of polymer processing (Eds J.R.A. Pearson and S.M. Richardson), Applied Science, 243 (1983)
- [20] V. Legat, J.M. Marchal, Int. J. Numerical Meth. Fluids 16, 29 (1993)
- [21] M. Fortin, Int. J. Numerical Meth. Fluids 1, 347 (1981)
- [22] V. Legat, J.M. Marchal, Int. J. Numerical Meth. Fluids 14, 609 (1992)
- [23] C. Reese, Proceedings ANTEC '94, 94 (1994)
- [24] M.J. Crochet, Rubber Chemistry and Technology, 62, 426 (1989)
- [25] M.J. Crochet, V. Legat, J. Non-Newtonian Fluid Mechanics, 42, 283 (1992)
- [26] W.J. Lunsman, L. Genesier, R.C. Armstrong, R.A. Brown, J. Non-Newtonian Fluid Mechanics, 48, 63 (1993)
- [27] H.K. Rasmussen, O. Hassager, J. non-Newtonian Fluid Mech. 46, 289 (1993)
- [28] J.M. Marchal, M.J. Crochet, J. Non-Newtonian Fluid Mech., 26, 77 (1987)

- [29] D. Rajagopalan, R.C. Armstrong, R.A. Brown, J. Non-Newtonian Fluid Mech., 36, 135 (1990)
- [30] F. Debae, V. Legat, M.J. Crochet, J. Rheology, 38, 421 (1994)
- [31] A. Goublomme, B. Draily, M.J. Crochet, J. non-Newtonian Fluid Mech., 44, 171 (1992)
- [32] D.D. Joseph, J. Matta, K. Chen, J. Non-Newtonian Fluid Mech. 24, 31 (1987)
- [33] R.J. Koopmans, Pol. Engng. & Science, 32, 1741 (1992)
- [34] B. Debbaut, B. Hocq, J. Non-Newtonian Fluid Mech., 43, 103 (1992)
- [35] B. Debbaut, Computational Fluid Dynamics 1992 (Ch. Hirsch ed.) 1027 (1992)
- [36] H. Nguyen, D.V. Boger, J. Non-Newtonian Fluid Mech. 7, 353 (1979)
- [37] D.V. Boger, M.J. Crochet, R.A. Keiller, J. Non-Newtonian Fluid Mech., 44, 267 (1992)
- [38] D.V. Boger, K. Walters, Rheological Phenomena in Focus, Elsevier (1993)
- [39] G.H. McKinley, W.P. Raiford, R.A. Brown, R.C. Armstrong, J. Fluid Mech. 223, 411 (1991)
- [40] B. Purnode, M.J. Crochet, to be published
- [41] R.B. Bird, P.J. Dotson, N.L. Johnson, J. Non-Newtonian Fluid Mech., 7, 213 (1980)
- [42] M.J. Crochet, B. Debbaut, J.M. Marchal, ZAMP, in press (1995)
- [43] H. Giesekus, Rheol. Acta, 8, 411 (1968)

von Karman Institute for Fluid Dynamics

Lecture Series 1995-03

INDUSTRIAL COMPUTATIONAL FLUID DYNAMICS

April 3 - 7, 1995

MODELLING OF FLOWS WITH UNKNOWN FREE SURFACES

S. Subbiah

Fluent Inc., U.S.A.

MODELLING OF FLOWS WITH UNKNOWN FREE SURFACES

S. Subbiah, Ph.D.
Fluent Inc.
10 Cavendish Court
Lebanon, NH 03766, U.S.A.

Contents

Introduction	1
1 Fixed Mesh Methods	1
1.1 The MAC method	2
1.2 The VOF method	4
1.3 Surface Tension Effects	5
2 Moving Mesh Methods	5
2.1 Lagrangian Treatment	6
2.2 Arbitrary Lagrangian Eulerian Treatment	6
2.3 Background Review	7
3 Variational Formulation	8
3.1 Spectral Element Discretization	10
3.2 Steady-State Solvers	11
3.3 Free Surface Algorithm for Low Surface Tension	15
3.4 Free Surface Algorithm for High Surface Tension	16
4 Conclusion	18

Modelling of Flows with Unknown Free Surfaces

S. Subbiah, Ph.D.
Fluent Inc.
10 Cavendish Court
Lebanon, NH 03766, U.S.A.

Introduction

This lecture reviews the computational approaches for the solution of the incompressible Navier-Stokes equations in a domain bounded in part by an unknown free surface whose location is desired to be tracked as part of the solution.

Free surface flows occur in many industrial processes where one or more of the fluid boundaries is unknown and is desired as part of the solution. Examples include coating flows, extrusion, coextrusion, melting/freezing processes, casting, mold filling, etc. From the modelling viewpoint, the presence of this unknown free boundary adds an extra level of complexity to the solution of the non-linear Navier-Stokes system. The free surface has to be represented and tracked in such a manner that appropriate boundary conditions can be applied on the free boundary, and the overall problem solved coupled to the main flow. Often this means that the CFD practitioner has to consider one of several choices in terms of how the free surface interacts with the computational mesh used to solve the flow equations:

- Fixed mesh (Eulerian)
- Moving mesh (Lagrangian)
- Moving mesh (Arbitrary Lagrangian-Eulerian)

1 Fixed Mesh Methods

Some of the earlier approaches to solving free boundary problems suggested treating the domain of interest by a computational mesh which is fixed in space and time. The free

surface is then tracked as an internal, migrating boundary whose position is tracked via a scalar representation of the presence of liquid.

1.1 The MAC method

The Marker And Cell Method (MAC), first proposed by Harlow and Welch (1965) was designed to model time-dependent, incompressible flows with free surfaces. The flow governing equations were solved over a fixed mesh using a finite difference discretisation.

$$\frac{\partial u}{\partial x} + \frac{\partial v}{\partial y} = 0 \quad (1)$$

$$\frac{\partial u}{\partial t} + u \frac{\partial u}{\partial x} + v \frac{\partial u}{\partial y} = -\frac{1}{\rho} \frac{\partial p}{\partial x} + \nu \left(\frac{\partial^2 u}{\partial x^2} + \frac{\partial^2 u}{\partial y^2} \right) + g_x \quad (2)$$

$$\frac{\partial v}{\partial t} + u \frac{\partial v}{\partial x} + v \frac{\partial v}{\partial y} = -\frac{1}{\rho} \frac{\partial p}{\partial y} + \nu \left(\frac{\partial^2 v}{\partial x^2} + \frac{\partial^2 v}{\partial y^2} \right) + g_y \quad (3)$$

The authors suggested a control volume discretization on a structured mesh, with a staggered representation of velocities and pressure on each cell. The MAC method then introduces “marker” particles into those cells that are filled with fluid at time $t = 0$. The solution procedure is then as follows:

- Solve the unsteady flow field (u, v, p) for one time step
 - on those cells with marker particles only
 - subject to specified boundary conditions
- Move each marker particle to a new position based upon the local velocity field.
- Determine the new free surface location.
- Resolve the unsteady flow field and continue.

The boundary condition that the authors applied on the free surface essentially imposed a normal stress balance across the free surface. For example, consider two fluids of viscosities μ_1 and μ_2 . Let the interfacial surface tension coefficient be σ and denote the surface curvature as κ . Then a normal stress balance yields:

$$\left(-p_1 + 2\mu_1 \frac{\partial u_n}{\partial n} \right) - \left(-p_2 + 2\mu_2 \frac{\partial u_n}{\partial n} \right) = \sigma \kappa \quad (4)$$

The above boundary condition can be further simplified if we were to make the following assumptions about the flow system:

- Let $\mu_1 \gg \mu_2$ (say, water and air).
- Let $\sigma = 0$ and let $p = 0$ on the free surface
- Then, the normal stress balance statement becomes:

$$-p_1 + 2\mu_1 \frac{\partial u_n}{\partial n} = p_2 = 0 \quad (5)$$

- Which yields a simplified set of b.c. on the free surface:

$$\begin{aligned} p &= 0 \\ \frac{\partial u_n}{\partial n} &= 0 \end{aligned}$$

To locate and describe the free surface, the authors define any cell with a marker particle that is adjacent to an empty cell as a surface cell. The free surface is then defined by the line segments connecting the outermost marker particles. With this approach, in general, the number of marker particles has to be greater than the number of cells for good resolution of the free surface location. In fact, the resolution of the free surface depends upon *both* the number of marker particles as well as the no. of cells.

Once all the boundary cells have been flagged with appropriate boundary conditions, the unsteady flow equations are solved for one time step. The authors used an explicit update here, which has a limitation on the size of the time step that can be taken (due to numerical stability constraints).

$$\Delta t < \frac{1}{2\nu} \left(\frac{\Delta x^2 \Delta y^2}{\Delta x^2 + \Delta y^2} \right) \quad (6)$$

The marker particles are then moved to their new positions x_m, y_m using locally averaged velocities u_m, v_m :

$$\begin{aligned} x_m^{t+1} &= x_m^t + u_m \Delta t \\ y_m^{t+1} &= y_m^t + v_m \Delta t \end{aligned}$$

The marker velocities are calculated as a weighted average of the nearest known cell velocities:

$$u_m = \frac{A_1 u_1 + A_2 u_2 + A_3 u_3 + A_4 u_4}{\Delta x \Delta y}$$

where A_i represents a weighting based upon the distance from the marker location to the nearest nodes where the velocity data is stored.

Although a powerful technique, the MAC method has some limitations:

- The calculation of the free surface location is very sensitive to no. of marker particles used.

- It is difficult to calculate surface curvatures accurately, and hence to include surface tension effects.
- In some cases, certain fluid cells within a domain might temporarily not contain any particles. Marking scheme should be sophisticated enough to ensure that false internal surfaces are not produced.
- Time step size is limited by Δx^2 and by ν^{-1} . Calculations for large mesh sizes and large values of viscosity can be computationally expensive.
- Inaccurate for long time span simulations (numerical smearing)

1.2 The VOF Method

The Volume Of Fluid (VOF) method was proposed by Hirt and Nichols (1981) to address some of the limitations of the MAC method. The main change is to move away from using marker particles, and instead, use a function F that indicates the volume of fluid in each cell. The discretisation continues to use a finite volume approach on a fixed mesh.

The function F is defined as the (normalized) volume of fluid in each cell.

$$\begin{aligned} F = 0 & \quad \text{Empty Cell} \\ F = 1 & \quad \text{Fluid Cell} \\ 0 < F < 1 & \quad \text{Surface Cell} \end{aligned}$$

The function is defined at the cell centers of each cell (only 1 storage word per cell). How is the free surface described with this approach? In an analogous manner to the MAC method, surface cells are those that contain non-zero values of F and are adjacent to at least one cell that has $F = 0$. Assume that the free surface boundary can be represented by a straight line cutting through the cell. The first step is to determine the slope of the free surface line for that cell. This is determined by noting that the normal direction on the free surface is the direction in which F is varying most rapidly. Next, the free surface boundary is located by finding the position at which the free surface intersects the known amount of fluid volume in the cell.

As with the MAC method, the pressure boundary condition is interpolated (or extrapolated) to ensure the correct pressures are posed on the surface cells. Once all the boundary cells have been flagged with the appropriate boundary conditions, the unsteady flow calculations are performed for the next time step.

The transport of the scalar F is defined as a purely convected process.

$$\frac{\partial F}{\partial t} + u \frac{\partial F}{\partial x} + v \frac{\partial F}{\partial y} = 0$$

The discretized form of the above equation for F is solved in each cell. Care must be taken to avoid the numerical dissipation of F during the solution (using upwinding, second-order upwinding, QUICK, etc.)

After the convective calculation is complete, a pass has to be made throughout the mesh to reset values of F .

- If $F < 0$, then $F = 0$.
- If $F > 1$, then $F = 1$.

These changes in F are also included in the accumulated volume change.

1.3 Surface Tension Effects

With the more accurate representation of the free surface location by the VOF method, it is possible to include surface tension effects in the free surface boundary conditions. Here,

- Normal stress:

$$p_{ambient} - p + 2\mu \frac{\partial u_n}{\partial n} = \sigma \kappa$$

- Tangential Stress:

$$\nu \left(\frac{\partial u_n}{\partial t} + \frac{\partial u_t}{\partial n} \right) = 0$$

However, the calculations are still limited by the accuracy of the curvature evaluation of the free surface. The solutions can be improved by the (costly) increase in mesh size.

In summary, the VOF method enables the natural tracking of complicated, colliding free surfaces. The method is best suited for modeling inviscid flows neglecting surface tension effects.

2 Moving Mesh Methods

The use of Eulerian methods (MAC, VOF) have traditionally involved large storage and computing resources. The need for large meshes comes about due to (a) the need to cover the entire possible range of fluid motion, and (b) the need to locate the free surface accurately. An alternate approach would be to fix a mesh on the fluid domain only such that:

- The mesh is only as large as the fluid domain
- The free surface is an explicit boundary of the mesh itself

2.1 Lagrangian Treatment

One approach is to fit the fluid domain with a mesh (BFC, finite element, etc.) The free surface then directly forms a portion of the mesh boundary. At every time step, the flow field is evaluated and all nodes (including the free surface nodes) are relocated with their local velocities. The advantage of this approach is that it is Compact and efficient. The disadvantage is that it is limited to small deformations only. (This approach is more popular in structural mechanics).

2.2 Arbitrary Lagrangian Eulerian Treatment

The Arbitrary Lagrangian Eulerian method (ALE) is also a moving mesh approach where only the fluid domain is meshed. The improvement comes from decoupling the free surface tracking from the bulk flow field analysis. The algorithm is as follows:

1. The nodes on the free surface are relocated based upon the surface flow field.
2. The surface nodes are smoothed (along the free surface) if excessive clustering is seen to have taken place.
3. The internal mesh is regenerated using the boundary nodes as constraints (minimizing mesh distortion).
4. The entire flow field (calculated on the old mesh) is mapped from the old mesh to the new mesh.
5. The flow equations are solved for the next time step on the new mesh.

Since the mesh deforms with the fluid, the use on an *unstructured* grid will allow for capturing truly arbitrary deformations. Since repeated mapping of data is called for and since this can lead to a diffusive corruption of the flow data, a *high-order, low diffusion* scheme would be an attractive choice. The *Spectral Element Method* provides both the unstructured grid as well as the high-order resolution, making it an attractive forum to explore free surface flows with the ALE approach.

Since the ALE approach allows us to track the surface explicitly, the curvature (κ) can also be evaluated accurately. As a result, the complete set of stress boundary conditions can be treated with this scheme.

Consider two fluids of viscosities μ_1 and μ_2 . Let the interfacial surface tension coefficient be σ and denote the surface curvature as κ . Then a normal stress balance yields:

$$\left(-p_1 + 2\mu_1 \frac{\partial u_n}{\partial n}\right) - \left(-p_2 + 2\mu_2 \frac{\partial u_n}{\partial n}\right) = \sigma \kappa \quad (7)$$

- And a tangential stress balance yields:

$$\mu_2 \left(\frac{\partial u_n}{\partial s} + \frac{\partial u_s}{\partial n} \right) - \mu_1 \left(\frac{\partial u_n}{\partial s} + \frac{\partial u_s}{\partial n} \right) = \frac{\partial \sigma}{\partial s} \quad (8)$$

Recently, Lee Ho et al. (1992) have applied a high-order finite element approach (spectral element method) towards the tracking of free boundary flow problems via an ALE scheme. In the spatial discretization procedure, a Legendre spectral element method is used to generate the discrete equations. For effective solution of the set of algebraic equations, the geometry is decoupled from the fluid velocity and pressure. In addition, two different algorithms are proposed depending on the importance of surface tension effects.

2.3 Background Review

Multi-phase and free-surface flows are encountered in a large number of important engineering applications, particularly in the area of material processing. As the geometry of the free boundary constitutes a part of the solution, its presence significantly complicates the solution of the Navier-Stokes equations. Analytical solutions of practical free boundary flow problems are virtually nonexistent, and increasingly numerical methods are employed for the design and analysis of these flow processes. Despite the many physical complexities embodied in the flow, most of these flow processes operate at a steady state. Thus, the flow characteristics at steady state is of practical interest for both design and analysis purposes. Moreover, many studies of flow instability require the availability of a (nominal) steady state to which a perturbation is superimposed. Hence, effective numerical techniques for the evaluation of steady state solutions are essential for these types of applications.

Transient algorithms can, of course, be used directly or in conjunction with extrapolation techniques to predict the steady state response. However, in practical flow systems the required physical models are often quite complex (such as variable fluid properties and nonlinear boundary conditions); these models often lead to multiple physical time scales which can preclude effective use of transient algorithms. For example, for explicit and semi-implicit algorithms (which do not require Newton-Raphson or similar equilibrium iterations), the size of the time step increment is restricted by stability requirement to be smaller than the smallest physical time scale, while the time required to reach steady state is governed by the largest physical time scale. In either case, the physical effect whose time scale is the most costly to accommodate (computationally) may not even be the dominant effect that influences the flow behavior. Thus, the end result is the requirement of a large number of time steps in order to obtain the steady state solution, which is computationally inefficient. Implicit transient algorithms are not restricted by stability requirement; however, the solution of the nonlinear equations at each time step generally requires equilibrium iterations which have to be repeated over many time steps (to reach steady state). Thus, this approach can be as computationally intensive as well. Clearly, specially designed steady algorithms are needed to adequately address the needs of these free-surface flow applications.

3 Variational Formulation

Consider viscous steady incompressible flow of a Newtonian fluid, with density ρ and viscosity μ , in a three-dimensional domain Ω . The domain boundary Γ is decomposed as $\Gamma = \Gamma_0 \cup \Gamma_\sigma$, with (Dirichlet) no-slip boundary conditions imposed on Γ_0 , and (Neumann) traction boundary conditions imposed on Γ_σ .

The equations governing the fluid flow are the steady Navier-Stokes and continuity equations which can be written as:

$$\rho u_j u_{i,j} = \tau_{ij,j} + f_i \quad \text{in } \Omega, \quad (2.1a)$$

$$u_{i,i} = 0 \quad \text{in } \Omega, \quad (2.1b)$$

subject to the boundary conditions

$$u_i = 0 \quad \text{on } \Gamma_0, \quad (2.2)$$

$$\tau_{ij} n_j = \sigma \kappa n_i + \nabla_i \sigma \quad \text{on } \Gamma_\sigma, \quad (2.3)$$

where u_i is the fluid velocity, f_i is the body force, and τ_{ij} is the stress tensor defined as

$$\tau_{ij} = -p \delta_{ij} + \mu (u_{i,j} + u_{j,i}), \quad (2.4)$$

where p is the pressure (relative to zero ambient) and δ_{ij} is the Kronecker delta. On the free surface Γ_σ , σ is the surface tension coefficient, n_i is the outward unit normal, ∇_i is the surface gradient operator, and κ is the curvature in two-dimensional geometry and twice the mean curvature in three-dimensional geometry (the curvature along a surface coordinate is considered positive if the liquid region below the free surface along that surface coordinate is concave). We shall use the following notation and conventions: Roman indices range from 1 to 3, a subscript comma denotes derivative (e.g., $u_{i,j} = \partial u_i / \partial x_j$), and repeated Roman indices are summed from 1 to 3. The governing equations are in reference to a Cartesian coordinate system, therefore we need not distinguish between covariant and contravariant components of vectors and tensors. However, this distinction is required in three-dimensional geometry if a surface-intrinsic representation is adopted on the free surface.

Let the two-dimensional free surface be described by a local curvilinear coordinate system r^α , $\alpha = 1, 2$, which are in general non-orthogonal. Recall several useful definitions from differential geometry [18]:

$$g_{\alpha i} = x_{i,\alpha}, \quad (2.5)$$

$$g_{\alpha i} g_{\beta i} = g_{\alpha\beta}, \quad (2.6)$$

$$g_{\alpha i} g_i^\beta = \delta_\alpha^\beta, \quad (2.7)$$

$$g = \sqrt{|g_{\alpha\beta}|}; \quad (2.8)$$

where $g_{\alpha i}$ is the covariant base vector, g_i^α is the contravariant base vector, $g_{\alpha\beta}$ is the covariant metric tensor, δ_α^β is the Kronecker delta. Using the above definitions, the surface gradient term in (2.3) can be expressed as

$$\nabla_i \sigma = g_i^\alpha \sigma_{,\alpha}, \quad (2.9)$$

where repeated Greek indices are summed from 1 to 2.

The variational form of (2.1) to (2.4) is given by [9-11]: find (u_i, p) , with $u_i \in H_0^1(\Omega)$ and $p \in L^2(\Omega)$, such that

$$\begin{aligned} \int_{\Omega} \{ \rho v_i u_{j,i} + v_{i,j} [-p \delta_{ij} + \mu (u_{i,j} + u_{j,i})] - v_i f_i \} dV - \\ I_\sigma(v_i) = 0 \quad \forall v_i \in H_0^1(\Omega), \end{aligned} \quad (2.10a)$$

$$\int_{\Omega} q u_{i,i} dV = 0 \quad \forall q \in L^2(\Omega); \quad (2.10b)$$

where v_i and q are test functions, $L^2(\Omega)$ is the space of functions which are square integrable, and $H_0^1(\Omega)$ is the space of functions which are in $L^2(\Omega)$, whose first derivatives are in $L^2(\Omega)$, and which vanish on Γ_0 . The term $I_\sigma(v_i)$ is the variational form that corresponds to natural imposition of the traction boundary conditions given in (2.3). In three-dimensional geometry, this form can be written as [11]:

$$I_\sigma(v_i) = \oint_{\gamma} \sigma v_i g g_i^\alpha e_{\alpha\beta} dr^\beta - \int_{\Gamma_\sigma} v_{i,\alpha} \sigma g_i^\alpha dA, \quad (2.11)$$

where γ is the line segment that bounds the free surface Γ_σ , $e_{\alpha\beta}$ is the permutation symbol ($e_{11} = e_{22} = 0$, $e_{12} = -e_{21} = 1$), and $dA = g dr^1 dr^2$; see Fig. 2.1.

Note that in two-dimensional geometry, (2.11) reduces to the following variational form which is presented in [4]:

$$I_\sigma(v_i) = (\sigma v_i t_i)|_a^b - \int_a^b v_{i,\zeta} \sigma t_i d\zeta, \quad (2.12)$$

where t_i is the unit tangent vector and ζ is the curvilinear coordinate on the free surface segment \overline{ab} ; see Fig. 2.2.

The variational forms given in (2.11) and (2.12) have the following important advantages which are discussed in [11]. First, it automatically generates the equivalent normal and

tangential traction conditions as given in (2.3), including the effect of variable surface tension (Marangoni flows) [19,20]. Second, in the subsequent domain decomposition it provides a natural (weak) condition for continuity of slope across elemental boundaries on the free surface. Third, it is entirely surface-intrinsic, with no need to reference global coordinates or locally orthogonal systems. Lastly, it requires a lower-order geometric representation when compared with formulations that use the mean curvature directly in the imposition of the normal traction boundary condition.

3.1 Spectral Element Discretization

In the spectral element discretization [12,13], we subdivide the domain into K disjoint elements (quadrilaterals in two-dimensional geometry and hexahedrons in three-dimensional geometry): $\bar{\Omega} = \bigcup_{k=1}^K \bar{\Omega}_k$, and we shall require that the variational statement be satisfied for the piecewise high-order polynomial subspaces for the velocity and pressure, that is, $(u_i)_h \in \mathcal{X}_h$ and $p_h \in \mathcal{M}_h$, where the subspaces \mathcal{X}_h and \mathcal{M}_h are defined as

$$\mathcal{X}_h = \mathcal{H}_0^1(\Omega) \cap \mathcal{P}_{N,K}(\Omega) , \quad (3.1a)$$

$$\mathcal{M}_h = \mathcal{L}^2(\Omega) \cap \mathcal{P}_{N-2,K}(\Omega) ; \quad (3.1b)$$

where $\mathcal{P}_{N,K}(\Omega) = \{\Phi \in \mathcal{L}^2(\Omega); \Phi|_{\Omega_k} \in \mathcal{P}_N(\Omega_k)\}$, and $\mathcal{P}_N(\Omega_k)$ denotes the tensor-product space of all polynomials of degree N or less with respect to each spatial variable. It is shown in [14-16] that the above choice of approximation spaces are compatible in the sense that spurious pressure modes are not present in the solution. In addition, the discretization error is only a constant away from the best fit in the given approximation spaces.

For numerical evaluation of the elemental integrals [13], we perform a mapping of the physical (x_1, x_2, x_3) -system into a local (r, s, t) -system : $(x_1, x_2, x_3)^k \in \Omega_k \Rightarrow (r, s, t) \in \Lambda \times \Lambda \times \Lambda$; $\Lambda =]-1, 1[$, and we define two integration rules, the first one (for the velocity mesh) by taking the tensor product of Gauss-Lobatto formulas, and the second rule (for the pressure mesh) by taking the tensor product of Gauss formulas.

We now introduce an interpolant Gauss-Lobatto-Legendre basis for the spectral element approximation space \mathcal{X}_h [13]:

$$(x_i)^k(r, s, t) = (x_i)_{lmn}^k h_l(r) h_m(s) h_n(t) , \quad (3.2)$$

where $(x_i)_{lmn}^k$ is the physical x_i -coordinate of local collocation point (l, m, n) of element k , $h_p(z)$ is the N th order elemental Lagrangian interpolant through the Gauss-Lobatto points, that is, $h_q(z_p) = \delta_{pq}$, and summation is performed for $l, m, n = 0, 1, 2, \dots, N$. Thus, the coordinate x_i , body force $(f_i)_h$, fluid velocity $(u_i)_h$ and test function $(v_i)_h$ are expanded in the same tensor-product form as given by (3.2). Similarly we introduce an interpolant Gauss-Legendre basis for the space \mathcal{M}_h and we expand the pressure p_h (and the test function q_h) as :

$$p_h^k(r, s, t) = \tilde{p}_{lmn}^k \tilde{h}_l(r) \tilde{h}_m(s) \tilde{h}_n(t), \quad (3.3)$$

where \tilde{p}_{lmn}^k is the pressure of element k , local collocation point (l, m, n) , $\tilde{h}_m(z)$ denotes the $(N-2)$ th order elemental Lagrangian interpolants through the Gauss points, and summation is performed for $l, m, n = 1, 2, \dots, (N-1)$.

The final discrete system of algebraic equations are obtained by imposing successively (at all degrees-of-freedom) test functions $(v_i)_h$ and q_h which are unity at one global collocation point while zero at all others, and we arrive at:

$$\mathbf{D}_i^T \mathbf{P} - \mathbf{A}_{ij} \mathbf{U}_j + \mathbf{F}_i + \mathbf{F}_{\sigma i} - \mathbf{C} \mathbf{U}_i = \mathbf{0}; \quad (3.4a)$$

$$\mathbf{D}_i \mathbf{U}_i = \mathbf{0}; \quad (3.4b)$$

where \mathbf{A}_{ij} is the discrete viscous coefficient matrix, \mathbf{D}_i is the discrete gradient matrix, \mathbf{U}_i and \mathbf{P} are vectors of the fluid velocity and pressure, respectively, at all the collocation points, \mathbf{F}_i is the body force vector, $\mathbf{F}_{\sigma i}$ is the surface force vector defined on Γ_σ that corresponds to $I_\sigma(v_i)$ in (2.10a), and \mathbf{C} comprises the advection contributions. Thus, (3.4) is the discrete spectral element equations that govern steady viscous incompressible free-surface flows. We note that since the free surface geometry is not known apriori, the nodal coordinates \mathbf{X}_i at steady state must be determined in conjunction with (3.4).

3.2 Steady-State Solvers

As the geometry of the computational domain constitutes part of the solution due to the presence of a free surface, an effective steady state solution strategy is to compute successive approximations of the solution via iteration. To this end, we consider the following iterative equations obtained by rewriting the discrete equations (3.4) in terms of the incremental solution variables and including the update of the nodal coordinates on the free surface Γ_σ :

$$\begin{aligned} (\mathbf{D}_i^m)^T \Delta \mathbf{P}^{m+1} - \mathbf{A}_{ij}^m \Delta \mathbf{U}_j^{m+1} - \Delta \mathbf{C}^m \Delta \mathbf{U}_i^{m+1} = \\ -(\mathbf{D}_i^m)^T \mathbf{P}^m + \mathbf{A}_{ij}^m \mathbf{U}_j^m - \mathbf{F}_i^m - \mathbf{F}_{\sigma i}^m + \mathbf{C}^m \mathbf{U}_i^m \end{aligned} \quad \text{in } \Omega, \quad (4.1a)$$

$$\mathbf{D}_i^m \Delta \mathbf{U}_i^{m+1} = -\mathbf{D}_i^m \mathbf{U}_i^m \quad \text{in } \Omega. \quad (4.1b)$$

$$\mathbf{H}^m \Delta \mathbf{X}_i^{m+1} = \Delta \mathbf{R}_i^m \quad \text{on } \Gamma_\sigma. \quad (4.2)$$

$$\mathbf{U}_i^{m+1} = \mathbf{U}_i^m + \Delta \mathbf{U}_i^{m+1} \quad \text{in } \Omega, \quad (4.3a)$$

$$\mathbf{P}^{m+1} = \mathbf{P}^m + \Delta \mathbf{P}^{m+1} \quad \text{in } \Omega. \quad (4.3b)$$

$$\mathbf{X}_i^{m+1} = \mathbf{X}_i^m + \Delta \mathbf{X}_i^{m+1} \quad \text{on } \Gamma_\sigma . \quad (4.4)$$

In the above set of iterative equations, the superscript m is the iteration counter, $\Delta \mathbf{U}_i$, $\Delta \mathbf{P}$ and $\Delta \mathbf{X}_i$ are vectors of the incremental nodal-point fluid velocity, pressure and coordinates, respectively; $\Delta \mathbf{C}$ denotes the linearized convection operator; \mathbf{H} is the curvature operator and $\Delta \mathbf{R}_i$ is the vector which stores the residual/source contribution, respectively, used in the free-surface geometry solution. Both \mathbf{H} and $\Delta \mathbf{R}_i$ in (4.2) must be formulated in conjunction with the surface force vector \mathbf{F}_σ in (4.1a); the selection of the appropriate formulation depends largely on the role played by surface-tension effects, as described in Sections 4.1 and 4.2 below. The following remarks apply concerning the above formulation.

First, note that the equations are completely general, as they are applicable to both two-dimensional and three-dimensional geometries, as well as to constant or variable material properties. Second, one can deliberately make use of a decoupling strategy in which the solution of the Navier-Stokes and continuity equations is decoupled from that of the geometry equations. That is, (4.1) and (4.2) are solved alternately based on the last computed solution rather than simultaneously. One of the disadvantages of such an approach could potentially be a slower convergence rate. However, the decoupled approach offers the following important advantages.

- The number of nodal degrees of freedom in either (4.1) or (4.2) is greatly reduced compared to that of a fully coupled approach. This is an important consideration when using direct solvers since for high-order discretization methods, the bandwidth of the assembled matrices are substantially larger than that of low-order methods.
- The decoupling of (4.1) and (4.2) facilitates easy switch of the free-surface boundary conditions between the kinematic and the dynamic conditions during the solution of these equations; this option allows for the design of a novel scheme which can achieve rapid convergence to steady state, as described in Section 4.2.
- The decoupled form allows for the possible use of different types of solvers for the solution of (4.1) and (4.2); this flexibility enables the employment of optimal solvers.
- This approach is easily extendable to the modelling of more complex flow physics; for example, the thermal energy transport equation as well as the transport equations for any other passive scalars can readily be introduced within the proposed framework (as an additional system of equations), without further increase in the size and bandwidth of the matrices.

Before we consider the details in the proposed algorithms, we briefly review some issues related to application of a transient free-surface algorithm from which important insights can be gained to benefit the design of effective steady free-surface algorithms. We consider a front-tracking transient algorithm which uses semi-implicit time integration schemes to decouple all nonlinearities; that is, the two-dimensional transient spectral element algorithm

[10] and its extension to three-dimensional geometry [11]. The use of a front-tracking approach requires an arbitrary Lagrangian-Eulerian description [9] and hence the employment of a mesh velocity w_i for which the following kinematic conditions must hold on the free surface:

$$w_i = (u_k n_k) n_i . \quad (4.5)$$

Using (4.5), a boundary-value-problem can be constructed by applying an appropriate elliptic operator to extend the mesh velocity into the interior domain. With the establishment of the mesh velocity field, the time evolution of the flow domain can be evaluated as

$$\frac{dx_i}{dt} = w_i . \quad (4.6)$$

Applying the semi-implicit strategy given in [10], the Stokes operator in the momentum equations is treated implicitly, while the convection operator is treated explicitly. In addition, explicit schemes are employed for (4.6) to decouple the Navier-Stokes equations from the geometry evolution equations. In this way, costly iterative procedures for implicit treatment of all nonlinearities and couplings can be effectively avoided.

In the time integration of the free-surface flow equations, a semi-implicit scheme gives rise to two criteria and consequently two step size restrictions; the more stringent of the two must be satisfied for stability. For the convection operator, the critical step size Δt_{crit}^c is given by the Courant condition:

$$\Delta t_{crit}^c \propto \frac{h}{V} , \quad (4.7)$$

where h is the minimum mesh spacing and V is the characteristic flow speed. For the geometry evolution given in (4.6), the critical step size Δt_{crit}^σ is given by [9]

$$\Delta t_{crit}^\sigma \propto \sqrt{\frac{\rho h^3}{\sigma \pi^3}} . \quad (4.8)$$

We can now identify several drawbacks which arise from the use of the above transient semi-implicit scheme for evaluation of the *steady state* free-surface solution. First, whenever the surface tension effect is dominant (as in the case of a large surface tension coefficient coupled with small physical dimensions), it is clear that the critical step size given in (4.8) can be severely restrictive. Second, when the steady state is reached, the mesh velocity is everywhere zero from (4.6). Consequently, at steady state (4.5) reduces to

$$u_i n_i = 0 . \quad (4.9)$$

Transient algorithms are not able to exploit this important kinematic condition effectively to

speed up the convergence to the steady state solution. Third, even when the surface tension effect is small, the free surface evolution as governed by the kinematic conditions (4.5) may still require a substantial number of steps to reach steady state if the steady state is very far from the initial state.

As the free surface geometry deforms from an initial (unsteady) state towards the steady state, the dominant physical effect that effectuates this deformation needs to be identified. Since the surface tension contribution is directly involved in the normal traction boundary condition on the free surface:

$$n_i \tau_{ij} n_j = \sigma \kappa, \quad (4.10)$$

it is therefore plausible that in order to design an effective steady state free-surface solution schemes, it is advantageous to distinguish between flows dominated by surface tension from those dominated by others. In this study we consider the following three major physical forces that influence the free surface flow behavior: inertia, viscous and surface-tension forces. The relevant non-dimensional groups that indicate the balance of these forces are: the Reynolds number (inertia versus viscous effects)

$$Re = \frac{\rho V L}{\mu}, \quad (4.11)$$

where L and V are the characteristic length and velocity, respectively; the capillary number (viscous versus surface tension effects)

$$Ca = \frac{\mu V}{\sigma}; \quad (4.12)$$

the Weber number (surface tension versus inertia effects)

$$W = \frac{\sigma}{\rho L V^2}. \quad (4.13)$$

We now consider effective use of the boundary conditions (4.9) and (4.10) for the computation of the free-surface geometry. For the case where the surface-tension effect is insignificant (that is, $Ca \gg 1$ when $Re \ll 1$, or $W \ll 1$ when $Re \gg 1$), the use of (4.10) is clearly inefficient since physical forces other than those of surface tension are determining the free surface geometry. In addition, the use of an analogous form of (4.5) in the successive approximation of the geometry solution is also ineffective since its solution mechanism is similar to that of the semi-implicit transient schemes. In this study we achieve substantial improvement in convergence to the steady state by treating the contribution $u_i n_i$ as a source term for an elliptic free-surface operator rather than as a kinematic condition. This strategy is presented in Section 4.1 below. In the design of an effective algorithm for the surface-tension dominant case (that is, $Ca \ll 1$ when $Re \ll 1$, or $W \gg 1$ when $Re \gg 1$),

we are able to make use of (4.9) and (4.10) alternately in a novel way to achieve very rapid convergence. This strategy is described in Section 4.2.

In the following sections, for clarity of presentation we only consider two-dimensional geometry even though all of the above derivations and discussions are applicable both to steady two-dimensional and three-dimensional free-surface flows.

3.3 Free Surface Algorithm for Low Surface Tension

In this section we present the solution algorithm which is effective for free-surface flows not dominated by surface-tension effect. This algorithm is denoted as the “low- σ ” algorithm, and it consists of the following steps.

Step 1

Solve the discrete Navier-Stokes and continuity equations (4.1) for which $\mathbf{F}_{\sigma i}$ on Γ_{σ} is computed by imposition of both the *tangential* and the *normal* traction boundary conditions according to the variational form (2.12).

Step 2

Compute the quantity $u_i n_i$ on the free surface Γ_{σ} ; this quantity should be equal to zero at steady state according to (4.9).

Step 3

Compute the incremental coordinates on the free surface Γ_{σ} by solving (4.2); for which the vector $\Delta \mathbf{R}_i$ corresponds to the contribution of the source term $u_i n_i$ (with appropriate scaling), and the curvature operator \mathbf{H} corresponds to the second derivative operator with respect to the curvilinear free-surface coordinate ζ . The variational form for the generation of (4.2) is given in (4.14).

Step 4

Extend the incremental coordinates on the free surface into the interior domain by solving a boundary value problem with an appropriate elliptic operator (such as the Laplacian), and then updating the coordinates of all collocation points.

Step 5

Repeat Step 1 to Step 4, for which the evaluation of all operators are based on the newly updated geometry, until convergence is achieved.

We next describe the basis for (4.2) in order to formulate the required curvature operator and other contributions. For Step 3, the geometry equation (4.2) is generated based

on the following variational form:

$$-\int_a^b v_{i,\zeta} \Delta x_{i,\zeta} d\zeta + (v_i \Delta x_{i,\zeta})|_a^b = \int_a^b \lambda v_i (u_k n_k) n_i d\zeta ; \quad (4.14)$$

where λ is a scaling factor which limits the size of Δx_i in each curvature solve. The use of (4.14) has the following advantages. First, the formulation is consistent; that is, the steady state solution obtained from applying the above steps satisfies both (4.9) and (4.10) on the free surface. Second, the use of the contribution $u_i n_i$ as a source term (rather than as a kinematic condition) provides a faster spread of the “local deformations” along the entire free surface. In this way, the elliptic solve can be considered as a relaxation technique which accelerates the propagation of information. Third, it is sufficient for $(\Delta x_i)_h \in \mathcal{H}^1$ in (4.14). Lastly, the corresponding operator \mathbf{H} , being elliptic, provides smooth free-surface updates and is therefore a robust technique for the free-surface geometry solution.

3.4 Free Surface Algorithm for High Surface Tension

In this section we first present the solution algorithm for surface-tension dominant free-surface flows, followed by the derivation of the variational form on which the algorithm is based. This algorithm is denoted as the “high- σ ” algorithm, and it consists of the following steps.

Step 1

Solve the discrete Navier-Stokes and continuity equations (4.1) subject to the following boundary conditions on the free surface Γ_σ : the traction conditions according to (2.12) in the direction *tangent* to Γ_σ , and the kinematic condition according to (4.9) in the direction *normal* to Γ_σ ; the resulting traction force vector is denoted as $\mathbf{F}_{\sigma i}^{\text{ss}}$.

Step 2

Recompute the traction forces on the free surface Γ_σ using the variational form (2.12) for both the *tangential* and *normal* directions; this traction force vector is denoted as $\mathbf{F}_{\sigma i}$. Next, evaluate the difference between $\mathbf{F}_{\sigma i}^{\text{ss}}$ from Step 1 and $\mathbf{F}_{\sigma i}$, and denote the result as the residual force vector $\Delta \mathbf{R}_i$. Note that $\Delta \mathbf{R}_i = \mathbf{0}$ if only if the steady state is reached.

Step 3

Apply (4.2) to compute the incremental coordinates on the free surface Γ_σ , where $\Delta \mathbf{R}_i$ is computed in Step 2. The curvature operator \mathbf{H} defined on Γ_σ correspond to a second derivative operator with respect to the curvilinear free-surface coordinate ζ . The variational form from which (4.2) is generated is derived below.

Step 4

Extend the incremental coordinates on the free surface computed in Step 3 into the interior domain by solving a boundary-value problem with an appropriate elliptic operator (such as the Laplacian), then update the coordinates of all collocation points.

Step 5

Repeat Step 1 to Step 4, for which the evaluation of all operators are based on the newly updated geometry, until convergence is achieved.

We now describe the basis (that is, the appropriate variational form) from which the curvature operator \mathbf{H} and the residual force vector $\Delta \mathbf{R}_i$ in (4.2), together with the surface traction vector $\mathbf{F}_{\sigma i}$ in (4.1a) are formulated. In Step 1, the Navier-Stokes and continuity equations are solved subject to the following boundary conditions:

$$u_i^{ss} n_i = 0, \quad (4.15a)$$

$$t_i \tau_{ij}^{ss} n_j = \sigma_{,\zeta}, \quad (4.15b)$$

where the superscript "ss" indicates the use of the steady-state kinematic conditions (4.9). We remark that (4.15a) is imposed as an essential boundary condition while (4.15b) is imposed as a natural boundary condition through the use of (2.12). Hence, the approximation solution space for both the fluid velocity u_i and test functions v_i has to be modified to accommodate the imposition of (4.9).

We note that there are two boundary conditions on Γ_σ in the normal direction; that is, in addition to the kinematic condition (4.9) there is the normal traction condition given by (4.10). If the steady state configuration has not been reached, then the solution τ_{ij}^{ss} will not satisfy (4.10), and a residual of normal traction will result. Since in the surface tension dominant case the deformation of the free surface is directly effectuated by surface tension forces, we make use of this residual normal traction to formulate a consistent "driving force" for computing corrections to the free-surface geometry:

$$\Delta I_\sigma(v_i) = \int_a^b v_i [\tau_{ij}^{ss} n_j - \sigma \kappa n_i - \sigma_{,\zeta} t_i] d\zeta; \quad (4.16)$$

which can be rewritten as

$$\Delta I_\sigma(v_i) = \int_a^b v_i [\tau_{ij}^{ss} n_j - (\sigma t_i)_{,\zeta}] d\zeta, \quad (4.17)$$

using the following relation on Γ_σ :

$$\kappa n_i = t_{i,\zeta}. \quad (4.18)$$

Next, we consider an update of the free-surface geometry as defined by a new tangent vector

$\hat{t}_i :$

$$\hat{t}_i = t_i + \Delta t_i . \quad (4.19)$$

We now require that the change in geometry should approach the steady state configuration for which $\Delta I_\sigma(v_i) = 0$. Using this condition and substituting (4.19) into (4.17) and using

$$\Delta t_i = \Delta x_{i,\zeta} , \quad (4.20)$$

we obtain

$$\int_a^b v_i (\sigma \Delta x_{i,\zeta})_{,\zeta} d\zeta = \int_a^b v_i [\tau_{ij}^{ss} n_j - (\sigma t_i)_{,\zeta}] d\zeta . \quad (4.21)$$

Lastly, we perform integration by parts on both sides of (4.21) to we arrive at the desired form:

$$\begin{aligned} - \int_a^b v_{i,\zeta} \sigma \Delta x_{i,\zeta} d\zeta + (v_i \sigma \Delta x_{i,\zeta})|_a^b = \\ \int_a^b [v_i \tau_{ij}^{ss} n_j + v_{i,\zeta} \sigma t_i] d\zeta - (v_i \sigma t_i)|_a^b . \end{aligned} \quad (4.22)$$

This is the consistent variational form from which the discrete equations given by (4.2) are generated. The advantage of this formulation is that it results in a symmetric operator for Δx_i which allows for use of inversion techniques such as preconditioned conjugate gradient iterations. In addition, the application of integration-by-parts implies that $(\Delta x_i)_h \in \mathcal{H}^1$ is sufficient.

4 Conclusion

The treatment of fluid flows with free surfaces has been reviewed with two viewpoints: (1) Eulerian (fixed mesh) approaches (MAC, VOF methods) and (2) Deforming mesh approaches (ALE). The strength of the Eulerian approaches in capturing complex free surface deformations (even to the point of rupture) has been highlighted, with the remark that the weakness lies in the effort needed to locate free surface positions exactly as well in being able to include surface tension effects.

The ALE approaches are restricted to less severe deformations, but can track free surface locations and surface tension effects readily. The application of the spectral element method towards the ALE tracking of unknown free surfaces has been described. Two algorithms are reviewed for the solution of steady viscous free-surface flows, the selection between the two depends on the role played by surface tension in the flow physics. The algorithms have the following important advantages: (1) it is based on a general three-dimensional

variational approach which provides a natural and consistent treatment of variable material properties, and which provides natural (that is, in a weak sense) continuity conditions for both traction and slope across interelemental boundaries; (2) the use of the spectral element method in the spatial discretization provides a high-order representation of both the fluid flow fields and the flow geometry and hence the advantage of yielding more accurate solutions at comparable computational resources when compared to low-order elements; and (3) the iterative scheme employed in the solution of the discretized equations are formulated in a decoupled form which minimizes the size of elemental (and global) matrices, allows for easy inclusion of additional transport equations, and provides flexibility for use of different solution strategies and solvers for different equations.

Acknowledgement

The author wishes to express his gratitude to Dr. Lee-Wing Ho (Nektonics Inc.) for some of the material presented in this lecture, and to the staff at Fluent Inc. for providing a stimulating environment for research and development.

References

1. A. Sidi, W.F. Ford and D.A. Smith, "Acceleration of convergence of vector sequences", *J. Num. Anal., SIAM* 23 (1986) 178-196.
2. R.E. Nickell, R.I. Tanner and B. Caswell, The solution of viscous incompressible jet and free-surface flows using finite-element methods, *J. Fluid Mech.* 65 (1974) 189-206.
3. P.W. Chang, T.W. Patten, F.T. Adams and B.A. Finlayson, Galerkin and collocation finite element methods for Newtonian and viscoelastic fluids, in E. Hinton and R.L. Taylor, editors, *Recent advances in numerical methods in fluids*, Vol. 1, Ch.4 (Pineridge, Swansea, 1980).
4. K.J. Ruschak, A method for incorporating free boundaries with surface tension in finite element fluid-flow simulation, *Int. J. Num. Meth, Eng.* 15 (1980) 639-648.
5. S.F. Kistler and L.E. Scriven, "Coating flow theory by finite element and asymptotic analysis of the Navier-Stokes system", *Int. J. Num. Meth. Fluids* 4 (1984) 207-229.
6. H.P. Wang and H.S. Lee, Numerical techniques for free and moving boundary problems, in C.L. Tucker (ed.) *Fundamentals of computer modeling for polymer processing*, Ch. 8 (Hanser Publisher, New York, 1989).
7. P.A. Sackinger and R.A. Brown, A finite element method for analysis of fluid flow, heat transfer and free interfaces in Czochralski crystal growth, *Int. J. Num. Meth. Fluids* 9 (1989) 453-492.
8. J.L. Chenot, P. Montmitonnet, A. Bern and C. Bertrand-Corsini, A method for determining free surfaces in steady state finite element computations, *Comp. Meth. App. Mech. Engng.* 92 (1991) 245-260.
9. L.W. Ho, A Legendre spectral element method for simulation of unsteady incompressible viscous free-surface flows, Ph.D. Thesis, Massachusetts Institute of Technology, 1989.
10. L.W. Ho and A.T. Patera, A Legendre spectral element method for simulation of unsteady incompressible viscous free-surface flows, *Comp. Meth. App. Mech. Engng.* 80 (1990) 355-366.
11. L.W. Ho and A.T. Patera, Variational formulation of three-dimensional viscous free-surface flows: natural imposition of surface tension boundary conditions, *Int. J. Num. Meth. Fluids* 13 (1991) 691-698.
12. A.T. Patera, A spectral element method for fluid dynamics; laminar flow in a channel expansion, *J. Comp. Phy.* 54 (1984) 468-488.

13. E.M. Rønquist, Optimal spectral element methods for the unsteady three-dimensional incompressible Navier-Stokes equations, Ph.D. Thesis, Massachusetts Institute of Technology, 1988.
14. C. Bernardi and Y. Maday, Analysis of a staggered grid algorithm for the Stokes equations, *Int. J. Num. Meth. Fluids*, Vol. 8, pp. 537-557, 1988.
15. Y. Maday and A.T. Patera, Spectral element methods for the incompressible Navier-Stokes equations, in A.K. Noor, editor, *State-of-the-art surveys in computational mechanics*, (ASME, New York, 1989).
16. Y. Maday and E.M. Rønquist, Optimal error analysis of spectral methods with emphasis on non-constant coefficients and deformed geometries, *Comp. Meth. App. Mech. Engng.* 80 (1990) 91-115.
17. I.G. Currie, *Fundamental mechanics of fluids*, (McGraw-Hill, New York, 1974).
18. W. Flügge, *Tensor analysis and continuum mechanics*, (Springer-Verlag, Berlin, 1972).
19. S.H. Davis, Thermocapillary instabilities, *Ann. Rev. Fluid Mech* 19 (1987) 403-435.
20. R.F. Probstein, *Physiochemical hydrodynamics*, Butterworths, 1989.
21. P.D. Thomas and R.A. Brown, LU decomposition of matrices with augmented dense constraints, *Int. J. Num. Meth. Engng.* 24 (1987) 1451-1459.
22. R.I. Tanner, *Engineering rheology*, (Oxford Univ. Press, Oxford, 1985).
23. H.E. LaBelle, Jr., EFG, the invention and application to sapphire growth, *J. Cryst. Growth* 50 (1980) 8-17.
24. Boysan, F., "A two-fluid model for FLUENT", Fluent Europe, Sheffield, England, November 1990.
25. Chan, K. S., Pericleous, K., and Cross, M., "Numerical Simulation of flows encountered during mold-filling", *Appl. Math. Modelling*, vol. 15, Nov-Dec, 1991.
26. Chan, R. K., and Street, R. L., "A computer study of finite-amplitude water waves", *J. Comp. Physics*, vol. 6, 68-94, 1970.
27. Harlow, F. H., and Shannon, J. P., *J. Appl. Phys.*, vol. 38, 3855, 1967.
28. Harlow, F. H., and Welch, J. E., "Numerical calculation of time-dependent viscous incompressible flow of fluid with free surface", *Physics of Fluids*, vol. 8, no. 12, 2182-2189, Dec. 1965.
29. Hirt, C. W., "Introduction to Numerical Solution of Industrial Flows", von Karman Institute for Fluid Dynamics, Lecture Series 1986-07, May, 1986.

30. Hirt, C. W., and Nichols, B. D., "Volume of fluid (VOF) method for the dynamics of free boundaries", J. Comp. Physics, vol. 39, 201-225, 1981.
31. Ho, L.-W., "A Legendre spectral element method for simulation of incompressible unsteady viscous free-surface flows", Ph.D. dissertation, M.I.T., 1989.
32. Ho, L.-W., and Ronquist, E. M., "Spectral element solution of steady incompressible viscous free surface flows", Proc. of the Int. Conf. Spectral and High Order Methods for PDEs, Le Corum, Montpellier, France, 1992.
33. RIPPLE – A computer program for incompressible flows with free surfaces, Computer Software Management and Information Center, University of Georgia, 382 East Broad Street, Athens, Georgia 30602.
34. Soulis, J. V., "Computation of two-dimensional dam-break flood flows", Int. J. Num. Meth. Fluids, vol. 14, 631-664, 1992.

von Karman Institute for Fluid Dynamics

Lecture Series 1995-03

INDUSTRIAL COMPUTATIONAL FLUID DYNAMICS

April 3 - 7, 1995

NUMERICAL SIMULATION OF COATING FLOWS USING NEKTON

S. Subbiah

Fluent Inc., U.S.A.

NUMERICAL SIMULATION OF COATING FLOWS USING NEKTON

S. Subbiah, Ph.D.
NEKTON Product Manager
Fluent Inc.
10 Cavendish Court
Lebanon, NH 03766, U.S.A.

Contents

Outline	1
The Spectral Element Method	1
Free Surface Modelling.....	2
Mesh Deformation Strategy.....	5
High Surface Tension Solution Algorithm.....	5
Low Surface Tension Solution Algorithm.....	6
Kinematic Algorithm	7
Reverse Roll Coating.....	7
Slide Coating.....	8
Slot Coating	9
Forward Roll Coating.....	10
Conclusions	11

Numerical Simulation of Coating Flows using NEKTON

S. Subbiah, Ph.D.
NEKTON Product Manager
Fluent Inc.
10 Cavendish Court
Lebanon, NH 03766, U.S.A.

Outline

This lecture reviews the application of a relatively new discretisation scheme, spectral elements, towards the modelling of coating flows. First, the numerical aspects of the spectral element method (SEM) are described, with some attention being given to the application of this method towards the modelling of unknown free surface problems. The boundary conditions applied at the free surface, as well as the tracking of the moving mesh boundary, are described next with some comment on the similarities and differences between the spectral element method and the traditional finite element method (FEM).

The capability of the SEM for modeling industrial coating flows is then demonstrated through the analysis of the reverse roll, slide, slot, and forward roll coating processes. Whenever possible, the results obtained are compared with experimental data in the published literature. The commercial software package NEKTON, based on the SEM, was used to obtain all of the flow solutions presented here.

The Spectral Element Method

The spectral element method was first proposed by Patera [1] in 1984. The computational domain is subdivided into macro-elements and the field variables (velocities, pressures and geometry) are expanded using high-order polynomials within each element. The basis functions are 4th - 14th order Legendre polynomials. Variational projection operators and Gauss-numerical quadrature are used to derive the discrete equations. The SEM is similar to p -type FEM, but combines the flexibility to model complex geometries with the rapid convergence

of spectral methods. Note that the macro-elements can have curved sides, which are also represented by high-order polynomials.

Like traditional FEM, the SEM shares all of the advantages of the variational approach, including the natural (weak) imposition of traction boundary conditions. The SEM uses an unequal-order discretization of velocity and pressure. That is, N^{th} -order polynomial expansions are used to represent the velocities while $N-2^{\text{th}}$ -order polynomials are used to expand the pressure field. This choice of approximation polynomials avoids spurious pressure modes in the solution and minimizes the discretization error.

Two other differences with traditional FEM are worth noting. First, to minimize the computational effort involved with matrix-matrix multiplications, tensor product sum factorization [2] is used. Also, each operator in the governing equations is solved separately and sequentially, primarily using iterative methods (such as pre-conditioned conjugate gradient).

Free Surface Modeling

The modeling of coating flows requires the ability to determine the location of one or more liquid free surfaces. In this section, we derive the variational form of the natural imposition of the free surface traction boundary condition to the governing Navier-Stokes equations.

We consider the viscous steady incompressible flow of a Newtonian fluid, with density ρ and viscosity μ , in a three-dimensional domain Ω . The domain boundary Γ is decomposed as $\Gamma = \Gamma_0 \cup \Gamma_\sigma$, with (Dirichlet) no-slip boundary conditions imposed on Γ_0 , and (Neumann) traction boundary conditions imposed on Γ_σ .

The equations governing the fluid flow are the steady Navier-Stokes and continuity equations which can be written as:

$$\begin{aligned} \rho u_j u_{i,j} &= \tau_{ij,j} + f_i & \text{in } \Omega \\ u_{i,i} &= 0 & \text{in } \Omega \end{aligned} \tag{1}$$

subject to the boundary conditions:

$$u_i = 0 \quad \text{on } \Gamma_0 \tag{2}$$

$$\tau_{ij} n_j = \sigma \kappa n_i + \nabla_i \sigma \quad \text{on } \Gamma_\sigma \tag{3}$$

where u_i is the fluid velocity, f_i is the body force and τ_{ij} is the stress tensor defined as:

$$\tau_{ij} = -p\delta_{ij} + \mu(u_{i,j} + u_{j,i}) \quad (4)$$

Here, p is the pressure (relative to zero ambient) and δ_{ij} is the Kronecker delta. On the free surface Γ_σ , σ is the surface tension coefficient, n_i is the outward unit normal, ∇_i is the surface gradient operator, and κ is the curvature in two-dimensional geometry and twice the mean curvature in three-dimensional geometry (the curvature along a surface coordinate is considered positive if the liquid region below the free surface along that surface coordinate is concave). We shall use the following notation and conventions: Roman indices range from 1 to 3, a subscript comma denotes derivative (e.g., $u_{i,j} = \partial u_i / \partial x_j$), and repeated Roman indices are summed from 1 to 3.

Let the two-dimensional free surface be described by a local curvilinear coordinate system r^α , $\alpha = 1, 2$, which are in general non-orthogonal. We recall several useful definitions from differential geometry [3]:

$$g_{\alpha i} = x_{i,\alpha} \quad (5)$$

$$g_{\alpha i} g_{\beta i} = g_{\alpha\beta} \quad (6)$$

$$g_{\alpha i} g_i^\beta = \delta_\alpha^\beta \quad (7)$$

$$g = \sqrt{|g_{\alpha\beta}|} \quad (8)$$

where $g_{\alpha i}$ is the covariant base vector, g_i^α is the contravariant base vector, $g_{\alpha\beta}$ is the covariant metric tensor, δ_α^β is the Kronecker delta. Using the above definitions, the surface gradient term in Eqn. (3) can be expressed as

$$\nabla_i \sigma = g_i^\alpha \sigma_{,\alpha} \quad (9)$$

where repeated Greek indices are summed from 1 to 2.

The variational form of Eqns. (1) to (4) is given by [4-6]: find (u_i, p) , with $u_i \in H_0^1(\Omega)$ and $p \in L^2(\Omega)$, such that

$$\int_\Omega \{ \rho v_i u_j u_{i,j} + v_{i,j} [-p\delta_{ij} + \mu(u_{i,j} + u_{j,i})] - v_i f_i \} dV - \\ I_\sigma(v_i) = 0 \quad \forall v_i \in H_0^1(\Omega)$$

$$\int_\Omega q u_{i,i} dV = 0 \quad \forall q \in L^2(\Omega) \quad (10)$$

where v_i and q are test functions, $L^2(\Omega)$ is the space of functions which are square integrable, and $H_0^1(\Omega)$ is the space of functions which are in $L^2(\Omega)$, whose first derivatives are in $L^2(\Omega)$, and which vanish on Γ_0 . The term $I_\sigma(v_i)$ is the variational form that corresponds to natural imposition of the traction boundary conditions given in Eqn. (3). In three-dimensional geometry, this form can be written as [6]:

$$I_\sigma(v_i) = \oint_\gamma \sigma v_i g g_i^\alpha e_{\alpha\beta} dr^\beta - \int_{\Gamma_\sigma} v_{i,\alpha} \sigma g_i^\alpha dA \quad (11)$$

where γ is the line segment that bounds the free surface Γ_σ , $e_{\alpha\beta}$ is the permutation symbol ($e_{11} = e_{22} = 0, e_{12} = -e_{21} = 1$), and $dA = g dr^1 dr^2$.

We remark that in two-dimensional geometry, Eqn. (11) reduces to the following variational form which is presented in [7]:

$$I_\sigma(v_i) = (\sigma v_i t_i)|_a^b - \int_a^b v_{i,\zeta} \sigma t_i d\zeta \quad (12)$$

where t_i is the unit tangent vector and ζ is the curvilinear coordinate on the free surface segment ab .

The variational forms given in Eqns. (11) and (12) have the following important advantages which are discussed in [6]. First, it automatically generates the equivalent normal and tangential traction conditions as given in Eqn. (3), including the effect of variable surface tension (Marangoni flows). Second, in the subsequent domain decomposition it provides a natural (weak) condition for continuity of slope across elemental boundaries on the free surface. Third, it is entirely surface-intrinsic, with no need to reference global coordinates or locally orthogonal systems. Lastly, it requires a lower-order geometric representation when compared with formulations that use the mean curvature directly in the imposition of the normal traction boundary condition.

The location of the free surface can be incremented by solving the curvature operator, which can be derived for high- and low-surface tension cases — see solution algorithms below. Thus, the relocation of the free surface during the solution process requires a mesh deformation algorithm.

The spectral element discretization of the variational statement given in Eqn. (10) proceeds as follows. The domain is subdivided into quadrilateral (2-D) or hexahedral (3-D) elements. We require that the variational statement be satisfied for the piecewise polynomial spaces: P_N for velocity and P_{N-2} for pressure. For the numerical evaluation of the elemental integrals, we map the physical (x_1, x_2, x_3) system to a local (r, s, t) system and use Gauss numerical integration. The interpolant Gauss-Lobatto-Legendre basis are introduced to expand the coordinates, body force, fluid velocity and test function v_i . We also introduce the Gauss-Legendre basis for expanding the pressure and test function q_h . The final discrete system of algebraic equations is obtained by imposing successively the test functions $(v_i)_h$ and q_h ,

which are unity at one global collocation point and zero at all others.

Mesh Deformation Strategy

Previous numerical methods for simulating free surface flows have used either spines, which allow free surface deformation with respect to a line, or elliptic mesh generation, which allows more general 2-D deformation of the free surface but with structured meshes. The approach taken in the present work uses a second order elliptic (elastostatic) operator [6] to extend the mesh velocity into the interior of the domain with a minimum of mesh distortion. This approach provides the flexibility of multi-dimensional adjustments to the mesh point locations and can be used on unstructured meshes.

The steps used by the surface-intrinsic moving mesh description are:

1. Solve for the fluid flow field.
2. Compute the new position of the free surface.
3. "Smooth" the nodal spacings along the free surface.
4. Extend the change in free surface mesh location into the interior of the domain (elastostatic solver).
5. Update the geometric coefficients.
6. Repeat until convergence.

The details involved in step #2 are described below for the cases of high and low surface tension. A complete derivation of these solution algorithms is given in [8].

High Surface Tension Solution Algorithm

For high surface tension cases (i.e., $Ca \ll 1$ or $We \gg 1$), the following algorithm is used for computing the change in free surface position. First, the Navier-Stokes equations are solved subject to the following "symmetry-like" boundary conditions on the free surface:

$$u_i n_i = 0 \quad (13)$$

$$t_i \tau_{ij} n_j = \sigma_{,\zeta} \quad (14)$$

The resulting traction force vector is denoted τ_{ij}^{ss} . Based on the current velocity field, we compute a point-by-point force balance:

$$r_i = \tau_{ij}^{ss} n_j - \sigma \kappa n_i - \sigma_{,\zeta} \quad (15)$$

Note that r_i is zero only at steady state. This residual traction is used as a driving force for computing corrections to the free surface location, Δx_i , according to:

$$-\int_a^b v_{i,\zeta} \sigma \Delta x_{i,\zeta} d\zeta + (v_i \sigma \Delta x_{i,\zeta})|_a^b = \int_a^b v_i r_i d\zeta \quad (16)$$

Low Surface Tension Solution Algorithm

For the case of low surface tension (i.e., $Ca \gg 1$ or $We \ll 1$), the Navier-Stokes equations are solved subject to both tangential and normal traction boundary conditions on the free surface:

$$n_i \tau_{ij} n_j = \sigma \kappa \quad (17)$$

$$t_i \tau_{ij} n_j = \sigma_{,\zeta} \quad (18)$$

Since the normal velocity $u \cdot \hat{n}$ on the free surface is in general non-zero, we can compute the following source term:

$$r_i = (u_k n_k) n_i \quad (19)$$

The source term r_i , with the appropriate scaling, drives the change in free surface position according to:

$$-\int_a^b v_{i,\zeta} \Delta x_{i,\zeta} d\zeta + (v_i \Delta x_{i,\zeta})|_a^b = \int_a^b \lambda v_i r_i d\zeta \quad (20)$$

where λ is a scale factor to ensure that $\Delta x_i < L_\Omega$.

Kinematic Algorithm

An alternate form of the low-surface tension algorithm advances the position of the free surface by deriving a mesh velocity on the free surface (which of course becomes zero at steady state). First, the governing fluid flow equations are solved subject to

$$n_i \tau_{ij} n_j = \sigma \kappa \quad (21)$$

$$t_i \tau_{ij} n_j = \sigma_{,\zeta} \quad (22)$$

on the free surface. This solution is then used to derive the mesh velocity on the free surface, w_i :

$$w_i = (u_k n_k) n_i \quad (23)$$

The change in mesh coordinates on the free surface is then given by the simple time integration:

$$\Delta x_i = w_i \Delta \tau \quad (24)$$

where $\Delta \tau$ is a pseudo-time step computed from the fluid velocity and mesh spacing on the free surface. Note that the solution of Eqn. 24 does not require iteration, thus the kinematic algorithm is less CPU-intensive compared with the two solution algorithms presented above. However, the $\Delta \tau$ does not honor the time step required for free surface stability and so, if surface tension effects are not completely negligible, the pseudo-time step must be reduced.

In the next sections, the SEM (implemented in our commercial software package) is used to solve several coating flows and comparison with available experimental and numerical results is given.

Reverse Roll Coating

The reverse roll coater is shown schematically in Figure 1. A thin layer of fluid approaches the nip gap from the lower right on the applicator roll at velocity V_a . The height of the arriving film is arbitrarily set to 1.25 times the gap height. Part of this fluid is transferred to the metering roll which is rotating in the opposite direction with velocity V_m . The result is a very precise thin film on the applicator roll which is later transferred to the web. The position of the dynamic contact line, where the free surface on the left touches the metering roll, is unknown and is sensitive to the roll speed ratio, V_m/V_a .

A series of solutions was obtained using the software for various roll speed ratios. The other governing parameters for the problem are:

- $Re = \frac{\rho V_a H_o}{\mu} \ll 1$
- $R/H_o = 1000$
- $Ca = \frac{\mu u}{\sigma} = 0.1$
- $R_m = R_a = R$

The spectral element mesh and boundary conditions for this problem are illustrated in Figure 2. 41 to 51 spectral elements, employing 4th-order polynomials, were typically used. The steady-state stream function contours for selected roll speed ratios are shown in Figure 3. In all cases, the flow is characterized by a large flow recirculation adjacent to the free surface on the right. For $V_m/V_a = 0.4$, the contact line position is well to the left of the minimum gap between the rolls and a second recirculation can be seen. As the speed of the metering roll is increased, the recirculation disappears and the contact line moves to the right and eventually passes through the gap. The change in the coating film thickness as a function of roll speed ratio is shown in Figure 4 and the SEM solutions are compared with the experimental and numerical results of Coyle, *et al.* [9]. At low speed ratios, the film thickness can be predicted via a lubrication approximation of the flow. However, as the speed ratio is increased, the thickness of the coating film reaches a minimum and then actually increases again as described in [9]. The computational results predict a minimum film thickness near $V_m/V_a = 0.9$ while Coyle's FEM results indicate a slightly higher value, $V_m/V_a = 1$. Some of the discrepancy between the SEM and FEM results is attributed to the different contact angles used. The experimental data show a minimum coating film thickness near $V_m/V_a = 0.9$, but show an overall larger film thickness because of the effect of ribbing on the film thickness measurements. Additional computational results are presented in [10].

Slide Coating

In conjunction with the Anitec Image Corporation, a division of International Paper, a combined experimental and analytical study of slide coating was conducted. The objectives of the study were to:

- establish the limits of operability, and to
- observe the behavior of the static and dynamic contact lines for different:
 - flow rates,

- web speeds, and
- vacuum pressures

A description of the experimental apparatus is given in [11]. The position of the wetting line on the slide face was captured on video tape as the vacuum pressure was varied. The wetting line position was then measured with respect to the slide nose. The software was used simulate the slide coater for a range of vacuum pressures. The spectral element mesh and boundary conditions used are shown in Figure 5. The velocity inlet boundary condition used was a fully-developed profile for a falling film on an inclined plane. The contours of stream function corresponding to a vacuum pressure of 0.65 inches of water are shown in Figure 6. For these conditions, the fluid wets the slide face and there is a recirculation in the bead. The free surface on the slide exhibits the tell-tale “standing wave” in response to the capillary pressure built up as the flow turns and is transferred to the moving web. The position of the static contact line on the slide face is compared in Figure 7 with experimental data for a several vacuum pressures. Good agreement is observed both in the trend and absolute value of the wetting length.

Slot Coating

A schematic diagram of the slot coater is given in Figure 8. The liquid is applied through the die slot to a moving web. Two free surfaces are formed: the upstream meniscus which may be pinned at one of the die lips and the free surface downstream formed by the coating film. In this study, the conditions corresponding to the experimental and numerical data of Sartor [12] were used to investigate the turning point behavior as the vacuum pressure on the upstream meniscus is increased. In Figure 9, the spectral element mesh and boundary conditions are illustrated. A fully-developed velocity profile was specified at the inlet. The other governing parameters for the problem are:

- $Re = 6.05$
- $Ca = 0.208$
- $St = \frac{\rho L^2 g}{\mu V} = 0.0575$
- $h = 84.7 \mu m, d_1 = 250 \mu m, d_2 = 271 \mu m, L = 1.016 mm$

The details of the flow field for two different vacuum pressures are shown in Figure 10 as stream function contours. Only a portion of the solution domain is shown. One can clearly see how the increased vacuum pressure causes the upstream meniscus to bow outward and the dynamic contact line to move upstream. As the vacuum is further increased, stable coating is no longer possible — this behavior is clearly illustrated by the trend in predicted

wetting line position displayed in Figure 11. For the critical vacuum pressure at this turning point, Sartor gives an experimental value of approximately 9.34 inches of water (± 4 percent) and a numerical (FEM) value of 9.84, certainly in good agreement with the present study for which we obtained a value of 9.03.

Forward Roll Coating

The governing parameters for the forward roll coating process are given in Figure 12. The height of the arriving film on the lower roll dictates the flow rate, which can be represented in non-dimensional form as:

$$\lambda = \frac{\int U dy}{2\bar{V}H_o}$$

where U is the horizontal velocity component, \bar{V} is the average roll velocity and the integration above is taken over the gap between the rolls. The point (X_m, Y_m) in Figure 12 is designated as the film split location. It is measured from the origin at the center of the gap between the two rolls and the distances are non-dimensionalized with respect to the roll half gap, H_o . If the rolls have the same radius and speed, the numerical analysis of the problem can exploit the line of symmetry as shown in Figure 13. Note that the velocity profile at the inlet is specified as a function of the average pressure as given by lubrication theory, see Coyle, *et al.* [13]. The other governing parameters used in the numerical study are:

- $R/H_o = 1000$
- $Re \ll 1$
- $Ca = 0.1$ to ∞

The stream function contours for three different values of Ca are depicted in Figure 14. As expected, the film split location moves away from the origin as the Capillary number is decreased and a recirculation zone develops adjacent to the free surface. Coyle, *et al.* have published the results of their FEM simulations, asymptotic analysis and lubrication approximation for the dimensionless flow rate and split point location over a range of operating conditions. For the conditions listed above ($Ca = \infty$), a comparison of these results with the computational solution is given in Table 1.

	λ	X_m
Lubrication theory	1.302	76.21
FEM (Coyle, <i>et al.</i>)	1.293	65.20
SEM (Present study))	1.293	65.69

For these conditions, the lubrication approximation compares well with both the FEM and SEM analyses, which are almost identical.

Conclusions

The spectral element method and surface intrinsic moving mesh strategy incorporated in our software have been shown to successfully address a range of industrial coating flows, including reverse roll, slide, slot and forward roll coating. The benefits of this approach that we have observed include the large radius of convergence afforded by the decoupled solution strategy, the capability of handling complex free surface deformations with no manual remeshing and the ability of the unstructured mesh to refine local flow details.

To eliminate the effort of mesh generation and supplying a good initial condition, we are presently completing work on a template-based approach to solving coating flows. In this approach, the user will select from a library of pre-solved templates the mesh and operating conditions that most closely resembles his problem. The actual boundary conditions and fluid properties can then be specified. The solver uses the existing solution as an initial condition and ramps the boundary conditions and fluid properties from the initial values to the user-supplied values over a number of iterations. We have found this to be a very time-effective way of solving many coating flows. Additionally, each converged solution can then be used as a template for further parametric analysis.

Acknowledgements

The author would like to acknowledge the contributions of Eric Grald, Mitali Chakrabarti, and Murali Kadiramangalam (of Fluent Inc.), Lee-Wing Ho (of Nektonics Inc.) and Marcello Schirru (University of Cagliari) in the preparation of examples shown in this lecture.

References

1. A. T. Patera, "A Spectral Element Method for Fluid Dynamics: Laminar Flow in a Channel Expansion", *Journal of Computational Physics*, Vol. 54, No. 3, 1984, pp. 468-488.
2. D. Gottlieb and S. A. Orszag, "Numerical Analysis of Spectral Methods: Theory and Applications", Regional Conference Series in Applied Mathematics, No. 26, *SIAM*, Philadelphia, 1977.
3. W. Flügge, *Tensor Analysis and Continuum Mechanics*, Springer-Verlag, Berlin, 1972.
4. L. W. Ho, "A Legendre Spectral Element Method for Simulation of Incompressible Unsteady Viscous Free Surface Flows", Ph.D. Dissertation, Dept. of Mech. Engineering, MIT,

1989.

5. L. W. Ho and A. T. Patera, "A Legendre Spectral Element Method for Simulation of Unsteady Incompressible Viscous Free Surface Flows", *Comput. Methods Appl. Mech. Eng.*, Vol. 80, 1990, pp. 355-366.
6. L.-W. Ho and A. T. Patera, "Variational Formulation of Three-Dimensional Viscous Free Surface Flows: Natural Imposition of Surface Tension Boundary Conditions", *Int. J. Num. Meth. Fluids*, Vol. 13(6), 1991, pp. 691-698.
7. K. J. Ruschak, "A Method for Incorporating Free Boundaries with Surface Tension in Finite Element Fluid Flow Simulation", *Int. J. Num. Meth. Eng.*, Vol. 15, 1980, pp. 639-648.
8. L. W. Ho and E. M. Rønquist, "Spectral Element Solution of Steady Incompressible Viscous Free-Surface Flows", in Proceedings of the International Conference on Spectral and High Order Methods for Partial Differential Equations, Montpellier, France, 1992 (North-Holland).
9. D. J. Coyle, C. W. Macosko and L. E. Scriven, "The Fluid Dynamics of Reverse Roll Coating", *AIChE Journal*, Vol. 36, No. 2, February 1990, pp. 161-174.
10. E. W. Grald and S. Subbiah, "Analysis of the Reverse Roll Coating Process with NEK-TON", IS&T 46th Annual Conference, May 1993.
11. J. Gephart, B. Peppard and S. Subbiah, "Spectral Element Modeling of Slide Coating Flows", IS&T 46th Annual Conference, May 1993.
12. L. Sartor, "Slot Coating: Fluid Mechanics and Die Design", Ph.D. Dissertation, Dept. of Chemical Engineering, University of Minnesota, 1990.
13. D. J. Coyle, C. W. Macosko and L. E. Scriven, "Film-Splitting Flows in Forward Roll Coating", *J. Fluid Mech.*, Vol. 171, 1986, pp. 183-207.

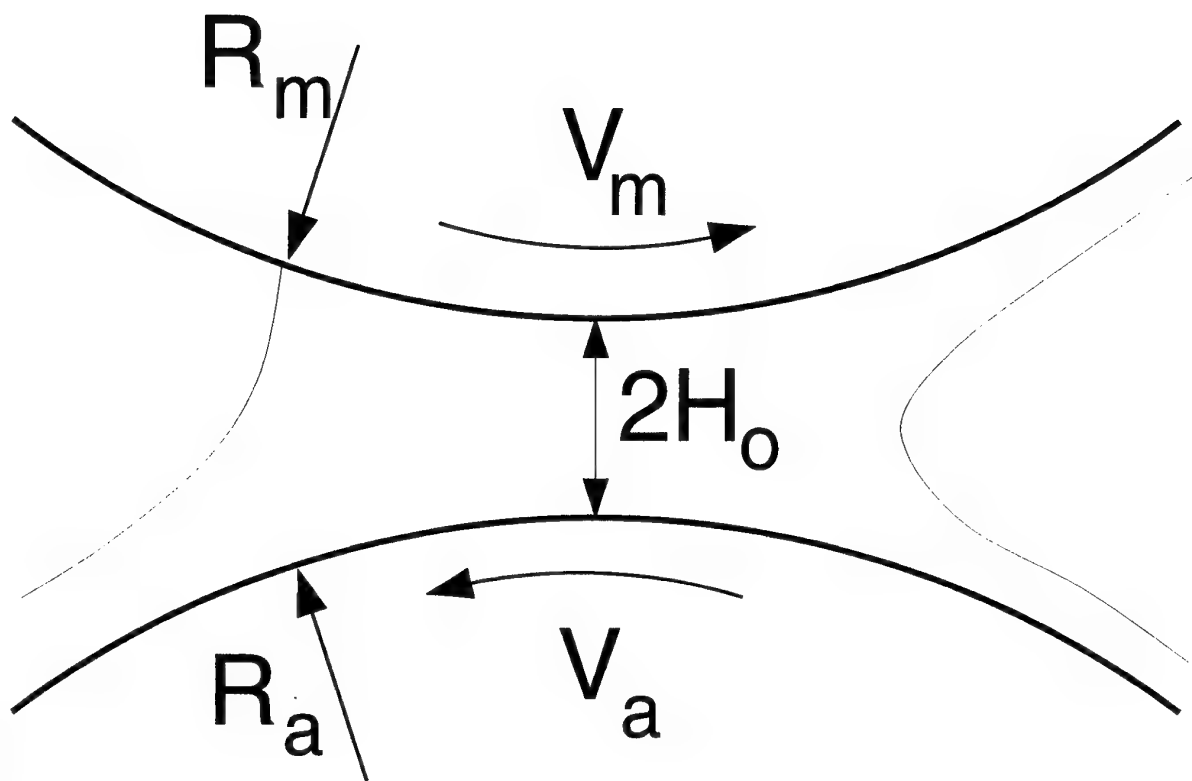


Figure 1: Schematic figure of reverse roll coater.

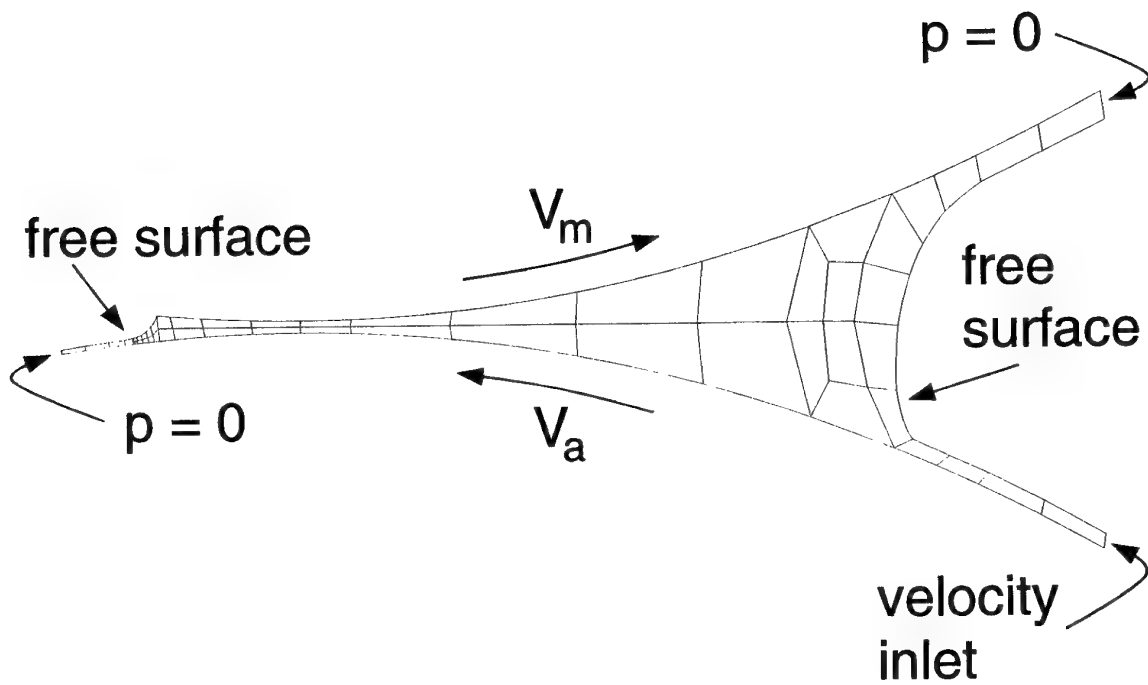


Figure 2: Spectral element mesh and boundary conditions for reverse roll coater.

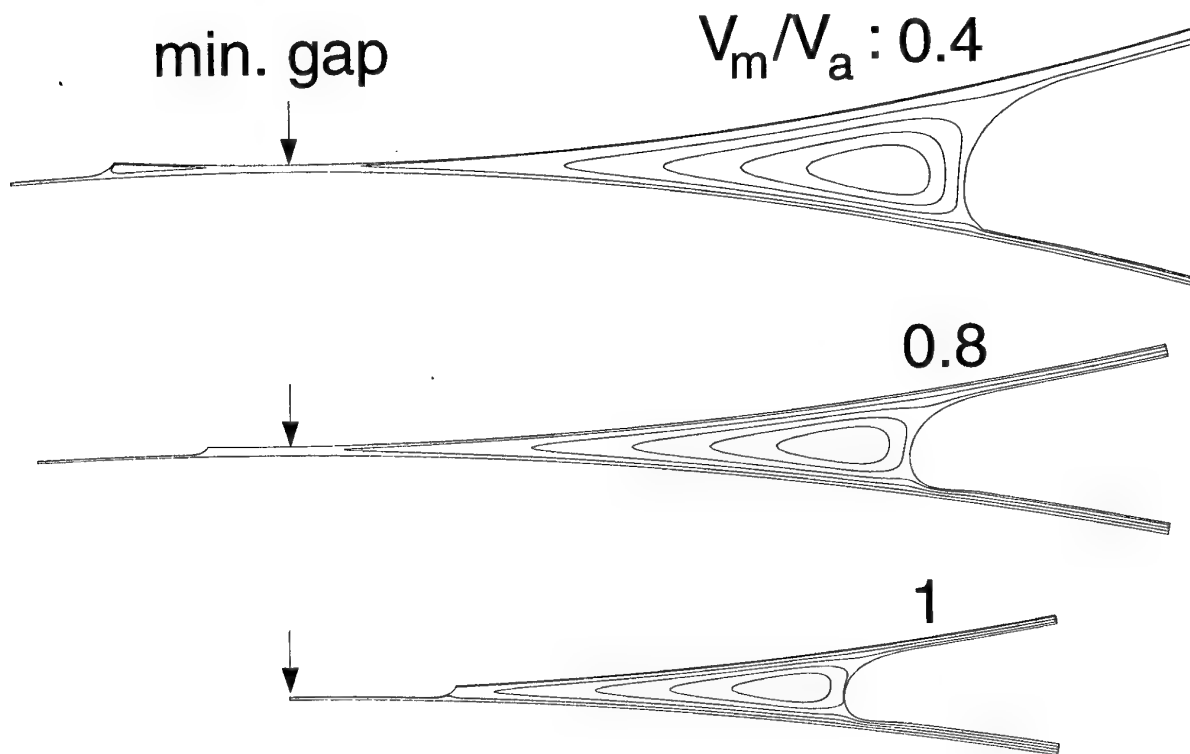


Figure 3: Stream function contours for three different roll speed ratios.

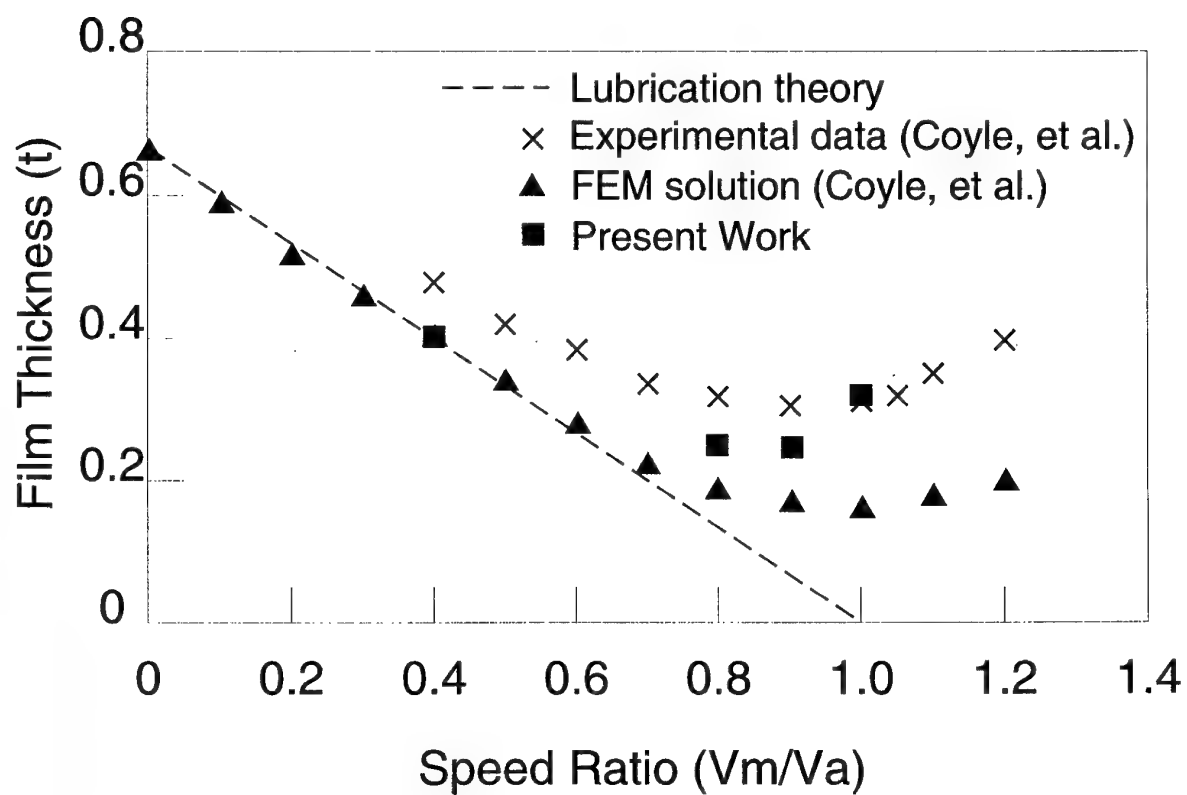


Figure 4: Comparison of film thickness as predicted by computational modeling with results from [9], as a function of roll speed ratio.

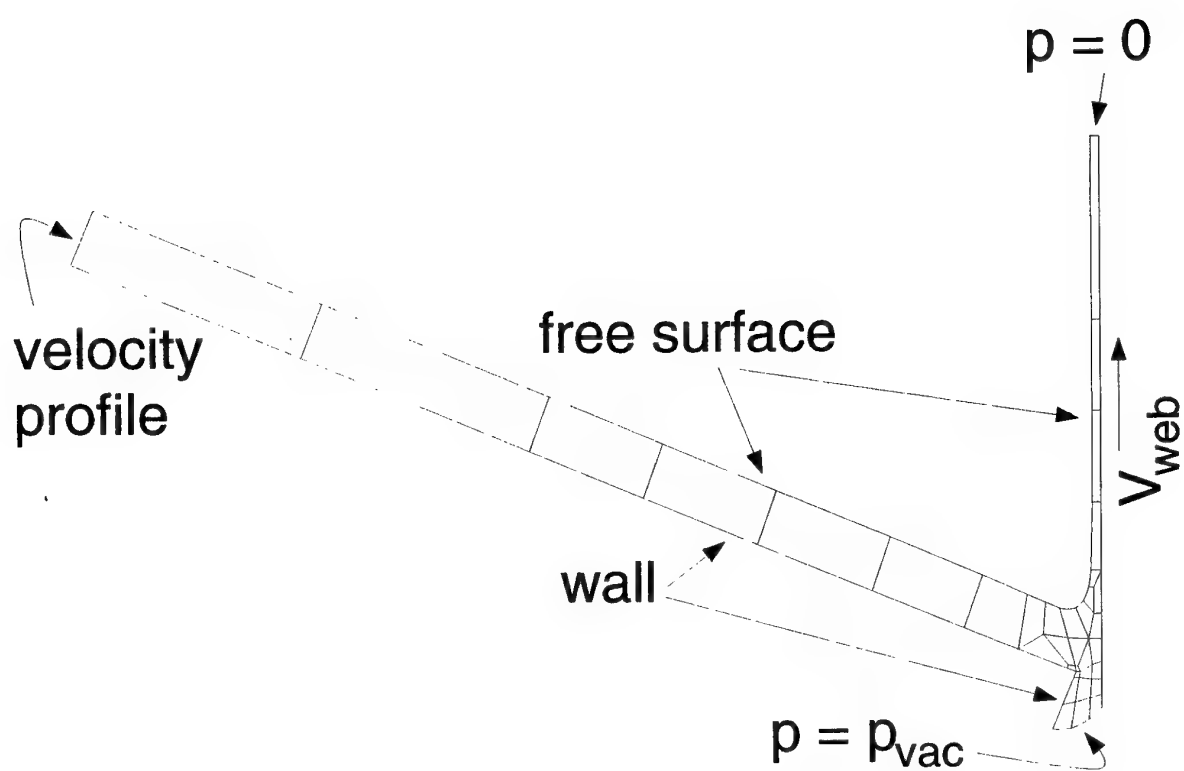


Figure 5: Spectral element mesh and boundary conditions for slide coater.

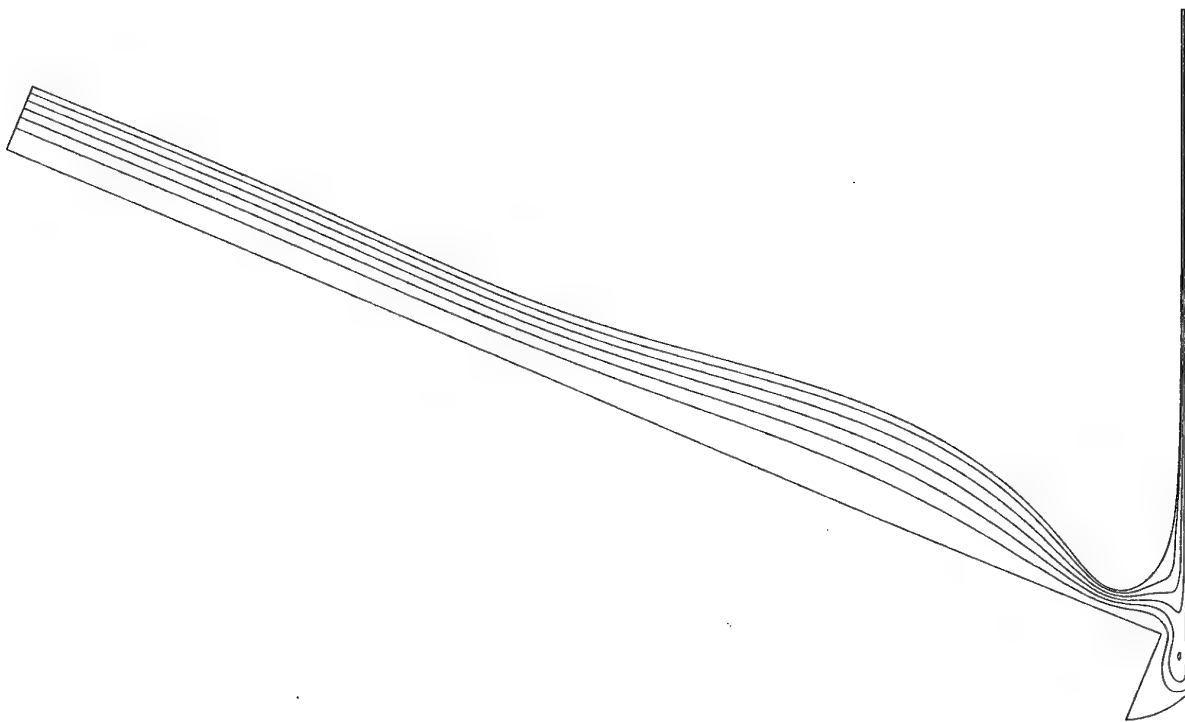


Figure 6: Stream function contours for slide coater.

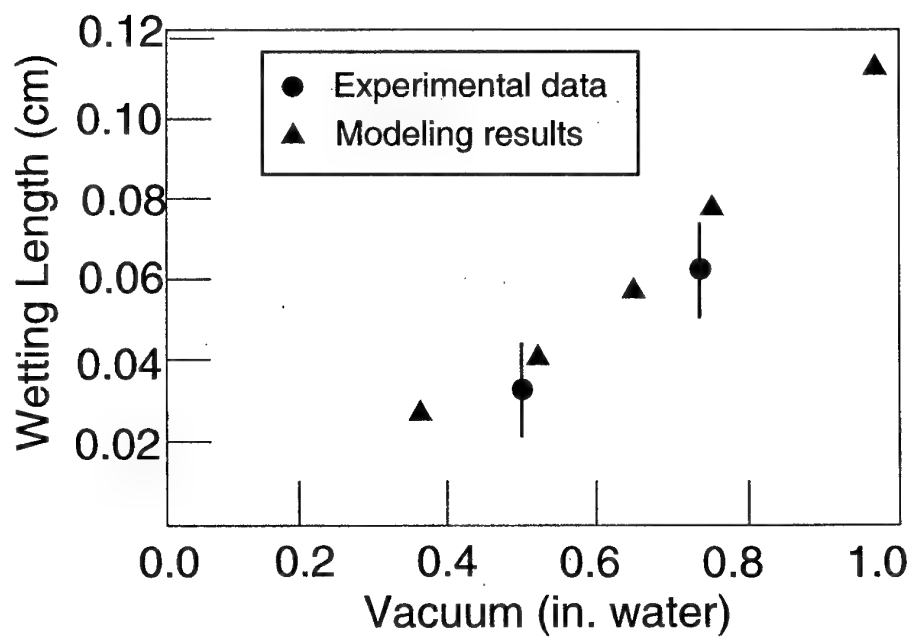


Figure 7: Comparison of wetting line position between computational modeling results and experimental measurements.

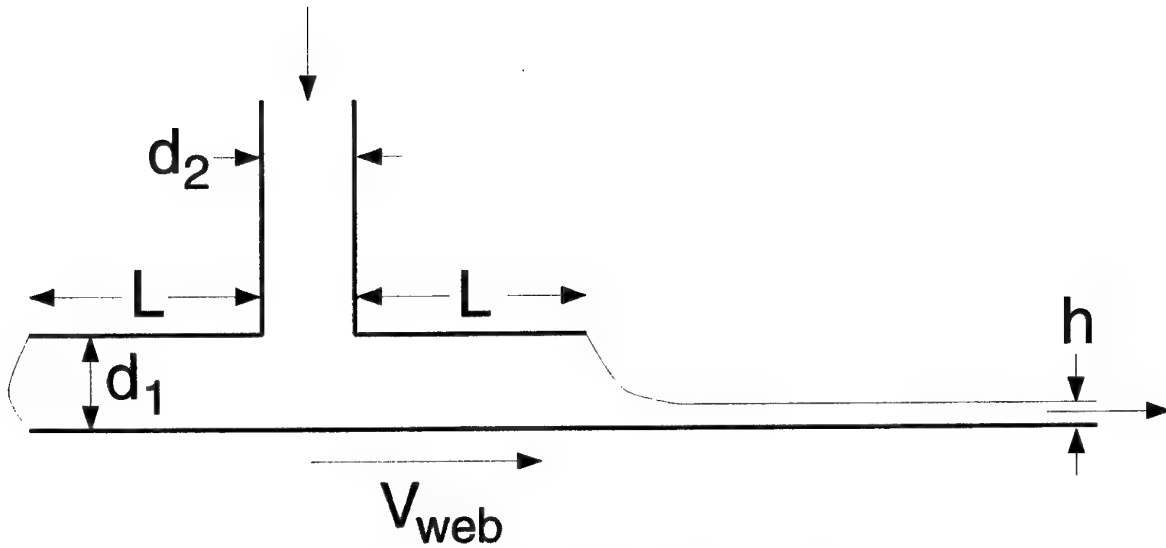


Figure 8: Schematic figure of slot coater.

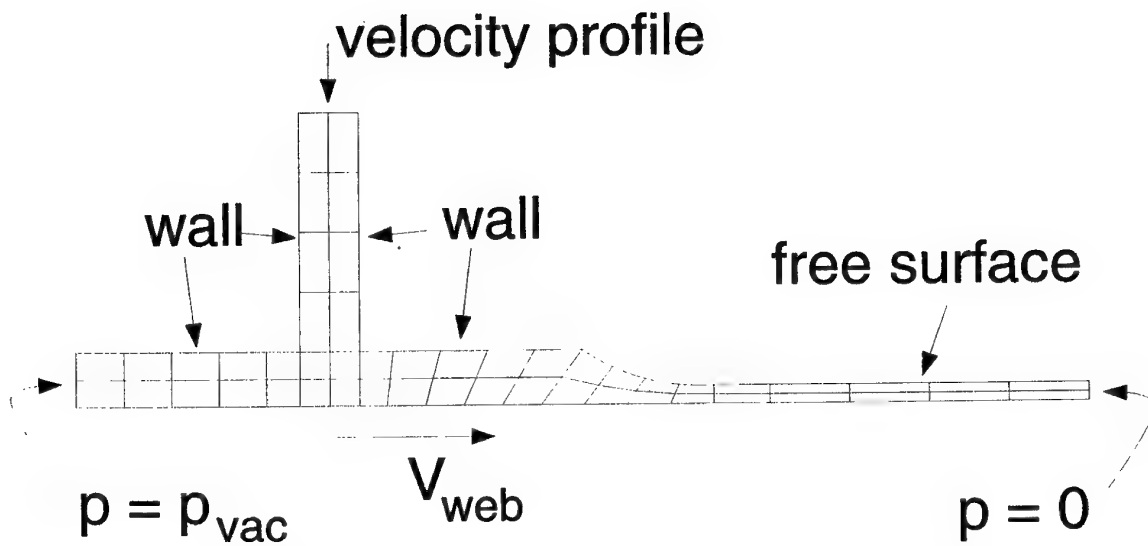


Figure 9: Spectral element mesh and boundary conditions for slot coater.

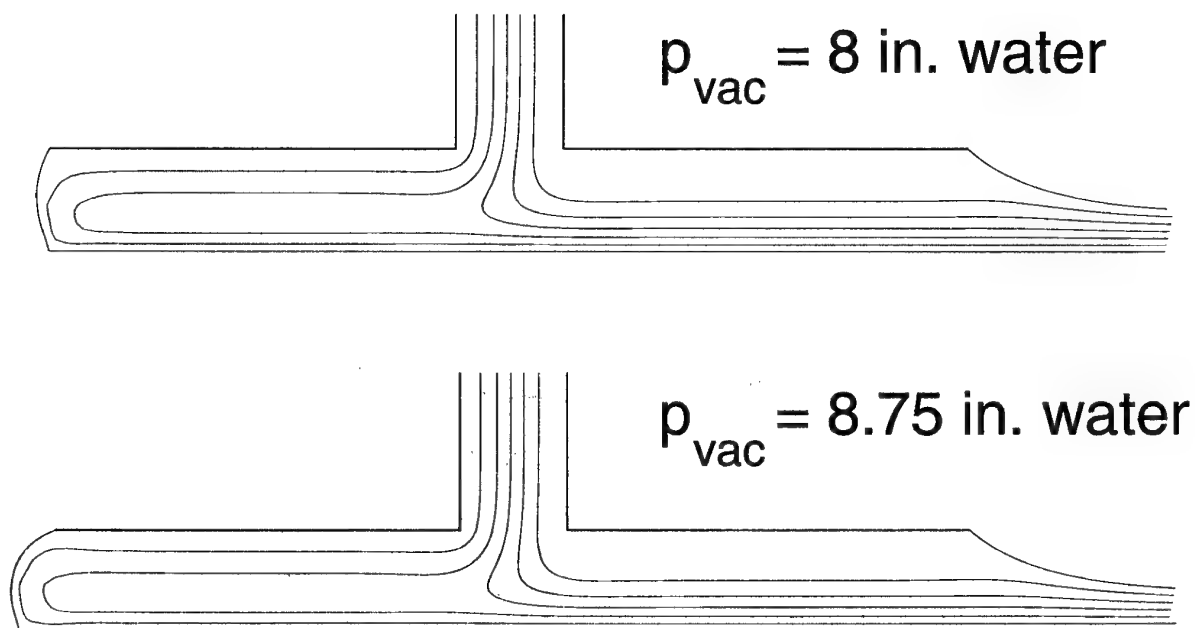


Figure 10: Stream function contours for two different vacuum pressures.

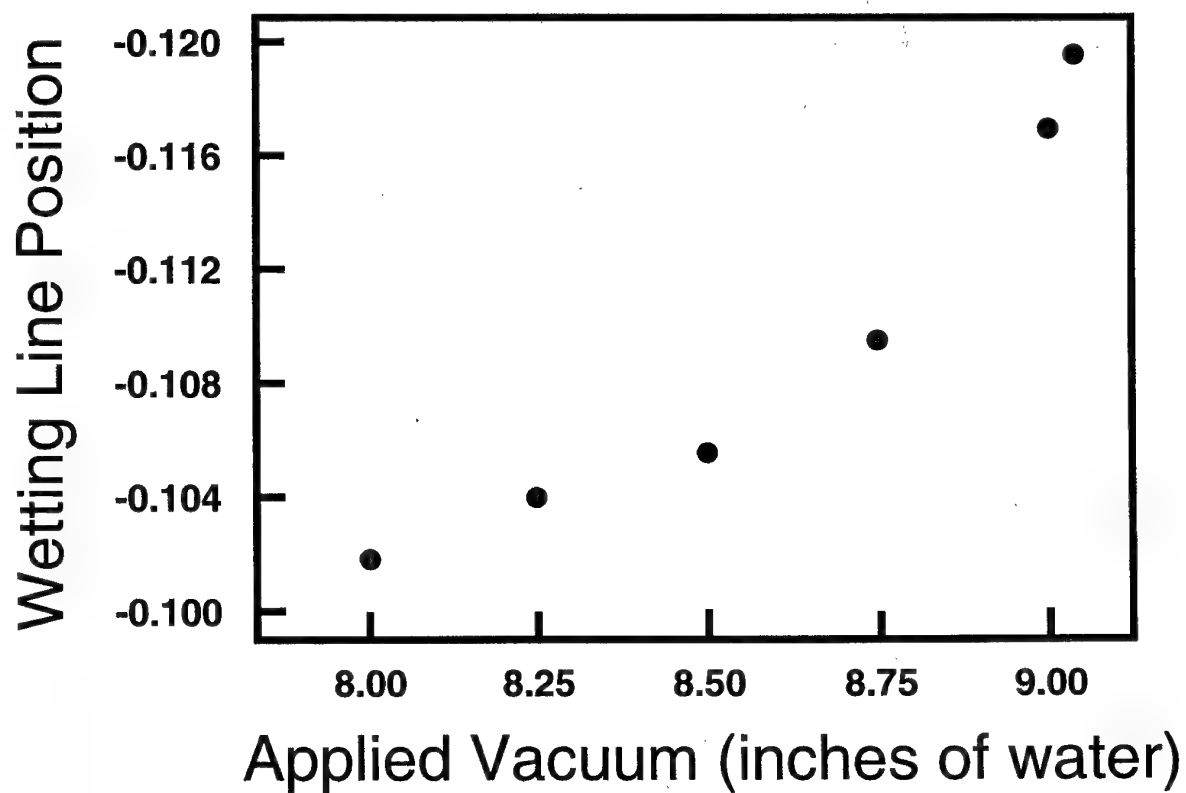


Figure 11: Computationally performed limiting point analysis.

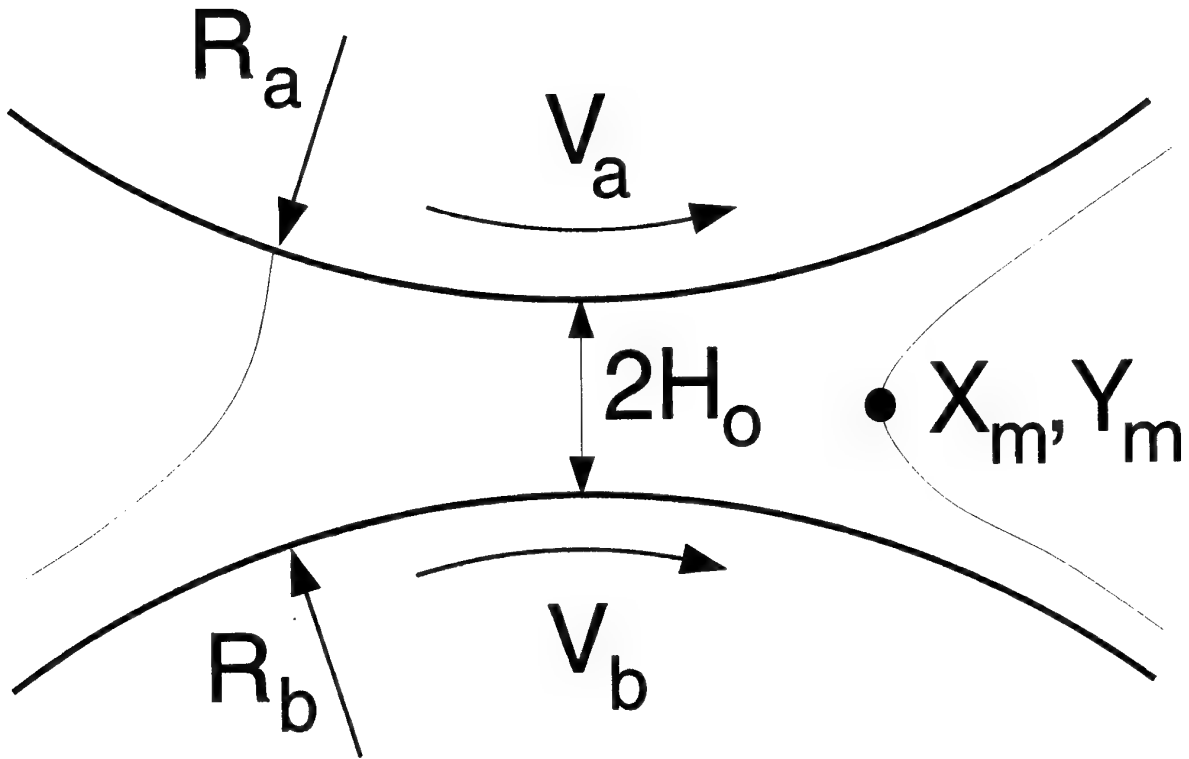


Figure 12: Schematic drawing of forward roll coater.

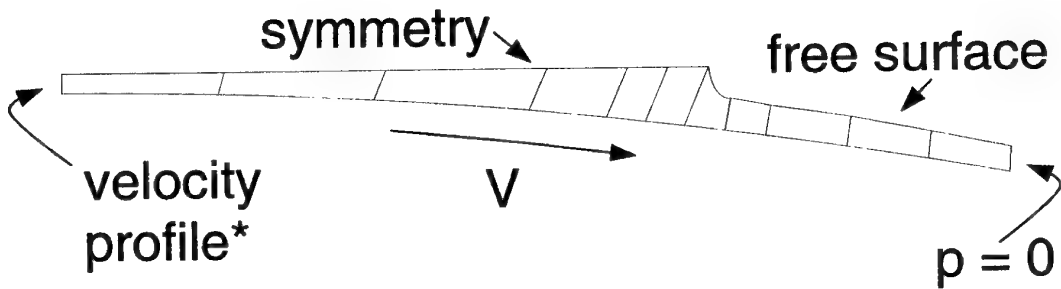
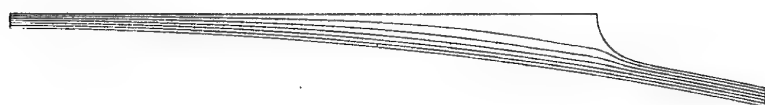


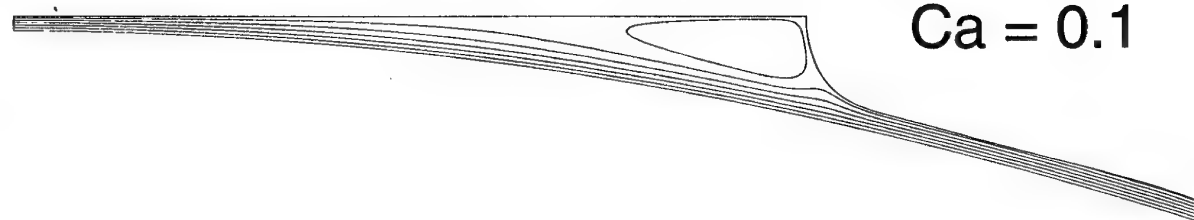
Figure 13: Spectral element mesh and boundary conditions for forward roll coater. *Velocity profile is a function of the average pressure at the inlet as given by [13].



$Ca = \infty$



$Ca = 0.51$



$Ca = 0.1$

Figure 14: Stream function contours for three Capillary numbers. Note: the scale in the vertical direction is magnified by a factor of 2.

von Karman Institute for Fluid Dynamics

Lecture Series 1995-03

INDUSTRIAL COMPUTATIONAL FLUID DYNAMICS

April 3 - 7, 1995

DISPERSION OF POLLUTANTS

E. Vergison
SOLVAY S.A., Belgium

CONTENTS

1. INTRODUCTION	1
2. THE INDUSTRIAL CONTEXT.....	3
3. MATHEMATICAL MODELS OF ENVIRONMENTAL FLOWS.....	8
3.1. EUROCHLOR : A MEDIUM RANGE ATMOSPHERIC DISPERSION MODEL	8
3.1.1. THE MATHEMATICAL MODEL.....	8
3.1.1.1. The basic physics.....	9
3.1.2. The EUROCHLOR code validation	15
3.1.2.1. Validation against wind tunnel tests.....	15
3.1.2.2. Validation against other mathematical models.....	16
3.2. SEVEX : A MESO-METEOROLOGICAL 3-D CODE.....	18
3.2.1. The SEVEX Source Term Module.....	20
3.2.1.1. The Instantaneous Releases.....	20
3.2.1.2. The Continuous Releases	22
3.2.2. The Meso-Meteorological module	24
3.2.3. The Lagrangian passive dispersion module	26
3.2.3.1. Model equations	27
3.2.4. Typical output from SEVEX.	29
3.3. DISCO : A 3-D MEDIUM RANGE ATMOSPHERIC DISPERSION MODEL	30
3.3.1. The DISCO Model	30
3.3.1.1. The Continuity Equation.....	30
3.3.1.2. The Momentum Equations.....	30
3.3.1.3. The Energy Equation.	31
3.3.1.4. The air and the pollutant as ideal gases.....	31
3.3.1.5. The (k, ϵ) Turbulence Closure.....	31
3.3.2. The Boundary conditions.....	33
3.3.3. The Initial conditions	33
3.3.4. The present state of DISCO.....	34
4. THE KNOWLEDGE BASED FRONT-END TECHNOLOGY	35
4.1. THE METEO PRE-PROCESSOR TO THE EUROCHLOR CODE.....	35
4.2. THE KNOWLEDGE BASED FRONT-END TECHNOLOGY.....	39
5. THE QUALITY ASSURANCE APPROACH FOR CALCULATION MODELS..	41
5.1. THE SCIENTIFIC QUALITY-ASSURANCE.	43
5.2. THE ALGORITHMIC QUALITY-ASSURANCE.....	44
5.3. THE COMPUTERISATION QUALITY-ASSURANCE	45
5.4. THE MAN-MACHINE INTERFACE QUALITY-ASSURANCE.....	45
5.5. MODEL VALIDATION AND ANALYSIS OF SENSITIVITY.....	46
6. CONCLUSION.....	57
BIBLIOGRAPHY	

ACKNOWLEDGEMENTS

Thanks are due to several people:

to Dr. Peter SHOPOV (Brussels Free University - B) who was very much involved in the DISCO Project, being in charge of most of the mathematical developments,

to Professor François RONDAY (University of Liège - B), Professor Christian DELVOSALLE (Faculté Polytechnique de Mons - B) and Dr. Guy SCHAYES (Université Catholique de Louvain - B) who kindly provided me with a full documentation on the SEVEX Project,

to Dr. Rex BRITTER (University of Cambridge - UK) and Professor Charles HIRSCH (Brussels Free University - B) for their encouragements when I was writing the Quality Assurance Guide for the evaluation of Environmental Mathematical Models; special thanks go to Rex who patiently read my French draft.

1. INTRODUCTION

Mathematical modelling of environmental flows is becoming increasingly used for quantification of Major Hazards, both in Industry and among Legal Authorities and specialized consultants. Compared to wind or water tunnels and to field test experiments, it offers a greater flexibility and can be run at lower costs.

In the field of Major Hazards, it is common knowledge that the quality of mathematical models and their **fitness for purpose** has not always been clearly established. The relatively large number of models developed on the market to date, in Universities, in Research Centres and in Industry means it is vital to assess the quality of each model individually as well as the quality of a model when compared with others.

In other words, to ensure that hazard studies remain as relevant and reliable as possible, it has become necessary, along with the scientific push, to judge more severely the quality of computerized models looked at as the vital part of a more general Problem Solving Environment context.

In this lecture we will focus on considering Mathematical Models involved in studying the consequences of major accidents i.e. on issues which are relevant to industrial concern as opposed to advanced architectures which are still in the scope of academic research.

The Mathematical Model terminology covers three main categories of models :

- Empirical Mathematical Models which can be distilled down to :
 - either smoothing experimental results with the aim to make them easy to interpret,
 - or statistical correlations between characteristic sizes of physical phenomena

Empirical Models should however not be confused with correlation models used to estimate the physical and chemical properties of chemical products likely to play a part in accident scenarios.

- Analytical Mathematical Models, exact or approximate solutions of simplified ones,
- Numerical Mathematical Models (computational models) which require a numerical algorithm and computation.

We will concentrate particularly on the latter as they are the more practised though at different levels of sophistication and complexity, and as the former two categories can be regarded as particular cases from the Quality-Assurance viewpoint which will be a major concern in this presentation.

On this matter, we have already mentioned the diversity, not to say the discrepancy, between mathematical models available today; to this should be added the diversity of end-users categories who may differ in the approach of analyzing the consequences of an accident. Thus, in addition to the problem of technical quality of a model; its **fitness for use** must also be judged. Models based on similar scientific foundations may behave very differently, for example :

- Models aimed at meeting emergency situations requiring real time measures and swift access to pre-calculated data.
- Models aimed at planning or establishing emergency plans usually requiring large numbers of tests covering a broad spectrum of scenarios.
- Models used in the most accurate calculations possible of the consequences of accidents which rely on advanced research and which do not normally worry about constraints in calculation time or hardware in general.

In this lecture, we will mostly focus on the second criterion; the first one will be evoked shortly.

In the first section, we specify what we mean by an Industrial Environment in the context of Risk Analysis.

In a second part, we review three models: one (EUROCHLOR) which is operational and has been used for more than ten years for assessing the consequences of heavy gas releases in medium range domains; one whose industrial β -test has just started (SEVEX) and which intends to predict the consequences of accidents at meso-scale level, and finally, one full 3D model (DISCO) whose aim is to replace EUROCHLOR in a medium term.

In the third section, we introduce a methodology for embedding numerical codes in so called Knowledge-Based Front-Ends (KBFEs); this technique was developed in the framework of an Esprit 2 Project [1] and aimed at enhancing the capabilities of existing numerical codes by adjunction of ruled-based expertise.

The last section is devoted to the Quality-Assurance approach as a means for evaluating Mathematical Models used to quantify the consequences of Major Hazards; it basically means :

- producing a structured measurement of the quality of a model which can be communicated to all the parties interested (Legal Authorities, Industries, Central and Local Administrations, Insurance Firms, Consultants, Question and Research Groups) ,
- authorising an open audit performed by an independent expert on the use of the model by end-users which should result in a written opinion as to the relevance of the results, the field of applicability of the model and the type of users it is aimed at ,
- providing the end-user with clear documentation on the field of applicability of the model, on its limitations and on the degree of accuracy of the results.

2. THE INDUSTRIAL CONTEXT

The domain of interest of Major Hazard studies typically ranges from a few hundred meters up to a few tenths of kilometers (sub-mesoscale) which means that we have in mind Plant Safety studies (basically an industrial concern) as well as Emergency Plan settings in case of an accident (basically a Legal Authorities concern).

The number and the types of scenarios of interest has dramatically increased in the past ten years; they must cover:

- various types of sources : jets, leaks, stack emissions, ground level sources,...
- various types of releases : instantaneous, short duration (~5 minutes), continuous.

Gases heavier or lighter than air are to be taken into account, either toxic or explosive; the size of the emissions may range from a few kilogrammes per second up to tons per second as shown in the figures below. In the past ten years we can say that we moved from realism to catastrophism !

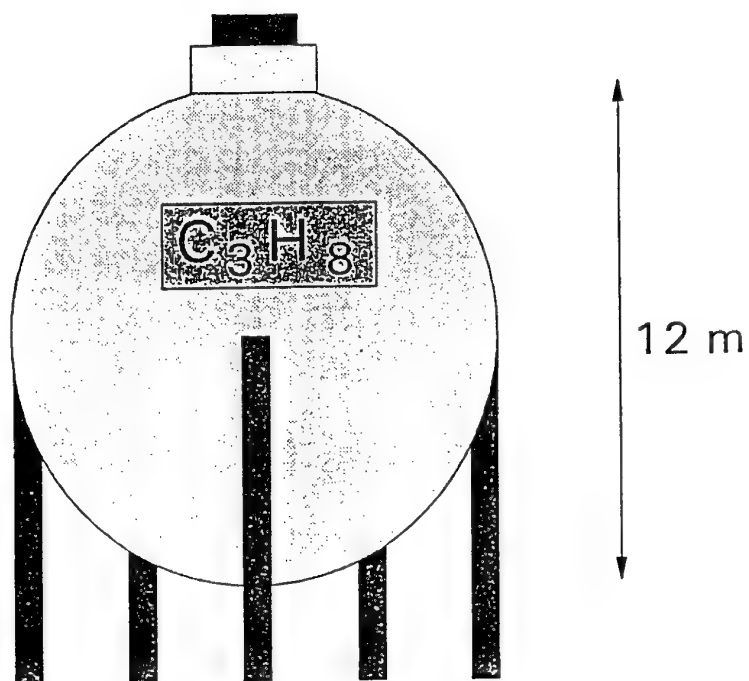


Figure 1 : A 370 ton sphere of Propane

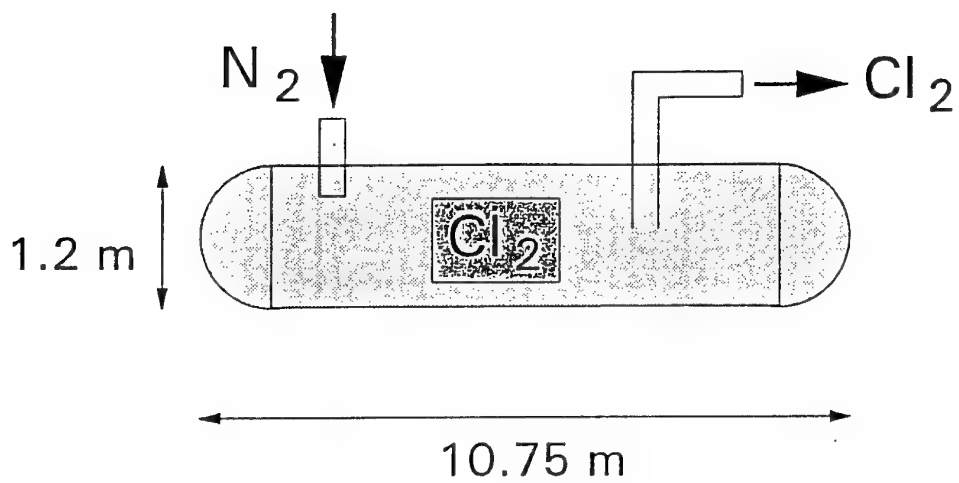


Figure 2 : A 55 ton wagon of Chlorine

Obstacles (buildings, forests, canyons, fences, water-ways,...) are to be taken into account explicitly as well as the site topography.

DISPERSION DE POLLUANTS ATMOSPHERIQUES

Champ des vitesses dans l'axe du vent

Conditions atmospheriques		Statistiques de l'essai	
Vitesse du vent a 10 m	: 3.0 (m/s)	Duree de la simulation	: 100 (s)
Gradient thermique au sol	: -1.000 (K/100m)	Maillage (90.0x 50.0)	: (5 x 4)
Hauteur de rugosite	: 0.100 (m)	Nombre d'iterations	: 450
Hauteur de l'atmosphere	: 562. (m)	Type de machine	: VAX8550
		Temps CPU total	: 860 (s)
		Pas de temps final	: 0.222 (s)

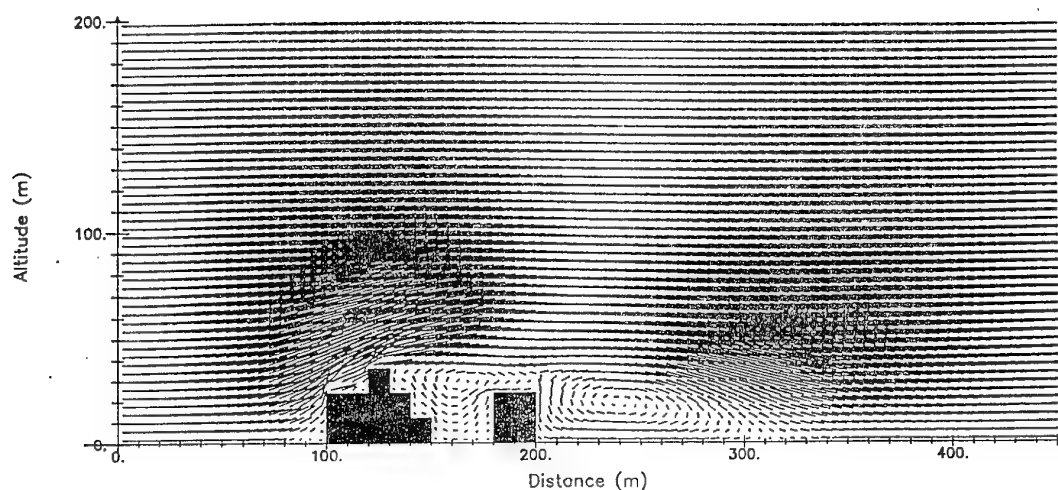


Figure 3 : The influence of buildings.

DISPERSION DE POLLUANTS ATMOSPHERIQUES

Champ des vitesses dans l'axe du vent

Conditions atmospheriques		Statistiques de l'essai	
Vitesse du vent a 10 m	: 4.0 (m/s)	Duree de la simulation	: 200 (s)
Gradient thermique au sol	: -1.000 (K/100m)	Maillage (160x100)	: (5.0 x 4.0)
Hauteur de rugosite	: 0.200 (m)	Nombre d'iterations	: 2244
Hauteur de l'atmosphere	: 881. (m)	Type de machine	: CRAY
		Temps CPU total	: 321 (s)
		Pas de temps final	: 0.089 (s)

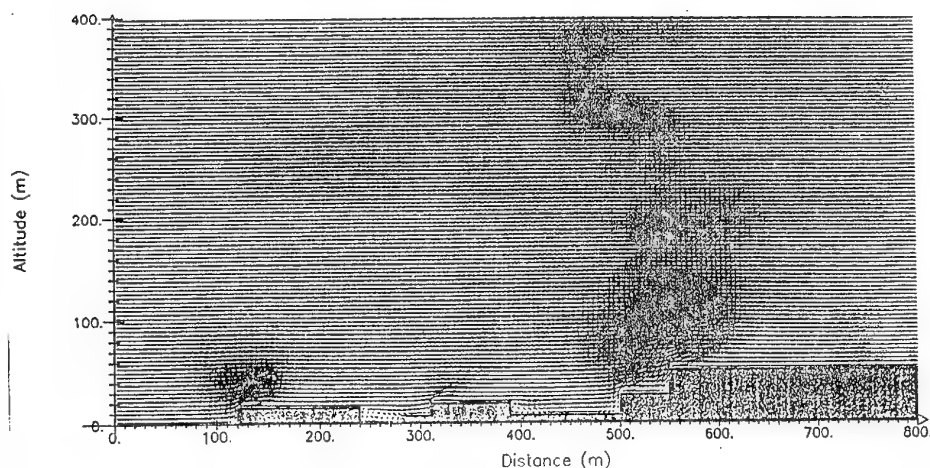


Figure 4 : The influence of topography

A full range of atmospheric conditions has also to be considered ranging from typical inversion situations with low wind speeds up to rather dispersive neutral cases.

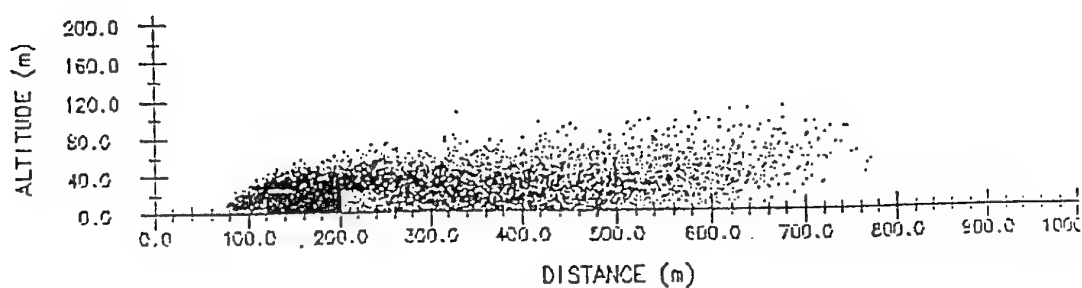
NEUTRAL ATMOSPHERE "D"

$$\Delta T = -1^{\circ}\text{C}/100\text{ m}$$

EMISSION DURATION : 120 s

$$Q = 3\text{ kg/s}$$

$$V_{10\text{ m}} = 3\text{ m/s}$$



STABLE ATMOSPHERE "F"

$$\Delta T = +2^{\circ}\text{C}/100\text{ m}$$

EMISSION DURATION : 120 s

$$Q = 3\text{ kg/s}$$

$$V_{10\text{ m}} = 3\text{ m/s}$$

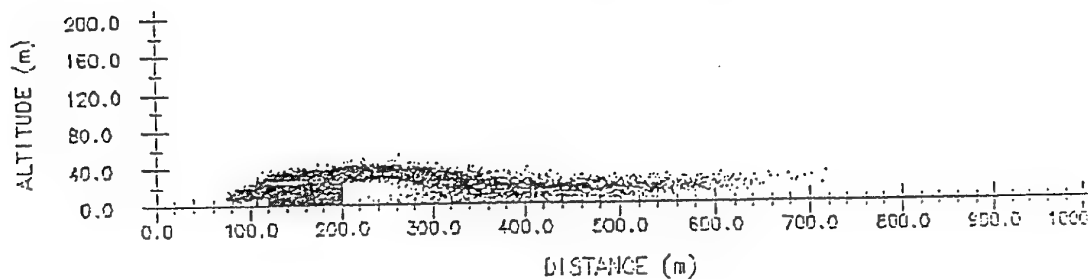


Figure 5 : The influence of the atmospheric thermal stratification

Also of significant importance is the fact that industrial people, as well as public authorities, are much more interested in the consequences of an accident than in its effects (see Fig. 6 below).

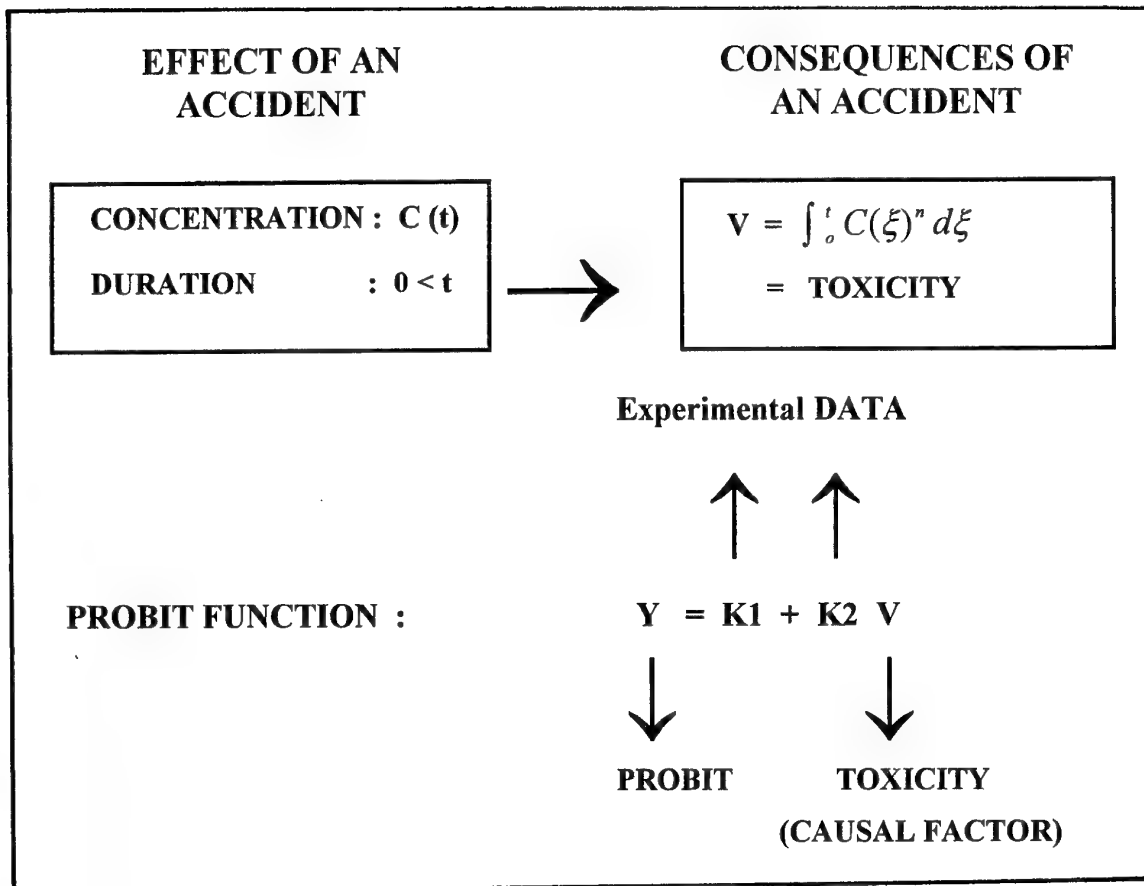


Figure 6 : Consequences of an accident versus effect

3. MATHEMATICAL MODELS OF ENVIRONMENTAL FLOWS

3.1. EUROCHLOR : A MEDIUM RANGE ATMOSPHERIC DISPERSION MODEL

The Eurochlor model [2,3,4] was initiated by the European Chlorine Producers Association EUROCHLOR (formerly BITC) and carried out at the von Karman Institute for Fluid Dynamics and the Solvay Central Research Laboratory; it has been designed to meet the following challenging objectives :

- it should be applicable to the study of toxics (rather than flammable gases) characterized by low concentrations at distances a long way from the source;
- it should be sufficiently rigorous to handle atmospheric turbulence in complex domains over a full range of atmospheric conditions;
- it should be capable of dealing with both continuous and instantaneous releases of passive gases and also gases which may be lighter or heavier than air;
- it should be capable to be run on a workstation.

We shall first review the basic physics the model is based on and say some words about its computerization. We then discuss the methodology that was developed in order to validate the model against wind tunnel and field test experiments on the one hand, and to simulate practical industrial cases on the other.

3.1.1. THE MATHEMATICAL MODEL

Insofar as Prandtl's concept of a purely laminar sub-layer near a smooth surface is not applicable to atmospheric flows, we have to introduce turbulence mechanisms in the conservation laws of fluid mechanics that express the problem mathematically.

The Reynolds decomposition acting on the state variables - wind velocities, viscosities, pressures, temperatures and concentrations - allows us to separate the average value effect from its purely turbulent counterpart; typically we obtain for the horizontal component of the velocity u , with straightforward notations :

$$u = U + u'$$

A full quantitative treatment of the derived system of equations would require a huge amount of both theoretical and computer work; it is however possible, by a judicious choice of approximations, to keep the problem sufficiently rigorous and tractable for solving a large range of industrial scenarios [5].

More precisely, although we must be aware that over a substantial range of applications, the source effects, where gravity spread dominates, interact with ambient turbulence effects, we have the feeling that, in the case of small up to medium size releases of toxic gases (no flammability problems), we are allowed to look at heavy gas releases as a transient disturbance of the atmospheric surface layer. The model describes the continuous transition from heavy gas controlled flow at ambient temperature to dispersion by ambient turbulent dispersion only.

3.1.1.1. The basic physics

One basic assumption the model is based on is that the pollutant is supposed not to interact dynamically or thermically with air, which in other terms means that any interaction between pollutant and air momentum can be neglected even in the source area [2,3,5]. It also means that whenever this assumption does not hold, in the case of high pressure jets for instance, we have to deal with the source term separately in order to estimate the gas cloud size at the end of this initial phase.

More precisely, the two first stages following the release, i.e. the one where the turbulence generated by the accidental release process is important, and the second phase, in which the heavy gas cloud slumps as a gravity flow, are supposed to be studied separately in order to provide the necessary source characteristics to get the study started at a stage where the major effects the cloud excess density and the ambient turbulence. Dilution effects for example, should be quantified separately. This last assumption is essential in the sense that it allows us to decouple the concentration diffusion equation from the turbulent flow balances.

From a mathematical point of view this led us to consider, on the one hand a two dimensional steady turbulent flow field and on the other a 3-D unsteady mass transfer balance.

Let us now review the other basic assumptions the model is based on :

The incompressibility of the atmospheric flow

The atmospheric flow is assumed to be incompressible, which means that dynamic effects on compressibility can be neglected [3,5].

$$\frac{\partial u}{\partial x} + \frac{\partial w}{\partial z} = 0$$

u denotes the horizontal component (x) of velocity and w the vertical (z) one.

This neither means, however, that air flow is incompressible nor that thermodynamic changes with height will not generate significant changes in density; in the latter case, temperature is assumed to be the main factor responsible for height-density variations.

The Boussinesq approximation and the gradient hypothesis for turbulent closure

Boussinesq's approximation neglects density variations insofar as they affect inertia and retains them only when combined with the acceleration of gravity in the buoyancy term of the momentum equation [3,5,6].

The gradient turbulent hypothesis, in direct analogy with laminar transport, relates the turbulent transport to the gradient of the transported quantity. Starting from the Reynolds decomposition which naturally induces turbulent stresses and heat fluxes, we adopt a closure which assumes that the turbulent stresses and the heat fluxes averages are proportional to their mean value counterparts:

$$-\frac{\partial \overline{u'^2}}{\partial x} = \frac{\partial}{\partial x} \left(\mu_x \frac{\partial U}{\partial x} \right) \quad ; \quad -\frac{\partial \overline{u'w'}}{\partial z} = \frac{\partial}{\partial z} \left(\mu_z \frac{\partial U}{\partial z} \right)$$

$$-\frac{\partial \overline{u'w'}}{\partial x} = \frac{\partial}{\partial x} \left(\mu_x \frac{\partial W}{\partial x} \right) \quad ; \quad -\frac{\partial \overline{w'^2}}{\partial z} = \frac{\partial}{\partial z} \left(\mu_z \frac{\partial W}{\partial z} \right)$$

$$-\frac{\partial \overline{u'T'}}{\partial x} = \frac{\partial}{\partial x} \left(\mu_{T,x} \frac{\partial T}{\partial x} \right) \quad ; \quad -\frac{\partial \overline{w'T'}}{\partial z} = \frac{\partial}{\partial z} \left(\mu_{T,z} \frac{\partial T}{\partial z} \right)$$

A major consequence of this type of closure is that the momentum and energy equations now contain viscous contributions, μ_x , μ_z , $\mu_{T,x}$ and $\mu_{T,z}$ (they still have to be modelled explicitly):

Momentum :

$$\frac{\partial u^2}{\partial x} + \frac{\partial (uw)}{\partial z} = \frac{\partial}{\partial x} \left(\mu_x \frac{\partial u}{\partial x} \right) + \frac{\partial}{\partial z} \left(\mu_z \frac{\partial u}{\partial z} \right) - \frac{\partial \Phi}{\partial x}$$

$$\frac{\partial(uw)}{\partial x} + \frac{\partial w^2}{\partial z} = \frac{\partial}{\partial x} \left(\mu_x \frac{\partial w}{\partial x} \right) + \frac{\partial}{\partial z} \left(\mu_z \frac{\partial w}{\partial z} \right) - \frac{\partial \phi}{\partial z} - g \frac{T - \theta_0}{\theta_0}$$

Energy :

$$\frac{\partial(uT)}{\partial x} + \frac{\partial(wT)}{\partial z} = \frac{\partial}{\partial x} \left(\mu_{T,x} \frac{\partial T}{\partial x} \right) + \frac{\partial}{\partial z} \left(\mu_{T,z} \frac{\partial T}{\partial z} \right)$$

Here u denotes the mean horizontal wind velocity, w the mean vertical wind velocity, x the downwind distance, z the altitude, μ the mechanical turbulent viscosity, ϕ the kinematic pressure, g the gravitational acceleration, T the temperature and θ_0 the reference potential temperature. In practice $\mu_{T,x} = \mu_x$ and $\mu_{T,z} = \mu_z$ due to the fact that the turbulent Prandtl number $P_r = \frac{\mu_x}{\mu_{T,x}} = \frac{\mu_z}{\mu_{T,z}}$ is assumed to be equal to unity.

The Nee-Kovasnay turbulence model

The way turbulent viscosity has been dealt with in the model is basically due to Nee and Kovasnay [7], who treated both vertical and downwind turbulent viscosities as scalar quantities that are subject to classical conservation laws; that is as quantities which are transported by advection, which are produced and/or destroyed. Moreover, they treated turbulent viscosity as a self-diffusive process, the diffusion coefficient being viscosity itself :

$$\begin{aligned} \frac{\partial(u\mu_x)}{\partial x} + \frac{\partial(w\mu_x)}{\partial z} &= \frac{\partial}{\partial x} \left(\mu_x \frac{\partial \mu_x}{\partial x} \right) + \frac{\partial}{\partial z} \left(\mu_z \frac{\partial \mu_x}{\partial z} \right) \\ &+ A (\mu_x - \gamma) \left| \frac{\partial u}{\partial z} + \frac{\partial w}{\partial x} \right| - \frac{B}{L_d^2} \mu_x (\mu_x - \gamma) \end{aligned}$$

γ denotes the kinematic air viscosity, A and B are model constants, L_d is a characteristic length scale.

The original Nee-Kovasnay model has been extended by adding a buoyancy production/loss term P_θ in the vertical turbulent viscosity balance in order to reflect the effect of temperature stratification on turbulence:

$$\begin{aligned} \frac{\partial(u\mu_z)}{\partial x} + \frac{\partial(w\mu_z)}{\partial z} &= \frac{\partial}{\partial x} \left(\mu_x \frac{\partial\mu_z}{\partial x} \right) + \frac{\partial}{\partial z} \left(\mu_z \frac{\partial\mu_z}{\partial z} \right) \\ &+ A(\mu_z - \gamma) \left| \frac{\partial u}{\partial z} + \frac{\partial w}{\partial x} \right| - \frac{B}{L_d^2} \mu_z (\mu_z - \gamma) + P_\theta \end{aligned}$$

Using the gradient Richardson number (Ri_g), the buoyancy production/loss term P_θ is expressed in the form

$$P_\theta = -C \frac{Ri_g}{Pr_t} (\mu_z - \gamma) \left| \frac{\partial u}{\partial z} + \frac{\partial w}{\partial x} \right|$$

where C is a model constant and Pr_t the turbulent Prandtl number.

Adding natural boundary conditions :

- a given upstream velocity profile,
- ground level values for the state variables (null velocity, given temperature), as well as along buildings,
- continuous flux conditions elsewhere (downstream and along the upper boundary),

the system is then solved numerically by using a time marching iterative procedure based on the Marker and Cell (MAC) finite difference scheme [8,9,10].

The MAC method, which was originally developed for calculating transient flows, has been used in the present work, as an iterative technique for getting the steady state of the Navier-Stokes equations. The original MAC technique was slightly adjusted by introducing an artificial viscous contribution [8], which places our formulation between the centered discretization and the full upstream one (Donor Cell).

Typically, we obtain for the convection terms, expressions like :

$$\frac{1}{4\partial y} \left[(v_{i,j} + v_{i+1,j})(u_{i,j} + u_{i,j+1}) + \alpha |v_{i,j} + v_{i+1,j}| (u_{i,j} - u_{i,j+1}) \right. \\ \left. - (v_{i,j-1} + v_{i+1,j-1})(u_{i,j-1} + u_{i,j}) - \alpha |v_{i,j-1} + v_{i+1,j-1}| (u_{i,j-1} - u_{i,j}) \right]$$

where α is an adjustable model parameter varying between 0 et 1; $\alpha=0$ leads to the original MAC formulation, while $\alpha=1$ corresponds to the Donor Cell one which introduces a significant artificial viscosity. The latter, only influences the transient state and by no way, penalizes the steady state.

However, the damping introduced by the artificial viscosity, if not controlled, will strongly affect the computer code performances; that is why we choose α , slightly larger than the maximum value of the quantities $\left| \frac{u\Delta t}{\Delta x} \right|$ and $\left| \frac{w\Delta t}{\Delta z} \right|$ as close as possible to 1 :

$$1 \geq \alpha \geq \max \left\{ \left| \frac{u\Delta t}{\Delta x} \right|, \left| \frac{v\Delta t}{\Delta y} \right| \right\}.$$

The restrictions made on the time step Δt , mainly come from the fact that the finite difference forms of the continuous equations account for transfers between adjacent cells.

The condition $\Delta t \leq \min \left\{ \frac{\Delta x}{|u|}, \frac{\Delta z}{|w|} \right\}$ which expresses the fact that the fluid is not allowed to flow across more than one computational cell in one time step, is natural in the sense that the convective flux approximations assume adjacent cell exchanges only.

On the other hand the "parabolic type" condition

$$\Delta t \leq \frac{1}{2} \left[\frac{1}{(1/\Delta x)^2 + (1/\Delta z)^2} \right] \min(1/\mu_x, 1/\mu_z)$$

limits the speed at which momentum of heat diffuses, again in order to keep the phenomenon inside one cell.

The Dispersion Model

It should be reminded that the pollutant dispersion balance is solved independently from the turbulent flow field; it is expressed by the equation :

$$\frac{\partial c}{\partial t} + \frac{\partial}{\partial x} \left[c \left(u - \frac{\mu_x}{c} \frac{\partial c}{\partial x} \right) \right] - \frac{\partial}{\partial y} \left(\mu_y \frac{\partial c}{\partial y} \right) + \frac{\partial}{\partial z} \left[c \left(w - \frac{\mu_z}{c} \frac{\partial c}{\partial z} \right) \right] = S$$

S being the source term.

In this three dimensional unsteady equation, the mass transfer coefficients are assumed equal to the mechanical ones; this is due to the fact that their ratio - the Schmidt number - is close to unity [5]. The dispersion equation is solved by using a Lagrangian discretization technique, the pollutant being considered as the sum of a sufficiently large number of particles moving in the previously calculated velocity field.

The diffusional velocities $\frac{\mu_x}{c} \times \frac{\partial c}{\partial x}$ and $\frac{\mu_z}{c} \times \frac{\partial c}{\partial z}$ are replaced by randomized ones [1,2,5]. The total displacement of a particle $d\vec{x}$ is assumed to be the sum of four terms :

$$d\vec{x} = \vec{v} dt + \sqrt{2\vec{\mu}} dW + \frac{\partial \vec{\mu}}{\partial z} dt + \frac{C}{\rho_{air}} y \frac{\Delta \rho}{\rho_{Poll}} dt^2$$

The first term is the advection contribution induced by the mean velocity field. The second term is the homogeneous turbulence contribution; entirely random, it is assumed to be of Gaussian probability with standard deviation $\sigma = \sqrt{2\mu_i \Delta t}$, $i = x, y$.

The third term takes into account the tendency of the pollutant to be transported in the direction of increasing turbulent length scales. This term proportional to the gradients of the typical turbulent parameters, does account for the mean "turbulent" displacement of the plume centroid [11].

The last term in the sum reflects the Archimedian force effects; ρ denotes the density, either of the air or of the pollutant, c is the pollutant concentration, g the gravitational acceleration and $\Delta \rho$ the excess of pollutant over air.

3.1.2. The EUROCHLOR code validation

The validation of the EUROCHLOR code was a key element of the study which was carried out both at the von Karman Institute for Fluids Dynamics and at the Solvay Research Laboratory; it required direct comparison with data obtained at full scale and from wind tunnel experiments. It was also necessary to check the code against other ones currently used in atmospheric dispersion prediction.

3.1.2.1. Validation against wind tunnel tests

A preliminary, but extensive, validation was undertaken at the von Karman Institute for Fluid Dynamics by comparing calculated values with wind tunnel data.

Among these tests, CBrF_3 (molar mass 149 g) releases from an elevated point source ($Z_{\text{source}} = 0.05\delta$, where δ is the boundary layer thickness) in an artificially thickened turbulent boundary layer seem to be particularly significant [12]. The wind tunnel which had a 180 mm by 350 mm rectangular cross section was characterized by a 2 m long test section. Vortex generators and surface roughness were used to generate a turbulent mean velocity profile close to the one in the atmospheric boundary layer.

Figure 7 compares the experimental and predicted decay of maximum concentration downstream of the source; apart from the near surroundings of the source, the two profiles are in agreement.

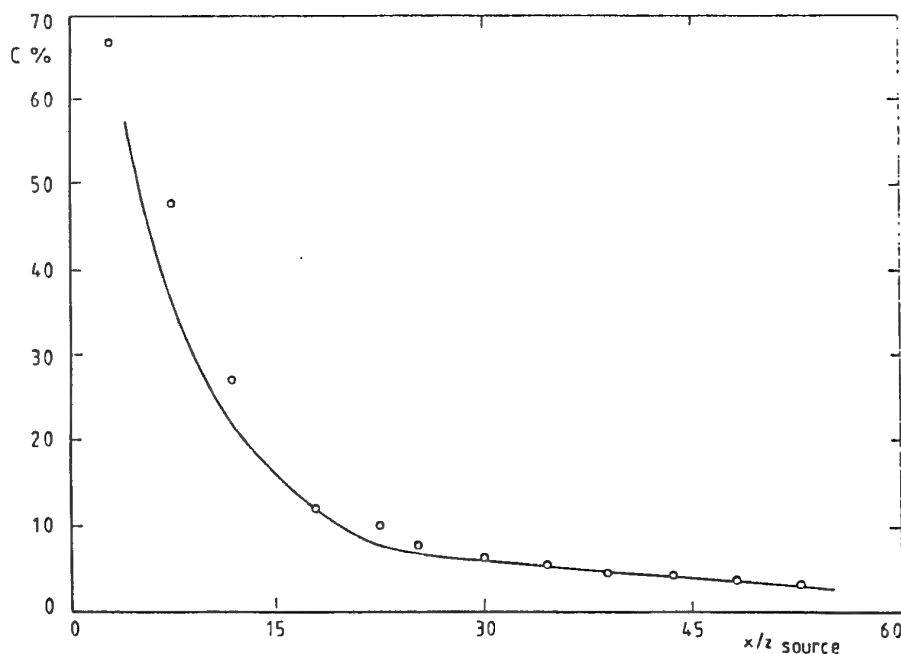


Figure 7 : Longitudinal decay of maximum concentration for heavy gases free dispersion from a point source: o Experiment and - Prediction

A more detailed study conducted by Riethmuller and Borrego [12] compares predicted and experimental concentration profiles at different longitudinal locations; it shows a quite good agreement apart from a slight underestimation of the plume spread quite near to the source.

3.1.2.2. Validation against other mathematical models

To ensure and check the robustness of the code and the soundness of the underlying physics, intensive tests were carried out by Solvay to show :

- the consistency with Gaussian models in typical free-field situations,
- the effect of the pollutant density on the dispersion process,
- the influence of atmospheric stability,
- the effect of the wind speed on dispersion,
- the dependence on the pollutant release rate,
- the influence of the emission duration,
- the prominent part played by buildings in the dispersion phenomena,
- the agreement with the results from the experimental releases of methane in the Burro tests (China Lake Experiments) and from the Thorney Island tests.

Examples are shown in Figures 8, 9 and 10 below :

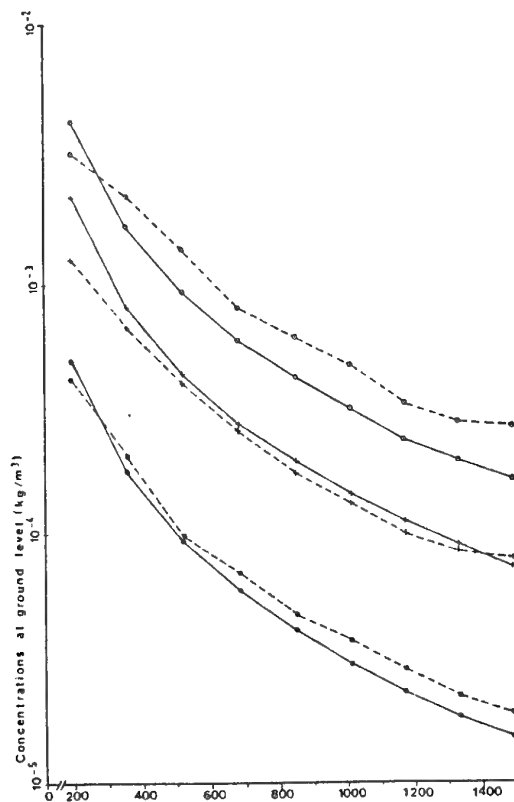


**Figure 8 : Comparison of the EUROCHLOR code with a GAUSSIAN Model :
the influence of stability**

The legend is : -+- Neutral Gauss, - + - neutral EUROCHLOR, -O- stable Gauss,
- O - stable EUROCHLOR, -●- unstable Gauss, and - ● - unstable EUROCHLOR.

The scenario characteristics are: continuous emission, free field, passive gas and source at ground level. The value for z_0 is 0.03 m, for u at 10 m : 3 m/s and for the flowrate : 1 kg/s.

The agreement between both models is good in spite of the fact that the Gaussian model is not really appropriate for emissions at ground level.

To show the influence of the wind speed on dispersion, we considered a 10 kg/s chlorine release in neutral atmospheric conditions, with 3 different wind speeds (5, 10 and 15 m/s).

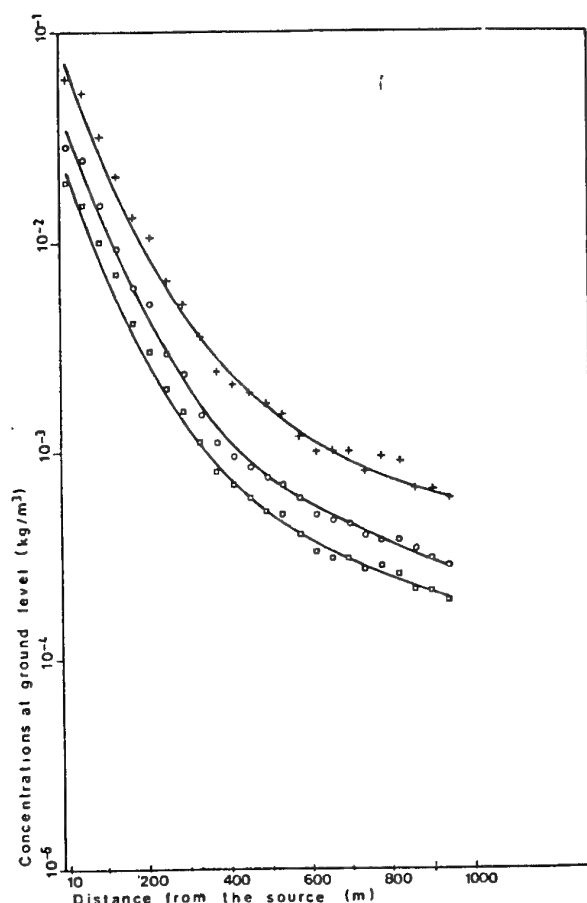


Figure 9 : The influence of Wind Speed in a Neutral Atmosphere

The legend is : $u(10 \text{ m}) = (+ : 5 \text{ m/s}, -O : 10 \text{ m/s} -\square : 15 \text{ m/s})$; in this test, $z_0 = 0.01 \text{ m}$ and the temperature gradient is $-1^\circ \text{C}/100\text{m}$.

As expected, dispersion is significantly improved as the wind speed increases .

In the next Figure, we show the influence of buildings. We must remind that due to the fact that the velocity field is 2-D, obstacles must be assumed to be infinite perpendicularly to the wind direction. This means that only a restricted selection of obstacles can be simulated, such as walls, large buildings, channels or roadways; in Figure 10, the 2-D buildings are interposed in the gas path and extend 80 m downwind.

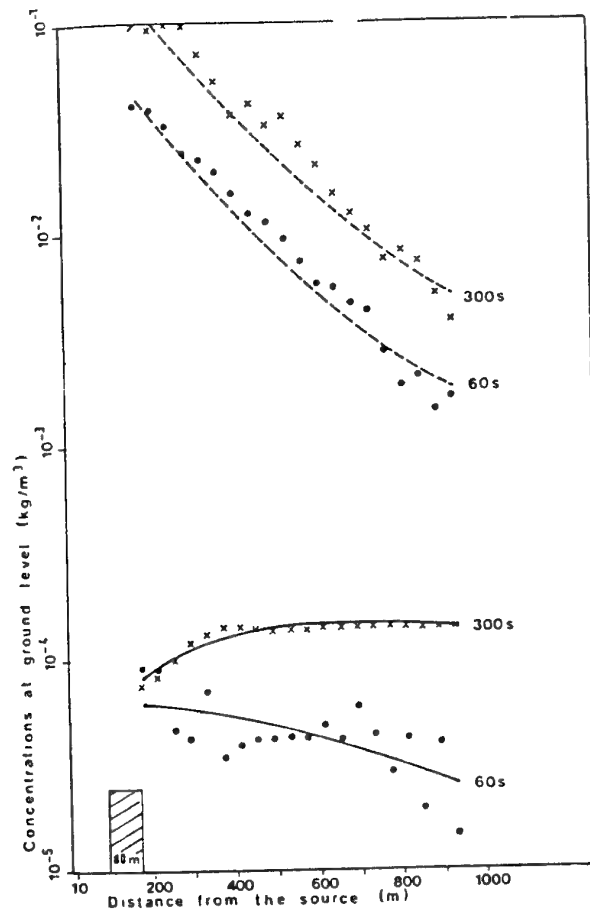


Figure 10 : The influence of 2-D buildings on Chlorine puffs in a Stable Atmosphere

The legend is : - x - Free Field (300 s); - * - with building (300 s); - ● - Free Field (60 s); - ● - with buildings (60 s).

The experimental conditions are : a source at ground level; $z_0 = 0.1$ m; $u(10 \text{ m}) = 2 \text{ m/s}$.
The building dimensions are respectively : length = 80 m, height = 24 m.

3.2. SEVEX : A MESO-METEOROLOGICAL 3-D CODE

The SEVEX initiative was started in the late eighties under the leadership of the Ministry of the Southern Region of Belgium (Région Wallonne), in cooperation with three Universities: the University of Louvain (UCL), the University of Liège (Ulg) and the Faculté Polytechnique de Mons (FPMs) [13,14,15].

The goal of the project was to provide Public Authorities in charge of Emergency Planning with a reliable quantification tool capable of helping them in setting up their emergency procedures.

In 1991, SOLVAY joined the Project Supervisory Committee and was asked in 1993 to re-engineer the existing codes and particularly to develop a user-friendly interface.

The SEVEX Code architecture is very similar tho the EUROCHLOR one as shown in the next Figure.

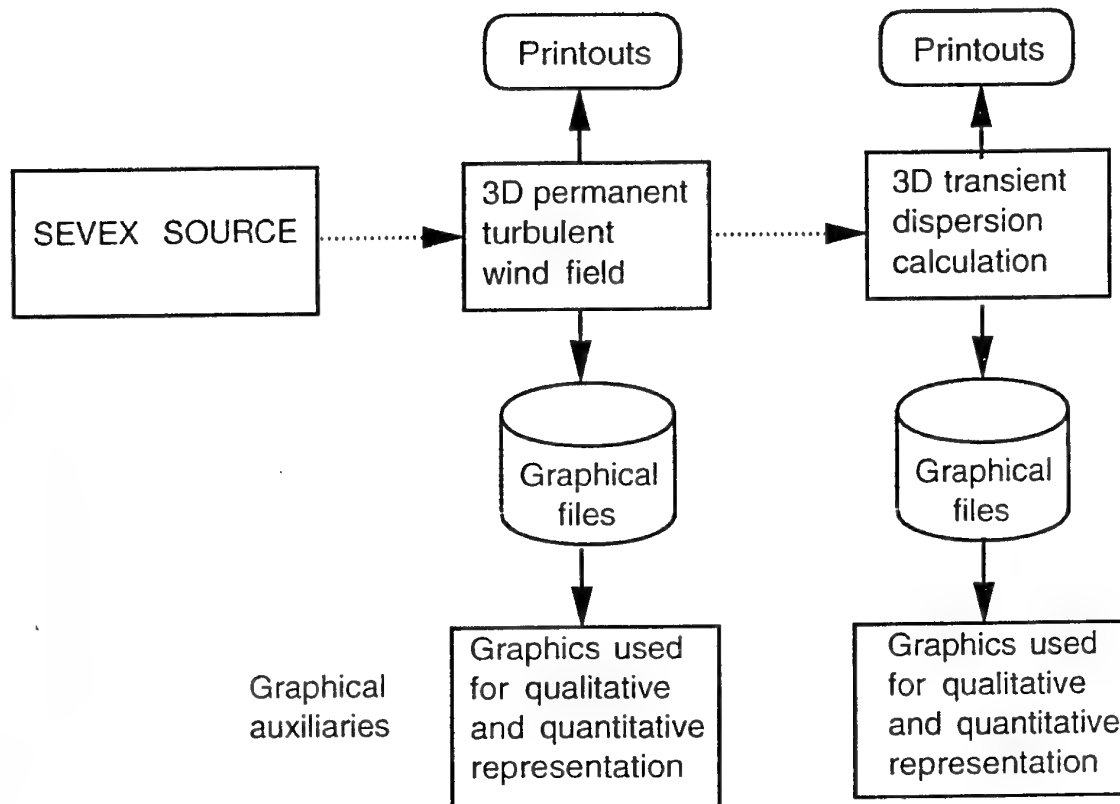


Figure 11 : The SEVEX Architecture.

The main differences between the SEVEX and the EUROCHLOR Models are :

- the Source module is much more sophisticated and can be compared with the best similar models on the market;
- the turbulent wind velocity field is based on a 3-D Meso-Meteorological Model originated from the Model developed by Bornstein in 1987 [16] and allows for long range dispersion simulations.

3.2.1. The SEVEX Source Term Module

In the Source Term Module, the gas is assumed to be confined in a cylinder with uniform concentration and temperature; gases of any density can be dealt with. Two types of releases, both of great interest, are considered: the **Instantaneous and the Continuous Releases**. The SEVEX Source Module actually solves the Boiling Liquid Expanding Vapor Explosion fireball (BLEVE), the Unconfined Vapor Cloud Explosion (UVCE) and the dispersion of a dense toxic gas. The BLEVE-fireball and the UVCE will not be treated here.

3.2.1.1. The Instantaneous Releases

Four quite different effects characterize the Source Term in this case:

- **The Initial phase**

The cold gas cloud is there assumed to be a cylinder with initial height (h) equal to its radius (R); the initial temperature is supposed to be the pollutant normal boiling point. The vapor fraction is computed on the basis of an adiabatic flash at atmospheric pressure.

- **The Gravity phase**

Due to the gravity effect (g), the gas cylinder gradually sinks down. The rate of change in the radius follows the semi-empirical law :

$$\frac{dR}{dt} = K \sqrt{gh \frac{\rho_{cloud} - \rho_{air}}{\rho_{air}}}$$

where K is an experimental coefficient whose value ranges between 1 and 1.44; ρ denotes the density.

The concentration is uniform in the cylinder and directly related to the mass and the volume of the cloud. The gravity phase is responsible for the radius increase and the decrease of the cloud height.

- **The Entrainment phase**

The entrainment of air in the gas cylinder induces cloud heating and increases its volume; natural and forced convection may generate additional heating of the cloud.

The rate of entrainment of air is given by :

$$\frac{d m_a}{d t} = \rho_{air} (\pi R^2) U_{top} + \rho_{air} (2 \pi R h) U_E$$

where :

$$U_E = \alpha_1 \frac{d R}{d t} \quad \text{denotes the entrainment velocity at the edge of the cylinder,}$$

$$U_{top} = \alpha_2 U_1 R_i^{-1} \quad \text{denotes entrainment velocity at the top and}$$

$$R_i = \frac{g l_s}{U_1^2} \frac{\rho_{cloud} - \rho_{air}}{\rho_{air}}$$

with U_1 the longitudinal turbulent velocity which is proportional to the friction velocity u^* : $U_f = c \cdot u^*$. The coefficients c and the characteristic turbulent length l_s are given in tables; they depend on the Pasquill Stability Classes and on the cloud height. The best values obtained so far for α_1 and α_2 are respectively 0.5 and 0.05.

When the temperature of the ground and of the cloud differ, convection (natural and forced) as well as solar and earth radiation must be incorporated. Liquid droplet vaporization and moisture are also taken into account in the enthalpy balance in order to get a better description of the physics.

The cloud is supposed to be advected downwind, with a wind speed estimated at mid-cloud height.

• The transition to the passive phase

Progressively the dilution of the gas increases and the diffusion becomes passive. Two tests are proposed:

- a first and very natural one compares the specific masses of the cloud and of air; typically a difference of 10^{-3} kg/m^3 is considered.
- a second test compares the rate of increase of the gas cloud radius due to gravitational effects to the one induced by turbulence..

Dispersion is then considered as passive when :

$$\frac{dR}{dt} = K \sqrt{\frac{gh}{\rho_{air}}} (\rho_{cloud} - \rho_{air}) \leq 2.14 \frac{d\sigma_y(x)}{dt}, \quad \text{with} \quad \frac{d\sigma_y(x)}{dt} = C^* u(t)$$

$u(t)$ denotes the wind speed at half cloud height; C^* is a constant depending on the Pasquill Stability Class and varying between 0.22 (class A) and 0.04 (class F).

After one of these criteria is satisfied, the cloud is supposed to diffuse as a passive constituent.

At this stage, the user has the choice between using a classical Gaussian model in which the radial and vertical dispersion coefficients are calculated according to Briggs [17], or to switch to a 3-D dimensional passive dispersion model in which case SEVEX is capable of taking complex terrains and orography into account.

The data to be transferred from the source term module to the 3-D dispersion model are characterizing the meteorology, of geographical nature (the topography, the surface roughness, ...), and the gas cloud characteristics (size, location,...). The gas with uniform concentration is supposed to be confined in a cylinder.

3.2.1.2. The Continuous Releases

The modeling of this type of release is subdivided into three parts: the jet phase, the dense cloud phase and the neutral cloud dispersion phase. Different scenarios of releases are considered: liquid, gaseous and flashing liquids, with and without friction through ducts.

The discharge rate and other characteristics like pressure, temperature, vapor fraction, velocity, ... are determined by more or less classical formulas.

• The Jet Phase

The model is based on the work by Iannello et al. [18]; the jet leaving the source expands and is computed by means of two dedicated sub-modules (this jet calculation is necessary both for further phases of dispersion and for the study of UVCEs).

- The Expansion Module

In this phase, the jet atomizes to droplets and flashes. 1-D momentum and energy conservation laws give the jet velocity after expansion and the partial vapor pressure in which the total pressure is supposed to be equal to the atmospheric one. The temperature is supposed to be the boiling point of the released chemical. The fraction of unflashed liquid leaving the jet and forming the rain-out liquid is then determined following a model developed by Wheatley [19].

- The Entrainment Module

The jet, at ambient pressure, is diluted by turbulent mixing with the atmosphere. A model based on the work of Ricou and Spalding [20] evaluates the mixing process. The 1-D spatial behavior of the temperature vapor fraction and composition is derived rigorously from the energy balance. The jet structure and its modelization remains as long as the momentum dominates over buoyancy and atmospheric turbulence effects. The Richardson number is introduced as a criterion to decide if the jet structure is still applicable.

• The Dense Cloud Dispersion Module

The dissipation of the jet structure can generate a dense cloud. The gas cloud forms a steady plume with a rectangular cross section; it is studied by means of a Box Model which is very similar to the one described in the case of an instantaneous release.

The parameters describing the evolution of the cloud are its height (h), its half width (L), its velocity (u) and its concentration (C).

The volume flow rate of the pollutant (Q_v) is given by the expressions:

$$Q_v = 2 L h u \quad \text{and} \quad C = \frac{Q}{Q_v}$$

- The Gravity Phase

The the cloud half width change in space is given by the expression:

$$\frac{d L}{d x} = \frac{K}{u} \sqrt{g h \frac{\rho_{cloud} - \rho_{air}}{\rho_{air}}}$$

- The Entrainment Phase

For the mass flow rate through a given cross section of the plume, we have

$$\frac{d Q_a}{d x} = 2 \rho_{air} L U_{Top} + 2 \rho_{air} h U_E,$$

the edge entrainment velocity U_E is expressed by: $U_E = \alpha_1 u \frac{d L}{d x}$ and the top

entrainment velocity U_{top} by: $U_{Top} = \alpha_2 U_1 Ri^{-1}$

As in the case of an instantaneous release, the downwind evolution of the characteristics (temperature, water vapor and composition) of the cloud is deduced from the enthalpy balance taking into account the liquid droplet vaporization and the incorporation of moisture.

• The Transition to Passive Diffusion

The criteria of transition from a dense to a passive dispersion are the same as in the case of an instantaneous release. Once neutral, the dispersion and the transport are driven by a 3D-Lagrangian model.

3.2.2. The Meso-Meteorological module

The meso-meteorological module calculates the 3-D wind and turbulence fields; the studied domain is centred around the location of the accident. The ground can be flat or hilly. This module is a 3-D Planetary Boundary Layer Model [21] originating from the URBMET model developed by Bornstein [16], in which the topography treatment and more refined surface influence have been adapted to our applications.

The model is governed by the Boussinesq flow equations and based on the vorticity formulation whose main advantage is that we can drop the density and pressure terms in the equations of motion. The horizontal turbulent viscosity and diffusivity are supposed to be equal : $10^3 \text{ m}^2/\text{sec}$ each.

The vertical turbulent viscosity λ_m and diffusivity λ_θ , in turn, are related to the mean turbulent kinetic energy $\varepsilon = \frac{1}{2} (u'^2 + v'^2 + w'^2)$ and to the mixing length l_k by $\lambda_m = C_m l_k \varepsilon^{0.5}$ and $\lambda_\theta = \alpha_\theta \lambda_m$, with $\alpha_\theta = 1.35$.

The mixing length l_k takes into account the atmospheric layer stability by integrating the Monin Obukov length. Moreover, in order to account for the anisotropy of the atmospheric turbulence, Therry and Lacarrère [22] suggested the following correction for l_k : $l_k = \left(\frac{w'^2}{\varepsilon} \right) l_\varepsilon$, where l_ε is given by :

$$\frac{1}{l_\varepsilon} = \frac{1}{k} + \frac{C_1}{ZI} - \left[\frac{1}{k} + \frac{C_2}{ZI} \right] m_1 m_2 + \frac{C_5}{l_s}$$

with : $m_1 = \frac{1}{[1 + (C_3 \cdot ZI) / k]}$

$$m_2 \begin{cases} = 0 & \text{if } L \geq 0 \\ = \frac{1}{[1 - (C_4 \times L) / ZI]} & \text{if } L < 0 \end{cases}$$

$$\frac{1}{1_s} \begin{cases} = 0 & \text{if } \frac{\partial \theta}{\partial z} \leq 0 \\ = \left[\frac{g \beta \frac{\partial \theta}{\partial z}}{\varepsilon} \right]^2 & \text{if } \frac{\partial \theta}{\partial z} > 0 \end{cases}$$

C_i are experimental constants, L is the Monin-Obukov length and ZI the height of the atmospheric boundary layer. K and θ are respectively the von Karman constant and the potential temperature.

Geographical maps provide altimetrical and roughness data of the studied region. A transformation for the vertical coordinate $z \rightarrow \eta$ is introduced and given by :

$$\eta = s \frac{z - z_g}{s - z_g}$$

with s , z and z_g respectively the altitude of the top of the studied domain, z the altitude of the courant point and z_g the altitude of the ground; it has the advantage to simplify the topography representation.

Near the ground, the surface layer with constant fluxes is treated analytically; modified logarithmic profiles [23] give the vertical distributions as a function of the atmospheric layer stability.

At each grid point, the model provides the vorticity, the wind velocity, the potential temperature and the friction velocity u^* . The model is solved using a $1 \text{ km} \times 1 \text{ km}$ horizontal grid. The vertical size of the mesh cells varies from 10 m to several hundred meters. The number of vertical grid points is 12. The horizontal size of the studied domain is $29 \text{ km} \times 29 \text{ km}$.

In order to delimit properly the risk areas, it is extremely important to consider not only the most frequent situations but also the worst meteorological conditions. A set of typical scenarios has been set up : 3 geostrophic wind speeds (4, 8, 12 m/sec), 12 or 16 directions and 2 stability classes, one corresponding to a covered sky during the day and the second to a clear night.

The meso meteorological module finally transfers information on the ground roughness, the turbulent velocity field and the data characterizing the stability of the atmospheric layer to the dispersion module.

3.2.3. The Lagrangian passive dispersion module

A Lagrangian particle diffusion method based on a scheme introduced by Yamada and Bunker [24] is used to calculate the transport and the dispersion of the released pollutant.

The principles the method is based on are:

- the mass of toxic gas is subdivided into a great number of elements or "particles";
- the size of each particle is finite and each particle has its own characteristics (velocity, temperature, pressure, concentration, ...);
- each particle is advected by air;
- the positions of the particles are updated every time step ($\Delta t \sim 10$ sec);
- the concentration at a particular location is the sum of all the contributions of the active particles.

The concentration following Yamada and Bunker [24] is :

$$C(x, y, \eta, t) = \frac{1}{(2\pi)^{1.5}} \sum_{p=1}^N \frac{M_p}{\sigma_{x_p} \times \sigma_{y_p} \times \sigma_{\eta_p}} \exp\left(-\frac{1}{2} \frac{(x_p - x)^2}{\sigma^2}\right) \exp\left(-\frac{1}{2} \frac{(y_p - y)^2}{\sigma^2}\right) \left\{ \exp\left(-\frac{1}{2} \frac{(\eta_p - \eta)^2}{\sigma_{\eta_p}^2}\right) + \exp\left(-\frac{1}{2} \frac{(\eta_p + \eta)^2}{\sigma_{\eta_p}^2}\right) \right\}$$

where M_p is the mass of particle p , (x_p, y_p, η_p) and $(\sigma_{x_p}, \sigma_{y_p}, \sigma_{\eta_p})$ respectively its coordinates and its geometrical characteristics; N refers to the total number of particles.

3.2.3.1. Model equations

• The velocity distribution

The position of a particle, at each time step Δt is expressed by the following equation :

$$x(t_{new}) = x(t_{old}) + \int_{t_{old}}^{t_{new}} u_p(x(t), t) dt \approx x(t_{old}) + u_p(t_{old}) \Delta t$$

Using the Reynolds decomposition : $\mathbf{u}_p = \mathbf{u}_m + \mathbf{u}_t$ where \mathbf{u}_m denotes the mean velocity calculated by the meso-scale meteorological model and \mathbf{u}_t the turbulent contribution, and if u' , v' , w' respectively represent the downwind, the crosswind and the vertical component of the turbulent velocity contribution, we get following Yamada :

$$\begin{aligned} u'(t + \delta t) &= a_u u'(t) + b_u \sigma_u \xi \\ v'(t + \delta t) &= a_v v'(t) + b_v \sigma_v \xi \end{aligned}$$

$$w'(t + \delta t) = a_w v'(t) + b_w \sigma_w \xi + (1 - a_w) TL_w \frac{\partial}{\partial z} \sigma_w^2$$

where $a_{u,v,w} = \exp\left(-\frac{\delta t}{TL_{u,v,w}}\right)$

$$b = \left(\sqrt{1 - a^2}\right)$$

$\sigma_{u,v,w}$ denote the standard deviations of the wind velocity fluctuations and $TL_{u,v,w}$ the Lagrangian time scales for the components of the velocity (u,v,w); ζ is a random number got from a Gaussian distribution with zero mean and unit variance.

The first term in the expressions above is an autocorrelation component of the wind velocity fluctuations; the second is directly associated to the turbulence in the planetary boundary layer and the last one in the third equation was introduced to avoid any accumulation of particles in regions of very weak turbulence.

The Lagrangian time scales depend on the stability within the planetary boundary layer and on the height of inversion. They are estimated as follows (Hanna [25] and Zannetti [26]) :

$$TL_u = 0.15 \frac{h_i}{\sigma_u} \left(\frac{z - z_g}{h_i} \right)^{0.5} \approx 0.15 \frac{h_i}{\sigma_u} \left(\frac{\eta}{h_i} \right)^{0.5}$$

$$TL_v = 0.15 \frac{h_i}{\sigma_v} \left(\frac{z - z_g}{h_i} \right)^{0.5} \approx 0.15 \frac{h_i}{\sigma_v} \left(\frac{\eta}{h_i} \right)^{0.5}$$

$$TL_w = 0.1 \frac{h_i}{\sigma_w} \left(\frac{z - z_g}{h_i} \right)^{0.8} \approx 0.1 \frac{h_i}{\sigma_w} \left(\frac{\eta}{h_i} \right)^{0.8}$$

with $\sigma_u = \sigma_v = 2u^* \left(1 - \frac{\eta}{h_i} \right)$ and $\sigma_w = 1.3u^* \left(1 - \frac{\eta}{h_i} \right)$,

u^* is the friction velocity and h_i the inversion height. If $\eta > 0.9h_i$ the computed values are those corresponding to $\eta = 0.9h_i$.

• The particle distribution

Each particle is to be looked at as the center of a puff. The distribution of mass around this center is assumed to be Gaussian; the variances are determined by integrating the velocity variances over the "history" of the puff. According to the classical theory of homogeneous turbulence it is given in the x direction by :

$$\sigma_x^2 = 2 \sigma_u^2 \int_0^t \int_0^z \exp \left(- \frac{\xi}{TL} \right) d\xi dz$$

This expression simplifies into :

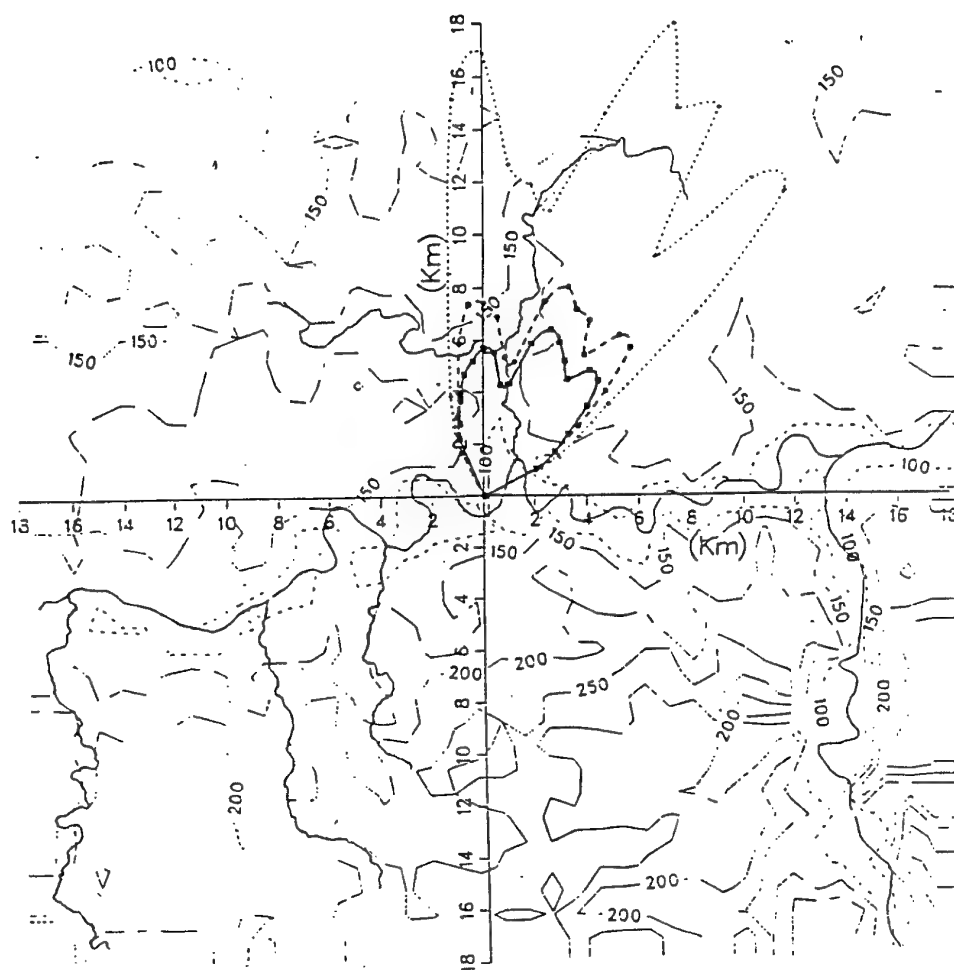
$$\sigma_x = \sigma_u t \quad \text{if } t \leq 2TL_u$$

$$\sigma_x^2 = 2\sigma_u^2 TL_u t \quad \text{if } t > 2TL_u$$

Similar expressions are obtained for the variances in the other space directions.

3.2.4. Typical output from SEVEX.

Specially dedicated to Emergency Planing issues, SEVEX outputs contours on maps covering the areas where SEVESO plants are located; these maps are delivered to the staff involved in Major Hazard exercises.



Cas de JOUR :

3-DISPERSION INST 55 t CHLOR

+ CONCENTRATION : 3.8 ppm

● CONCENTRATION : 15.0 ppm

■ CONCENTRATION : 25.0 ppm

Vent à 10.0 mètres

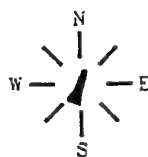


Figure 12 : A SEVEX typical graphical output

3.3. DISCO : A 3-D MEDIUM RANGE ATMOSPHERIC DISPERSION MODEL

After a more than ten years use of the EUROCHLOR Model, there was a need for extending its capabilities in order to handle more complex scenarios [27,28]. DISCO intends not only to extend the 2-D turbulent field modelling of the EUROCHLOR code to a 3-D one, but it is aimed at:

- giving a better description of the turbulent flow field based on a (k, ϵ) approach,
- giving a better description of the turbulence around obstacles, which is one of the weaknesses of the Lagrangian approach. **This pactically means that the pollutant mass balance and the Navier-Stokes equations are not anymore decoupled,**
- providing the end-user with a better numerical solver, both from a convergence and an accuracy point of view,
- providing the end-user with a more user-friendly interface with powerful vizualization capabilities,
- offering good computing performances.

The decision was taken not to develop such a code internally, but to start from a commercial general purpose hydrodynamic code (PHOENICS) which already disposes of rather good visualization facilities

3.3.1. The DISCO Model

The basic equations, boundary and initial conditions DISCO is based on are described below; then follows a description of the source term.

3.3.1.1. The Continuity Equation

As in the EUROCHLOR Model, the atmospheric flow is supposed to be incompressible; with straightforward notations :

$$\frac{\partial U_i}{\partial x_i} = 0$$

3.3.1.2. The Momentum Equations

The momentum conservation principle leads to :

$$\frac{\partial U_i}{\partial t} + \frac{\partial U_i U_j}{\partial x_j} = - \frac{\partial p}{\partial x_i} + \frac{\partial}{\partial x_j} \left(\mu_t \frac{\partial U_i}{\partial x_j} \right) + F_i$$

where the body force has the form $F_i = \frac{\rho - \rho_a}{\rho} g_i$, μ_t denotes the turbulent viscosity and ρ and ρ_a the density of the pollutant and air, respectively.

3.3.1.3. The Energy Equation.

The energy transport is given by:

$$\frac{\partial \Theta}{\partial t} + U_j \frac{\partial \Theta}{\partial x_j} = \frac{\partial}{\partial x_j} \left(\frac{\mu_t}{Pr} \frac{\partial \Theta}{\partial x_j} \right)$$

where Θ denotes the potential temperature.

3.3.1.4. The air and the pollutant as ideal gases.

Both the air and the pollutant are assumed to be ideal gases : $P = R \rho \frac{T}{M}$

It allows us to express the body force in the momentum equation explicitly; the expressions are different when expressed in mass fraction q :

$$\frac{\rho - \rho_a}{\rho} = \frac{M_g - M_a}{M_g} q \quad \text{or in volume fraction } \omega: \quad \frac{\rho - \rho_a}{\rho} = \frac{(M_g - M_a) \omega}{(M_g - M_a) \omega + M_a}$$

3.3.1.5. The (k,ε) Turbulence Closure.

The turbulent eddy viscosity μ_t is modeled as a function of the turbulent kinetic energy (TKE) and its dissipation :

$$\mu_t = C_\mu \frac{k^2}{\varepsilon}; C_\mu = 0.09$$

The equations for k and ε are respectively:

$$\frac{\partial k}{\partial t} + \frac{\partial U_i k}{\partial x_j} = \frac{\partial}{\partial x_j} \left(\mu_t \frac{\partial k}{\partial x_j} \right) + P_k + G_k - \varepsilon$$

and

$$\frac{\partial \varepsilon}{\partial t} + \frac{\partial U_i}{\partial x_j} \varepsilon = \frac{\partial}{\partial x_j} \left(\frac{\mu_t}{\sigma_\varepsilon} \frac{\partial \varepsilon}{\partial x_j} \right) + \frac{\varepsilon}{k} \left[C_{\varepsilon 1} P_k + C_{\varepsilon 1} (1 - C_{\varepsilon 3}) G_k - C_{\varepsilon 2} \varepsilon \right]$$

with

$$P_k = \mu_t \left(\frac{\partial u_i}{\partial x_j} + \frac{\partial u_j}{\partial x_i} \right) \frac{\partial u_i}{\partial x_j},$$

$$C_{\varepsilon 1}=1.44; C_{\varepsilon 2}=1.92; \sigma_\varepsilon=1.3; C_{\varepsilon 3}=0 \text{ if } G_k > 0; C_{\varepsilon 3}=1 \text{ if } G_k < 0$$

It can be seen that the equation for ε is relatively more complicated and includes a number of turbulence modelling constants.

The presence of the pollutant strongly affects the buoyancy production/loss term G_k whose modelling is responsible, to a great extent, for the quality of the results; its modelling is connected to the density gradient within the limits of the eddy diffusivity approach [29]; it is expressed by:

$$G_k = -g \frac{\mu_t}{Pr_t} \left\{ \frac{1}{1 + \sigma_\omega \omega} \left[\frac{1}{T} \frac{\partial \Theta}{\partial z} - \sigma_\omega \left[\frac{\partial \omega}{\partial z} - \frac{1}{T} \left(\frac{\partial \Theta}{\partial z} - \lambda \right) \omega \right] \right] \right\}$$

where $\sigma_\omega = (M_g - M_a)/M_a$; Θ is the potential temperature and ω the pollutant volume fraction.

This expression reduces to a more classical form when the contaminant volume concentration approaches zero or is nearly passive.

When expressed in mass fraction form, the expression for G_k is somewhat more complicated:

$$G_k = -g \frac{\mu_t}{Pr_t} \left\{ (1 - \sigma_q q) \frac{1}{T} \frac{\partial \Theta}{\partial z} - \sigma_q \left[\left(1 + \frac{\sigma_q}{1 - \sigma_q q} \right) \frac{\partial q}{\partial z} - \frac{1}{T} \left(\frac{\partial \Theta}{\partial z} - \lambda \right) q \right] \right\}$$

where $\sigma_q = (M_g - M_a)/M_g$.

The turbulent Prandtl number is taken equal to 1, the same value as in the EUROCHLOR code; **let us however notice that PHOENICS can not handle more general values.**

The Contaminant Concentration Balance

The concentration transport equation has the same form in mass and volume fraction; in mass fraction q we have:

$$\frac{\partial q}{\partial t} + U_j \frac{\partial q}{\partial x_j} = \frac{\partial}{\partial x_j} \left(\frac{v_t}{Pr} \frac{\partial q}{\partial x_j} \right)$$

3.3.2. The Boundary conditions

Typical boundary conditions, near the ground, for the velocity, the turbulent kinetic energy and its dissipation are:

$$U = \frac{U_\tau}{K} \ln \left(\frac{Z}{Z_0} \right); \quad k = \frac{U_\tau^2}{\sqrt{(C_\mu)}}; \quad \varepsilon = C_\mu^{3/4} \frac{k^{3/2}}{K_z}$$

K being the von Karman constant and z the altitude.

For the contaminant mass fraction and the potential temperature, we assume respectively:

$$\frac{\partial q}{\partial x_n} = 0; \quad \Theta = \Theta_{ground}$$

3.3.3. The Initial conditions

The initial conditions for DISCO are deduced from a source area model [30,31], they are only needed for instantaneous releases.

The processes near the source, in turn, are complicated and have to be modelled separately. In DISCO as in many 3D similar models [1], a relatively simple approach was used which assumes uniform contaminant concentrations in the vicinity of the source. It consists of calculating a realistic volume of diluted contaminant at ambient temperature (the same technique was used in the EUROCHLOR code).

Typical conditions near the source are :

$$U_{source} = \frac{Q}{\rho_{source} A_{source}}; \quad \frac{\partial \Theta}{\partial y} = 0; \quad \frac{\partial k}{\partial y} = 0; \quad \frac{\partial \varepsilon}{\partial y} = 0$$

$$\frac{\mu_t}{Pr} \frac{\partial q}{\partial x_n} = -V_{source} (q_0 - q)$$

Other variants of the conditions for k and ε have been tested but no substantial difference has been observed.

The top region

$$W = 0; \quad \frac{\partial U}{\partial z} = \frac{\partial V}{\partial z} = \frac{\partial T}{\partial z} = \frac{\partial q}{\partial z} = \frac{\partial k}{\partial z} = \frac{\partial \varepsilon}{\partial z} = 0$$

The lateral planes

$$W = 0; \quad \frac{\partial U}{\partial y} = \frac{\partial V}{\partial y} = \frac{\partial T}{\partial y} = \frac{\partial q}{\partial y} = \frac{\partial k}{\partial y} = \frac{\partial \varepsilon}{\partial y} = 0$$

The outlet

$$\frac{\partial U}{\partial x} = \frac{\partial V}{\partial x} = \frac{\partial W}{\partial x} = \frac{\partial T}{\partial x} = \frac{\partial q}{\partial x} = \frac{\partial k}{\partial x} = \frac{\partial \varepsilon}{\partial x} = 0$$

The inlet

$$V = W = q = 0; \quad U = U_{inlet}; \quad k = k_{inlet}; \quad \varepsilon = \varepsilon_{inlet}; \quad \Theta = \Theta_{inlet}$$

The inlet quantities are computed from the above specified mathematical model with periodic boundary conditions and over a flat terrain; actually this problem is to be considered as a 1-D problem in the vertical direction [31].

3.3.4. The present state of DISCO

DISCO is presently tested on a qualitative base. Tests with or without buildings, with heavy of passive contaminants are underway. Up to now, no anisotropy has been taken into account for in the turbulent flow field.

4. THE KNOWLEDGE BASED FRONT-END TECHNOLOGY

The motivation for enhancing the capabilities of existing user software such as CFD codes by the application of Knowledge Based Systems (KBS) and Human Computer Interface (HCI) techniques was twofold:

- existing environmental CFD codes represent a body of valuable knowledge which in most cases is difficult to use because the knowledge it encapsulates is inherently complex and is presented through a poor, out-of-date user interface,
- part of the domain knowledge relies on common sense and can only be formalized in terms of production or inference rules.

Some attempts in this direction were already made at Solvay [4], which led to the development of pre-processors to existing codes; they however suffer from a lack of genericity as we show in the example below.

4.1. THE METEO PRE-PROCESSOR TO THE EUROCHLOR CODE.

The Mathematical Model EUROCHLOR is based on handles physical quantities such as the roughness height z_0 , the Monin-Obukhov length L and the friction velocity u^* , quantities which are naturally related both to the mechanically and thermally induced turbulence and to the dispersive behavior of the atmospheric surface layer. Industrial users are more familiar with an expression of the Pasquill stability classes, with a typical velocity at some reference height (usually 10 m) and roughness height as given in the tables below.

Wind speed at 10 m	Daytime insolation			Night time cloud cover thinly overc.	
m/s	Strong	Moderate	Slight	or > 4/8 cloud	or < 3/8 cloud
< 2	A	A - B	B	---	---
2 - 3	A - B	B	C	E	F
3 - 5	B	B - C	C	D	E
5 - 6	C	C - D	D	D	D
> 6	C	D	D	D	D

Table 1 : Pasquill stabil. classes related to wind speed and insolation

Pasquill stability class	Ambient temperature gradient			
	Less	then	- 1.90	C/100 m
A : very unstable	- 1.90	to	- 1.70	C/100 m
B : unstable	- 1.70	to	- 1.50	C/100 m
C : slightly unstable	- 1.50	to	- 0.50	C/100 m
D : Neutral	- 0.50	to	+ 1.50	C/100 m
E : slightly stable	More	then	+ 1.50	C/100 m
F : stable				

Table 2 : Pasquill stability classes versus thermal stratification

A pre-processor asking for these data, called METEO, was developed in order to calculate the relevant information for running the code. The physics it relies upon essentially relates the Monin-Obukhov length L which expresses the height at which thermal stresses balance the mechanical ones and the friction velocity u^* to practical data as shown below [5] :

- the bulk Richardson Number :

$$R_B = \frac{g}{T_o} \times \frac{\Delta \theta}{U^2} \times Z$$

- the Monin-Obukhov Length :

$$L = -R_B \times P_R^{-1} \times \frac{\ln\left(\frac{h_2}{h_1}\right) - \psi_h\left(\frac{h_2}{L}\right) + \psi_h\left(\frac{h_1}{L}\right)}{\left[\ln\left(\frac{Z}{Z_o}\right) - \psi_m\left(\frac{Z}{L}\right)\right]^2}$$

- the friction velocity :

$$u^* = \frac{ku}{\ln\left(\frac{Z}{Z_o}\right) - \psi_m\left(\frac{Z}{L}\right)}$$

h_1 and h_2 are typical heights between which the temperature Θ has been measured (in practice, temperature will not be measured at ground level), z_o is the roughness height to characterize the small scale irregularities of the surface, u the wind velocity at height z and g the gravity acceleration.

ψ_h and ψ_m are empirical functions which may be formulated as follows :

- *neutral stability conditions* ($dT/dz = -1 \text{ K/ 100 m}$) :

$$\psi_m = 0$$

$$\psi_h = 0$$

- *stable stability conditions* ($dT/dz > -1 \text{ K/ 100 m}$) :

$$\psi_m = -5 \frac{Z}{L}$$

$$\psi_h = -8 \frac{Z^2}{L^2} - 8 \frac{Z}{L}$$

- *unstable stability conditions* ($dT/dz < -1 \text{ K/ 100 m}$) :

$$\psi_m = \ln \frac{(1+x)^2 (1+x^2)}{8} - 2 \arctg(x) + \frac{\pi}{2}$$

$$\text{where : } x = \left(1 - 15 \times \frac{Z}{L}\right)^{\frac{1}{4}}$$

$$\psi_h = 2 \ln \frac{1+y}{2} \quad \text{where } y = \left(1 - 9 \frac{Z}{L}\right)^{\frac{1}{2}}$$

The resulting EUROCHLOR code architecture is shown in Figure 13 below.

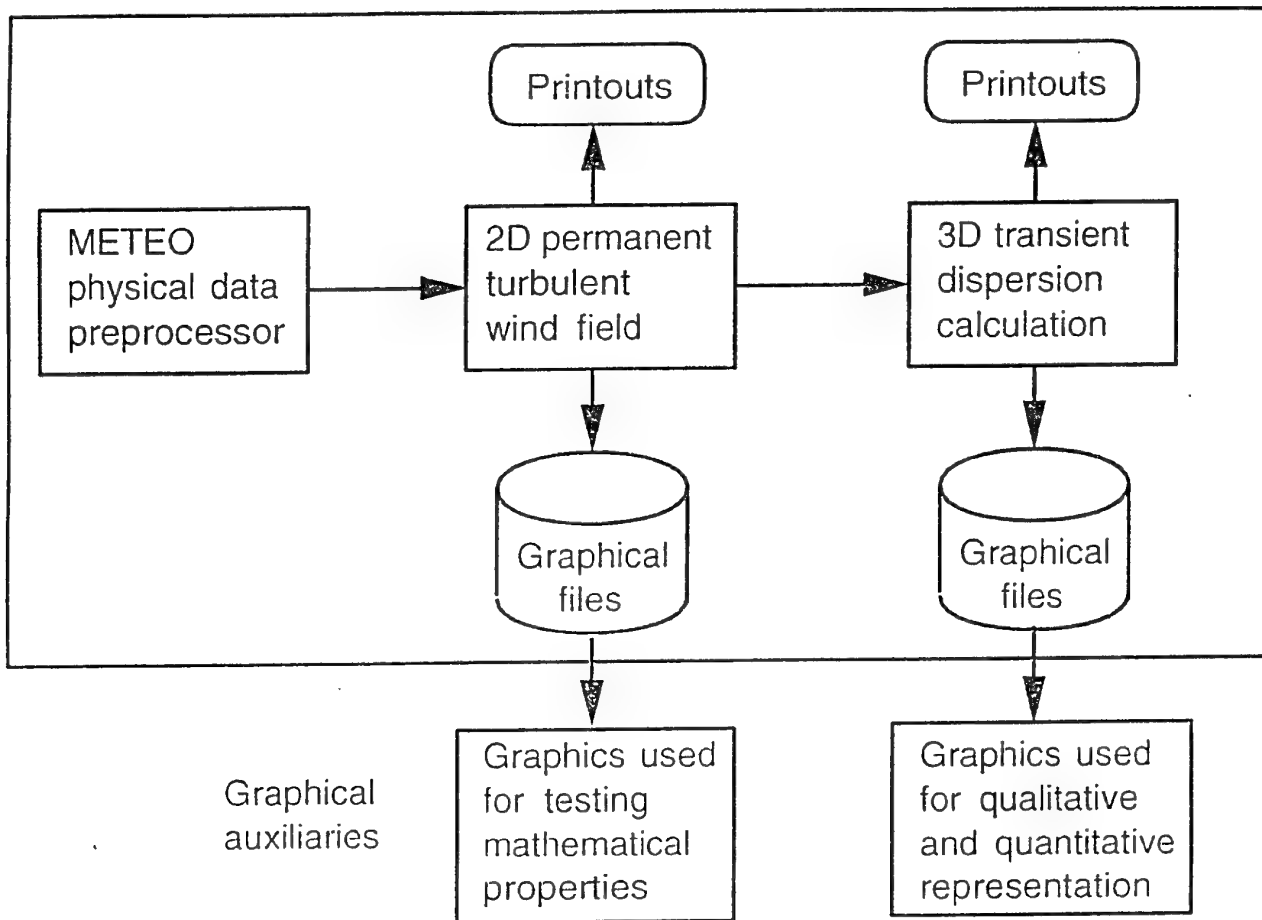


Figure 13 : The preprocessed EUROCHLOR Code architecture.

When developing the METEO pre-processor, the intention was twofold:

- to keep the input data tractable to industrial end-users,
- to balance the uncertainty on the information supplied to the model and the model inherent inaccuracy.

METEO was not able however to deal with common sense or expertise expressed in terms of rules close to the natural language. That is why a new approach called the Front-End Based Technology was investigated.

4.2. THE KNOWLEDGE BASED FRONT-END TECHNOLOGY

The KBFE technology was developed in the framework of an ESPRIT 2 project called FOCUS (No 2620) which started in december 1989 and finished mid 1994 [1,32,33]. Its main features are genericity, modularity and re-usability.

The purpose of the Front-End is to fill in the gap between the End-Users, typically Safety Engineers, and with the Back-Ends, typically EUROCHLOR or SEVEX. In addition to traditional computerized pre-processors like METEO, KBFEs should be capable to handle common sense, decision rules or rules of thumb which are quite frequent in the definition of Major Hazard scenarios. How to get the roughness height or the initial pollutant dilution factor may proceed from such a pragmatic approach, as well as the management of the constraints induced by the domain of applicability of the CFD code.

The expertise which traditionally lies in the hands of experts or consultants should, to some extent be captured, formalized and computerized [34] as shown in Figure 14 below.

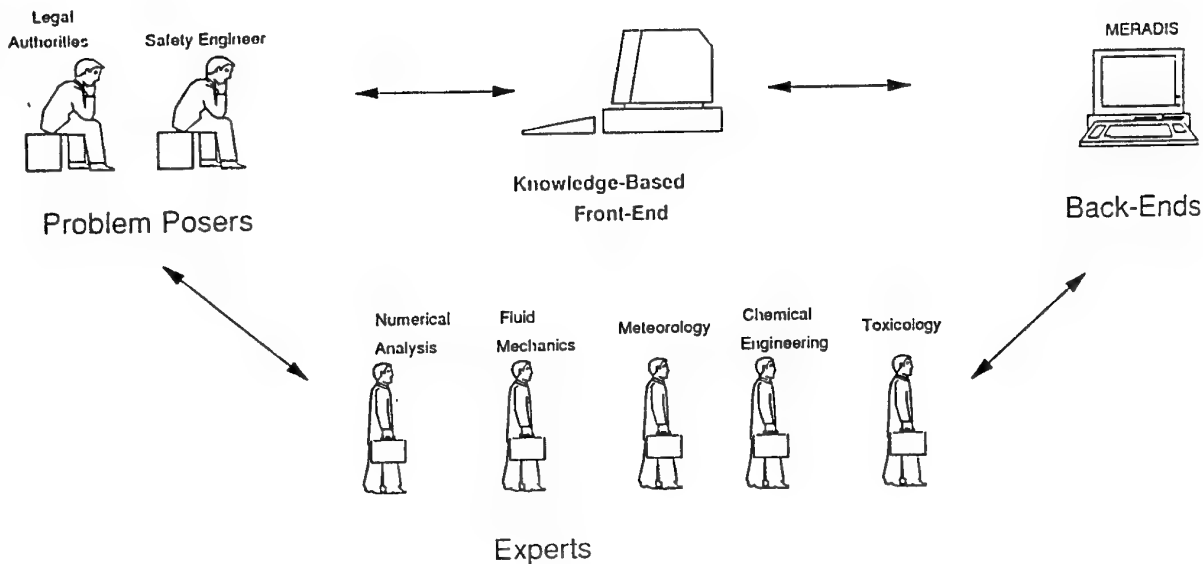


Figure 14 : The Knowledge Based Front-End Philosophy.

The Knowledge Based Front-End architecture is based on a communication harness which provides the framework for the interaction between end users, the application codes considered as Back-Ends and the knowledge-based modules

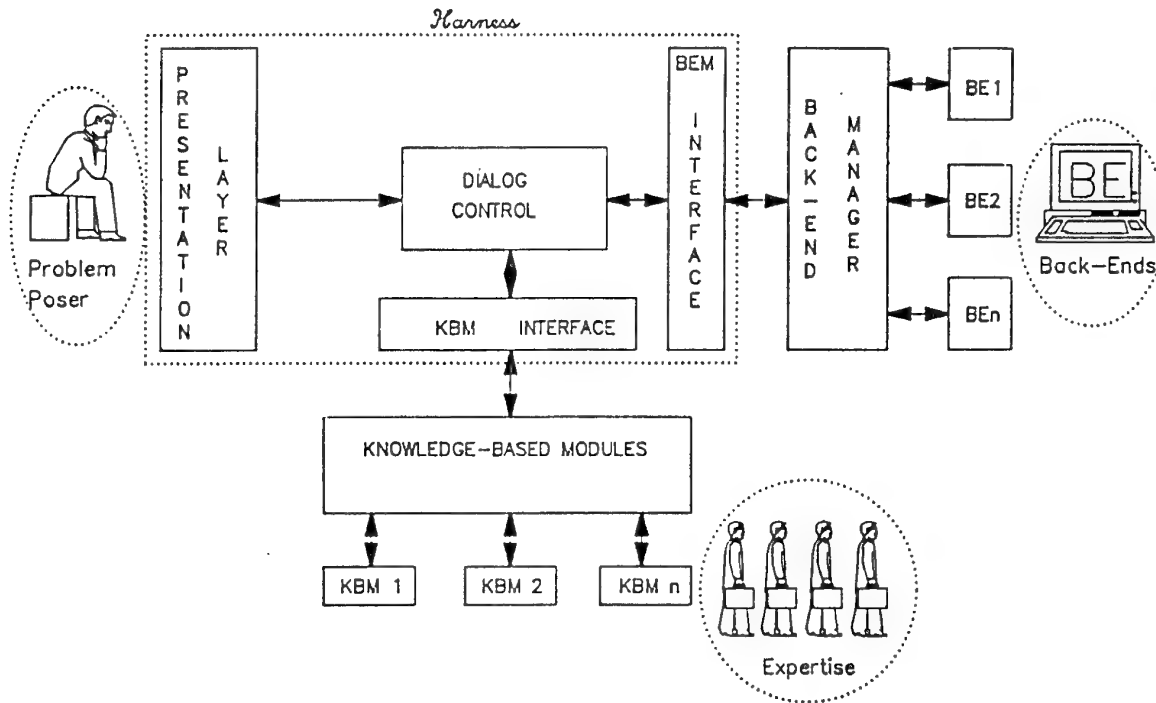


Figure 15 : The Knowledge Based Front-End Architecture.

The interactions between the KBFE and the Back-Ends are conceptually quite simple, they consist of:

- producing a structured input file with all the parameters of a simulation,
- reading and interpreting the output file(s) produced by the back-ends.

The End-User should however be provided with clear assistance and guidance when entering and validating the data and with reliable reason maintenance and adaptive dialogue capabilities. The SEDIS project that intends to produce a Knowledge Based Front-End to the EUROCHLOR code is still ongoing although with low priority. The specifications for a first prototype have been outlined and preliminary knowledge elicitation is achieved. The next steps will be structuring the knowledge and designing the Human Computer Interface [35], tasks that revealed much more complex and costly than it was expected.

The future of Knowledge-Based Systems will of course depend on the quality of the embedded CFD software; it seems however that the initial trend consisting of developing KBFE architectures, 'just' front-ending expertise to CFD codes will move to a more general Problem Solving Environment offering real time capabilities.

5. THE QUALITY ASSURANCE APPROACH FOR CALCULATION MODELS

Today there is quite an impressive number of computerised models covering various aspects of risk analysis; their quality however varies drastically and their reliability and field of application are not always well defined.

We can see only too clearly that the field of application, the limitations and even the use of models are very often poorly understood by end-users. The fact that this kind of tool is based on non-trivial scientific considerations may represent a considerable obstacle when making it available to users spread over a range of different activities or unable to acquire a thorough understanding of complex systems.

There is a wide gulf between the scientific community, at the heart of developments and research, and the industrial world. The first group which is well aware of the theoretical foundations of models considerably underestimates the gap separating an academic prototype from a validated industrial software, applicable in real cases. The second group often underestimates the need to invest in an understanding of models, or even how they are computerised, preferring to use "black boxes" whose inescapable "advantage" is to conceal the difficulties to users who do not have to worry about the relevance of the model.

In the framework of a working group, funded by the Directorate General XII of the European Commission (Model Evaluation Group), Dr. Rex Britter [36] stressed the need for methods and tools to evaluate and improve the quality of models. He also set out the bases for an evaluation protocol allowing the end-user to grasp the objectives, field(s) of application and limitations of the models unambiguously [37,38]. We ourselves have formalised this step [39], intending to provide users with industrial-type simulation tools, a straightforward procedure to evaluate the quality of calculation models of Major Hazard Consequences.

This procedural step naturally covers the following fields:

- Evaluation of the scientific quality of the mathematical model.
- Validation of the model in terms of all available techniques : analysis of sensitivity to physical parameters, comparison with experimental results, comparisons with other models and "benchmark exercises".
- Computation and algorithmic aspects requiring qualities of reliability, robustness and ease of maintenance.
- User-friendliness and fitness of the Man-Machine Interface to users' needs.
- Scientific and technical documentation for the model and its computerisation.

This step is definitely placed in the "Quality-Assurance" framework and is justified below.

A quality approach can be justified by the desire to clarify a field which is still blurred around the edges. In practical terms, this means :

- Producing a structured measurement of the quality of a model which can be communicated to all the interested parties (Legal Authorities, Industries, Central and Local Administrations, Insurance Firms, Consultants, Question and Research Groups).
- Authorising an open audit on the use of the model by end-users. This audit should result in a written opinion as to the relevance of the results, the field of applicability of the model and the type of users it is aimed at.
- Providing the end-user with clear documentation on the field of applicability of the model and the degree of accuracy of the results.

By means of these three initiatives, we should be able :

1. firstly, to encourage **and assist** the development and maintenance of quality models satisfying the "Fitness for purpose" criterion;
2. secondly, reduce any distortions existing between the models;
3. next, identify those improvements required for future models;
4. finally and especially, satisfy the expectations of users by satisfying the "Fitness for use" criterion.

The Quality approach for Environmental Calculation Models is based on 5 concepts :

- Scientific quality-assurance,
- Algorithmic quality-assurance,
- Computerisation quality-assurance,
- Man-Machine Interface quality-assurance,
- Model validation and analysis of sensitivity.

It presupposes two things :

- a clear definition of the end-users' expectations including amongst others :
 - the scale of the problem,
 - the types of scenario to be handled,
 - the nature and degree of accuracy of results to be provided;
- that the data used during the validation process are themselves subject to a certification process **by those who have established the Databases** in terms of the quality-assurance criteria.

5.1. THE SCIENTIFIC QUALITY-ASSURANCE.

This is based on a detailed presentation of the model, its underlying hypotheses and/or physical approximations, its limitations and duly motivated answers to the following questions :

- Is the mathematical modelling targeted at a given type of problem ? Does it cover the physical nature of the problem ? Totally or partially ?
- Do the hypotheses and/or approximations correctly reflect the main physical effects, omitting any side effects if the case arises ? Do they correctly take scale effects into consideration ?

- Can the limitations of the model be justified, primarily with regard to the problem in question ? Can they be removed and at what cost ?
- Is there a guarantee that no non-scientific constraint, e.g. hardware type, is behind excessive simplifications of the model ?

Scientific quality-assurance should also be capable of addressing the experimentation if this proves necessary, notably to support any choices made or validate the hypotheses.

Finally, scientific quality-assurance involves active participation in scientific events at the highest level as well as encounters with specialists. The same remark can be made for algorithmic quality-assurance which we will be covering in the next paragraph.

5.2. THE ALGORITHMIC QUALITY-ASSURANCE

This affects the numerical strand i.e. the approached formulation of the mathematical model to computer treatment. Algorithmic quality-assurance is characterised by three concepts :

- the stability of the scheme,
- the convergence of the scheme and,
- the accuracy of the scheme.

This strand of the modelling is very often hidden from the user for the obvious reason that (s)he is, in most cases, incompetent in this field, and questioning on numerical aspects may well perturb him(her).

We should remember that mathematical convergence is usually determined by stability and the numerical schemes used are supposed to be stable. By contrast, accuracy is closely linked to the grid, and it should be ensured that the code can converge towards the machine-zero, i.e. the residues do not stay and stagnate in terms of the number of iterations. In addition, the real accuracy involves defining the level of error as a function of the grid and verifying the slope (in a logarithmic graph). Another major condition to be determined is the refinement threshold from which point the solution is independent of the grid. This is clearly a function of the kind of problem, but it is only in this case that the validation of the physical models and the study of sensitivity described in paragraph 4.5. hereafter can be estimated objectively.

5.3. THE COMPUTERISATION QUALITY-ASSURANCE

This paragraph deals with how the models and, in particular, their numerical approximations have been computerised. At this stage, no consideration relating to the physical nature of the problem is included (other than those translating a direct influence of the physical nature on the calculation techniques being proposed), nor the algorithm itself.

We focus here on the quality (translation and performance) of the computer coding of numerical algorithms and relevant databases. In particular, the coding should either be an exact translation of the numerical algorithms and there should be no drift with regard to the analytical model.

In addition, the code's architecture should be modular and in particular the expert user should check experimentally the results announced in 5.2. **by himself**. The effort made in this field should also be considered at as early a stage as possible in the development of the computerised model for two reasons :

1. It is undesirable that, while the programme is being operated for practical purposes, questions which are of a purely mathematical nature should be considered.
2. The operating cost of the model, whether expressed as the number of operations (computational costs) or in currency (financial costs), depends crucially on the quality of the computerisation.

For the relevant Databases for the model, it must be carefully assured that :

- they are structured according to a standardised format if possible, and portable;
- their content has been validated and certified by experts. This validation and certification work is crucial both regarding the physical/chemical and cartographic data, including land characteristics;
- their content is accessible to the expert user.

5.4. THE MAN-MACHINE INTERFACE QUALITY-ASSURANCE

The Man-Machine Interface (MMI) strand involves the computerised interface enabling the end-user to interact with the application programme, both in terms of acquiring data and interpreting results. The MMI must be designed to allow the user to carry out his task successfully, in a user-friendly way and with the provision of any help necessary.

In particular, the MMI must help a user to check the adequation between the scenario being offered and the model underlying the application programme; it should be designed so that the system is in the service of the user and not the other way round.

5.5. MODEL VALIDATION AND ANALYSIS OF SENSITIVITY

The word validation is used in the strict sense of the term, as is the verification of suitability between those results predicted theoretically and experimental results. The term experimental results is used in the broad sense to mean :

- the results of real scale tests (field tests),
- the results of wind tunnel tests,
- results of "laboratory" or "pilot" scale tests,
- results provided by other models,
- benchmarking exercises.

The validation of a computerised mathematical model involves the prerequisite of the existence of validated databases and accessibility to these databases. **The validation supposes that the experimental results have not been used when developing the model itself.**

This exercise is usually a complex one, costly in terms of time for thought and use of the computer; it is often accompanied by qualitative validations and an analysis of sensitivity to the physical parameters intervening in the model. It may even require experimentation itself!

Qualitative validations are often the only ones that can be considered in the hypothesis of very complicated scenarios.

Analyses of sensitivity are intended to study the variability of results in terms of the variability of the physical and mathematical parameters of the model. Analyses of sensitivity for physical parameters are used to characterise the level of uncertainty of the model; they must contribute to defining the validity ranges.

QUESTIONNAIRE ON SCIENTIFIC QUALITY-ASSURANCE

- ◇ Do you have the context in which the mathematical model¹ was developed ?
- ◇ Are the model's designers accessible ?
If yes : - where ? [name(s), address(es)]
 - how ? (E-mail)
- ◇ Do you have a detailed mathematical description of the model including :
 - general equations for the model ?
 - the hypotheses and/or physical approximations leading to the operational model ?
 - the equations for the operational model ?
 - the initial conditions and/or boundary conditions ?
 - the internal parametrisation of the equations ?
- ◇ Is the mathematical description easily accessible ?
 - in the literature ?
 - from the model's designers ?
- ◇ Are the limitations of the model :
 - justified primarily from a physical reasoning ?
If yes : which ?
 - directly related to a specific industrial problem ?
If yes : which ?
 - independent of software constraints ?
(SW)
 - independent of hardware constraints ?
(HW)
- ◇ Has the model been validated ?
If yes : by whom ?
 where ?
 when ?
 in what context ?
 - with real scale tests (field tests)
 - with wind tunnels
 - with hydraulic tunnels
 - by inter-model comparisons
 - using laboratory or pilot experimentations
- ◇ Has the model encountered the opinion of specialists in :
 - international conferences ?
 - seminars or workshops ?
 If yes : where ?
 when ?
- ◇ Has the model been submitted to the opinion of industrial experts ?
If yes : to whom ?
 where ?
 when ?
 how ?

¹ Whenever the term "mathematical model" or simply "model" is used, it is a general term which in some cases can actually cover several models.

QUESTIONNAIRE ON ALGORITHMIC QUALITY-ASSURANCE

- | | |
|---|--|
| <p>◇ What algorithm² is used to discretise the mathematical model ?</p> <p>◇ Who was responsible for this choice ?</p> <p>◇ What are the references for the proposed model ?</p> <p>◇ Has the stability of the numerical scheme been studied ?
 If yes : by whom ?
 where ?
 when ?
 is the scheme unconditionally stable ?
 conditionally stable ?</p> <p>◇ Is the numerical scheme convergent ?
 If yes : who demonstrated this result ?
 where ?</p> <p>◇ What is the accuracy of the numerical scheme ?</p> <p>◇ Has a comparative study with other algorithms been made ?
 If yes : by whom ?
 where ?
 when ?
 are the results of this study available ?</p> <p>◇ What justified the choice of the algorithm :
 - its accuracy ?
 - its robustness ?
 - its ease of implementation ?</p> <p>◇ Can the algorithm be vectorised ?
 If yes : has it been vectorised ?</p> <p>◇ Can the algorithm be parallelised ?
 If yes : has it been parallelised ?</p> | |
|---|--|

- ◇ In what language(s) has the software been coded ?
- ◇ Are the source codes accessible ?
If yes : where ?
 how ?
If no : why not ?
- ◇ Is it structured in functional modules ?
- ◇ Is there a conceptual analysis file ?
If yes : where is it accessible ?
- ◇ Is there an organisational analysis file ?
If yes : where is it accessible ?
- ◇ Is the software documented ?
If yes : in which language(s)
- ◇ Is the user-interface functionally decoupled from the application modules ?
- ◇ Is/are the computer language(s) used standardised ?
If yes : is it the standardised version of the language(s) (without extension) that
has been used ?
- ◇ Is the code portable ?
If not : what proportion of the code is not portable ?
 why hasn't it been designed to be portable ?
- ◇ Is there an implementation procedure ?
If yes : where is it accessible ?
- ◇ Is there a user's manual ?
If yes : where is it accessible ?
- ◇ Is the software maintained ?
If yes : by whom ?
 where ?
 how ?
If no : why not ?

QUESTIONNAIRE ON COMPUTERISATION QUALITY-ASSURANCE

- ◇ On what computer platform(s) is the software available ?

- ◇ If the software was to be run on several machines, are the software versions the same release ?

- ◇ Is there a code version in single-length precision (32 bits) ?
 - If yes : is this precision enough ?
 - have comparisons with a double-length precision version of the code been made ?
 - If yes : by whom ?
 - where ?
 - on which machine(s) ?
 - have the results been included in an accessible report ?
 - If no : why not ?

- If no : why not ?

- ◇ Have the topographic data been structured to be portable where necessary ?
 - If yes : by whom ?
 - how ?
 - are they available ?
 - if yes : where ?
 - If no : why not ?

- ◇ Have the results of the calculation (e.g. field of wind and/or field of concentration) been structured to be portable ?
 - If yes : by whom ?
 - how ?
 - are they available ?
 - if yes : where ?
 - If no : why not ?

- ◇ Has a particular structure for files reserved for graphic designs been provided ?
 - If yes : what is it ?
 - If no : why not ?

QUESTIONNAIRE ON COMPUTERISATION QUALITY-ASSURANCE

- | | |
|--|--|
| <p>◇ Has the type of graphism used by the code been standardised (GKS, PHIGS, POSTSCRIPT, ...) ?</p> <p style="padding-left: 20px;">If yes : what standard is it based on ?</p> <p style="padding-left: 20px;">If no : why not ?</p> <p style="padding-left: 40px;">which solution has been adopted ?</p> <p>◇ Does the software require portions of code covered by external licences ?</p> <p style="padding-left: 20px;">If yes : how much does it cost ?</p> <p style="padding-left: 40px;">can these portions of code be easily replaced (at low cost) ?</p> <p>◇ Is the supply of the code accompanied by training in its use ?</p> <p>◇ Is there a Help Desk in the case of difficulties ?</p> <p style="padding-left: 20px;">If yes : where ?</p> <p style="padding-left: 40px;">accessible when ?</p> <p style="padding-left: 40px;">accessible how ?</p> | |
|--|--|

QUESTIONNAIRE ON THE QUALITY-ASSURANCE OF SENSITIVITY ANALYSIS

Analysis of mathematical sensitivity :

- ◇ Are the results of the calculation independent of the mathematical parametrisation ?
(answer only if the question is pertinent to the model)
 - spatial grid ?
 - time steps ?
 - relaxation parameters ?
 - artificial viscosity coefficients ?
 - criteria for stopping in iterative procedures ?
 - initial conditions used in iterative procedures ?
- ◇ Is the user capable of controlling these various points easily by himself ?

Analysis of physical sensitivity :

- ◇ Did the variability studies of calculation results concerning the physical parametrisation of the model cover the following :
 - the internal parameters of the model ?
If yes : what tests were made ?
by whom ?
where ?
the results : are they accessible ?
have they been published ?
have they been expertised ?
if yes : which expertise ?
by whom ?
where ?
 - the physical data of the programme ?
If yes : what tests have been made ?
by whom ?
where ?
the results : are they accessible ?
have they been published ?
have they been expertised ?
if yes : which expertise ?
by whom ?
where ?

- 0 Have the results of the model been compared with those from real scale tests ?
If no : why not ?
- If yes :
- Which ones ?
 - On what scenario platform ?
 - Did this platform have the consent of experts :
 - . from Industry ?
 - . from the competent Legal Authorities ?
 - . from specialised Consultants ?
 - Have the data relating to the scenarios and the results of the simulations been published ?
- If yes : by whom ?
where ?
when ?
- If no : why not ?
- 0 Have the data and the results of the various scenarios been analysed critically by external experts ?
- If yes : by whom ?
where ?
when ?
how ?
- If no : why not ?
- 0 Have the results of the model been compared with those from wind tunnel tests ?
- If no : why not ?
- If yes :
- Which ones ?
 - On what platform of scenarios ?
 - Has this platform had the consent of the experts :
 - . from Industry ?
 - . from the competent Legal Authorities ?
 - . from specialised Consultants ?
 - Have the data relating to the scenarios and the results of the simulations been published ?
- If yes : by whom ?
where ?
when ?
- If no : why not ?
- Have the data and the results of the various scenarios been analysed critically by external experts ?
- If yes : by whom ?
where ?
when ?
how ?
- If no : why not ?

If no : why not ?

If yes :

- Which ones ?
- On which scenario platform ?
- Has this platform had the consent of experts :
 - . from Industry ?
 - . from the competent Legal Authorities ?
 - . from specialised Consultants ?
- Have the data relating to scenarios and the results of the simulations been published ?

If yes : by whom ?

where ?

when ?

If no : why not ?

- Have the data and the results of the various scenarios been analysed critically by external experts?

If yes : by whom ?

where ?

when ?

how ?

If no : why not ?

If no : why not ?

If yes :

- Which ones ?
- On which scenario platform ?
- Has this platform had the consent of experts :
 - . from Industry ?
 - . from the competent Legal Authorities ?
 - . from specialised Consultants ?
- Have the data relating to scenarios and the results of the simulations been published ?

If yes : by whom ?

where ?

when ?

If no : why not ?

- Have the data and the results of the various scenarios been critically analysed by external experts ?

If yes : by whom ?

where ?

when ?

how ?

If no : why not ?

QUESTIONNAIRE ON VALIDATION QUALITY-ASSURANCE

◇ Have the results of the model been compared with those coming from other models ?

If yes :

- With which models ?
- On what scenario platform ?
- Has this platform had the consent of experts :
 - . from Industry ?
 - . from the competent Legal Authorities ?
 - . from specialised Consultants ?
- Have the data relating to scenarios and the results of the simulations been published ?

If yes : by whom ?

where ?

when ?

If no : why not ?

- Have the data and the results of the various scenarios been critically analysed by external experts ?

If yes : by whom ?

where ?

when ?

how ?

If no : why not ?

◇ Have the results of the model been critically analysed in a "benchmark exercise" ?

If yes : by whom ?

where ?

when ?

how ?

is a report available ?

QUESTIONNAIRE ON THE MAN-MACHINE INTERFACE QUALITY-ASSURANCE

- ◇ What category of users is the code aimed at ?
 - a fluid mechanics expert ?
 - an atmospheric physics expert ?
 - an engineer responsible for Industrial safety studies?
 - an engineer responsible for Emergency Plans with Legal Authorities ?
 - a Consultant in the field of major hazards ?

- ◇ Has the user-interface been developed with the help of end-users ?
 If yes : which ones ?
 where ?
 how ?

- ◇ Has the user-interface been evaluated (usability assessment) :
 - by end-users ?
 If yes : which ones ?
 where ?
 under what conditions ?
 is a final report available ?
 if yes : where ?
 If no : why not ?

 - by software engineering specialists ?
 If yes : which ones ?
 where ?
 under what conditions ?
 is a final report available ?
 if yes : where ?
 If no : why not ?

 - by cognitician engineers ?
 If yes : which ones ?
 where ?
 under what conditions ?
 is a final report available ?
 if yes : where ?
 If no : why not ?

 - by ergonomists ?
 If yes : which ones ?
 where ?
 under what conditions ?
 is a final report available ?
 if yes : where ?
 If no : why not ?

6. CONCLUSION

Starting from the observation that :

- an intensive use is made of the mathematical models as quantification tools for the consequences of Major Hazards,
- this use is going to increase,
- little has been done to formalise the evaluation of existing models and increase the transparency of the ins and outs of these models to the user,
- models are only a part of a larger Problem Solving Environment context

we wanted, in a practical sense, to set out the bases for a strict Quality-Assurance approach from our industrial experience.

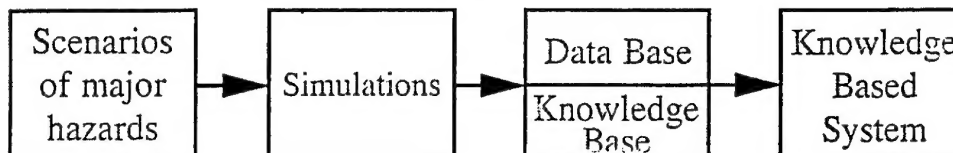
The questionnaire technique used in this work has been structured in such a way that a "task chain" approach, to be carried out by experts with different skills : modelling experts, physicists, chemists, engineers, mathematicians, computer experts, ergonomists and end-users.

Environmental Mathematical Modelling cannot be seen as an isolated discipline anymore; although it provides people with an essential simulation tool, its capabilities must be enhanced by domain knowledge in order to get a reliable and robust consequence analysis tool for industrial purposes.

In terms of strategy, the management of Quantified Major Hazards is to be thought of as a two phase strategy as shown in figure 16 below:

- the first one based on off-line simulations and
- the second structured as a real time operational system.

PHASE 1 : Off-line simulations



PHASE 2 : On line system

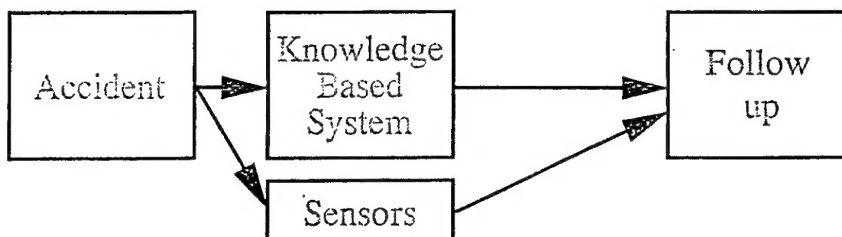


Figure 16 : Strategy for Major Hazard Consequences Management.

BIBLIOGRAPHY

1. ESPRIT 2 PROPOSAL FOCUS (Front-Ends for Open and Closed User Systems) Proposal Nr 2620, Contract Technical Annex, October 1988, revised January 1991.
2. J. VAN DIEST, J.-C. BASLER, C. BENOCCI, D. OLIVARI, M.-L. RIETHMULLER and E. VERGISON, Atmospheric dispersion of heavy gases in a complex environment, C.E.C. contract n° ENV 713-B CRS, Final report, Brussels, 1986.
3. A. FOUSSAT, Dispersion turbulente d'un polluant dans l'atmosphère, Thèse de Doctorat (Ph.D), Université Libre de Bruxelles & von Karman Institute, Brussels, 1980.
4. E. VERGISON, J. VAN DIEST and J.-C. BASLER, Atmospheric dispersion of toxic gases in a complex environment, Journal of Hazardous Materials, 22, 1989, pp. 331-357.
5. P. SCHREURS, Mathematical modelling of the dispersion of accidental releases of heavy gases at ground level in an industrial environment, Ph.D. THESIS, Katholieke Universiteit Leuven, Leuven, 1983.
6. J.-A. BUSINGER, H. TENNEKES, J.-C. WYNGAARD and S.-J. CAUCHE, A short course on atmospheric turbulence and air pollution modelling, The Hague, D. Reidel Publ. Co. Dordrecht, 1981.
7. V.W. NEE and L.S.G. KOVASZNAY, Simple phenomenological theory of turbulent shear flows. Phys. Fluids, 12 (3), 1969, pp. 473-484.
8. C.W. HIRT and J.-L. COOK, Calculating 3-D flows around structure and over flat terrain J. Comp. Phys., 1, 1972.
9. J.-E. WELCH, F.-H. HARLOW, J.-P. SHANNON and B.-J. DALY, The Mac Method - A computer technique for solving viscous, incompressible, transient fluid-flow problems involving free surfaces. Los Alamos Laboratory, LA-3425, Los Alamos, NM, 1969.
10. A.-A. AMSDEN and F.-H. HARLOW, The SMAC method : a numerical technique for calculating incompressible fluid-flows. Los Alamos Laboratory, LA-4370, Los Alamos, NM, 1970.
11. C. BENOCCI, D. OLIVARI and E. VERGISON, Modelling of turbulent dispersion of neutral and buoyant contaminants released from 2-D sources, von Karman Institute Technical Note 150, March 1984.
12. M.-L. RIETHMULLER and C. BORREGO, Measurements and predictions of complex turbulent flows, von Karman Institute LS 1980-03.

13. J.-M. LEVERT, C. DELVOSALLE and F. BENJELLOUN, Rapport de Synthèse, Projet Sevex, Vol. 1, Région Wallonne, 1992.
14. G. SCHAYES, B. MOYAUX, Projet Sevex, Rapport de synthèse, Vol. 3, Région Wallonne, 1992.
15. T. BOUROUAG, J.-F. DELIEGE, J.-P. DZISIAK, E. EVERBECQ and F. RONDAY, Les industries à risques majeurs en Région Wallonne. Rapport n° 4, Centre Environnement, Université de Liège, 1992.
16. R.-D. BORNSTEIN et al., Modeling the Polluted Coastal Urban Environment Vol. 1, EPRI Report EA-5091, 1987.
17. G.-A. BRIGGS, Diffusion Estimation for Small Emissions, ATDL Rep. n° 79, ATDL, P.O. Box E, Oak Ridge, TN 37830, 1973.
18. V. IANNELLO et al., 6th Symp. on Loss Prevention and Safety Promotion in the Process Industries, 58-1, Oslo, Norway, 1989.
19. C. J. WHEATLEY, Factors affecting cloud formation from releases of liquefied gases, I. Chem.E. Symposium on "Refinement of estimates of the consequences of heavy toxic vapor releases", 1986.
20. F.-P. RICOU and D.-B. SPALDING, J. Fluid Mechanics, 11(1), 21, 1961.
21. G. SCHAYES and Ph. THUNIS, Contribution n° 68, Université Catholique de Louvain, Institut d'Astronomie et de Géophysique Georges Lemaître, Chemin du Cyclotron, 2-B.1348 Louvain-la-Neuve, Septembre 1990.
22. G. TERRY and P. LACARRERE, Improving the Eddy Kinetic Energy Model for Planetary Boundary Layer Description. Bound. Layer Met. 25, 1983, pp. 63-88.
23. J.-F. LOUIS, A parametric model of vertical eddy fluxes in the atmosphere, Bound. Layer Meteor. 17, 1979, pp. 187-202.
24. T. YAMADA and BUNKER, Development of a nested grid second moment turbulence closure model and application to the 1982 Ascot Brush Creek data simulation, J. Atm. Sc. 27, 1988, pp. 562-578.
25. S. HANNA, Application in air pollution modelling. In Atmospheric Turbulence and Air Pollution Modelling, Ed. F. Nieuwstadt and H. Van Dop, Reidel, 1982, pp. 275-310.
26. P. ZANETTI, Lagrangian dispersion models. In Air Pollution Modelling Comp. Mech. Publ., Van Nostrand Reinhold, New York, 1990, pp. 185-222.
27. P.-J. SHOPOV, Complex Heavy Gas Dispersion - Part 1 : Bibliographic Research, Solvay, Direction Centrale Technique, 310, rue de Ransbeek, B-1120 Brussels, September 1993.

28. P.-J. SHOPOV, Complex Heavy Gas Dispersion - Part 2: Mathematical Modelling - Solvay, Direction Centrale Technique, 310, rue de Ransbeek, B-1120 Brussels, September 1993.
29. P.-J. SHOPOV, Conservation equation models and software for industrial risk assesment, In Computer Techniques in Environmental Studies V (v.1), Pollution Modelling, Ed. P. Zanetti, 1994, pp. 289-298.
30. P.-J. SHOPOV, Complex Heavy Gas Dispersion - Part 3 : The DISCO Model - Coding, testing and validation, Solvay, February 1995.
31. P.-J. SHOPOV, Compatibility of the boundary and the initial conditions in the DISCO Model, SOLVAY Internal Report, June 1994.
32. Y. DUTRON, B. GOVAERTS, E. VERGISON, February 1994, Esprit 2, Project FOCUS 2620, Specification of Problem Domains, Deliverable 3.1., January 1989.
33. Y. DUTRON, P. DE TOFFOL, T. ENGELS, B. GOVAERTS and E. VERGISON, Esprit 2, Project FOCUS 2620, SEDIS, A knowledge-based system for toxic gas dispersion simulation, Deliverable 3.7., September 1991.
34. J. THORBURN (1992) - How to size the domain of Major Hazard Scenarios in presence of obstacles, SOLVAY S.A., 310, rue de Ransbeek, B-1120 Brussels.
35. M. BROU, Evaluation d'interfaces logicielles Homme-Machine de Programmes de Calcul de Risques Majeurs, SOLVAY S.A., 310, rue de Ransbeek, B-1120 Bruxelles, 1993.
36. R.-E. BRITTER, The Evaluation of Technical Models used for Major-Accident Hazard Installations Department of Engineering, University of Cambridge, Trumpington Sheet, Cambridge CB2 1PZ, UK, August 1991.
37. Guidelines for Model Developers, Model Evaluation Group, E.C., Directorate-General XII, May 1994.
38. Model Evaluation Protocol, Model Evaluation Group, E.C., Directorate-General XII, May 1994.
39. E. VERGISON, Quality-Assurance Guide for the evaluation of mathematical models used to simulate and quantify the consequences of Major Hazards, SOLVAY S.A., Internal Report, September 1994.